

Bio-flotation: Bacterial Cell Hydrophobicity and Adhesion to Mineral Surfaces

By

Belinda Jean Bleeze

*Thesis
Submitted to Flinders University
for the degree of*

Doctor of Philosophy

College of Science and Engineering
March 2023

TABLE OF CONTENTS

Table of Contents.....	i
Abstract.....	v
Declaration.....	vii
Acknowledgements.....	viii
List of Publications	x
List of Figures	xii
List of Tables	xxii
Abbreviations.....	xxiii
1 Introduction.....	1
1.1 References.....	3
2 Literature Review	5
2.1 Sulfide minerals.....	5
2.1.1 Pyrite (Py).....	5
2.1.2 Chalcopyrite (Cp).....	7
2.1.3 Haematite (Hm)	9
2.1.4 Arsenopyrite (Asp)	9
2.1.5 Environmental Impact of Transition Metal Sulfide.....	10
2.2 Mineral Processing.....	12
2.2.1 Froth Flotation	13
2.2.2 Flotation Reagents	15
2.2.3 Micro Flotation	19
2.3 Microorganisms in Minerals Processing	19
2.3.1 Bacteria and archaea	20
2.3.2 Microbe – Mineral interaction.....	25

2.3.3	Bioleaching.....	27
2.3.4	Bio-flotation	29
2.3.5	Bio reagents	31
2.4	Biofilms and Extracellular Polymeric Substances.....	32
2.5	Objectives.....	37
2.6	References.....	38
3	Experimental and Techniques	45
3.1	Introduction.....	45
3.2	Material.....	45
3.2.1	Minerals	45
3.2.2	Archaea and Bacteria	46
3.2.3	Flotation setup/glassware	49
3.3	Experimental and Analysis	50
3.3.1	Scanning Electron Microscopy.....	50
3.3.2	Bio-Flotation Studies.....	53
3.3.3	X-Ray Diffraction	55
3.3.4	Photoemission Electron Microscopy	56
3.3.5	X-Ray Photoelectron Spectroscopy.....	60
3.3.6	Extracellular Polymeric Substance (EPS) Extraction and analysis.....	65
3.3.7	Fourier Transform Infrared Spectroscopy	69
3.3.8	Contact Angle Measurements	72
3.4	References.....	74
4	Selective Attachment of <i>Leptospirillum ferrooxidans</i> for the Separation of Chalcopyrite and Pyrite through Bio-flotation.....	80
4.1	Introduction.....	80
4.2	Experimental	81

4.2.1	Mineral Samples	81
4.2.2	Bacterial Culture and Adjustment to Mineral.....	82
4.2.3	Scanning Electron Microscopy (SEM)	82
4.2.4	Micro-Flotation Studies	83
4.3	Results and Discussion	84
4.3.1	Culture Growth and Monitoring	84
4.3.2	Attachment Studies	90
4.3.3	Micro-Flotation Studies	114
4.4	Conclusions.....	125
4.5	References.....	127
5	Leptospirillum Ferrooxidans Interaction with Chalcopyrite, Pyrite and Haematite for Separation Through Bio-flotation	132
5.1	Introduction.....	132
5.2	Experimental	133
5.2.1	Extracellular Polymeric Substance Supernatant.....	133
5.2.2	Mineral Preparation.....	133
5.2.3	Captive Bubble Contact Angle	134
5.2.4	FTIR-ATR Analysis.....	134
5.2.5	Photoemission Electron Microscopy	135
5.3	Results and Discussion	136
5.3.1	Micro-Flotation Studies	136
5.3.2	Contact Angle.....	146
5.3.3	Photoelectron Emission Microscopy Analysis	150
5.3.4	Spatial Distribution Overlay	169
5.4	Conclusions.....	170
5.5	References.....	172

6	<i>Acidithiobacillus ferrooxidans</i> Application in Bio-Flotation Separation of Chalcopyrite and Pyrite	177
6.1	Introduction.....	177
6.2	Experimental	178
6.2.1	Mineral Samples	178
6.2.2	Bacterial Culture and Adjustment to Mineral.....	178
6.2.3	Micro-Flotation Studies	178
6.2.4	Analysis	179
6.3	Results and Discussion	179
6.3.1	Culture Growth	179
6.3.2	Attachment Studies	184
6.3.3	Micro-Flotation Studies	198
6.3.4	XPS Analysis.....	206
6.4	Conclusions.....	222
6.5	References.....	224
7	Conclusions and Furture Directions	228
7.1	Conclusions.....	228
7.2	Future Directions.....	230
7.3	References.....	234
	Appendix I: Bio-flotation Literature Comparison	xiii
	Appendix II: Procedures	xvii
	Nuclear Magnetic Resonance Spectroscopy (NMR).....	xxi
	Appendix III: Sulfur XPS.....	xxvi
	Appendix IV: EDAX Anaysis	xxvii

ABSTRACT

Precious and core metals, such as copper, are essential for the development and improvement of modern-day technologies. As a high proportion of precious metals are found in sulfide minerals, the efficiency of sulfide mineral beneficiation processes is significant. Current beneficiation processes, namely froth flotation, are optimised for high-grade ore using harmful inorganic chemicals to produce a separation efficiency of no more than 80%. This inefficient separation leads to high metal content in mine tailings, which has been linked to environmental issues such as acid mine drainage. As the depletion of high-grade ore continues, beneficiation processes need to evolve to produce more efficient and ecofriendly refinement processes for low-grade ore.

This thesis investigates the optimisation of chalcopyrite recovery through bio-flotation from a mixed mineral system using bioleach microbes, *Leptospirillum ferrooxidans* and *Acidithiobacillus ferrooxidans*, and their metabolic products. To identify the conditions for optimal recovery, the impact of growth conditions on the behaviour of *Leptospirillum ferrooxidans* and *Acidithiobacillus ferrooxidans*, and composition of their Extracellular Polymeric Substances (EPS), is required. Investigating this will increase the understanding around what parameters in the bio-flotation system influences the separation and recovery of chalcopyrite.

A combination of microscopic and spectroscopic techniques were used to investigate the interactions between both *L. ferrooxidans* and *A. ferrooxidans* with pyrite and chalcopyrite mineral surfaces. These interactions are key in understanding microbial, and bio-reagent, implications on minerals processing of sulfide minerals. Scanning electron microscopy was used to determine preferential attachment and mechanisms of both *L. ferrooxidans* and *A. ferrooxidans*. Preferential attachment was observed for *L. ferrooxidans* but not *A. ferrooxidans*. This indicates *A. ferrooxidans* has greater resilience to changing growth conditions and toxic metals, stemming from their ability to utilize both iron and sulfur oxidative pathways to produce energy. This study indicates that the mechanism of attachment is dependent on the growth condition and not the bacterial strain.

Evidence of EPS production and biofilm formation was identified in both bacterial strains with discernible differences observed in the presence and attachment. The *A. ferrooxidans* were identified to produce both EPS and biofilm before the *L. ferrooxidans*. Investigating the link between metabolic products and flotation behaviour was made through micro-flotation tests. The presence of bacterial cells, either *L. ferrooxidans* or *A. ferrooxidans*, directly impacts the recovery of mineral by increasing the suppression of all minerals within the system. Removal of cells from the system resulted in selective suppression of pyrite, with the degree of suppression dependent on the strain and growth condition. Contact angle measurements support this, with an increase in heterogeneity and wettability of the pyrite surface when exposed to EPS supernatant and minimal change observed on the chalcopyrite surface.

Photoemission spectroscopy and X-ray photoelectron spectroscopy was used to analyse the surface states of pyrite and chalcopyrite exposed to bacterial cells and extracellular polymeric substances. Investigation of the surface chemistry changes can help the flotation behaviour observed be further understood. Analysis confirms the EPS can interact with mineral surfaces with and without the presence bacterial cells. PEEM analysis indicates that the EPS components show preferential oxidation of pyrite in a mixed mineral system, with preferential attachment of EPS to pyrite up to 72 h. The increase in complex organic molecules, identified to contain amides and carboxylic acids, correlates with the changes in flotation behaviour, with the primary EPS component identified as polysaccharides. This finding supports the notion that EPS and its composition is a key factor in the successful separation of chalcopyrite from pyrite in bio-flotation.

DECLARATION

I certify that this thesis does not incorporate, without acknowledgement, any material previously submitted for a degree or diploma in any university; and the research within will not be submitted for any other future degree or diploma without the permission of Flinders University; and to the best of my knowledge and belief, does not contain any material previously published or written by another person except where due reference is made in text.

..... Date 01 / 08 / 2022

(Signature)

ACKNOWLEDGEMENTS

First and foremost, I would like to thank my supervisor Professor Sarah Harmer. Over the journey of my PhD you provided support, wisdom and encouragement – I would not have made it to the end without your kindness or patience. The opportunities you provided, both scientifically and personally, encouraged me to grow as a scientist and as a person.

This project would not have come to fruition without the dedication and hard work of the technical and support staff who assisted me throughout my PhD. This includes the staff of Microscopy Australia (Flinders Microscopy and Microanalysis, and Adelaide Microscopy), Flinders Analytical, Future Industries Institute (University of South Australia) and the National Synchrotron Radiation Research Centre, who were incredibly generous with their time and knowledge. In particular, I would like to thank Kane and Kanis from NSRRC for their hospitality and generosity through the late nights at the PEEM beamline. I would also like to acknowledge the Australian Research Council for the funding (FT110100099) and the International Synchrotron Access Program (ISAP). Aspects of this project would not have been possible without this funding.

To the Harmer research group, past and present, thank you. I appreciate every piece of glassware that you scrubbed, every autoclave run you did, and every minute spent on the pH probe to adjust the many litres of media required to keep the lab running. I also appreciate the lifelong friendships that were formed. Specifically, I would like to thank Zoe Pettifer and Sian LaVars for the late-night dumpling feeds, coffee dates, keeping me sane. I would also like to thank my PhD peers Reece, Meghan, and Emily – your positivity and solidarity helped me when the PhD life became isolating and daunting.

Finally, I would like to thank my support network of family and friends. Each and every one of you have enabled me to pursue my passion. To my mother and father, thank you for teaching me resilience and patience, both have been instrumental throughout my study. Thank you for always being in my corner; I could never thank you enough for the home cooked meals, the unconditional love, and the unwavering support. To my friends, thank you for understanding my absence and loving me anyway. I appreciate all the meals, caffeine, hugs and laughs you have provided and shared with me. Most of all I would like to thank my partner, Ian, you have

experienced every high and every low of my PhD and never complained. Without your love, support and encouragement I would not be where I am or who I am without you – I love you.

LIST OF PUBLICATIONS

Journal Articles

Bleeze, B., Zhao, J., & Harmer, S. L. (2018). Selective Attachment of *Leptospirillum ferrooxidans* for Separation of Chalcopyrite and Pyrite through Bio-Flotation. *Minerals*, 8(3), 86.

Oral Presentations

Bleeze, B. J., Perkins, M. V. and Harmer, S. L. (2018) Investigating the Surface Chemistry Responsible for the Successful Separation of Pyrite from Chalcopyrite via Bio-flotation. ICONN 2018 International Conference on Nanoscience and Nanotechnology, 29 January – 2 February 2018, Wollongong, Australia.

Poster Presentations

Bleeze, B. J. and Harmer, S. L. (2015) Separation of Chalcopyrite and Pyrite through Bio-flotation. Centre for NanoScale Science and Technology Annual Conference, 17 June 2015, Tonsley Adelaide, Australia.

Bleeze, B. J. and Harmer, S. L. (2015) Separation of Chalcopyrite and Pyrite using Bio-flotation. PacificCHEM, 15-20 December 2015, Hawaii, America.

Bleeze, B. J. and Harmer, S. L. (2016) Separation of Chalcopyrite and Pyrite through Bio-flotation. ICONN 2016 International Conference on Nanoscience and Nanotechnology, 7-11 February 2016, Canberra, Australia.

Bleeze, B. J., Perkins, M. V. and Harmer, S. L. (2016) Bioflotation: Bacterial Cell Hydrophobicity and Adhesion to Mineral Surfaces. Centre for Nanoscale Science and Technology Annual Conference, 14 June 2016, Tonsley Adelaide, Australia.

Bleeze, B. J., Perkins, M. V. and Harmer, S. L. (2017) Identification of Surface Chemical States responsible for Mineral Separation through Bio – Flotation. Centre for Nanoscale

Science and Technology Annual Conference, 13th June 2017, Tonsley Adelaide, Australia.

Bleeze, B. J., Perkins, M. V. and Harmer, S. L. (2018) Detection and Mapping of eDNA in *Leptospirillum ferrooxidans* Extracellular Polymeric Substance. Centre for Nanoscale Science and Technology Annual Conference, 14th June 2018, Tonsley Adelaide, Australia.

LIST OF FIGURES

Figure 2.1: The unit cell structure of cubic pyrite (FeS_2 ; image adapted from Hicks, et al. [10])	6
Figure 2.2: The unit cell structure of chalcopyrite (image adapted from Mehl, et al. [16]).....	8
Figure 2.3: Unit cell structure of hematite (image adapted from Mehl, et al. [16])	9
Figure 2.4: Pourbaix diagram of pyrite (a, at 25°C), chalcopyrite (b, at 21°C) and haematite (c, at ambient temperature); adapted from Kocabag, et al. [35] pyrite, Fairthorne, et al. [36] chalcopyrite, and Shimizu, et al. [37] haematite.	12
Figure 2.5: Schematic Representation of a Froth Flotation Cell showing mineral attachment to air bubbles (image obtained from Napier-Munn and Wills [4])	14
Figure 2.6 Mineral recovery curve for micro flotation showing the influence of particle size [4].....	19
Figure 2.7: Schematic of the three microbe-mineral contact mechanisms. Adapted from Crundwell [32]	26
Figure 2.8: Reaction pathways for metal extraction from metal sulfides using <i>A. ferrooxidans</i> (<i>A. f</i>) and <i>L. ferrooxidans</i> (<i>L. f</i>) . Image from Blowes, et al. [6] adapted from Sand, et al. [69].....	28
Figure 2.9: Schematic of biofilm formation on a surface. Adapted from Pinto, et al. [95]	33
Figure 3.1: Growth phases of cultures. Lower curve: concentration of cells against time. Upper curve: Rate of growth expected for respective phase. Vertical dotted marks represent the limits of phases. Image from Monod [4]	48
Figure 3.2: Schematic of the modified Hallimond tube for micro-flotation set up.....	50
Figure 3.3: Schematic illustrating the possible electron interactions which occur during scanning electron microscopy, showing the production of secondary electron, back scattered electron, and characteristic x-ray.....	51
Figure 3.4: Optics schematic for the photoemission electron microscopy (PEEM) end-station, from [http://efd.nsrrc.org.tw/EFD.php?num=242]	56
Figure 3.5: Schematic of XPS sample preparation process.....	61
Figure 3.6: Schematic of an ATR-FTIR system from Ausili, et al. [75]	69
Figure 3.7: Schematic representation of the three phase contact line at equilibrium, adapted from Abaka-Wood, et al. [84].....	72

Figure 4.1: Growth curve of <i>L. ferrooxidans</i> in HH media with soluble Fe ²⁺ monitored over 240 h	85
Figure 4.2: Fe ²⁺ iron concentration of <i>L. ferrooxidans</i> grown on HH media with iron sulfate heptahydrate solution	86
Figure 4.3: Growth curve of <i>L. ferrooxidans</i> adapted to pyrite in HH media, monitored over 55 days.....	87
Figure 4.4: Growth curve of <i>L. ferrooxidans</i> adapted to chalcopyrite in HH media, monitored over 55 days.....	88
Figure 4.5: Growth curve of <i>L. ferrooxidans</i> adapted to arsenopyrite in HH media, monitored over 50 days.....	89
Figure 4.6: SEM images of the ‘honey comb’ structure observed on pyrite at 48 h (a), and PolyP and media salt precipitation observed on chalcopyrite at 24 h (b); imaged at an accelerating voltage of 20 kV, spot size of 3 (a) and 4 (b), with a magnification of 5000x (a) and 25000x (b).....	91
Figure 4.7: SEM images of impurities observed in the HH media controls for pyrite (a and b) and chalcopyrite (c and d); imaged at a magnification of 3000x (a and b), 12000x (c) and 6000x (d) and an accelerating voltage of 10kV (a, b and d) and 5kV (c).....	92
Figure 4.8: SEM image of pyrite particles exposed to HH media at exposure times 0 h (a – b), 2 h (c – d) and 12 h (e – f); imaged at a magnification of 1200x (b, d and f), 3000x (a), and 6000x (c and e), with an accelerating voltage of 10 kV.....	93
Figure 4.9: SEM image of chalcopyrite particles exposed to HH media at exposure times 0 h (a), 2 h (b – c) and 12 h (d), imaged at a magnification of 3000x (a), 4000x (b), 12000x (c) and 14000x (d), with an accelerating voltage of 5 kV	94
Figure 4.10: SEM image of pyrite particles exposed to HH media at exposure times 24 h (a – c) and 36 h (d – f); imaged at a magnification of 3000x (a) and 6000x (b – f), with an accelerating voltage of 10 kV	96
Figure 4.11: SEM image of chalcopyrite particles exposed to HH media at exposure times 24 h (a – b), 36 h (e) and 48 h (d), imaged at a magnification of 3000x (d), 6000x (a and c) and 12000x (b), with an accelerating voltage of 5 kV (b) and 10 kV (a, c and d).....	96
Figure 4.12: SEM image of pyrite particles exposed to HH media at exposure times 48 h (a – b), 60 h (c – d) and 72 h (e – f); imaged at a magnification of 3000x (c and e), 6000x (a, b and f) and 12000x (d), with an accelerating voltage of 10 kV.....	98

Figure 4.13: SEM image of chalcopyrite particles exposed to HH media at exposure times 60 h (a), 72 h (b) and 168 h (c and d), imaged at a magnification of 6000x (a and d) and 12000x (b and c), with an accelerating voltage of 10 kV.....99

Figure 4.14: SEM image of *L. f* adjusted to pyrite exposed to pyrite particles in HH media at exposure times 0 h (a – b) and 2 h (c – f); imaged at a magnification of 6000x (a, c, d and f), 1600x (b) and 12000x (e), with an accelerating voltage of 5 kV.....101

Figure 4.15: SEM image of *L. f* adjusted to pyrite exposed to pyrite particles in HH media at an exposure time of 12 h; imaged at a magnification of 2400x (a), 5000x (b), and 10000x (c and d), with an accelerating voltage of 5 kV.....102

Figure 4.16: SEM image of *L. f* adjusted to pyrite exposed to pyrite particles in HH media at an exposure time of 24 h; imaged at a magnification of 5000x (a and d), and 10000x (b and c), with an accelerating voltage of 5 kV103

Figure 4.17: SEM image of *L. f* adjusted to pyrite exposed to pyrite particles in HH media at an exposure time of 36 h; imaged at a magnification of 5000x (a and c), and 10000x (b and d), with an accelerating voltage of 5 kV104

Figure 4.18: SEM image of *L. f* adjusted to pyrite exposed to pyrite particles in HH media at an exposure of 48 h (a – c) and 60 h (d – f); imaged at a magnification of 6000x (a, d and f), 12000x (c and e), and 24000x (b) with an accelerating voltage of 10 kV105

Figure 4.19: SEM image of *L. f* adjusted to pyrite exposed to pyrite particles in HH media at an exposure time of 72 h (a and b) and 168 h (c and d); imaged at a magnification of 6000x (a and b), 16000x (d) and 24000x (e) with an accelerating voltage of 10 kV (a and b) and 5 kV (c and d).....106

Figure 4.20: SEM image illustrating attachment of *L. f* adjusted to pyrite to impurities at 60 h (a) and leaching at 168 h (b); imaged at a magnification 3000x (a) and 6000x (b) with an accelerating voltage of 10 kV107

Figure 4.21: SEM image of *L. f* adjusted to chalcopyrite exposed to chalcopyrite in HH media at exposure time of 0 h (a – b), 2 h (c – d) and 12 h (e – f); imaged at a magnification of 6000x (a – c) and 12000x (d – f) with an accelerating voltage of 10 kV (a – b) and 5 kV (c – f).....108

Figure 4.22: SEM image of *L. f* adjusted to chalcopyrite exposed to chalcopyrite in HH media at exposure time of 24 h (a), 36 h (b), 48 h (c and d), 60 h (e) and 72 h (f); imaged at a

magnification of 3000x (a and b), 6000x (c – e) and 16000x (f) with an accelerating voltage of 10 kV (a, b, e and f) and 5 kV (c and d).....	110
Figure 4.23: SEM image of <i>L. f</i> adjusted to chalcopyrite exposed to chalcopyrite in HH media at exposure time of 168 h; imaged at a magnification of 8000x (a) and 3000 (b) with an accelerating voltage of 10 kV	111
Figure 4.24: FTIR-ATR of pyrite showing unreacted pyrite (a), pyrite in HH media at 0 h (b), pyrite in HH media at 168 h (c), and pyrite exposed to <i>L. f</i> at 168 h (d).....	113
Figure 4.25: FTIR-ATR of chalcopyrite showing unreacted chalcopyrite (a), chalcopyrite in HH media at 0 h exposure (b), chalcopyrite in HH media at 168 h (c), and chalcopyrite exposed to <i>L. f</i> at 168 h (d).....	114
Figure 4.26: Differential flotation test recovery for HH Media control pH 1.8 as collector-free flotation tests (a); in the presence of PIPX collector (b)	115
Figure 4.27: Differential flotation test recovery from HH Media control pH 1.8 in the presence of NaHSO ₃ depressor as collector-free flotation tests (a); in the presence of PIPX collector (b).....	116
Figure 4.28: Differential flotation test recovery from Milli-Q pH 9 as collector-free flotation tests (a); in the presence of PIPX collector (b)	117
Figure 4.29: Differential flotation test recovery from <i>L. f</i> grown in HH media with iron sulfate as collector-free flotation tests (a); in the presence of PIPX collector (b)	119
Figure 4.30: Differential flotation test recovery from <i>L. f</i> adapted to pyrite as collector-free flotation tests (a); in the presence of PIPX collector (b)	120
Figure 4.31: Differential flotation test recovery from <i>L. f</i> adapted to chalcopyrite as collector-free flotation tests (a); in the presence of PIPX collector (b).....	121
Figure 4.32: Differential flotation test recovery from <i>L. f</i> adapted to arsenopyrite as collector-free flotation tests (a); in the presence of PIPX collector (b)	122
Figure 4.33: Differential flotation test recovery from EPS supernatant of <i>L. f</i> adapted to pyrite as collector-free flotation tests (a); in the presence of PIPX collector (b).....	123
Figure 4.34: Differential flotation test recovery from EPS supernatant of <i>L. f</i> adapted to chalcopyrite as collector-free flotation tests (a); in the presence of PIPX collector..	124
Figure 4.35: Differential flotation test recovery from EPS supernatant of <i>L. f</i> adapted to arsenopyrite as collector-free flotation tests (a); in the presence of PIPX collector .	125

Figure 5.1: Single mineral micro-flotation for baseline conditions as a collector-free and in the presence of collector at 48 h and 72 h exposures	137
Figure 5.2: pH (a) and Eh (b) measurements for baseline single mineral flotation tests.....	139
Figure 5.3: Single mineral micro-flotation tests as collector-free and in the presence of collector for mineral exposed to EPS supernatant at an exposure of 48 h and 72 h exposures.....	140
Figure 5.4: pH (a) and Eh (b) measurement for EPS supernatant single mineral flotation tests	142
Figure 5.5: Recovery of Cp, Py and Hm differential micro-flotation tests as a function of time in baseline conditions as collector-free flotation tests and in the presence of PIPX collector	144
Figure 5.6: Recovery of Cp, Py and Hm differential micro-flotation tests as a function of time exposed to EPS supernatant as collector-free and in the presence of PIPX collector	145
Figure 5.7: pH (a) and Eh (b) measurement for the mixed mineral flotation tests with HH media and EPS supernatant.....	146
Figure 5.8: FTIR-ATR Analysis of pyrite and chalcopyrite exposed to EPS supernatant of <i>L. ferrooxidans</i> adapted to chalcopyrite showing unreacted pyrite (a), unreacted chalcopyrite (b), pyrite at 48 h (c), chalcopyrite at 48 h (d), pyrite at 72 h (e) and chalcopyrite at 72 h (f).....	149
Figure 5.9: Corresponding PEEM image (background removed) of the leading adsorption edge for the EPS supernatant 48 h fresh at (a) 931.2 eV and (b) 932.9 eV. FOV = 450 μm	152
Figure 5.10: TEY Cu $L_{2,3}$ -edge NEXAFS spectrum for mixed mineral coupon exposed to (a) HH media control 48 h; (b) HH media control 72 h; (c) EPS supernatant 48 h – frozen; (d) EPS supernatant 72 h; (e) EPS supernatant 48 h – fresh; (f) EPS supernatant 7 days.....	154
Figure 5.11: TEY Fe $L_{2,3}$ -edge NEXAFS spectrum for mixed mineral coupon exposed to (a) HH media control 48 h; (b) HH media control 72 h; (c) EPS supernatant 48 h – frozen; (d) EPS supernatant 72 h; (e) EPS supernatant 48 h – fresh; (f) <i>L. f</i> on Cp 72 h; (g) EPS supernatant 7 days	157
Figure 5.12: Extracted Fe L_3 -edge spectra collected from the stack of the 48 h EPS supernatant (frozen) sample identifying (a) oxidised chalcopyrite (b) pyrite (c)	

haematite and (d) RGB overlay of mapped spectra; inset images illustrate what regions correspond with the spectra. FOV = 450µm	159
Figure 5.13: Extracted Fe L _{2,3} – edge spectra collected from the stack of the 72 h EPS supernatant sample identifying (a) chalcopyrite (b) pyrite (c) haematite and (d) RGB overlay of mapped spectra; inset images illustrate which regions correspond to the respective spectrum. FOV = 450µm	160
Figure 5.14: Extracted Fe spectra from the residual of the three-component fit for 72 h EPS supernatant sample, the inset image illustrates the region where the spectrum is found. FOV = 450µm.....	161
Figure 5.15: Extracted Fe L _{2,3} – edge spectra collected from the stack of the 7-day EPS supernatant sample identifying (a) chalcopyrite (b) pyrite (c) haematite and (d) RGB overlay of mapped spectra; inset images demonstrate the regions where the respective spectrum is identified. FOV = 450µm	162
Figure 5.16: TEY O K-edge NEXAFS spectrum for (a) HH media control 48 h; (b) HH media control 72 h; (c) EPS supernatant 48 h – Frozen; (d) EPS supernatant 72 h; (e) EPS supernatant 48 h – Fresh; (f) <i>L. f</i> adjusted to Cp 72 h; (g) EPS supernatant 7-days...	164
Figure 5.17: O K-edge images of EPS supernatant exposed samples for 48 h (a-d) and 72 h (e-f) at a photon energy of 530 eV (a), 531.3 eV (b and e), 532.3 eV (c) and 537 eV (d and f). FOV = 450 µm.....	165
Figure 5.18: Images of the EPS supernatant 72 h samples showing the spatial distribution of carbon at 288 eV (a), 290 eV (b) and iron at 708.5 eV (c). FOV = 450 µm.	168
Figure 5.19: TEY C K-edge spectrum for mixed mineral coupons exposed to (a) HH media control 48 h; (b) HH media control 72 h; (c) EPS supernatant 48 h frozen; (d) EPS supernatant 72 h; (e) EPS supernatant 7-day; (f) <i>L. f</i> Cp 72 h	169
Figure 5.20: RGB overlay for EPS Supernatant samples at 48 h – frozen (a); 72 h (b), where Red = Copper, Green = Carbon, and Blue = Oxygen. FOV = 450 µm.....	170
Figure 6.1: Growth of <i>Acidithiobacillus ferrooxidans</i> on HH media with iron sulfate over 240 hours.....	180
Figure 6.2: Growth of <i>Acidithiobacillus ferrooxidans</i> adjusted to pyrite in HH media monitored over 55 days	181
Figure 6.3: Growth of <i>Acidithiobacillus ferrooxidans</i> adjusted to chalcopyrite over 55 days	182

Figure 6.4: Growth of *Acidithiobacillus ferrooxidans* adjusted to arsenopyrite over 55 days183

Figure 6.5: SEM image of impurities observed within the pyrite samples, showing a particle with multiple cleavages at 0 h (a) and multiple particles cemented together at 48 h (b); imaged at a magnification of 8000x (a), 4000x (b) and an accelerating voltage of 10 kV185

Figure 6.6: SEM image of *A. f* adjusted to pyrite exposed to pyrite particles in HH media at 0 h (a) and 2 h (b-d) imaged at a magnification of 8000 x (a) and 6000 x (b-d) and an accelerating voltage of 10 kV186

Figure 6.7: SEM image of *A. f* adjusted to pyrite particles at 12 h imaged at a magnification of a 6000x and an accelerating voltage of 5 kV (a) and 10 kV (b-d).....187

Figure 6.8: SEM image of *A. f* adjusted to pyrite exposed to pyrite particles at 24 h (a – c) and 36 h (d – f) imaged at a magnification of 6000x (a), 5000x (b), 10000x (c), 8000x (d and f), and 4000x (e); and an accelerating voltage of 10 kV (a – d) and 5 kV (e and f)188

Figure 6.9: SEM image of *A. f* adjusted to pyrite exposed to pyrite particles at 48 h exposure imaged at a magnification of 12000x (a), 15000x (b), and 8000x (c and d); and an accelerating voltage of 5 kV (a and b) and 10 kV (c and d)189

Figure 6.10: SEM image of *A. f* adjusted to pyrite exposed to pyrite particles at 60 h (a-c) and 72 h (d-f) imaged at a magnification of 10000 x (a, c and d), 20000 x (b), 5000 x (e) and 12000 x (f); and an accelerating voltage of 5 kV (a-c), 10 kV (d and f) and 20 kV (e)190

Figure 6.11: SEM image *A. f* adapted to pyrite exposed to pyrite showing attachment to particles of impurity at 72 h exposure, imaged at a magnification of 5000x (a) and 12000x (b) and an accelerating voltage of 20 kV191

Figure 6.12: SEM image of *A. f* adapted to chalcopyrite exposed to chalcopyrite at an exposure of 0 h (a – c) and 2 h (d – f) imaged at a magnification of 12000x (a, b and e), 24000x (e), 3000x (d), and 6000x (f); with an accelerating voltage of 10 kV.....192

Figure 6.13: SEM image of *A. f* adapted to chalcopyrite exposed to chalcopyrite at an exposure of 12 h (a – c) and 24 h (d – f) imaged at a magnification of 6000x (a, d and f) and 12000x (b, c and f); with an accelerating voltage of 10 kV193

Figure 6.14: SEM image of *A. f* adapted to chalcopyrite exposed to chalcopyrite at an exposure of 36 h (a – c) and 48 h (d – f) imaged at a magnification of 12000x (a and f), 16000x (b), 8000x (c and d), and 6000x (e); with an accelerating voltage of 10 kV ..194

Figure 6.15: SEM image of *A. f* adapted to chalcopyrite exposed to chalcopyrite at an exposure of 60 h (a – c) and 72 h (d – f) imaged at a magnification of 8000x (a and e), 12000x (b), 4000x (c), 16000x (d), and 6000x (f); with an accelerating voltage of 10 kV195

Figure 6.16: SEM image of *A. f* adapted to chalcopyrite exposed to chalcopyrite at an exposure of 168 h imaged at a magnification of 10000x (a and c), 5000x (b) and 20000 (d); with an accelerating voltage of 10 kV.....196

Figure 6.17: SEM image of *A. f* adapted to chalcopyrite exposed to chalcopyrite showing the attachment to particles of impurity at 2 h (a and b), 24 h (e) and 36 h (d), imaged at a magnification of 12000x (a – c) and 8000x (d) with an accelerating voltage of 10 kV197

Figure 6.18: FTIR-ATR of pyrite showing pyrite in HH media at 0 h exposure (a), pyrite exposed to *A. f* at 186 h (b), chalcopyrite in HH media at 0 h exposure, and chalcopyrite exposed to *A. f* at 168 h (d)198

Figure 6.19: Differential flotation test recovery for *A. f* grown on iron sulfate as collector-free flotation tests (a); in the presence of PIPX collector (b).....200

Figure 6.20: Differential flotation test recovery for *A. f* adjusted to pyrite as collector-free flotation tests (a); in the presence of PIPX collector (b)201

Figure 6.21: Differential flotation test recovery for *A. f* adjusted to chalcopyrite as collector-free flotation tests (a); in the presence of PIPX collector (b).....202

Figure 6.22: Differential flotation test recovery for *A. f* adjusted to arsenopyrite as collector-free flotation tests (a); in the presence of PIPX collector (b).....203

Figure 6.23: Differential flotation test recovery for EPS supernatant of *A. f* adjusted to pyrite as collector-free flotation tests (a); in the presence of PIPX collector (b)204

Figure 6.24: Differential flotation test recovery for EPS supernatant of *A. f* adjusted to chalcopyrite as collector-free flotation tests (a); in the presence of PIPX collector (b)205

Figure 6.25: Differential flotation test recovery for EPS supernatant of <i>A. f</i> adjusted to arsenopyrite as collector-free flotation tests (a); in the presence of PIPX collector (b)	206
Figure 6.26: SEM image of pyrite illustrating copper impurities on the pyrite surface	207
Figure 6.27: Survey scan of unreacted pyrite, HH media controls and <i>A. f</i> exposed pyrite samples, collected at -165 °C with a monochromatic aluminium K α source.....	209
Figure 6.28: High-resolution Fe 2 <i>p</i> spectra 700 – 740 eV (a) and the difference from the unreacted spectrum through subtraction (b), collected at -165°C with a monochromatic Al K α source	211
Figure 6.29: High-resolution Sulfur 2 <i>p</i> spectra 160 – 173 eV (a) and enlarged S 2 <i>p</i> 3/2 (b) of unreacted pyrite, HH media controls and <i>A. f</i> exposed samples, collected at -165 °C with a monochromatic aluminium K α source.....	212
Figure 6.30: Component fits of high-resolution S (2 <i>p</i> _{3/2}) spectra of unreacted pyrite (a) 24 h HH exposure (b) 48 h HH exposure (c) 72 h HH exposure (d) 168 h HH exposure (e), conducted at -165 °C with the enlarged 171 – 163 eV area of the respective scan displayed on the right.....	214
Figure 6.31: Component fits of high-resolution S (2 <i>p</i> _{3/2}) spectra of unreacted pyrite (a) 24 h HH exposure (b) 48 h HH exposure (c) 72 h HH exposure (d) 168 h HH exposure (e), conducted at ambient temperature (18.4 – 21.7 °C) with the enlarged 171 – 163 eV area of the respective scan displayed on the right	215
Figure 6.32: Component fits of high-resolution S 2 <i>p</i> spectra of <i>A. f</i> exposed Py at 24 h (a) 48 h (b) 72 h (c) and 168 h (d), conducted at -165 °C with the enlarged 171 – 163 eV area of the respective scan displayed on the right	216
Figure 6.33: Component fits of high-resolution S 2 <i>p</i> spectra of <i>A. f</i> exposed Py at 24 h (a) 48 h (b) 72 h (c) and 168 h (d), conducted at ambient temperature (18.4 – 21.7 °C) with the enlarged 171 – 163 eV area of the respective scan displayed on the right.....	217
Figure 6.34: Component fits of C 1 <i>s</i> spectra of unreacted Py cold stage (a) ambient (b) and the HH media exposures for 24 h cold stage (c) 24 h ambient (d) 48 h cold stage (e) 48 h ambient (f) 72 h cold stage (g) 72 h ambient (h) 168 h cold stage (i) 168 h ambient (j), cold stage scans were conducted at -165 °C and ambient scans between 18.4 and 21.7 °C.....	219

Figure 6.35: Component fits of C 1s spectra of *A. f* exposures to pyrite for 24 h cold stage (a) 24 h ambient (b) 48 h cold stage (c) 48 h ambient (d) 72 h cold stage (e) 72h ambient (f) 168 h cold stage (g) 168 h ambient (h), cold stage scans were conducted at -165 °C and ambient scans between 18.4 and 21.7 °C220

Figure 7.1: FTIR-ATR analysis of EPS precipitate from extraction showing *L. ferrooxidans* adapted to chalcopyrite (a), adapted to arsenopyrite (b), and *A. ferrooxidans* adapted to chalcopyrite (c) adapted to arsenopyrite (d)231

Figure 7.2: Epifluorescence of eDNA in the DAPI and GFP region showing auto-fluorescence on the pyrite negative control (a), positive control of 0.1µg/mL DNA in HH Media for 24 h on pyrite (b), pyrite exposed to EPS from *L. ferrooxidans* adapted to chalcopyrite for 24 h (c), and 48 h (d)233

Figure 0.1: Hydrolysis, reduction and acetylation reaction for polysaccharidesxxiii

Figure 0.1: EDAX of impurity with multiple faces/cleavages observed in the chalcopyrite sample.....xxvii

Figure 0.2: EDAX of impurity with multiple thin layers suspected to be a clay like mineralxxviii

Figure 0.3: EDAX of the cubic impurity found in chalcopyrite, with the lead:sulfur ratio indicating a galena phasexxix

Figure 0.4: EDAX of precipitated salts on the pyrite surface.....xxx

Figure 0.6: EDAX of singular cubic debris on the pyrite surface.....xxxi

LIST OF TABLES

Table 2.1: Structural breakdown of EPS components including the effect, nature and role of components as displayed in Flemming, et al. [97]	33
Table 3.1 ICP-MS/OES elemental composition of mineral wt(%)	45
Table 3.2: C 1s K-edge NEXAFS transitions	59
Table 3.3: Binding Energy Reference Table for C 1s, N 1s, O 1s and Fe 2p	63
Table 3.4: Binding energy reference table for sulfur species	64
Table 3.5: Reference table for FTIR peak absorbance	70
Table 4.1: Conditioning of samples at an exposure time of 12 h, 24 h, 36h, 48 h, 60 h and 72 h	83
Table 4.2: Calculated particle size distribution of pyrite and chalcopyrite +38 -75 μm fraction	100
Table 5.1: Change in contact angle ($^\circ$) of mineral tiles of pyrite and chalcopyrite showing the static contact angle (ϑ), advancing contact angle (ϑ_A), receding contact angle (ϑ_R), and contact angle hysteresis (H_w)	148
Table 5.2: ΔE and intensity ratio parameters for the Fe $L_{2,3}$ -edge spectra illustrated in Figure 5.11	156
Table 5.3: C 1s K-edge NEXAFS transitions	166
Table 6.1: Summary of micro-flotation test conditions.....	178
Table 6.2: Elemental composition (At %) of survey scans for unreacted pyrite and pyrite exposed to HH media	210
Table 6.3: Elemental composition (At%) of survey scans for pyrite exposed to <i>A. f.</i>	210
Table 6.4: High resolution C 1s component fit information for cold stage scans	218
Table 6.5: High resolution O 1s component fit information for cold stage scans. FWHM held constant at 1.55	221
Table 0.1:.....	xiv
Table 0.1: High-resolution S 2p fit component information for cold stage scans.....	xxvi
Table 0.2: High-resolution S 2p fit component information for ambient scans.....	xxvi

ABBREVIATIONS

Abbreviation	Definition
<i>A. f</i>	<i>Acidithiobacillus ferrooxidans</i>
Asp	Arsenopyrite
BSE	Back scattered electron
BSA	Bovine Serum Albumin
Cp	Chalcopyrite
dsDNA	Double stranded DNA
EDAX	Energy Dispersive Analysis by X-ray
EMPA	Electron microprobe analysis
EPS	Extracellular Polymeric Substance
FID	Free induction decay
FOV	Field of view
FTIR-ATR	Fourier Transform Infrared Attenuated Total Reflection
GDP	Gross Domestic Product
GFP	Green Fluorescent Protein
Hm	Haematite
IR	Infrared
ICSD	Inorganic Crystal Structure Database
<i>L. f</i>	<i>Leptospirillum ferrooxidans</i>
M. Q	Milli – Q
NEXAFS	Near Edge X-ray Absorption Fine Structure
NMR	Nuclear Magnetic Resonance
PEEM	Photoemission Electron Microscopy
PIPX	Potassium Isopropyl Xanthate
ppm	Parts per million
psia	Pound per square inch absolute
Py	Pyrite
QXRD	Quantitative X-ray Diffraction
RF	Radio frequency
RPM	Rotations per minute
SE	Secondary electron
SEM	Scanning Electron Microscopy
ssDNA	Single stranded DNA
TEY	Total Electron Yield
XPS	X-ray Photoemission Spectroscopy
XRD	X-ray Diffraction

1 INTRODUCTION

With approximately 240,000 km² of Earth's land area affected by mining [1], negative effects of the mining/minerals processing sector are continuously being scrutinised. While the mining sector is currently Australia's largest primary industry, and was responsible for 10.4% of Australia's Gross Domestic Product (GDP) between 2019 and 2020, environmental costs and challenges remain [2]. As the mining sector and demand for precious metals increases, the high purity resources are predicted to decrease, leading to the need for more efficient processing procedures for low grade ore [1,3,4]. As lower grade ore has more impurities, the resulting ore mineralogy is complex, creating challenges for separation [5]. Therefore, separation and refinement will likely become a key process in copper recovery. Consequently, the use of bacteria in minerals processing has been investigated, with the main focus concerning leaching, environmental impact and economic viability of minerals processing [4,6]. Bio-beneficiation through bio-leaching of sulfide minerals has been thoroughly studied, with the focus primarily on mesophilic iron and/or sulfur oxidising microbes *Acidithiobacillus ferrooxidans* (*A. f* formally *T. ferrooxidans*), *Acidithiobacillus thiooxidans* (*A.t*), and *Leptospirillum ferrooxidans* (*L. f*) [5,7-15]. More recently, bio-flotation has been investigated for the beneficiation of low-grade ore with the focus on the replacement of traditional reagents with bacteria and their metabolic products. This field of research has advanced through the pioneering work of Natarajan et al. [7,8,15-21].

Separation of chalcopyrite from gangue minerals such as pyrite is commonly achieved through a physico-chemical technique known as froth flotation [22]. The selective modification of the surface physico-chemical properties of the minerals is crucial for successful separation, the addition of inorganic and highly selective chemicals such as xanthates and cyanides are often used to enhance the efficiency of separation [18,22]. The use of these chemicals along with sulfide mineral processing are known to have a detrimental effect on the environment through their contribution to acid mine drainage [6,20].

This thesis has been divided into seven chapters, with the following chapter presenting a detailed literature review of the current literature surrounding sulfide minerals processing including the fundamentals of the theory, methods and approaches required for this project. Materials and general methodologies for this study are presented in chapter three. This

includes detailed information of the minerals used, including mineralogical and compositional information, growth conditions of the bacteria and Archaea, and analysis techniques.

Chapters four to eight are devoted to the experimental investigation and discussion of results. Each of these experimental chapters contains an introduction into the research field, including where the research contributes to knowledge, presentation of results with a discussion of their implications, followed by a summary of the section.

Chapter four presents the preliminary bio-flotation studies of *Leptospirillum ferrooxidans* for the separation of pyrite and chalcopyrite. This chapter includes the optimisation of the modified Hallimond tube for micro-flotation experiments. This investigation was carried out to determine the differences in attachment behaviour of the microbes grown in different growth conditions, and to determine potential bio-reagents.

Chapter five further investigates the use of *Leptospirillum ferrooxidans* EPS components for the validity of use as a bio-reagent mineral separation. This chapter includes surface chemistry analysis of chalcopyrite, pyrite and haematite using photoemission electron microscopy to explore the interactions between EPS components and mineral surface.

Chapter six expands on the ideas presented in the previous chapters, with a more widely known and used bio-leach microbe *Acidithiobacillus ferrooxidans* in the pyrite-chalcopyrite mineral system. This increases the complexity of the investigation as the bacterial strain oxidises both iron and sulfur, leading to differences in the bio-flotation behaviour in the system. Surface chemistry of pyrite interaction with *Acidithiobacillus ferrooxidans* was investigated through X-ray photoelectron spectroscopy.

Chapter seven presents the overall conclusions of the work presented in this thesis and the future directions. The studies identified in the future directions will lead to an increased understanding of the microbe – mineral interaction and their potential applications in minerals processing.

1.1 References

1. Haferburg, G.; Kothe, E. Microbes and metals: interactions in the environment. *Journal of Basic Microbiology* **2007**, *47*, 453-467, doi:10.1002/jobm.200700275.
2. Casey, J.P. In numbers: how mining came to be Australia's most profitable sector. Available online: <https://www.mining-technology.com/features/in-numbers-how-mining-came-to-be-australias-most-profitable-sector/> (accessed on August 22, 2021).
3. Milosavljević, M.M.; Marinković, A.D.; Rančić, M.; Milentijević, G.; Bogdanović, A.; Cvijetić, I.N.; Gurešić, D. New eco-friendly xanthate-based flotation agents. *Minerals* **2020**, *10*, 350.
4. Dwyer, R.; Bruckard, W.J.; Rea, S.; Holmes, R.J. Bioflotation and bioflocculation review: microorganisms relevant for mineral beneficiation. *Mineral Processing and Extractive Metallurgy* **2012**, *121*, 65-71, doi:10.1179/1743285512y.0000000005.
5. Govender, Y.; Gericke, M. Extracellular polymeric substances (EPS) from bioleaching systems and its application in bioflotation. *Minerals Engineering* **2011**, *24*, 1122-1127, doi:10.1016/j.mineng.2011.02.016.
6. Bleeze, B.; Zhao, J.; Harmer, S.L. Selective Attachment of *Leptospirillum ferrooxidans* for Separation of Chalcopyrite and Pyrite through Bio-Flotation. *Minerals* **2018**, *8*, 86.
7. Harneit, K.; Göksel, A.; Kock, D.; Klock, J.-H.; Gehrke, T.; Sand, W. Adhesion to metal sulfide surfaces by cells of *Acidithiobacillus ferrooxidans*, *Acidithiobacillus thiooxidans* and *Leptospirillum ferrooxidans*. *Hydrometallurgy* **2006**, *83*, 245-254.
8. Lavallo, L.; Giaveno, A.; Pogliani, C.; Donati, E. Bioleaching of a polymetallic sulphide mineral by native strains of *Leptospirillum ferrooxidans* from Patagonia Argentina. *Process Biochem* **2008**, *43*, 445-450, doi:10.1016/j.procbio.2007.10.019.
9. Olson, G.J. Rate of Pyrite Bioleaching by *Thiobacillus ferrooxidans*: Results of an Interlaboratory Comparison. *Appl Environ Microbiol* **1991**, *57*, 642-644.
10. Sand, W.; Gehrke, T. Extracellular polymeric substances mediate bioleaching/biocorrosion via interfacial processes involving iron(III) ions and acidophilic bacteria. *Res Microbiol* **2006**, *157*, 49-56, doi:10.1016/j.resmic.2005.07.012.
11. Sand, W.; Gerke, T.; Hallmann, R.; Schippers, A. Sulfur chemistry, biofilm, and the (in) direct attack mechanism—a critical evaluation of bacterial leaching. *Applied Microbiology and Biotechnology* **1995**, *43*, 961-966.
12. Sand, W.; Rohde, K.; Sobotke, B.; Zenneck, C. Evaluation of *Leptospirillum ferrooxidans* for Leaching. *Appl Environ Microbiol* **1992**, *58*, 85-92.
13. Schippers, A.; Jozsa, P.; Sand, W. Sulfur chemistry in bacterial leaching of pyrite. *Appl Environ Microbiol* **1996**, *62*, 3424-3431.
14. Sharma, P.K.; Das, A.; Rao, K.H.; Forssberg, K.S.E. Surface characterization of *Acidithiobacillus ferrooxidans* cells grown under different conditions. *Hydrometallurgy* **2003**, *71*, 285-292, doi:10.1016/S0304-386x(03)00167-1.
15. Zhu, J.; Li, Q.; Jiao, W.; Jiang, H.; Sand, W.; Xia, J.; Liu, X.; Qin, W.; Qiu, G.; Hu, Y. Adhesion forces between cells of *Acidithiobacillus ferrooxidans*, *Acidithiobacillus thiooxidans* or *Leptospirillum ferrooxidans* and chalcopyrite. *Colloids and Surfaces B: Biointerfaces* **2012**, *94*, 95-100.
16. Chandraprabha, M.N.; Natarajan, K.A.; Somasundaran, P. Selective separation of arsenopyrite from pyrite by biomodulation in the presence of *Acidithiobacillus ferrooxidans*. *J Colloid Interf Sci* **2004**, *276*, 323-332, doi:10.1016/j.jcis.2004.03.047.

17. Chandraprabha, M.N.; Natarajan, K.A.; Modak, J.M. Selective separation of pyrite and chalcopyrite by biomodulation. *Colloids Surf B Biointerfaces* **2004**, *37*, 93-100, doi:10.1016/j.colsurfb.2004.06.011.
18. Chandraprabha, M.N.; Natarajan, K.A. Surface chemical and flotation behaviour of chalcopyrite and pyrite in the presence of *Acidithiobacillus thiooxidans*. *Hydrometallurgy* **2006**, *83*, 146-152, doi:10.1016/j.hydromet.2006.03.021.
19. Deo, N.; Natarajan, K.A. Interaction of *Bacillus polymyxa* with some oxide minerals with reference to mineral beneficiation and environmental control. *Minerals Engineering* **1997**, *10*, 1339-1354, doi:10.1016/S0892-6875(97)00125-8.
20. Patra, P.; Natarajan, K. Microbially enhanced removal of pyrite and chalcopyrite from oxide gangue minerals with reference to desulfurization of tailings. *Minerals and Metallurgical Processing* **2004**, *21*, 169-178.
21. Subramanian, S.; Santhiya, D.; Natarajan, K.A. Surface modification studies on sulphide minerals using bioreagents. *International Journal of Mineral Processing* **2003**, *72*, 175-188, doi:10.1016/S0301-7516(03)00097-8.
22. Napier-Munn, T.; Wills, B.A. *Wills' mineral processing technology: an introduction to the practical aspects of ore treatment and mineral recovery*; Butterworth-Heinemann: 2011.

2 LITERATURE REVIEW

2.1 Sulfide minerals

Sulfide minerals make up a small percentage of the Earth's crust, with a large portion containing metallic elements [1,2]. Metal sulfides are the primary source of precious and base metals [3], with a general chemical formula of A_mX_p ; where A represents the smaller atom, which can be one or more metals, and X represents sulfur [2]. The more common metals present in transition metal sulfides are iron (Fe), copper (Cu), nickel (Ni), silver (Ag), cobalt (Co), and zinc (Zn); while the trace elements include calcium (Ca), vanadium (V), chromium (Cr), manganese (Mn), platinum (Pt), and gold (Au) [2]. As not all sulfide minerals contain valuable or precious metals and are therefore seen to contain no commercial significance or net worth and are deemed as gangue minerals [4]. Separation of the valuable (ore) and non-valuable (deemed as waste rock) components is required before the metallic component can be refined. Beneficiation of sulfide-rich ore results in the refinement of precious metals but also contributes to environmental issues such as acid mine drainage (AMD) [5,6].

2.1.1 Pyrite (Py)

Pyrite (FeS_2) is the most common iron sulfide mineral in the Earth's crust and is found in a wide range of geological formations from sedimentary deposits to hydrothermal veins and a constituent of metamorphic rock [2,4,7]. Visually it has a brassy-yellow appearance, causing it to be commonly mistaken for gold, giving rise to its colloquial name 'Fool's gold'. However, pyrite's physical properties, such as weight and hardness, make it easily distinguishable from gold. In the cubic unit cell of pyrite, the iron atoms are octahedrally coordinated to the sulfur atoms [7,8], as pictured in Figure 2.1 below. This unit cell structure results in an overall negative charge on the mineral surface [9]. The oxidation state of iron existing as low spin Fe (II) and the sulfur exists as S (- I) [7,8]. Impurities, such as arsenic and selenium, can exist in the lattice by substituting into the sulfur site.

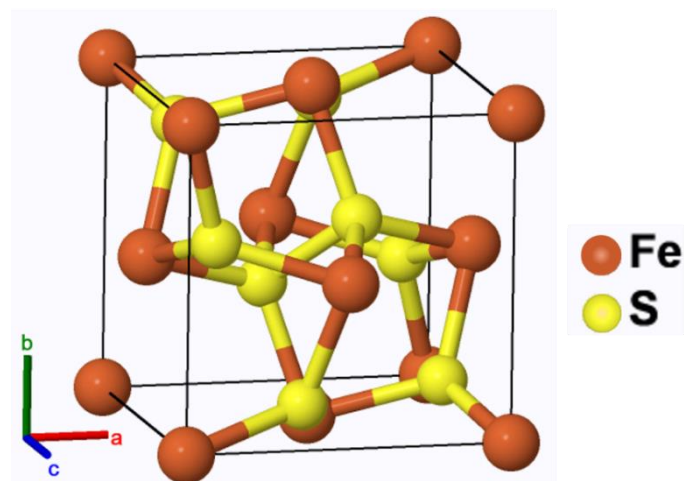
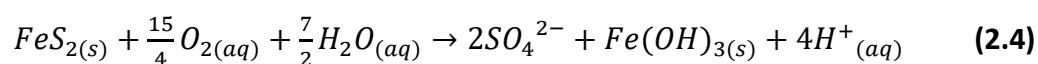
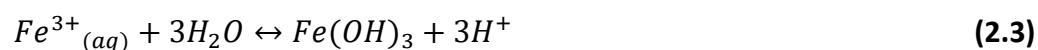
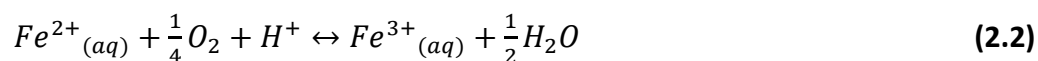
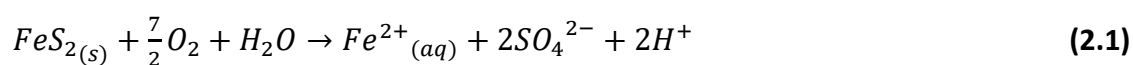


Figure 2.1: The unit cell structure of cubic pyrite (FeS_2 ; image adapted from Hicks, et al. [10])

Pyrite is commonly associated with many other sulfide minerals in sulfide-rich ores, coal deposits, and can exist as veins of impurities in precious metals such as gold, nickel and sometimes cobalt [6]. In comparison to the other minerals it is associated with, pyrite has no significant net worth or commercial value it is regarded as a gangue mineral [11].

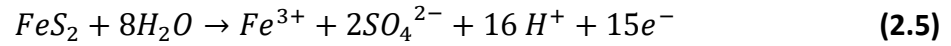
2.1.1.1 Pyrite Oxidation

Pyrite oxidation is a complex process, which can occur in both oxygenated and anoxic systems and can involve chemical, biological or electrochemical reactions [6]. Reaction with atmospheric oxygen produces Fe^{2+} and SO_4^{2-} in a ratio of 1:2, as shown by equation 2.1 [6]. Further oxidation can occur, producing $\text{Fe}^{3+}_{(aq)}$ and Fe^{3+} oxyhydroxides ($\text{Fe}(\text{OH})_3$, FeOOH and Fe_2O_3), as represented in equations 2.2 and 2.3, with the overall reaction shown in equation 2.4. The $\text{Fe}(\text{OH})_3$ species in the equations are a surrogate for the oxyhydroxide species [6]



The initial oxidation of pyrite involves the adsorption of O_2 and H_2O to the surface at the Fe^{2+} sites, creating various intermediate states of iron oxyhydroxides [6]. The Fe^{3+} ions produced continues the oxidation of pyrite [6]. Conditions such as O_2 and Fe^{3+} concentration, Eh and pH

can influence oxidation. This is shown by Equation 2.5, which represents the process of electrochemical oxidation of pyrite. This indicates that the oxidation involves the formation of a thiosulfate ion before the iron sulfate is formed [12].



2.1.2 Chalcopyrite (Cp)

Chalcopyrite is a copper iron sulfide with the chemical formula $CuFeS_2$, with the oxidation states Cu(I), Fe(III) and S(-II) [7,8]. The unit cell of chalcopyrite is tetragonal, where the iron and copper atoms are tetrahedrally bound to the sulfur atoms, alternating along the c-axis, as illustrated in Figure 2.2 below [8]. Chalcopyrite is considered a valuable mineral as it is the most abundant and economical source of copper [4,6,13]. Copper is the most important, non-ferrous metal; therefore, importance is placed on recovery of copper from its ores [4,11,13]. Chalcopyrite is commonly found in mixed mineral systems, where it is inter-grown with other sulfide minerals such as pyrite, sphalerite, bornite, galena, and chalcocite. In some cases, it is also associated with other mineral phases that contain valuable metals and/or transition metals, or other gangue minerals such as quartz [4,6,11,14,15]. The purity or grade of the ore is determined by the amount of gangue minerals present; the more gangue minerals present, the lower the grade.

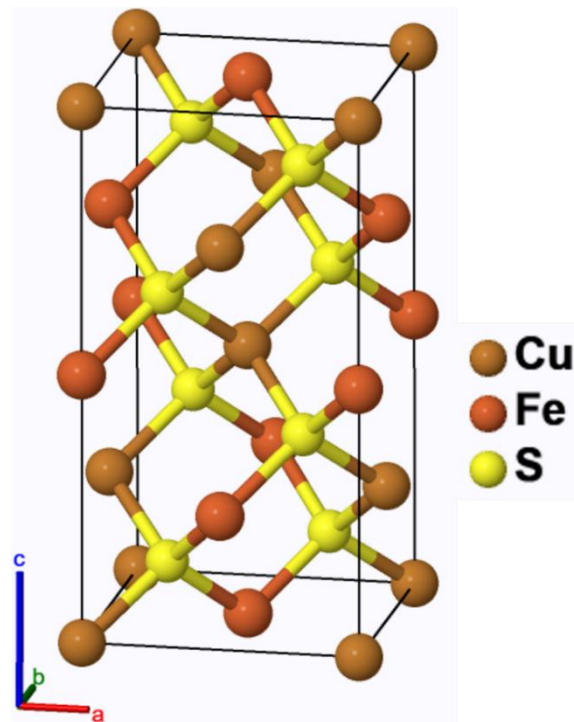
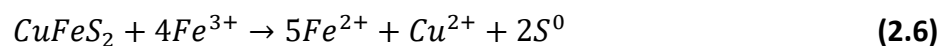


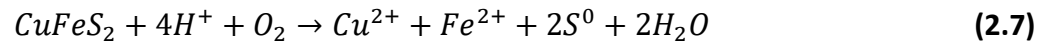
Figure 2.2: The unit cell structure of chalcopyrite (image adapted from Mehl, et al. [16])

2.1.2.1 Chalcopyrite Oxidation

Reaction with atmospheric oxygen produces a ferric oxyhydroxide layer on the surface, which can include regions of iron deficiency composed of CuS_2 [6]. This layer of CuS_2 becomes thicker when formed in acidic environments and with the presence of elemental sulfur [6]. The reaction for chalcopyrite oxidation in acidic conditions and in the presence of ferric ions is shown below in equation 2.6 [6].



This process also releases ferrous ions, which can be rapidly oxidised to ferric ions in the presence of iron oxidising bacteria. The presence of ferric ions in acidic sulfate solutions can enhance the oxidation and dissolution of copper bearing ore [6]. Galvanic interactions can also influence the dissolution of chalcopyrite, with the presence of pyrite enhancing the dissolution [6]. Further research by Hiroyoshi, et al. [17] indicates that ferric iron and dissolved oxygen present in the acidic environments releases copper ions into solution. Oxidation by dissolved oxygen is shown in equation 2.7 below.



2.1.3 Haematite (Hm)

Haematite, is an iron oxide mineral with a chemical formula of Fe_2O_3 and a trigonal crystal structure, shown in Figure 2.3. Haematite is an important iron mineral due to its high iron content and it is often associated with pyrite, quartz, calcite, rutile, amethyst, goethite, fluorite, magnetite and dolomite [18]. Haematite is also commonly associated with rare earth elements and considered a gangue [19].

Haematite is a polar mineral, with greater polarity than pyrite and chalcopyrite due to the oxides and hydroxides at the surface. Iron ores such as hematite, and goethite are floated by collectors such as amines, oleates, sulfanates or sulfates [1,4].

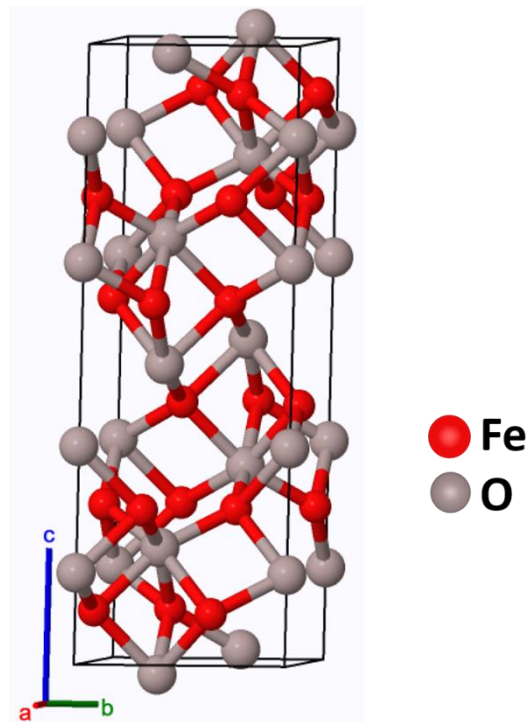


Figure 2.3: Unit cell structure of hematite (image adapted from Mehl, et al. [16])

2.1.4 Arsenopyrite (Asp)

Arsenopyrite is the primary arsenic bearing mineral [20], and an ideal chemical formula for arsenopyrite is FeAsS . However natural arsenopyrites have been noted to have a chemical composition ranging from $\text{FeAs}_{0.9}\text{S}_{1.1}$ – $\text{FeAs}_{1.1}\text{S}_{0.9}$ [21]. Mössbauer spectroscopy studies conducted by Vaughan and Craig [7], and Bindi, et al. [22] indicates an oxidation state of Fe

(II), S (-I), and As (-I), with Silva, et al. [21] suggesting both sulfur and arsenic are present as dianions and iron trivalent.

Arsenopyrite is commonly found with iron and nickel sulfides such as pentlandite and pyrite [2,8] and is of interest as gold is preferentially associated with the arsenopyrite matrix in refractory sulfide ore [23]. Therefore the separation of arsenopyrite from gangue minerals, such as pyrite, becomes important for the economical extraction of gold along and the removal of arsenic compounds in the environment from pyrite tailings [23]. Separation of pyrite and arsenopyrite presents difficulties as the two minerals exhibit similar flotation behaviours [23].

Selective separation of arsenopyrite from pyrite and chalcopyrite through the use of oxidising agents (permanganates and addition of sulfur dioxide) has been studied [23]. *A. f* has been used to selectively depress py in the aspy system in acidic and neutral pH ranges [23]. Dissolution of arsenopyrite by *L. f* has been investigated along with the bacterial leaching pattern and the composition of EPS [24].

2.1.4.1 Arsenopyrite Oxidation

The oxidation process of arsenopyrite releases both sulfur and arsenic [6]. Similarly to chalcopyrite and pyrite, arsenopyrite can oxidise in the presence of atmospheric oxygen. Buckley and Walker [25] investigated the effects of oxidative environments on arsenopyrite, reporting rapid oxidation in the presence of atmospheric oxygen. In the presence of atmospheric oxygen the arsenic is oxidised to As (III), more rapidly than the iron and sulfur [6,25]. While in acidic environments, the oxidation of arsenopyrite results in a sulfur rich surface environment [6]. In conditions which resemble acid mine drainage environments, arsenopyrite is found to be more reactive than other sulfide minerals such as sphalerite, chalcopyrite, pyrite and galena [6,26].

2.1.5 Environmental Impact of Transition Metal Sulfide

Beneficiation of sulfide-rich ore results in large amounts of waste rock. The waste rock is composed of gangue minerals and often includes low-grade ore which is below the cut-off grade [6], both of which can contain sulfide minerals. Oxidation of these components can produce between 100 to 50,000 ppm H₂SO₄ which can dissolve and release heavy metal ions

such as copper, cobalt, nickel and mercury into the surrounding environment, usually into the water flowing through the waste [6,27].

Sulfide minerals are highly reactive and oxidise when exposed to atmospheric oxygen [6]. The high reactivity is due to the large number of oxidation states of the atoms within the mineral complex, meaning the oxidation reaction is dependent on the mineral [28]. The production of sulfuric acid during oxidation can accelerate the oxidation process through the production of hydrogen ions. The acidic environment also increases the solubility of heavy metal ions, creating an acidic cocktail of heavy metals which can leak into fresh water sources [29,30]. This becomes problematic, as pH neutralisation of the acidic mixture results in the precipitation of heavy metals. This reaction is the basis of AMD.

The mechanisms of degradation of metal sulfides are still under investigation. This is due to the complexity of the reactions which can take place on the mineral surface. These can be influenced by biochemical interactions, electrochemical interactions and the surface chemistry [28,31]. The dissolution of sulfide minerals, and the resulting surface speciation, is influenced by the kinetics of the surrounding environment [32-34]. Controlling these environmental conditions is difficult, therefore it is important to understand the potential states that can occur on the surface as multiple reactions are possible [1]. These reactions can also influence the hydrophobicity of the mineral phase, and therefore the recovery depending on the recovery technique.

Pourbaix diagrams are used to illustrate the effect of pH against the equilibrium potential of electrochemical reactions. These diagrams are used to identify thermodynamically stable phases within an electrochemical system. Below in Figure 2.4 the Pourbaix diagrams for pyrite (a), chalcopyrite (b) and haematite (c) are shown.

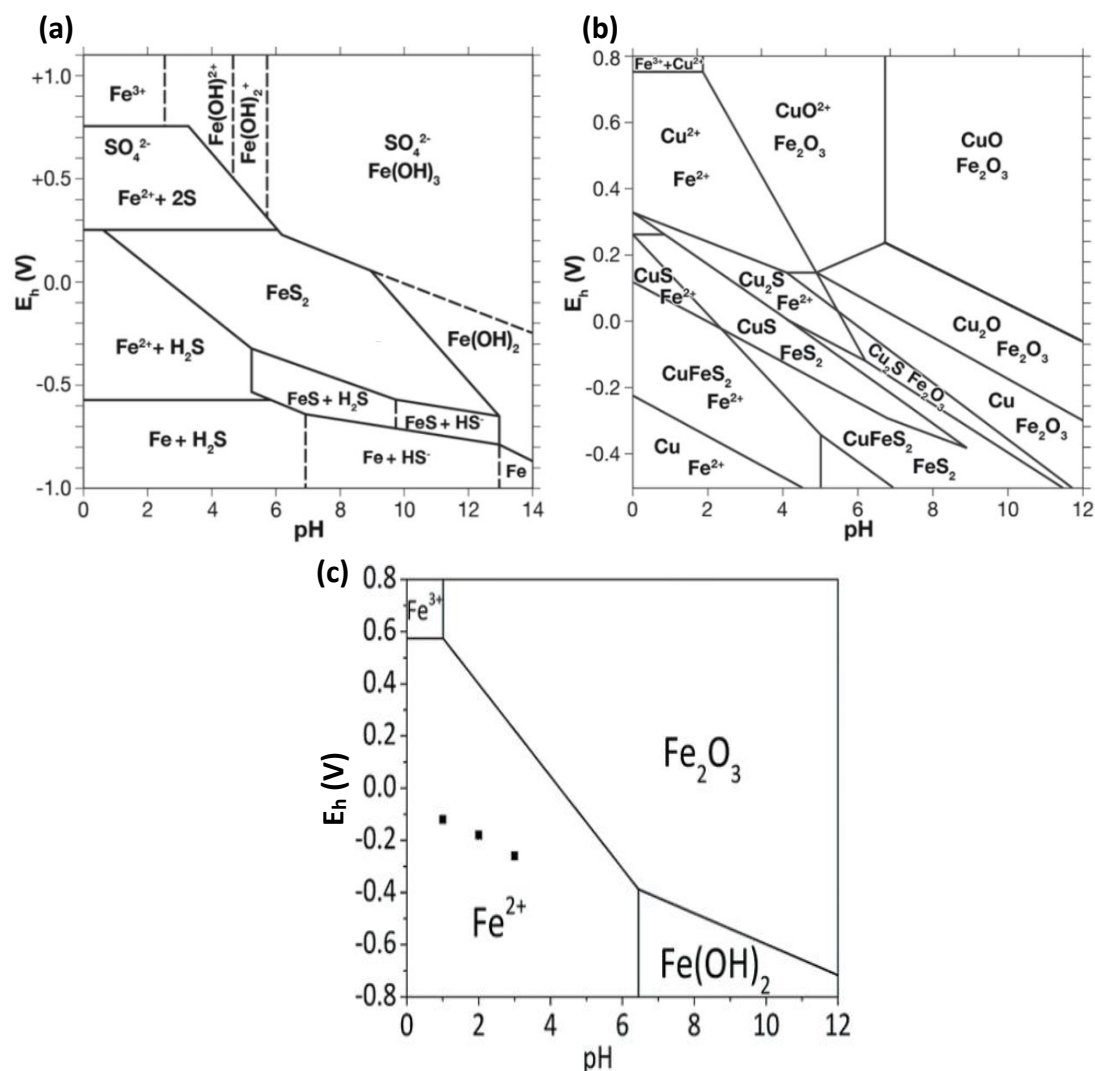


Figure 2.4: Pourbaix diagram of pyrite (a, at 25°C), chalcopyrite (b, at 21°C) and haematite (c, at ambient temperature); adapted from Kocabag, et al. [35] pyrite, Fairthorne, et al. [36] chalcopyrite, and Shimizu, et al. [37] haematite.

2.2 Mineral Processing

Minerals processing is the refinement and beneficiation of mineral ore for the purpose of separating the valuable portion from the commercially worthless portion, known as gangue [4]. The mining industry currently uses a range of separation techniques, with each technique employed for different mineral systems depending on the chemistry of the system [4]. The two major steps (comminution and concentration) in minerals processing is accompanied by multiple smaller and important steps including sizing of the ore, screening, classifying and dewatering of the mineral pulp [4].

Wills [1] highlights five important mineralogical properties which are important for physical ore concentration. These properties are: magnetic properties – ferromagnetic and paramagnetic minerals such as iron and non-ferrous ore can be separated by magnetic separators; electrical conductivity – conductive and non-conductive minerals can be separated; specific gravity – mass effects for differential movement producing less environmental pollution; optical and radioactive – also known as sorting; surface properties – utilizes hydrophobic and hydrophilic surface properties and is the most common method for sulfide minerals [1,4]. In some cases the ore roasting or heat treatment is used to effect major chemical properties, such as conversion non-magnetic iron to a ferromagnetic form to make the ore more suitable for certain processing [4].

The efficiency of these separation methods are important as elements such as aluminium (Al), iron (Fe) and magnesium (Mg) are present in amounts of above 2% in the Earth's crust [4]. While other important elements such as copper (Cu) are present in less than 0.1% [4]. As these industrially important elements exist in such small amounts, over 240,000 km of the Earth is affected by mining and mineral processing [38]. This environmental impact is increased when recovery processes such as heap and dump leaching are used. Both heap and dump leaching have been used to recover metals such as copper from low grade ore [17].

2.2.1 Froth Flotation

Froth flotation was originally developed to treat sulfide ores of copper, lead and zinc, however, further developments in the field has allowed it to expand to include oxides and non-metallic ores [4]. The invention of this process was revolutionary as it allows the processing of low-grade and complex ore bodies which would normally be classed economically worthless [4]. The flotation of low-grade and complex ores has been made economically viable through micro-flotation processes [4,19]. This method is still the most widely used method for the separation of sulfide ores [4,39].

Froth flotation is a physico-chemical separation technique which utilizes the difference in the surface chemistry and hydrophobicity of the mineral particles [4,19]. This separation process relies heavily on the ability of certain mineral particles adhering to the air bubbles being passed through the system. The surface properties can be enhanced and altered through the

addition of chemicals to the system. These chemicals are classed as collectors, depressors/modifiers and frothers which is discussed in 2.2.2 Flotation Reagents below.

Separation via froth flotation can work in two ways: direct and indirect flotation. Direct flotation occurs when the target mineral (mineral of interest) is hydrophobic and has an increased affinity to the rising air bubbles, being floated and collected [4]. Where indirect flotation occurs when the target mineral is suppressed in solution and the gangue mineral has an increased affinity to the rising air bubble and is collected [4]. Pecina, et al. [40], states that the efficiency of majority of the flotation systems can be represented by the first order reaction rate shown in Equation 2.7 below where R represents the cumulative recovery of mineral, t represents flotation time and k is the kinetic constant of flotation.

$$R = 1 - \exp^{-kt} \quad (2.8)$$

A schematic of a traditional flotation cell used in froth flotation is shown in Figure 2.5 [4]. A gas, in this case, labelled as air is passed through the agitator to produce the bubbles which are then passed through the mineral pulp within the cell. The sole purpose of the agitator is to agitate the pulp, increasing the probability of mineral particles interacting with the bubbles. As the bubbles pass through the system, hydrophobic mineral particles adhere to the surface of the bubble while the hydrophilic particles remain suspended in the pulp. A mineralised froth is formed on the top of the pulp as the bubbles surface and collected; separating the two phases of mineral.



Figure 2.5: Schematic Representation of a Froth Flotation Cell showing mineral attachment to air bubbles (image obtained from Napier-Munn and Wills [4])

There are multiple factors which can contribute to the efficiency of separation which includes the treatment of the ore before flotation and the Eh and pH of the pulp [4]. Two of the most important factors are the particle size and the bubble size, which are directly related to each other. The bubbles passed through the system needs to be of an adequate size to support the weight and size of the desirable mineral, but also small enough so the affinity of the gangue mineral is not increased. Likewise, if the mineral particles are too fine, regardless of the surface properties, they all have an increased affinity to the bubble surface. While larger particles can become too heavy meaning the bubble can no longer support the mineral causing it to become detached or causing the bubble to break. Efficiency in terms of particle size is discussed in more detail in Section 2.2.3 Micro Flotation below.

2.2.2 Flotation Reagents

To enhance the effectiveness of the separation, chemicals are added into the flotation matrix, these chemicals are referred to as flotation reagents [41]. There are different classes of reagents which enhance several factors, such as froth stability (frothers), collection through hydrophobic effects (collectors), and depression through hydrophilic effects (depressors/modifiers) [41]. In conventional froth flotation methods, highly selective inorganic modifiers such as cyanides, sulfides and ferro-cyanides are used [42]. These reagents are comprised of two main functional groups; donor atom or ligand, and a substituent group – hydrophobic for frothers and collectors, and hydrophilic for depressors/modifiers [41]. These reagents can be modified to suit particular mineral systems or given separations by altering the structural features, particularly the hydrocarbon (C – H) chain [39,41].

An issue with commercial reagents, such as sodium cyanide, sodium dichromate, sulfur dioxide, arsenic trioxide and phosphorous pentasulfide, is their susceptibility to oxidation in the presence of dissolved oxygen [43]. These chemicals are also often added in excess and as they are not environmentally friendly researchers have been investigating for a greener alternative [4].

2.2.2.1 Frothers

A stable froth is required for collection of the floated fraction, if the air bubbles do not form a stable froth they burst dropping the mineral attached to the bubble [1]. Surfactants are used

in the flotation processes to produce a stable froth and are referred to as frothers. These surfactants are neutral molecules and can be separated into soluble and partially-soluble sub groups [41]. The ideal frother only influences the liquid phase and does not interact with the mineral surface, however in reality interactions between the frother and mineral surface and other flotation reagents do occur [1]. Therefore, selecting the correct frother for the targeted ore and mineral system requires testing [1]. In some systems, such as sulphide mineral, multiple frothers are used to control the dynamics of the separation [1].

Heteropolar organic molecules, such as polypropylene glycol and ethers, are used as frothers as they are capable of interacting with the air-water interface [1,41]. The polar group of the molecule interacts with the water and becomes hydrated, while the non-polar hydrocarbon chain is attracted to the air phase [1]. The interaction between the aqueous phase and air phase with the molecule stabilises the air bubble by reducing the surface tension. Therefore, it is important that the frother molecules are partially water soluble to have an even dispersion throughout the system to optimise the efficiency [1]. The most common functional groups used in frothers are hydroxyl, carboxyl, carbonyl, amino groups and sulpho groups [1,41]

2.2.2.2 Collectors

Collectors are sometimes referred to as promoters as they enhance the separation and recovery. Collectors attach to the mineral surface through electrostatic bonds, chemical adsorption and van der Waals forces [1,39], increasing the hydrophobicity of the mineral particle [1,4] and thereby facilitating bubble attachment. To increase the separation of mineral particles the collector must be able to overcome the galvanic interactions occurring between the mineral particles. Galvanic interactions between a noble (cathodic, electron acceptor) and an active (anodic, electron donor) mineral reduce the floatability of the noble mineral. The effects on the active mineral is minimal [14].

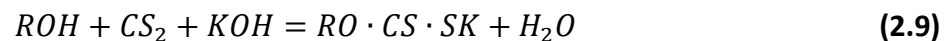
Collectors can be separated into two sub groups: ionic and non-ionic, and are usually organic compounds [1,41]. However, in sulfide mineral separation these classifications are not required as the collectors attach to the minerals surface through chemisorption [41]. Therefore, selection of collector is determined by the targeted separation and the chemistry

of the collector. Collectors are usually complex heteropolar asymmetric molecules with polar and non-polar functionalities, fatty acids, amines and xanthates are examples [1,41].

For collectors to be effective, they need to be able to attach to the mineral surface with their polar group, creating a non-polar hydrophobic layer around the mineral. Due to this, the concentration of collector is important for optimal recovery. If the concentration is too high, then the collectors can form multiple layers on the minerals surface thereby reversing the effect of the collector [1]. In complex systems more than one collector is often used to target different mineral phases.

2.2.2.2.1 Xanthates

Xanthates are anionic ionising collectors, which are best suited for sulfide ore including complex sulfide ore [4,44,45]. Xanthates are a class of organic thiocarbonate salts [44,46] with a general formula of $R - OCS_2^-$, where R represents a hydrocarbon chain [47]. Xanthates are classed as toxic, hazardous and flammable by the Australian Dangerous Goods (ADG) code, as the solids are susceptible to spontaneous combustion and environmentally hazardous [48]. Xanthates have been widely used in the beneficiation of sulfide and oxide minerals since early 20th century [1,39,44,47]. Xanthates are formed through the reaction of an alkali hydroxide such as KOH, a carbon disulfide, and an alcohol (given as ROH), as shown in Equation 2.9 below [1].



Due to the toxicity of xanthates, there are multiple environmental and health implications for their use in minerals processing [39]. Part of this toxicity arises from the formation of carbon disulfide (CS_2) during decomposition [47]. Xanthates are water soluble, with acidic environments promoting dissociation and protonation of the xanthate ion [44]. Protonation of the xanthate ion accelerates the decomposition, which is not seen in neutral and basic conditions, therefore alkaline conditions are preferred for xanthate use [1,44,49,50]. The study by Iwasaki and Cooke [50] illustrates that as the acidity of the solution increases so does the rate of decomposition. Xanthates can react with oxidising agents resulting in the formation of dixanthogens, and metallic ions resulting in heavy metal xanthates [44]. The formation of the heavy metal xanthate is what leads to the surface chemistry change from

hydrophilic to hydrophobic, while dixanthogens can decrease the selectivity of the collector [1,44].

There are multiple theories for the adsorption mechanism of xanthates to a sulfide mineral surface [44], with the mechanism determined by the xanthate structure and the targeted mineral [39]. Napier-Munn and Wills [4] established that the interaction between xanthate collector anions and sulfur on the mineral surface requires previous oxidation of the surface. This oxidation of the surface may also result in the formation of elemental sulfur, which is hydrophobic [1]. As oxidation of the sulfide mineral results in negative electrical double layer, it is predicted that the activation of the mineral is due to the attachment of a neutral/uncharged molecule such as xanthic acid or dixanthogen [44]. According to Klimpel [45], a potential of +0.13 V is required for disulfide and dixanthogens to form on the surface of both pyrite and chalcopyrite. However, it is noted by Milosavljević, et al. [39] that the adhesive power and effectiveness can be impacted by the structure and length of the hydrocarbon chain.

2.2.2.3 Modifiers and Depressors

Modifiers refer to chemicals which can modify certain aspects of the flotation system, such as pH, viscosity and froth [41]. Depressors are a sub-group of modifiers, which are used to increase the selectivity of the collectors [1]. The chemicals used as depressors are a lot more varied than those used for frothers and collectors. The reaction pathways are also more complex and not completely understood making selective depression of minerals harder than selective recovery [1].

Cyanides are widely used depressants for pyrite and sphalerite associated with copper, lead and zinc ores [1]. Cyanide is used as it can desorb copper ions from the surface of minerals and can react with copper in the pulp solution which contribute to copper activation [1]. Sodium cyanide and modified polysaccharides are the most common depressors used, as they are suitable at both neutral and acidic pH [1,14,41]. Cyanides are highly toxic and contribute to environmental issues, therefore there is a need for environmentally friendly alternatives.

2.2.3 Micro Flotation

Micro-flotation works on the same principles as that of froth flotation, but on a smaller scale. The finer particle size used in micro flotation allows better separation of low grade and complex ores [4]. The effect of particle size on mineral recovery is shown in Figure 2.6 below. The recovery curve shows a relationship between the particle size and optimal recovery. The curve indicates that the optimal particle size is between 35 μ m and 150 μ m. This is explained by the adhesion force between the mineral particle and the air bubble. For adhesion to occur, the bubble needs to be able to displace the surrounding liquid from the mineral particle [4]. As the particle size increases, this adhesion force is reduced leading to an increase in particles attaching to the bubble. When the adhesion force is smaller than the weight of the particle, the bubble can no longer support the mineral particle and the bubble is 'dropped' or the bubble bursts [4]. Therefore, the bubble size to particle size is a key factor relating to the separation of minerals via flotation.



Figure 2.6 Mineral recovery curve for micro flotation showing the influence of particle size [4]

Galvanic interactions can also influence the efficiency of separation. Galvanic interactions between the minerals depends on the active or noble character of the minerals [51]. These galvanic interactions have more effect on the flotation behaviour of the noble mineral than the active mineral [14,51].

2.3 Microorganisms in Minerals Processing

Biogeochemistry is a discipline with great importance due to the potential for bioremediation of sub surface sites that are contaminated by metal and radionucleotide [52]. Microorganisms play an important role in many ecosystems including the water, carbon, sulfur and nitrogen

cycles [6]. This diversity of roles throughout the different cycles allows microorganisms to survive in harsh conditions, including acidic mine effluents where conditions are acidic and resources are finite [6]. Microorganism catalysis of the available sulfide minerals in these conditions accelerates the reduction of compounds to sulfate [6].

2.3.1 Bacteria and archaea

The diversity of microorganisms involved in these biogeochemical cycles creates a challenge when characterising the cells present. A common method for characterising the cell structure is the use of Gram staining. The cell is either Gram positive (retains the stain) or Gram negative (does not retain the stain). The Gram stain uses the difference in structure and composition of the cell wall and outer membrane to determine the cell as either Gram-negative or Gram-positive [53].

The cell wall of a Gram-positive cell is thicker with the composition primarily consisting of peptidoglycan containing sugar derivatives and amino acids [53]. The composition of the cell wall contributes to the overall charge of the cell, with sugar alcohols, glycerol, ribitol, and teichoic amino acid all holding a negative charge [53]. Gram-negative cells have an increase in complexity due to a second lipid bilayer in the outer membrane. This second bilayer consists of phospholipids which contain proteins (primarily porins) and lipopolysaccharides which are lipids and polysaccharides linked together [53,54]. It is the arrangement of these proteins and polysaccharides on the outer membrane which influence the overall charge of the cell [53]. The surface of the bacterial cell carries a net negative charge under most physiological conditions with electrostatic forces, hydrophobic, entropic, acid-base, hydrogen bonding and Van der Waals interactions playing an important role in bacterial adhesion [54].

Chemolithoautotrophic bacteria are carbon fixing bacteria which derive necessary carbon for metabolic processes from carbon dioxide in their environment. These bacteria also derive their energy from inorganic compounds such as nitrogen, iron or sulfur. The carbon source and energy source for these bacteria are completely separate [55]. These bacteria are generally capable of operating their central carbohydrate metabolism in both anabolic and catabolic directions for long and short term adaptation [56]. For iron oxidizing bacteria, their energy comes from the regeneration of the ferrous ion as an electron donor, where the

charge of the iron changes from ferrous Fe^{2+} to ferric Fe^{3+} and enters the propagation cycle which accelerates the acidification [38].

Bacterial cells can be motile by means of an appendage(s) on the cell wall known as flagellum. The chemosensory system of the cell can regulate the motility by controlling the flagellar rotation [57]. This means that the bacterial cells are attracted by certain chemicals and repelled by others [57]. The cell does this by reading chemical signals/information received from the environment through transmembrane proteins known as transducers or methyl-accepting chemotaxis proteins (MCPs) [57]. This immobilization can offer remediation, recovery and electrification applications [54].

Microorganisms can adjust their growth rate to facilitate a limiting nutrient in their environment by adjusting their molecular composition to the variations in their surroundings [55]. Nutrient deficiencies are not always limited to the one nutrient, in cases where double or multiple limitations occur it is expected that microbial growth could show a different molecular reorganisation as reflected by a new metabolic profile [55]. Bastias and Gentina [55] looked at the limitations of growth parameters of CO_2 and Fe^{2+} in the presence of a Fe^{3+} inhibitory concentration [55]. It was found that the metabolic parameters varied and depended on these concentrations and it was determined that the bacterial oxidation rate of Fe^{2+} is directly related to the production rate of Fe^{3+} [55]. This was supported by Kleerebezem and van Loosdrecht [58], who determined that the substrate conversion is completely proportional to microbial growth in a tightly coupled process.

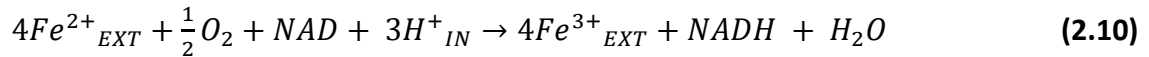
2.3.1.1 *Leptospirillum ferrooxidans*

Leptospirillum ferrooxidans are an iron-oxidizing bacteria in the shape of a small, curved rod measuring approximately 0.3-0.6 by 1 -3.3 μm in size and have been noted as a pioneer microbe due to their role in carbon and nitrogen fixation in early soil ecosystems [58-61]. As an iron-oxidizing bacteria, they are labelled as chemolithoautotrophic and acidophilic with a vibro shape [56,60-62]. *L. ferrooxidans* are classed as acidophilic because they thrive in acidic conditions [6,60]. Chemolithotrophic indicates that the bacterium utilizes the bedrock to produce their own energy source through chemical reactions such as iron oxidation [6,24]. It is the energy and reducing power derived from these reactions that is used for multiple metabolic processes in the cell which includes carbon dioxide (CO_2) and nitrogen fixation [56].

Assimilation of carbon and nitrogen occurs through different sources, such as the atmosphere or the growth medium and both processes are conducted through different enzymes within the cell [56]. It is believed that acetyl – CoA (acetyl coenzyme A) is responsible for carbon assimilation where the carbon dioxide is captured by tetrahydrofolate cofactor and then reduced to a methyl group [56]. There are two enzymes responsible for nitrogen assimilation that has been noted in literature and they are nitrogenase and ammonia permease. However, Merino, et al. [56] believes that even though the genome includes the nitrogenase encoding gene, the nitrogenase within the cell could be inactive due to its sensitivity to oxygen [56,59].

L. ferrooxidans are a gram negative bacteria [56,60] with the cell membrane containing a protein of 80kDa range [57]. The growth rate is approximately 0.1 – 1 hour [58] and produces pseudococci, vibrios and spirilla shaped cells [60]. Growth conditions for *L. ferrooxidans* differs between studies, but it is agreed that the growth medium needs to contain an iron (II) concentration, constant temperature at 28°C (as it is mesophilic), with an optimal pH of 2.5 – 3 but an acceptable pH range of 1.5 – 4 [9,60]. This bacterium is also commonly found underground at mine sites and has been linked to acid mine drainage, due to their iron oxidizing capabilities [6]. Evidence suggests that *L. ferrooxidans* are the dominant species associated with mineral dissolution in acid mine waters [24]. Certain strains of this bacteria can have a single polar flagellum which allows them to be motile, similar to *A. ferrooxidans* [57,60]. From this motility it was found by Acuna, et al. [57] that metal ions such as Ni²⁺, Fe²⁺ and Cu²⁺ act as attractants, while amino acids such as aspartate acted as a repellent [57]. It was also found that nickel increased methylation while aspartate decreased the methylation of proteins [57]. Fluorescence in situ hybridization (FISH) has successfully been used to detect the *L. ferrooxidans* cells [58].

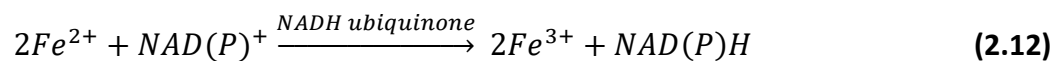
L. ferrooxidans lack the ability to utilize sulfur or thiosulfates which means their sole method of energy production is via iron oxidation of Fe (II) to Fe (III) [6,60]. The inability to utilise sulfur generates a higher affinity to ferrous iron and a higher tolerance to Fe (III) inhibition and allows the microorganism to survive at higher redox potentials than other chemolithotrophs [6,61]. Merino, et al. [56], and Stoytcheva, et al. [61] uses Equation 2.10 below to illustrate the ferrous iron oxidation reaction involved in the cells metabolism using the coenzyme nicotinamide adenine dinucleotide (NAD).



In this reaction the ferrous iron is an electron donor, using oxygen as the electron acceptor [56,61]. The protons that are consumed in this process enter into the cell via the adenosine triphosphate (ATP) synthetase complex which is embedded into the cells inner membrane [56]. The ADP is then coupled with the extrusion $3H^+$ and inorganic phosphate (Pi) as shown in Equation 2.11 below [56].

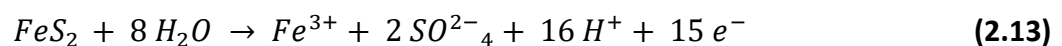


The reductive power comes from the electron transfer between the ferrous iron and the NADH to reduce it to NAD(P) as illustrated in Equation 2.12 below [56].



This metabolic behaviour is quite similar to that of *Acidithiobacillus thiooxidans*, which are the most extensively characterized iron oxidizing, acidophilic bacteria [61].

Rojas-Chapana and Tributsch [12] studied the electrochemical process of pyrite oxidation using *L. ferrooxidans*. It was determined that the oxidation involves the formation of a thiosulfate ion before the formation of iron sulfate, according to the following reaction as shown in Equation 2.13 [12]:



It was also determined, that through this oxidation process, Extracellular Polymeric Substances (EPS) are excreted by the cell and are involved in the storage and uptake of electro dense nanoparticles [12,24]. This adsorption leads to a distinctive assemblage in the exopolymeric capsule which coats the bacterial cell [12]. The chemiotactic nature of *L. ferrooxidans* is a strong driving force for biofilm formation and the bacterial – mineral interactions.

Although, original studies concluded that the *L. ferrooxidans* were unable to oxidise the iron on the surface of pyrite and chalcopyrite, it was found that adaption occurs over several weeks and subcultures, before they had the ability to oxidise the surface [60]. Vilinska and Rao [62] studied the influence *L. ferrooxidans* had on the bio-flotation and bio-flocculation

the pyrite and chalcopyrite system. Through adsorption studies and Hallimond flotation tests, it was determined that there was a greater cell adsorption, greater depression effect and greater flocculation behaviour for chalcopyrite [62].

The effects of *L. ferrooxidans* on the kinetics of sulfide ore flotation of chalcopyrite, sphalerite and pyrrhotite using a xanthate collector was studied by Pecina, et al. [40]. While Zhu, et al. [63] reported that mineral exposure to *L. ferrooxidans* altered the surface charge and hydrophobicity of the mineral particles. These results are similar to those that occur when the minerals are exposed to chemicals such as xanthates and cyanides [63]. Zhu also reports that the degree of change due to the bacterial cells is influenced by the adhesion force of the cells and that of the Extracellular Polymeric Substances excreted by the cells, which mediates the macro – mineral interaction [63]. A study conducted by Rojas-Chapana and Tributsch [12] found that as the leaching of pyrite progressed, the cells began to store electro-dense nanoparticles into the EPS. These particles become embedded in the exopolymeric capsule, coating the cell surface, leading to distinctive bio-mineralised assemblages [12]. While the literature suggests that *L. ferrooxidans* have been thoroughly investigated for their role in bioleaching and mineral flotation, there are limited investigations surrounding the use and composition of EPS.

2.3.1.2 *Acidithiobacillus ferrooxidans*

Acidithiobacillus ferrooxidans, formerly *Thiobacillus ferrooxidans*, is the most commonly studied iron oxidising microorganism and is part of the consortium of microorganisms used for recovery of copper and gold [6,64,65]. Bharadwaj and Ting [66] notes a particular interest in their use as a spent catalyst in petroleum production. Similar to *L. ferrooxidans*, *A. ferrooxidans* are chemolithotrophic, mesophilic and acidophilic thriving in ambient temperatures and acidic conditions (pH 1.5 – 6.0) [6]. *A. ferrooxidans* are able to oxidise both iron and sulfur, while also being able to fix both carbon and nitrogen [65]. Unlike *L. ferrooxidans*, *A. ferrooxidans* are an obligate aerobe, requiring a carbon source (CO₂) for growth [6].

A. ferrooxidans are found naturally at acidic sites which are normally associated with pyrite, such as mine drainage sites and coal wastes [65]. This is due to their ability to utilize the Fe (II) and S⁰ for energy and electron requirements, which is an important role in the

biogeochemical cycling of iron and sulfur [6,65]. Their ability to adapt to different pH and metal concentrations makes them an effective catalyst for sulfides, including in mine waste [6]. However, *A. ferrooxidans* are more susceptible to ferric iron inhibition than *L. ferrooxidans* [61].

Barreto, et al. [65] determined in their study that the formation of biofilm is a prerequisite for mineral dissolution in the presence of *A. ferrooxidans*. It was also noted that the biofilm formation was accompanied by the production of extracellular polymeric substances (EPS) [65].

2.3.2 Microbe – Mineral interaction

Recent literature suggests that the initial adhesion of microbial cells is primarily governed by both specific (stereochemical) and non-specific (physicochemical) molecular interactions between the cell and the mineral surface [53,67]. These properties on a cell surface arise from the structure and arrangement of membrane components such as proteins and polysaccharides, therefore chemical composition plays an important role in adhesion behaviour [53]. Currently there are two theories to predict the primary attachment of cell to solid substrates such as minerals and to other cells. These methods are the Derjaguin – Landau – Verwey – Overbeek (DLVO) theory and the extended Derjaguin – Landau – Verwey – Overbeek theory [53]. Both theories are concerned with double layer forces that occur between charged objects across liquids and Van de Waals forces to estimate the actual interaction potential between particles.

Attachment of bacterial cells to solid substrates is accompanied by the excretion of extracellular polymeric substances (EPS) [54]. This excretion of EPS activates adhesion by changing the charge of the bacterial envelope through the trapping of near surface or structural ions on the mineral surface [54]. The EPS can both chemically bond with surface of the solid substrate and intermediate/promote the nutrition/respiration chemical reactions [54]. This attachment of microorganism cells and their metabolites facilitate hydrometallurgical leaching and show promise in mineral beneficiation processes such as flotation and flocculation [42,54]. There are three proposed mechanisms for cell adhesion and charge transfer mechanisms for bio-modification of mineral surfaces [32,42,51,53,54,62,68], these are:

- i. Direct Contact: Attachment of the microbial cell onto the surface of the solid substrate. The cell and its enzymes have a direct interaction with the surface. This can also include charge transfer reactions.
- ii. Indirect Contact: Cells adhere to the mineral surface and create a reaction space. Microbial catalysis of oxidation and/or reduction reactions occur within this reaction space. This mechanism is sometimes referred to as the cooperative mechanism.
- iii. Indirect Non-Contact: Cells remain planktonic and do not physically interact with the mineral surface. This mechanism uses shuttle compounds, such as Fe^{3+} ions, to react with the mineral surface and is often regulated by organic compounds like quinone. This mechanism also includes the adsorption and/or chemical reaction with metabolic products, such as EPS, extracellular proteins, and extracellular polysaccharides.

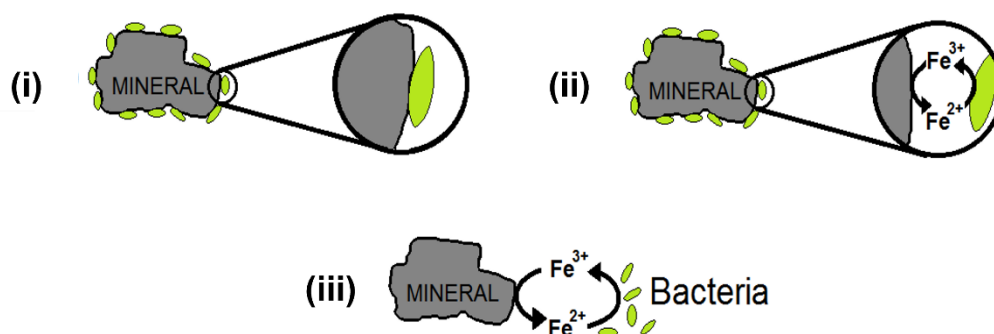
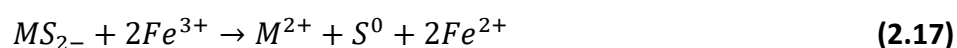
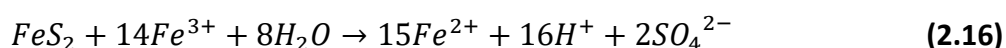
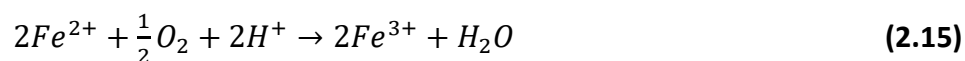
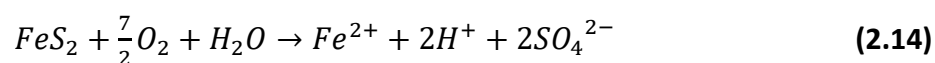
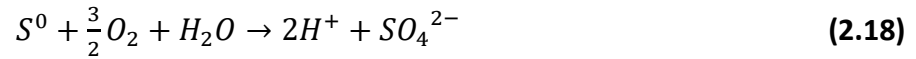


Figure 2.7: Schematic of the three microbe-mineral contact mechanisms. Adapted from Crundwell [32]

The direct interaction can be summarised by the Equations 2.14 and 2.15 below, while the indirect interaction is summarised by Equations 2.16, 2.17 and 2.18, using pyrite as an example [6].





The ability of *A. ferrooxidans* to oxidise sulfur in the absence of iron ions is used as support for the direct mechanism [6]. However, previous studies suggest that only Fe (III) ions and protons are able to dissolve metal sulfides and that microorganisms regenerate these components [6,31,69]. Spectroscopy has opened the door to understanding the key mechanisms due to bio-modification of surfaces [52]. The surface of the bacterial cells are small scale active sites on the mineral surface for nucleation and propagation [52]. These active sites result in both stable and transient small scale surface chemical heterogeneities [52].

Studies from Harneit, et al. [9] looked at *A. ferrooxidans*, *A. thiooxidans* and *L. ferrooxidans* attachment on pyrite, chalcopyrite, quartz, sphalerite and galena [9]. Primary attachment of the microbes was found to occur in areas which contain visible defects and the attachment was found to be selective [9], with most strains being mineral selective and restricted to crystal boundaries with the bacteria attaching readily through chemotaxis [9]. A monolayer of cells or single cells were observed on the surface after as little as 24 hour exposure [9]. These microbes can also accumulate metal cations through three different pathways: metabolic – independent, passive and metabolic – dependent [38]. These are similar to the interactions illustrated in Figure 2.7. The accumulation of the metal cations is determined by two characteristics of the bacterial cell, these being the sorptivity of the cell envelope and the capacity of the cytosol [38].

2.3.3 Bioleaching

Bioleaching is a leaching process where microorganism and their metabolic pathways are used as catalysts in the oxidation of metallic sulfides [70]. This process converts the ore into soluble metallic ions and sulfuric acid at a faster rate than chemical leaching [13,56,66,69-73]. Although only a few decades old, this minerals processing technique has been used as a low-cost process to extract metals from low grade ore and proven to be more environmentally friendly than traditional sulfide mineral processing techniques [55,66,70]. Bioleaching is environmentally benign in comparison to chemical leaching as strong chemicals, high temperatures and pressures are not required [66]. With the technical and economic advantages, bioleaching of sulfide mineral systems have been thoroughly investigated for the

recovery of copper, uranium, refractory gold and other precious/semi-precious metals [55,74]. The mesophilic iron and sulfur oxidising bioleach microbes *A. ferrooxidans*, *A. thiooxidans*, *L. ferrooxidans*, and *Acidithiobacillus caldus* (*A.c*) are bacterial strains which have been isolated from leaching sites and investigated for the use in sulfide mineral systems [7,9,11,31,42,54,63,71,74-79].

Microbes have been used in the oxidative dissolution processes of sulfide minerals for several decades [6]. It has been theorised that the catalysis action of the microbes occurs through either a direct or indirect mechanism [6]. The direct mechanism assumes that the microbial cells are directly responsible for the oxidative reactions through attachment of the cells on the mineral surface. While the indirect mechanism assumes that the cells are responsible for the oxidation through indirect reactions of the surface. These mechanisms have also been referred to as contact leaching (direct) and cooperative dissolution (indirect) [80]. These two mechanisms, while oxidising the sulfide, produce different oxidation pathways as picture in Figure 2.8. The thiosulfate mechanism suggests the formation of sulfate through a thiosulfate intermediate. In the occurrence of a direct mechanism, the thiosulfate intermediate is not observed. Likewise, the polysulfide mechanism results in the production of sulfate through a polysulfide intermediate. This pathway represents an indirect mechanism. This ability to oxidise sulfide minerals via different pathways is what leads to a wide application in bioleaching [6,69,80].

Image removed due to copyright restriction

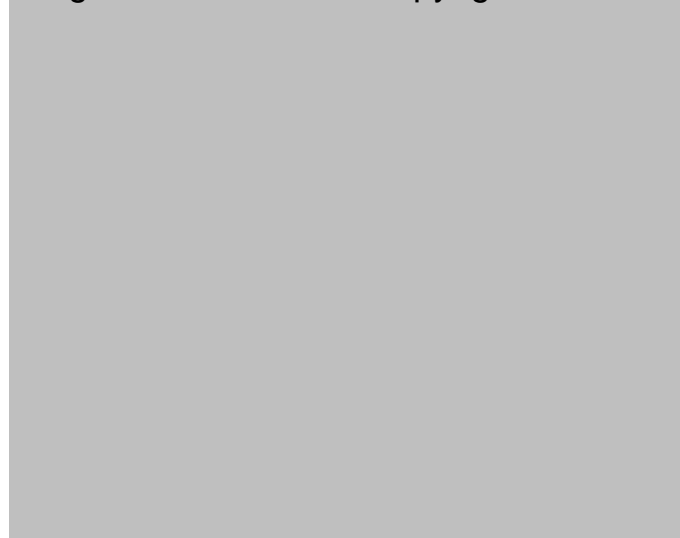


Figure 2.8: Reaction pathways for metal extraction from metal sulfides using *A. ferrooxidans* (*A. f*) and *L. ferrooxidans* (*L. f*) . Image from Blowes, et al. [6] adapted from Sand, et al. [69]

Rojas-Chapana and Tributsch [12] used mixed cultures of these sulfur-oxidising mesophilic microorganisms for the bio-desulfurisation of high sulfur coals and the biological removal of sulfur and ash from fine grained high pyritic sulfur coals. Similarly, Sand, et al. [77] and Lavalle, et al. [74] used these bacteria in both single and mixed cultures to test the effect of temperature range on their iron oxidising capabilities and growth kinetics at a range of temperatures [74,77]. The influence of pH on the growth kinetics and iron oxidation was also studied by Lavalle, et al. [74].

Rao, et al. [54] observed autotrophic and heterotrophic bio-solubilization and bioleaching of sulfide ores, waste and low grade mineral including soils and mud, lateritic or copper converter slag, fly ash and electronic waste material [54]. The application of bioleaching technology has also been used for the recovery of phosphorus from different phosphate ore [12]. The bioleaching of pyrite has also been studied, with bacterial attachment observed with the presence of local forms of corrosion in the form of surface pitting [12]. It was also determined that the contact mechanism of bacteria plays an important role in the dissolution of pyrite [9].

Bioleaching investigations have also had a particular interest in thermophiles, as they demonstrate a higher rate of metal solubilisation than mesophilic bacteria [13,66,71,72]. Thermophiles have been proven useful in the extraction of metals from industrial waste, including sewer sludge, spent batteries, fly ash and electronic scrap.

The microorganisms used to facilitate hydrometallurgical leaching have also shown great promise in other mineral beneficiation techniques such as bio-flotation and bio-flocculation [54]. The study conducted by Gu, et al. [81] showed a change in the surface properties of pyrrhotite when exposed to *Leptospirillum firriphilum* and *Acidithiobacillus caldus* [81].

2.3.4 Bio-flotation

Bio-flotation is a biotechnology 'green chemistry' approach to solving the conundrum of mineral recovery and environmental impact [54]. Bio-flotation works on the principles of froth flotation; however, the synthetic flotation reagents are replaced with microbes, which naturally occur at mine sites, and their metabolites. The microorganisms and their metabolites can act as bio reagents by exhibiting hydrophobic or hydrophilic properties when

adhered to the surface [42,82], replacing the need for traditional flotation reagents such as xanthates and cyanides. In comparison to the inorganic compounds used in conventional flotation, bacteria and their metabolites are non-toxic and environmentally benign [42]. The selective flotation and/or depression of sulfides and oxides has been studied with a variety of different microbes, with the use of heterotrophic and chemolithotrophic bacteria being used in bio-flotation processes for at least the last two decades [42]. These microbes include *Mycobacterium pheli*, *Rodococcus opacus*, *Acidithiobacillus thiooxidans*, *Acidithiobacillus ferrooxidans* and *Leptospirillum ferrooxidans* [42]. Currently bio-flotation is conducted at micro-flotation scales, with literature summary of the parameters used for recent studies shown in Appendix I: Bio-flotation Literature Comparison. While bio-flotation has been investigated over the last few decades, the summary presented in Appendix I indicates there are still many variables to investigate thoroughly. These variables include strain of bacteria, gas used for flotation, concentration of reagents/cells and exposure conditions [40,83,84]. Understanding the impact of these variable on different mineral systems will help optimise the process. The use of *A. ferrooxidans* and *L. ferrooxidans* for application in bio-flotation has been investigated, with recent studies focusing on selective attachment and EPS expression [11,15,23,85].

A. ferrooxidans have been investigated for their effect on iron sulfide flotation due to their ability to oxidize iron and inorganic sulfur compounds [86]. Bio-flotation studies using *A. ferrooxidans* and EPS products have included the separation of pyrite from chalcopyrite and arsenopyrite [15,23,87,88]. These studies suggest selective attachment to pyrite occurs with irreversible attachment to pyrite observed within minutes [88], while attachment to chalcopyrite was observed after 12 days, allowing for successful separation [89]. The enhanced absorption of cells on pyrite resulted in selective depression of pyrite over chalcopyrite and arsenopyrite, and greater dissolution was observed in the presence of active cells with EPS [9,15,23,28]. Investigations into the effect of EPS on the bio-modulation of pyrite and chalcopyrite found cells with EPS resulted in a lower recovery than the free extracted EPS alone [42].

Similarly, Chandrababha and Natarajan [14] found that interactions between both pyrite and chalcopyrite with *A. thiooxidans* rendered the mineral surface hydrophilic. This resulted in an isoelectric shift of both minerals to a higher pH which was assessed through electrophoretic

mobility [14]. In this system, pyrite was selectively depressed at both neutral and acidic pH with successful flotation of chalcopyrite. Floatability of pyrite was increased with the addition of collector and in the presence of cells at a low pH [14]. This can be explained through the formation of alkyl xanthate species on the surface [14]. In aqueous systems alkyl xanthate is physisorbed to the surface of pyrite, increasing the hydrophobic properties of the surface and therefore the floatability. In the case of chalcopyrite, these alkyl xanthate ions are strongly chemisorbed to the surface through the coordination to specific copper sites on the mineral surface, forming the highly hydrophobic copper (I) alkyl xanthate [14]. Likewise the study conducted by Chandrababha, et al. [15] found that pyrite was suppressed after biomodulation. However, the pyrite was activated when conditioned with chalcopyrite due to the copper ions in solution. Chandrababha, et al. [15] also determined a relationship between the pH and pyrite floatability; acidic environments increased floatability and alkaline environments decreased floatability.

Govender and Gericke [42] investigated the influence of free EPS on the separation of chalcopyrite and pyrite. Interestingly, a maximum yield of 77% was reported for single mineral chalcopyrite flotation, with the chalcopyrite yield decreasing in differential flotations with pyrite. This study also concluded that prior conditioning of pyrite with *A. ferrooxidans* can reduce xanthate use [42].

2.3.5 Bio reagents

Bio reagents or biological reagents refer to chemicals that are of biological origin such as an enzyme, protein or sugar. As bio reagents are organically occurring compounds, they produce less damage to the environment and have been proposed as replacements for the chemicals currently used in traditional flotation processes. Bio-flotation and bio-flocculation processes are concerned with a minerals response to bio reagents [54]. The bio reagents and microorganisms used alter the physicochemical properties of the mineral surface, these properties being: atomic and electronic structure, net charge/potential, acid/base properties and the wettability of the surface [54]. Microbes have been known to play an important role in bio modulation of minerals using biological compounds such as biopolymers, including lignocellulose, chitin and polysaccharides, such as dextrin and guar gum [38,84]. The microbial cell and/or the metabolic products can directly or indirectly modify the surface chemistry of

the mineral similar to surfactant molecules [42]. The method and mechanism by which the modification occurs changes depending on the bio reagent.

These characteristics are dependent on the presence of the non-polar and polar functional groups present on the cellular surface of the microbe [42]. The non-polar groups include hydrocarbon chains while the polar groups include carboxyl, hydroxyl and phosphates [42]. The study by Subramanian, et al. [84] has proposed a chemical complexation mechanism between polysaccharides and the mineral surface, where the hydroxyl groups present in the polysaccharide interact with the metal hydroxides on the mineral surface through hydrogen bonding and chemical forces [84]. Subramanian, et al. [84] also discuss a theory where the polysaccharides act as a Bronsted acid and the hydroxyl groups act like a Bronsted base, which leads to better attachment in basic conditions [84]. The adsorption of proteins is proposed to be different, using electrostatic forces, hydrogen bonding, hydrophilic interactions along with Van der Waals interactions [84]. The study conducted by Deo and Natarajan [90] indicates the presence of proteins on the surface increases the hydrophobic properties, while enhanced hydrophilicity was observed with the presence of polysaccharides.

2.4 Biofilms and Extracellular Polymeric Substances

Microbial cells can grow in association with surfaces in aqueous environments, this attachment of cells to the surface is the initial step which leads to Extracellular Polymeric Substances excretion and the formation of biofilms [67,91]. EPS is known to mediate the attachment of microbes, *A. ferrooxidans*, *A. thiooxidans* and *L. ferrooxidans*, to growth substrates such as metal sulfides [9,92], but EPS also plays a pivotal role in biofilm formation. The schematic presented in Figure 2.9 shows the cell cycle on a surface and the formation of biofilm. When planktonic cells interact with a surface, they are reversibly attached until EPS is secreted to 'stick' them in place. Once the cells are irreversibly attached to the surface, they start to replicate, forming a microcolony. As the microcolony grows, the EPS produced crosslinks and complexes to form structured aggregates, becoming a biofilm [9,93-95].

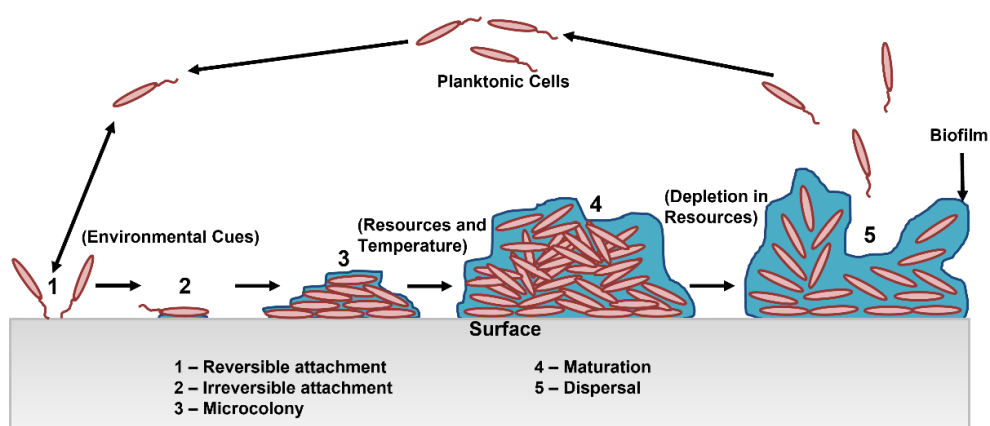


Figure 2.9: Schematic of biofilm formation on a surface. Adapted from Pinto, et al. [95]

The main role of the biofilm matrix is to protect the microbial community but also facilitates the structural organisation and influences metal adsorption and immobilization [91]. The biofilm matrix is highly hydrated and constructed of EPS components to keep cells together and retain water [96,97]. Interactions between the EPS components activate the biofilm matrix [97]. These interactions between the EPS components produces stability through the entanglement of biopolymers, crosslinking via multivalent cations and hydrophobic interactions [97]. This can be done by altering the surface chemistry of the underlying substrate [96]. The molecular adhesion of cells to a solid substrate includes hydrophobic, electrostatic, covalent and polymer – polymer interactions between the EPS and substrate surface [96]. Harneit, et al. [9] has successfully visualised the biofilm matrix using atomic force microscopy (AFM). Each component present within the EPS has a different role in the biofilm matrix, as seen in Table 2.1 below.

Table 2.1: Structural breakdown of EPS components including the effect, nature and role of components as displayed in Flemming, et al. [97]

Effect of EPS Component	Nature of EPS Component	Role in Biofilm
Constructive	Neutral polysaccharides Amyloids	Structural components Structural components
Sorptive	Charged or hydrophobic polysaccharides	Ion exchange, sorption
Active	Extracellular enzyme	Polymer degradation
Surface – Active	Amphiphilic Membrane residues	Interfacial interactions Export from cell, sorption
Informative	Lectins Nucleic acids	Specificity, recognition Genetic information, structure

Redox active	Bacterial refractory polymers	Electron donor or acceptor?
Nutritive	Various polymers	Source of C, N and P

The EPS excreted by microorganisms is a complex mixture of polymers which includes products derived from lysis and hydrolysis of organic matter [92]. The EPS is incredibly important to cells as it determines the immediate conditions of the surrounding microenvironment [97]. These conditions change depending on the composition of EPS but include the porosity, density, water content, charge, sorption properties, hydrophobicity and mechanical stability [97]. It has been widely noted that the EPS is mainly composed of proteins, polysaccharides (neutral sugars), lipids (free fatty acids), carbohydrates and humic substances. Other components such as glycoproteins, glycolipids, uronic acid, extracellular DNA or nucleic acids and the presence of iron (II) ions have also been found in EPS [9,42,91,92,97]. The composition of EPS has been documented to change depending on the strain of bacteria and external factors such as growth medium and incubation conditions [92]. He, et al. [92] found that the concentration of EPS produced and the chemical composition of the EPS is linked to the bacteria type. Mesophilic bacteria have a higher content of polysaccharide, while the thermophilic stains have less [92]. Jiao, et al. [91] quantitatively and qualitatively compared the chemical composition of EPS from a mid-developmental stage biofilm (DS1) and a mature biofilm (DS2). It was found that more than twice the amount of EPS was derived from the DS2 biofilm than the DS1 biofilm with significant compositional differences [91]. From this study it was concluded that the composition of EPS from acidic biofilms is dependent on the maturity and controlled by the microbial communities and their geochemical environment [91].

A range of bacteria and archaea including *Acidianus brierleyi*, *Acidianus manzaensis*, *Metallosphaera sedula*, *Sulfolobus metallicus*, *Acidithiobacillus ferrooxidans*, *Leptospirillum ferriphilum* and *Sulfobacillus thermos-sulfidooxidans* were analysed by He, et al. [92] for a comparison of EPS components in different conditions. A comparison of medium and incubation conditions of different temperatures and pH were used to analyse the difference in the protein content, polysaccharide content, iron content and galacturonic acid content in the EPS excreted [92]. It was found that the bioleach microbes produce a higher amount of EPS when grown on pyrite than sulfur or ferrous ions [92].

Harneit, et al. [9] studied the difference of growth medium on the composition of the EPS produced from *L. ferrooxidans* and *A. ferrooxidans*. The cultures were grown on pyrite, sulfur and iron (II) ions [9]. It was found that for both the *L. ferrooxidans* and the *A. ferrooxidans*, the EPS of the pyrite grown cells and the iron (II) grown cells contained iron (II) ions and uronic acid, while the sulfur grown cells did not [9].

Recent studies by Hippe [60] and Harneit, et al. [9] focused on the growth of *L. ferrooxidans* on pyrite and chalcopyrite and the composition of EPS excreted. Harneit, et al. [9] found the EPS composition to be glucose, glucuronic acid, fatty acids and iron ions where 16% was attributed to sugars, 2.3% was iron ions and the was fatty acids. Hippe [60] found the EPS to be mainly comprised of neutral sugars, iron species and some uronic acid. The presence of the iron species suggests that the EPS is a prerequisite for the attachment of bacteria to the metal sulfide surface and chemical attack [60]. The physiological conditions allow the EPS to render the cell as a net positive charge [9]. The EPS complexed to iron (III) ions enables the cells to attach primarily to the pyrite surface by electrostatic interactions as pyrite is negatively charged [9]. Harneit, et al. [9] claims that the dissolution of mineral takes place within the reaction space which involves EPS containing iron (III) complex. He, et al. [92] believes that the EPS could act with concentrated ferric ions to form a special layer in which the mineral is oxidised by the ferric ions releasing an energy source such as sulfur and ferrous ions into the surroundings [92]. Hippe [60] also examined the cell free extract and found that it contained ribulose biphosphate carboxylase activity, which demonstrates the autotrophic nature [60].

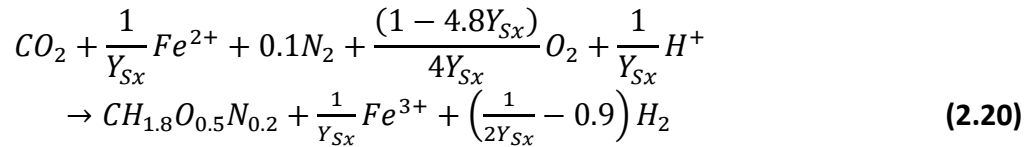
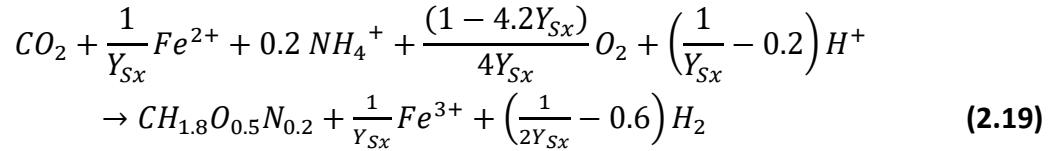
The speciation and distribution of metals in many subsurface and aquatic environments can be controlled by the binding of heavy metals onto the surface of both minerals and bacteria [96]. This means that the EPS could potentially have a significant effect on metal adsorption characteristics and acid-base properties of the bacterial cells [96]. The high binding constant and binding enthalpy of EPS indicates that they are a thermodynamically favourable ligand to heavy metals [98]. The enthalpy of these reactions indicates that it is an exothermic reaction when metal ions bind to the EPS [98]. This metal chelation by EPS is a crucial mechanism in the natural detoxification of heavy metals and hence a vital process in bioremediation [91]. The EPS helps prevent microbes against heavy metal toxicity through its capacity to bind with metals, although the binding mechanisms and strengths are not well documented [98].

Equilibrium adsorption experiments, isothermal titration calorimetry and potentiometric titration techniques were used to investigate the adsorption of Cu^{2+} in montmorillonite and goethite by EPS extracted from *Pseudomonas putida*. The results indicate that the Cu^{2+} ions mainly interact with the carboxyl and phosphoryl groups as inner sphere complexes on EPS molecules and their composites with mineral [96]. While a similar study by Sheng, et al. [98] determined that metal binding to EPS greatly influenced the distribution of heavy metals in microbial aggregates and found that humic acid and proteins are strong ligands for Cu^{2+} , with the possibility of the Cu^{2+} ions bonding with the oxygen atom in the carboxyl groups within the EPS. The binding process was found to be exothermic and thermodynamically favourable through calculation of enthalpy and binding capacity constant [98]. It was found that the increase of pH resulted in an increase of binding sites for Cu, Pb and Cd, whereas the binding constant did not indicate this variation for all at a pH of 7 [96].

Harneit, et al. [9] also looked at the growth of *A. ferrooxidans* on iron (II) ions and pyrite with sulfur and *A. thiooxidans* grown on sulfur. It was found that the sugar component of the EPS was composed of rhamnose, fructose, xylose, mannose, glucose and glucuronic acid, with a range of fatty acids and iron ions [9]. Likewise, Jiao, et al. [91] found the glycosyl composition to be galactose, glucose, heptose, rhamnose and mannose. While Lima, et al. [99] found that the composition of monosaccharides in the EPS of *Agaricus brasiliensis* were as follows: mannose (58.7%), galactose (21.4%), glucose (13.1%), rhamnose (3.9%) and xylose (2.8%).

A large quantity of aromatic structures are within the EPS as well as unsaturated fatty acid chains with fluorescent characteristics [98]. The fluorescent characteristics can be used to provide information about the structure, functionality, configuration and heterogeneity of the EPS [98]. Thermodynamic analysis is carried out using calorimetry as all physical, chemical and biological processes are accompanied by heat exchanges [98]. Analysis of EPS has been conducted through multiple techniques. He, et al. [92] analysed the protein content through a protein dye method, polysaccharide content was analysed through the anthrone method and galacturonic acid was analysed using fosulfuric acid-carbazole colorimetry [92]. Other studies have used the Bradford assay to analyse protein content, phenol-sulfuric assay to analyse the carbohydrate content and uronic acid assay for the uronic acid content [28]. No previous studies of *A. ferrooxidans*, *L. ferrooxidans* and *A. thiooxidans* on different growth conditions and EPS composition have been conducted [92].

Merino, et al. [56] formulated an equation of biomass formation by assuming the composition of $CH_{1.8}O_{0.5}N_{0.2}$, as shown in Equations 2.19 and 2.20 with each equation representing a different nitrogen sources.



Where Y_{Sx} represents the biomass yield of the ferrous iron. This reaction gives the sulfide minerals a high affinity to ferrous ion and a low sensitivity to ferric ion inhibition, giving this reaction importance in bioleaching [56].

2.5 Objectives

The objective of this study is to optimise the recovery of chalcopyrite through bio-flotation from a mixed mineral system. To achieve this, there are two key elements to be investigated. These are:

- I. The impact of growth conditions on the behaviour of the bioleach microbes *Leptospirillum ferrooxidans* and *Acidithiobacillus ferrooxidans*.
- II. The relationship between the microbe behaviour, Extracellular Polymeric Substances composition and flotation behaviour of sulfide minerals.

This will be achieved through cell attachment studies, surface analysis using spectroscopic techniques and micro-flotation tests.

2.6 References

1. Wills, B.A. *Mineral processing technology: an introduction to the practical aspects of ore treatment and mineral recovery*, 4th ed.; Pergamon Press: New South Wales, Australia, 1988.
2. Berry, L.G.; Mason, B. *Elements of Mineralogy*; W. H. Freeman: San Francisco, 1968.
3. The Editors of Encyclopaedia Britannica. Sulfide Mineral. *Encyclopedia Britannica*: 2018.
4. Napier-Munn, T.; Wills, B.A. *Wills' mineral processing technology: an introduction to the practical aspects of ore treatment and mineral recovery*; Butterworth-Heinemann: 2011.
5. Sullivan, P.J.; Yelton, J.L.; Reddy, K. Iron sulfide oxidation and the chemistry of acid generation. *Environmental Geology and Water Sciences* **1988**, *11*, 289-295.
6. Blowes, D.; Ptacek, C.; Jambor, J.; Weisener, C. The geochemistry of acid mine drainage. *Treatise on geochemistry* **2003**, *9*, 149-204.
7. Vaughan, D.J.; Craig, J.R. *Mineral chemistry of metal sulfides*; Cambridge University Press Cambridge: 1978; Vol. 493.
8. Vaughan, D.J. *Sulfide mineralogy and geochemistry*; Mineralogical Society of America: 2006; Vol. 61.
9. Harneit, K.; Göksel, A.; Kock, D.; Klock, J.-H.; Gehrke, T.; Sand, W. Adhesion to metal sulfide surfaces by cells of *Acidithiobacillus ferrooxidans*, *Acidithiobacillus thiooxidans* and *Leptospirillum ferrooxidans*. *Hydrometallurgy* **2006**, *83*, 245-254.
10. Hicks, D.; Mehl, M.J.; Gossett, E.; Toher, C.; Levy, O.; Hanson, R.M.; Hart, G.; Curtarolo, S. The AFLOW library of crystallographic prototypes: part 2. *Computational Materials Science* **2019**, *161*, S1-S1011.
11. Bleeze, B.; Zhao, J.; Harmer, S.L. Selective Attachment of *Leptospirillum ferrooxidans* for Separation of Chalcopyrite and Pyrite through Bio-Flotation. *Minerals* **2018**, *8*, 86.
12. Rojas-Chapana, J.A.; Tributsch, H. Interfacial activity and leaching patterns of *Leptospirillum ferrooxidans* on pyrite. *FEMS Microbiology Ecology* **2004**, *47*, 19-29, doi:10.1016/S0168-6496(03)00221-6.
13. Konishi, Y.; Tokushige, M.; Asai, S.; Suzuki, T. Copper recovery from chalcopyrite concentrate by acidophilic thermophile *Acidianus brierleyi* in batch and continuous-flow stirred tank reactors. *Hydrometallurgy* **2001**, *59*, 271-282, doi:10.1016/S0304-386x(00)00173-0.
14. Chandraprabha, M.N.; Natarajan, K.A. Surface chemical and flotation behaviour of chalcopyrite and pyrite in the presence of *Acidithiobacillus thiooxidans*. *Hydrometallurgy* **2006**, *83*, 146-152, doi:10.1016/j.hydromet.2006.03.021.
15. Chandraprabha, M.N.; Natarajan, K.A.; Modak, J.M. Selective separation of pyrite and chalcopyrite by biomodulation. *Colloids Surf B Biointerfaces* **2004**, *37*, 93-100, doi:10.1016/j.colsurfb.2004.06.011.
16. Mehl, M.J.; Hicks, D.; Toher, C.; Levy, O.; Hanson, R.M.; Hart, G.; Curtarolo, S. The AFLOW Library of Crystallographic Prototypes: Part 1. *Computational Materials Science* **2017**, *136*, S1-S828, doi:<https://doi.org/10.1016/j.commatsci.2017.01.017>.
17. Hiroyoshi, N.; Hirota, M.; Hirajima, T.; Tsunekawa, M. A case of ferrous sulfate addition enhancing chalcopyrite leaching. *Hydrometallurgy* **1997**, *47*, 37-45, doi:[https://doi.org/10.1016/S0304-386X\(97\)00032-7](https://doi.org/10.1016/S0304-386X(97)00032-7).

18. The Editors of Encyclopaedia Britannica. Hematite. Available online: <https://www.britannica.com/science/hematite> (accessed on
19. Abaka-Wood, G.B.; Addai-Mensah, J.; Skinner, W. A study of flotation characteristics of monazite, hematite, and quartz using anionic collectors. *International Journal of Mineral Processing* **2017**, *158*, 55-62, doi:<https://doi.org/10.1016/j.minpro.2016.11.012>.
20. Corkhill, C.L.; Vaughan, D.J. Arsenopyrite oxidation—A review. *Applied Geochemistry* **2009**, *24*, 2342-2361.
21. Silva, J.C.M.; De Abreu, H.A.; Duarte, H.A. Electronic and structural properties of bulk arsenopyrite and its cleavage surfaces – a DFT study. *RSC Advances* **2015**, *5*, 2013-2023, doi:10.1039/C4RA13807D.
22. Bindi, L.; MOËLO, Y.; Léone, P.; Suchaud, M. Stoichiometric arsenopyrite, FeAsS, from La Roche-Baloue quarry, Loire-Atlantique, France: Crystal structure and mossbauer study. *The Canadian Mineralogist* **2012**, *50*, 471-479, doi:10.3749/canmin.50.2.471.
23. Chandraprabha, M.N.; Natarajan, K.A.; Somasundaran, P. Selective separation of arsenopyrite from pyrite by biomodulation in the presence of Acidithiobacillus ferrooxidans. *J Colloid Interf Sci* **2004**, *276*, 323-332, doi:10.1016/j.jcis.2004.03.047.
24. Corkhill, C.L.; Wincott, P.L.; Lloyd, J.R.; Vaughan, D.J. The oxidative dissolution of arsenopyrite (FeAsS) and enargite (Cu₃AsS₄) by Leptospirillum ferrooxidans. *Geochimica Et Cosmochimica Acta* **2008**, *72*, 5616-5633, doi:10.1016/j.gca.2008.09.008.
25. Buckley, A.N.; Walker, G.W. The surface composition of arsenopyrite exposed to oxidizing environments. *Applied Surface Science* **1988**, *35*, 227-240, doi:[https://doi.org/10.1016/0169-4332\(88\)90052-9](https://doi.org/10.1016/0169-4332(88)90052-9).
26. Rimstidt, J.D.; Chermak, J.A.; Gagen, P.M. Rates of reaction of galena, sphalerite, chalcopyrite, and arsenopyrite with Fe (III) in acidic solutions. ACS Publications: 1994.
27. Hoffert, J.R. Acid Mine Drainage. *Ind Eng Chem* **1947**, *39*, 642-646, doi:10.1021/ie50449a020.
28. Gehrke, T.; Telegdi, J.; Thierry, D.; Sand, W. Importance of Extracellular Polymeric Substances from Thiobacillus ferrooxidans for Bioleaching. *Appl Environ Microbiol* **1998**, *64*, 2743-2747.
29. Ighalo, J.O.; Kurniawan, S.B.; Iwuozor, K.O.; Aniagor, C.O.; Ajala, O.J.; Oba, S.N.; Iwuchukwu, F.U.; Ahmadi, S.; Igwegbe, C.A. A review of treatment technologies for the mitigation of the toxic environmental effects of acid mine drainage (AMD). *Process Safety and Environmental Protection* **2022**, *157*, 37-58, doi:<https://doi.org/10.1016/j.psep.2021.11.008>.
30. Akcil, A.; Koldas, S. Acid Mine Drainage (AMD): causes, treatment and case studies. *Journal of Cleaner Production* **2006**, *14*, 1139-1145, doi:<https://doi.org/10.1016/j.jclepro.2004.09.006>.
31. Sand, W.; Gerke, T.; Hallmann, R.; Schippers, A. Sulfur chemistry, biofilm, and the (in) direct attack mechanism—a critical evaluation of bacterial leaching. *Applied Microbiology and Biotechnology* **1995**, *43*, 961-966.
32. Crundwell, F.K. The dissolution and leaching of minerals: Mechanisms, myths and misunderstandings. *Hydrometallurgy* **2013**, *139*, 132-148.
33. Khoshkhou, M. Chalcopyrite Dissolution in Sulphate-Based Leaching and Bioleaching Systems. Luleå tekniska universitet, 2014.

34. Zhang, Y.; Zhao, H.; Qian, L.; Sun, M.; Lv, X.; Zhang, L.; Petersen, J.; Qiu, G. A brief overview on the dissolution mechanisms of sulfide minerals in acidic sulfate environments at low temperatures: Emphasis on electrochemical cyclic voltammetry analysis. *Minerals Engineering* **2020**, *158*, 106586, doi:<https://doi.org/10.1016/j.mineng.2020.106586>.
35. Kocabag, D.; Shergold, H.L.; Kelsall, G.H. Natural oleophilicity/hydrophobicity of sulphide minerals, II. Pyrite. *International Journal of Mineral Processing* **1990**, *29*, 211-219, doi:[https://doi.org/10.1016/0301-7516\(90\)90054-3](https://doi.org/10.1016/0301-7516(90)90054-3).
36. Fairthorne, G.; Fornasiero, D.; Ralston, J. Effect of oxidation on the collectorless flotation of chalcopyrite. *International Journal of Mineral Processing* **1997**, *49*, 31-48, doi:[https://doi.org/10.1016/S0301-7516\(96\)00039-7](https://doi.org/10.1016/S0301-7516(96)00039-7).
37. Shimizu, K.; Tschulik, K.; Compton, R. Exploring the mineral–water interface: reduction and reaction kinetics of single hematite (α -Fe₂O₃) nanoparticles. *Chemical science* **2016**, *7*, 1408-1414.
38. Haferburg, G.; Kothe, E. Microbes and metals: interactions in the environment. *Journal of Basic Microbiology* **2007**, *47*, 453-467, doi:10.1002/jobm.200700275.
39. Milosavljević, M.M.; Marinković, A.D.; Rančić, M.; Milentijević, G.; Bogdanović, A.; Cvijetić, I.N.; Gurešić, D. New eco-friendly xanthate-based flotation agents. *Minerals* **2020**, *10*, 350.
40. Pecina, E.T.; Rodriguez, M.; Castillo, P.; Diaz, V.; Orrantia, E. Effect of Leptospirillum ferrooxidans on the flotation kinetics of sulphide ores. *Minerals Engineering* **2009**, *22*, 462-468, doi:10.1016/j.mineng.2008.12.008.
41. Chander, S.; Nagaraj, D.R. FLOTATION | Flotation Reagents. In *Encyclopedia of Separation Science*, Wilson, I.D., Ed. Academic Press: Oxford, 2007; <https://doi.org/10.1016/B978-012226770-3/10665-Xpp>. 1-14.
42. Govender, Y.; Gericke, M. Extracellular polymeric substances (EPS) from bioleaching systems and its application in bioflotation. *Minerals Engineering* **2011**, *24*, 1122-1127, doi:10.1016/j.mineng.2011.02.016.
43. Liu, Q.; Zhang, Y.H.; Laskowski, J.S. The adsorption of polysaccharides onto mineral surfaces: an acid/base interaction. *International Journal of Mineral Processing* **2000**, *60*, 229-245, doi:10.1016/S0301-7516(00)00018-1.
44. Tipman, N.R. The reactions of potassium ethyl xanthate in aqueous solutions. The University of British Columbia, 1970.
45. Klimpel, R.R. Froth Flotation. In *Encyclopedia of Physical Science and Technology (Third Edition)*, Meyers, R.A., Ed. Academic Press: New York, 2003; <https://doi.org/10.1016/B0-12-227410-5/00262-3pp>. 219-234.
46. The Editors of Encyclopaedia Britannica. Xanthate. Available online: <https://www.britannica.com/science/xanthate> (accessed on
47. Shen, Y.; Nagaraj, D.; Farinato, R.; Somasundaran, P. Study of xanthate decomposition in aqueous solutions. *Minerals Engineering* **2016**, *93*, 10-15, doi:10.1016/j.mineng.2016.04.004.
48. Chemwatch. Potassium Isopropylxanthate. Available online: <https://jr.chemwatch.net/chemwatch.web/home#> (accessed on 16 July).
49. Houot, R.; Duhamet, D. Floatability of Chalcopyrite in the Presence of Dialkyl-Thionocarbamate and Sodium-Sulfite. *International Journal of Mineral Processing* **1993**, *37*, 273-282, doi:10.1016/0301-7516(93)90031-5.

50. Iwasaki, I.; Cooke, S.R. The decomposition of xanthate in acid solution. *Journal of the American Chemical Society* **1958**, *80*, 285-288.
51. Rao, M.K.Y.; Natarajan, K.A. Electrochemical Effects of Mineral Mineral Interactions on the Flotation of Chalcopyrite and Sphalerite. *International Journal of Mineral Processing* **1989**, *27*, 279-293.
52. Geesey, G.G.; Neal, A.L.; Suci, P.A.; Peyton, B.M. A review of spectroscopic methods for characterizing microbial transformations of minerals. *J Microbiol Methods* **2002**, *51*, 125-139.
53. Dwyer, R.; Bruckard, W.J.; Rea, S.; Holmes, R.J. Bioflotation and bioflocculation review: microorganisms relevant for mineral beneficiation. *Mineral Processing and Extractive Metallurgy* **2012**, *121*, 65-71, doi:10.1179/1743285512y.0000000005.
54. Rao, K.H.; Vilinska, A.; Chernyshova, I.V. Minerals bioprocessing: R & D needs in mineral biobeneficiation. *Hydrometallurgy* **2010**, *104*, 465-470, doi:10.1016/j.hydromet.2010.01.016.
55. Bastias, M.; Gentina, J.C. Variables affecting the growth and ferrous oxidation capacity of *L. Ferrooxidans* in continuous culture. *Hydrometallurgy* **2010**, *104*, 351-355, doi:10.1016/j.hydromet.2010.04.015.
56. Merino, M.P.; Andrews, B.A.; Asenjo, J.A. Stoichiometric model and metabolic flux analysis for *Leptospirillum ferrooxidans*. *Biotechnol Bioeng* **2010**, *107*, 696-706, doi:10.1002/bit.22851.
57. Acuna, J.; Rojas, J.; Amaro, A.M.; Toledo, H.; Jerez, C.A. Chemotaxis of *Leptospirillum ferrooxidans* and other acidophilic chemolithotrophs: comparison with the *Escherichia coli* chemosensory system. *FEMS Microbiol Lett* **1992**, *75*, 37-42, doi:10.1111/j.1574-6968.1992.tb05390.x.
58. Kleerebezem, R.; van Loosdrecht, M.C.M. Thermodynamic and kinetic characterization using process dynamics: Acidophilic ferrous iron oxidation by *Leptospirillum ferrooxidans*. *Biotechnol Bioeng* **2008**, *100*, 49-60, doi:10.1002/bit.21745.
59. Fujimura, R.; Sato, Y.; Nishizawa, T.; Oshima, K.; Kim, S.W.; Hattori, M.; Kamijo, T.; Ohta, H. Complete genome sequence of *Leptospirillum ferrooxidans* strain C2-3, isolated from a fresh volcanic ash deposit on the island of Miyake, Japan. *J Bacteriol* **2012**, *194*, 4122-4123, doi:10.1128/JB.00696-12.
60. Hippe, H. *Leptospirillum* gen. nov. (ex Markosyan 1972), nom. rev., including *Leptospirillum ferrooxidans* sp. nov. (ex Markosyan 1972), nom. rev. and *Leptospirillum thermoferrooxidans* sp. nov. (Golovacheva et al. 1992). *International Journal of Systematic and Evolutionary Microbiology* **2000**, *50 Pt 2*, 501-503, doi:10.1099/00207713-50-2-501.
61. Stoytcheva, M.; Zlatev, R.; Magnin, J.-P.; Ovalle, M.; Valdez, B. *Leptospirillum ferrooxidans* based Fe²⁺ sensor. *Biosensors and Bioelectronics* **2009**, *25*, 482-487.
62. Vilinska, A.; Rao, K.H. *Leptospirillum ferrooxidans*-sulfide mineral interactions with reference to bioflotation nad bioflocculation. *Transactions of Nonferrous Metals Society of China* **2008**, *18*, 1403-1409.
63. Zhu, J.; Li, Q.; Jiao, W.; Jiang, H.; Sand, W.; Xia, J.; Liu, X.; Qin, W.; Qiu, G.; Hu, Y. Adhesion forces between cells of *Acidithiobacillus ferrooxidans*, *Acidithiobacillus thiooxidans* or *Leptospirillum ferrooxidans* and chalcopyrite. *Colloids and Surfaces B: Biointerfaces* **2012**, *94*, 95-100.

64. Donati, E.R.; Sand, W. *Microbial processing of metal sulfides*; Springer: Dordrecht, Netherlands, 2007.
65. Barreto, M.; Jedlicki, E.; Holmes, D.S. Identification of a gene cluster for the formation of extracellular polysaccharide precursors in the chemolithoautotroph *Acidithiobacillus ferrooxidans*. *Appl Environ Microbiol* **2005**, *71*, 2902-2909, doi:10.1128/AEM.71.6.2902-2909.2005.
66. Bharadwaj, A.; Ting, Y.-P. Bioleaching of spent hydrotreating catalyst by acidophilic thermophile *Acidianus brierleyi*: Leaching mechanism and effect of decoking. *Bioresource Technology* **2013**, *130*, 673-680, doi:<https://doi.org/10.1016/j.biortech.2012.12.047>.
67. Li, Q.; Yang, B.; Zhu, J.; Jiang, H.; Li, J.; Zhang, R.; Sand, W. Comparative Analysis of Attachment to Chalcopyrite of Three Mesophilic Iron and/or Sulfur-Oxidizing Acidophiles. *Minerals* **2018**, *8*, 406, doi:10.3390/min8090406.
68. Crundwell, F.K. How do bacteria interact with minerals? *Hydrometallurgy* **2003**, *71*, 75-81.
69. Sand, W.; Gehrke, T.; Jozsa, P.-G.; Schippers, A. (Bio) chemistry of bacterial leaching—direct vs. indirect bioleaching. *Hydrometallurgy* **2001**, *59*, 159-175.
70. Mitsunobu, S.; Zhu, M.; Takeichi, Y.; Ohigashi, T.; Suga, H.; Jinno, M.; Makita, H.; Sakata, M.; Ono, K.; Mase, K., et al. Direct Detection of Fe(II) in Extracellular Polymeric Substances (EPS) at the Mineral-Microbe Interface in Bacterial Pyrite Leaching. *Microbes Environ* **2016**, *31*, 63-69, doi:10.1264/jsme2.ME15137.
71. Mikkelsen, D.; Kappler, U.; Webb, R.; Rasch, R.; McEwan, A.; Sly, L. Visualisation of pyrite leaching by selected thermophilic archaea: nature of microorganism–ore interactions during bioleaching. *Hydrometallurgy* **2007**, *88*, 143-153.
72. Segerer, A.; Neuner, A.; Kristjansson, J.K.; Stetter, K.O. *Acidianus infernus* gen. nov., sp. nov., and *Acidianus brierleyi* comb. nov.: facultatively aerobic, extremely acidophilic thermophilic sulfur-metabolizing archaeobacteria. *International Journal of Systematic and Evolutionary Microbiology* **1986**, *36*, 559-564.
73. Sand, W.; Gehrke, T.; Hallmann, R.; Schippers, A. Towards a Novel Bioleaching Mechanism. *Mineral Processing and Extractive Metallurgy Review* **1998**, *19*, 97-106, doi:10.1080/08827509608962432.
74. Lavallo, L.; Giaveno, A.; Pogliani, C.; Donati, E. Bioleaching of a polymetallic sulphide mineral by native strains of *Leptospirillum ferrooxidans* from Patagonia Argentina. *Process Biochem* **2008**, *43*, 445-450, doi:10.1016/j.procbio.2007.10.019.
75. Olson, G.J. Rate of Pyrite Bioleaching by *Thiobacillus ferrooxidans*: Results of an Interlaboratory Comparison. *Appl Environ Microbiol* **1991**, *57*, 642-644.
76. Sand, W.; Gehrke, T. Extracellular polymeric substances mediate bioleaching/biocorrosion via interfacial processes involving iron(III) ions and acidophilic bacteria. *Res Microbiol* **2006**, *157*, 49-56, doi:10.1016/j.resmic.2005.07.012.
77. Sand, W.; Rohde, K.; Sobotke, B.; Zenneck, C. Evaluation of *Leptospirillum ferrooxidans* for Leaching. *Appl Environ Microbiol* **1992**, *58*, 85-92.
78. Schippers, A.; Jozsa, P.; Sand, W. Sulfur chemistry in bacterial leaching of pyrite. *Appl Environ Microbiol* **1996**, *62*, 3424-3431.
79. Sharma, P.K.; Das, A.; Rao, K.H.; Forsberg, K.S.E. Surface characterization of *Acidithiobacillus ferrooxidans* cells grown under different conditions. *Hydrometallurgy* **2003**, *71*, 285-292, doi:10.1016/S0304-386x(03)00167-1.

80. Tributsch, H. Direct versus indirect bioleaching. *Hydrometallurgy* **2001**, *59*, 177-185, doi:[https://doi.org/10.1016/S0304-386X\(00\)00181-X](https://doi.org/10.1016/S0304-386X(00)00181-X).
81. Gu, G.H.; Zhao, K.L.; Qiu, G.Z.; Hu, Y.H.; Sun, X.J. Effects of *Leptospirillum ferriphilum* and *Acidithiobacillus caldus* on surface properties of pyrrhotite. *Hydrometallurgy* **2009**, *100*, 72-75, doi:10.1016/j.hydromet.2009.09.007.
82. Dubel, J.; Smith, R.W.; Misra, M.; Chen, S. Microorganisms as chemical reagents: The hematite system. *Minerals Engineering* **1992**, *5*, 547-556, doi:[https://doi.org/10.1016/0892-6875\(92\)90233-Y](https://doi.org/10.1016/0892-6875(92)90233-Y).
83. Patra, P.; Natarajan, K.A. Microbially induced flocculation and flotation for separation of chalcopyrite from quartz and calcite. *International Journal of Mineral Processing* **2004**, *74*, 143-155, doi:10.1016/j.minpro.2003.10.006.
84. Subramanian, S.; Santhiya, D.; Natarajan, K.A. Surface modification studies on sulphide minerals using bioreagents. *International Journal of Mineral Processing* **2003**, *72*, 175-188, doi:10.1016/S0301-7516(03)00097-8.
85. Kinnunen, P.; Miettinen, H.; Bomberg, M. Review of Potential Microbial Effects on Flotation. *Minerals* **2020**, *10*, 533.
86. Patra, P.; Natarajan, K. Microbially enhanced removal of pyrite and chalcopyrite from oxide gangue minerals with reference to desulfurization of tailings. *Minerals and Metallurgical Processing* **2004**, *21*, 169-178.
87. Hosseini, T.R.; Kolahdoozan, M.; Tabatabaei, Y.S.M.; Oliazadeh, M.; Noaparast, M.; Eslami, A.; Manafi, Z.; Alfantazi, A. Bioflotation of Sarcheshmeh copper ore using *Thiobacillus ferrooxidans* bacteria. *Minerals Engineering* **2005**, *18*, 371-374, doi:10.1016/j.mineng.2004.06.005.
88. Ohmura, N.; Kitamura, K.; Saiki, H. Mechanism of Microbial Flotation Using *Thiobacillus-Ferrooxidans* for Pyrite Suppression. *Biotechnol Bioeng* **1993**, *41*, 671-676, doi:10.1002/bit.260410611.
89. He, H.; Xia, J.L.; Hong, F.F.; Tao, X.X.; Leng, Y.W.; Zhao, Y.D. Analysis of sulfur speciation on chalcopyrite surface bioleached with *Acidithiobacillus ferrooxidans*. *Minerals Engineering* **2012**, *27*, 60-64, doi:10.1016/j.mineng.2011.12.012.
90. Deo, N.; Natarajan, K.A. Interaction of *Bacillus polymyxa* with some oxide minerals with reference to mineral beneficiation and environmental control. *Minerals Engineering* **1997**, *10*, 1339-1354, doi:10.1016/S0892-6875(97)00125-8.
91. Jiao, Y.; Cody, G.D.; Harding, A.K.; Wilmes, P.; Schrenk, M.; Wheeler, K.E.; Banfield, J.F.; Thelen, M.P. Characterization of extracellular polymeric substances from acidophilic microbial biofilms. *Appl Environ Microb* **2010**, *76*, 2916-2922, doi:10.1128/AEM.02289-09.
92. He, Z.G.; Yang, Y.P.; Zhou, S.; Hu, Y.H.; Zhong, H. Effect of pyrite, elemental sulfur and ferrous ions on EPS production by metal sulfide bioleaching microbes. *Transactions of Nonferrous Metals Society of China* **2014**, *24*, 1171-1178, doi:10.1016/S1003-6326(14)63176-9.
93. Mahdavi, M.; Ahmad, M.; Haron, M.; Namvar, F.; Nadi, B.; Rahman, M.; Amin, J. Synthesis, surface modification and characterisation of biocompatible magnetic iron oxide nanoparticles for biomedical applications. *Molecules* **2013**, *18*, 7533-7548.
94. Toyofuku, M.; Inaba, T.; Kiyokawa, T.; Obana, N.; Yawata, Y.; Nomura, N. Environmental factors that shape biofilm formation. *Bioscience, biotechnology, and biochemistry* **2015**, *80*, 1-6, doi:10.1080/09168451.2015.1058701.

95. Pinto, A.; Cerqueira, M.; Bañobre-López, M.; Pastrana, L.; Sillankorva, S. Bacteriophages for Chronic Wound Treatment: From Traditional to Novel Delivery Systems. *Viruses* **2020**, *12*, 235, doi:10.3390/v12020235.
96. Fang, L.; Huang, Q.; Wei, X.; Liang, W.; Rong, X.; Chen, W.; Cai, P. Microcalorimetric and potentiometric titration studies on the adsorption of copper by extracellular polymeric substances (EPS), minerals and their composites. *Bioresource Technol* **2010**, *101*, 5774-5779, doi:10.1016/j.biortech.2010.02.075.
97. Flemming, H.-C.; Neu, T.R.; Wozniak, D.J. The EPS matrix: the “house of biofilm cells”. *Journal of bacteriology* **2007**, *189*, 7945-7947.
98. Sheng, G.P.; Xu, J.; Luo, H.W.; Li, W.W.; Li, W.H.; Yu, H.Q.; Xie, Z.; Wei, S.Q.; Hu, F.C. Thermodynamic analysis on the binding of heavy metals onto extracellular polymeric substances (EPS) of activated sludge. *Water Res* **2013**, *47*, 607-614, doi:10.1016/j.watres.2012.10.037.
99. Lima, L.F.; Habu, S.; Gern, J.C.; Nascimento, B.M.; Parada, J.L.; Nosedá, M.D.; Goncalves, A.G.; Nisha, V.R.; Pandey, A.; Soccol, V.T., et al. Production and characterization of the exopolysaccharides produced by *Agaricus brasiliensis* in submerged fermentation. *Appl Biochem Biotechnol* **2008**, *151*, 283-294, doi:10.1007/s12010-008-8187-2.

3 EXPERIMENTAL AND TECHNIQUES

3.1 Introduction

To better understand and optimise the bio-flotation separation of chalcopyrite from pyrite, a study investigating the microbe – mineral interactions and the connection between growth conditions and the composition of extracellular polymeric substance (EPS) excretion was necessary. To achieve this, a combination of chemical and physical analysis techniques were employed. The use of bio-flotation studies in combination with surface sensitive spectroscopic techniques, played a key role in this project.

3.2 Material

3.2.1 Minerals

Natural mineral samples of pyrite (Huanzala mine, Peru), chalcopyrite (China) and arsenopyrite (China) were sourced from GEODiscovery (The Willyama Group, New South Wales, Australia). The haematite (unknown origin) sample was also sourced from GEODiscovery (The Willyama Group, New South Wales, Australia). Chemical analysis of the mineral was conducted through total acid digestion using inductively coupled plasma mass spectrometry (ICP-MS; Perkin Elmer NexION 350D), inductively coupled plasma optical emission spectroscopy (ICP-OES; Perkin Elmer Optima), and quantitative microprobe (Cameca SXFive electron microprobe at 20 kV and a specimen current of 20 nA). Quantitative X-Ray Diffraction (QXRD; Bruker D8 Advanced Eco Bragg-Brentano geometry Co K α) with an internal standard of analytical grade corundum (Al₂O₃) was used to confirm the mineral phases present. Elemental analysis of pyrite, chalcopyrite and arsenopyrite is shown in Table 3.1.

Table 3.1 ICP-MS/OES elemental composition of mineral wt(%)

	S	Fe	Cu	Na	Mg	Al	P	Ca	As
Chalcopyrite[^]	29.7	25.6	29.0	0.01	0.06	0.09	1.32	2.89	-
Pyrite	51.6	45.4	0.07	-	0.01	0.02	-	0.03	-
Arsenopyrite	29.7	53.0	0.32	0.01	0.10	0.34	-	0.32	3.56

The elemental analysis conducted by ICP-MS/OES and microprobe, with confirmation from QXRD, indicated that pyrite was the primary mineral phase for the pyrite sample. The purity of pyrite was calculated to be 96.4%. Similarly, chalcopyrite was identified as the primary phase in the chalcopyrite sample with a calculated purity of 83.5%. Analysis of the arsenopyrite indicated that the sample was low grade with a calculated purity of 8.7%, with the primary phases identified as iron sulfides and iron oxides. While this sample was low grade, it was still deemed suitable for bacterial adaptation. The haematite was analysed through QXRD only, the composition determined to be a combination of different iron oxide phases. The primary phase was confirmed to be haematite with a purity of 77%.

3.2.1.1 Mineral Crushing and Grinding

Mineral crushing was conducted at the Future Industries Institute, the University of South Australia. Mineral samples were ground to a D_{80} of 50 μm , where 80% of the mineral particles has a diameter of 50 μm or less, using a rubber lined Galigher mill in water, with steel rods as the grinding media. The resulting pulp was wet sieved into three different size fractions of - 38 μm , +38 – 75 μm , and +75 μm . Mineral fractions were stored at -80°C in sealed containers purged with nitrogen [1].

3.2.2 Archaea and Bacteria

3.2.2.1 *Leptospirillum ferrooxidans* and *Acidithiobacillus ferrooxidans*

Active growing cultures of bacterial strains *Leptospirillum ferrooxidans* (DSM 2705) and *Acidithiobacillus ferrooxidans* (DSM 14882) were obtained from DSMZ (Braunschweig, Germany). Base cultures of *Leptospirillum ferrooxidans* (*L. f*) and *Acidithiobacillus ferrooxidans* (*A. f*) are grown as a 1% inoculate in modified *Leptospirillum* HH media (solution A and B). Mineral cultures are grown as a 10% inoculate in modified *Leptospirillum* HH media (solution A) with 20 grams of 38 - 75 μm mineral (pyrite, chalcopyrite or arsenopyrite). All cultures were inoculated at late exponential phase and maintained at 30°C and 155rpm on a rotary shaker.

3.2.2.1.1 Growth medium – Modified *Leptospirillum* HH medium

Modified *Leptospirillum* HH media was made in two parts; Solution A and Solution B. Solution A consists of $(\text{NH}_4)_2\text{SO}_4$ (132 mg), $\text{MgCl}_2 \cdot 6\text{H}_2\text{O}$ (53 mg), KH_2PO_4 (27 mg), $\text{CaCl}_2 \cdot 2\text{H}_2\text{O}$ (147 mg) in 950mL of ultrapure Milli – Q water, adjusted to a pH of 1.8 using 10N H_2SO_4 . Solution B is

an iron (II) sulfate solution comprised of $\text{FeSO}_4 \cdot 7 \text{H}_2\text{O}$ (20 g) in $0.25\text{N H}_2\text{S}$ (50mL). Solutions A and B are sterilised separately in an autoclave (121°C and a pressure of approximately 29.6 psia) before being mixed prior to inoculation.

3.2.2.2 Culture Growth and Monitoring

Cell quantification is usually determined through either live-dead counts or counts through the use of a Neubauer chamber (hemocytometer) [2]. Live-dead counts require staining of cells, which presents difficulties in Gram-negative cells. Culture growth and cell concentration was monitored through cell counts using a Hemocytometer at 40 times magnification using an Olympus BH-2 optical microscope. The cell concentration was calculated using the equation below in Equation 3.1 [3].

Prior to sampling, the culture is gently swirled to increase the likelihood of a homogeneous sample A 500 μL aliquot is taken from the culture using an automated pipette, with a 10 μL aliquot injected into the hemocytometer. The cell concentration was calculated using 5 grid squares of $2.5 \mu^2$ with a volume of $2.5 \times 10^{-7} \text{mL}$. Counts were conducted in technical replicates and an average cell concentration calculated.

$$\text{Cells} = \left(\frac{\text{number of cells counted}}{(\text{proportion of chamber counted})(v_{\text{squares counted}})} \right) \left(\frac{\text{volume of diluted sample}}{v_{\text{original culture}}} \right) \quad (3.1)$$

The growth curves obtained are assessed for the six distinct growth phases expected throughout the culture's growth cycle. The six phases are: lag phase, acceleration phase, exponential phase, retardation phase, stationary linear phase and the decline phase, shown in Figure 3.1 [4]. These growth phases indicate the growth rate of the culture, which is dependent on the strain and growth environment. At the point of inoculation, the growth rate of the culture is equivalent to zero and labelled the lag phase (phase 1). The initial increase of cell concentration occurs at a rapid rate, which is considered the acceleration phase (phase 2). This is followed by the exponential phase (phase 3). The culture moves from the acceleration phase to the exponential phase when the cell concentration increases at a steady rate. At the end of the exponential phase, the rate of cell replication starts to steadily decrease, which is known as the retardation phase (phase 4). The steady decrease in cell replication rate then leads into the linear stationary phase (phase 5), where the rate of cell

replication is equivalent to the rate of cell death. Eventually, the equilibrium will be shifted as the rate of cell death becomes greater than the rate of cell replication, this is the decline growth phase (phase 6). It is possible for one or several of these growth phases to be absent, depending on the growth conditions and the length of the phases [4].

Image removed due to copyright restriction



Figure 3.1: Growth phases of cultures. Lower curve: concentration of cells against time. Upper curve: Rate of growth expected for respective phase. Vertical dotted marks represent the limits of phases. Image from Monod [4]

3.2.2.3 Ferrous Ion Titrations

As *L. ferrooxidans* and *A. ferrooxidans* have the ability to oxidise ferrous iron (Fe II) to ferric iron (Fe III), the concentration of ferrous ions in solution over time can indicate growth of the cultures. The ferrous ion concentration was monitored through oxidation – reduction titrations with cerium (IV) sulfate, as the oxidising agent, and 1,10-phenanthroline indicator (0.025 molL^{-1}). The net ionic equation is seen below in Equation 3.2 [5].



The ferrous iron concentration is calculated using the titre value of the cerium (IV) sulphate and the molar ratio in Equation 3.2 above, and the molar concentration equation in Equation 3.3, where c = concentration, n = number of moles and v = volume.

$$c = \frac{n}{v} \quad (3.3)$$

At each time frame, 10 mL samples were taken from the culture and passed through a 0.22 μ m sterilized, single use membrane filter for the removal of cells and mineral particles, if present. After filtration, Eh and pH measurements were taken before splitting the sample into 3mL aliquots and placed into a clean 100mL conical flask. To each aliquot, two drops of 1, 10-phenanthroline indicator was added and the sample was titrated against cerium (IV) sulphate until a colour change (red to blue) was observed.

3.2.2.4 Extracellular Polymeric Substance (EPS) Supernatant

EPS supernatant was harvested from upscaled late exponential phase cultures. Cultures were scaled up to a total volume of 1 L using the growth medium ratios outlined above in Section 3.2.2.1, with the initial concentration of cells held as a constant at 1.5 $\times 10^7$ cells/mL. Mineral particles were removed from the culture through vacuum filtration, using a 5 μ m Millipore SMWP mixed cellulose membrane. The filtrate was then centrifuged at 15,000 rpm to pellet and remove cells. To ensure all cells were removed, the decanted supernatant was then filtered through a 0.2 μ m Millipore Isopore hydrophilic membrane, with the filtrate classed as the free EPS supernatant [1].

3.2.3 Flotation setup/glassware

The modified Hallimond tube was designed with a P4 sinter to achieve an optimal bubble size suitable for the +38 -75 μ m fraction size. The modified Hallimond tube is comprised of two segments, the flotation chamber and the collection tube, as shown in the schematic in Figure 3.2. The flotation chamber has a volume capacity of 50mL, while the bubble size is determined by the flow rate through the sinter. As discussed in Section 2.2.3 above, the bubble size required is determined by the particle size, with the optimal bubble size for + 38 μ m – 75 μ m fraction size is in the range of 0.6 mm and 1.0 mm. Glassware was produced by Emerald Scientific Glassblowing & Signs (South Australia, Australia).

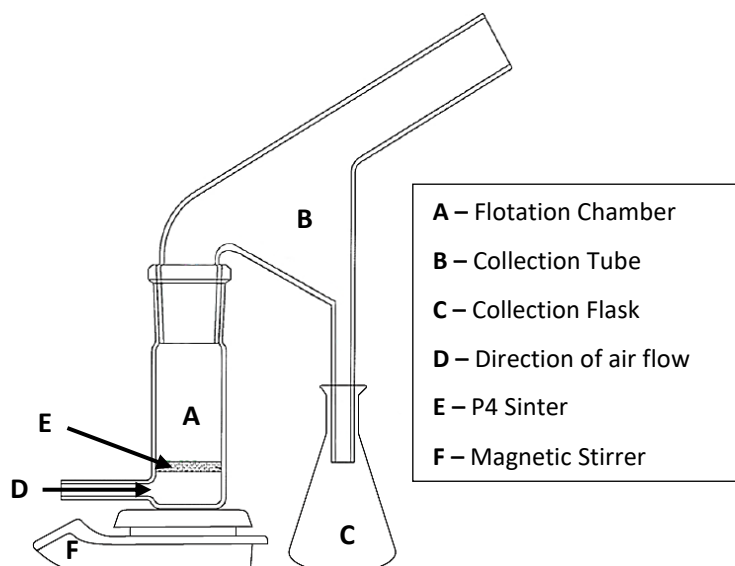


Figure 3.2: Schematic of the modified Hallimond tube for micro-flotation set up

3.3 Experimental and Analysis

3.3.1 Scanning Electron Microscopy

3.3.1.1 Background

Scanning Electron Microscopy (SEM) is a microscopic imaging technique which uses a focused beam of high-energy electrons; allowing greater magnification, higher levels of detail and complexity of samples in comparison to traditional microscopic imaging techniques [6]. A number of interactions occur when the incident electrons of the electron beam interact with the sample surface; these include the production of photoelectrons, Auger electrons, fluorescent photons and secondary electrons. SEM measures the secondary electrons, backscattered electrons (from elastic scattering) and the characteristic x-rays emitted via the interaction between the sample and the beam, producing morphological and elemental information of the sample [6]. These interactions are illustrated in

Figure 3.3 below.

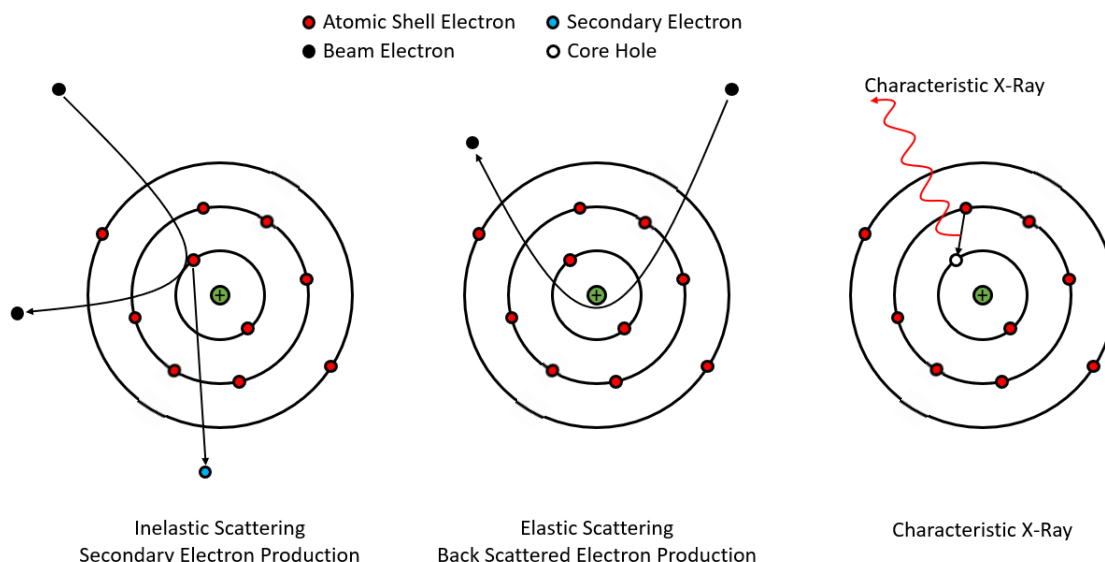


Figure 3.3: Schematic illustrating the possible electron interactions which occur during scanning electron microscopy, showing the production of secondary electron, back scattered electron, and characteristic x-ray

The most common and surface sensitive imaging mode of operation is the secondary electron (SE) mode, producing high resolution morphological information of samples. In this mode, the electron beam interacts with the top few atomic layers of the sample, allowing for loosely bound electrons to be emitted from the surface as low energy (approximately 2 – 50 eV) secondary electrons. These electrons are created through an inelastic collision; where an incident electron collides with an atom within the sample and knocks out a previously bound electron. Since these interactions are inelastic, the energy of the secondary electrons is reduced and therefore the escape depth is minimised, thus delivering surface sensitive micrographs.

Information relating to the elemental distribution of the sample can be gathered through the Back Scattered Electron (BSE) mode. Backscattered electrons originate from the primary electron beam and have scattered elastically from the surface before being detected. In this mode, the energy of the electrons is greater than the SE mode, therefore there is a larger interaction volume in the material. The energy of the scattered electrons is dependent on the atomic mass of the atom of which the electron beam interacts with. Atoms with a larger molecular weight, scatter electrons with a higher energy, while lower molecular weight atoms scatter electrons with a lower energy. The energy difference of these electrons is conveyed in the image by intensity. Therefore, the contrast in the electron micrographs measured with backscattered electrons can give an indication of heterogeneity of the composition of the

sample's surface. However, physical characteristics of the sample can impact the brightness of the image obtained through back scattered electron imaging.

The most compositional information is obtained from the characteristic x-rays. Characteristic x-rays are produced during the inelastic electron-matter interaction, when an outer electron relaxes to fill a core hole. Core holes are produced by Bremsstrahlung x-rays as they excite and ionise the inner electrons. Due to the large attenuation length, the characteristic x-rays create a greater interaction volume in comparison to SE and BSE interactions. The energy of the x-rays are characteristic to the composition of the sample, meaning they can be used for Energy Dispersive Analysis by X-ray (EDAX) (also known as Energy Dispersive X-ray Spectrometry (EDS)) to determine elemental composition. The intensity of the characteristic x-rays is dependent not only on the quantity of each element present, but also the cross section for the X-ray emission, as the bulk composition can influence inner shell ionisation. Therefore, this technique can allow qualitative analysis of the composition of the sample by producing a ratio for the elements present. Electron microprobe analysis (EMPA) uses an especially sensitive EDS detector, with correct calibration, to provide quantitative chemical analysis of samples. The sampling size for the x-ray beam is approximately 5µm in width with a sampling depth of approximately 1 – 2 µm.

3.3.1.2 Sample Preparation

Pure mineral samples with a fraction size of +38 – 75 µm were sterilized via ultraviolet light prior to bacterial exposure. Cell exposure occurred at a starting cell concentration of 1.5×10^7 cells/mL of the culture adapted to the respective mineral. Samples were maintained at a constant temperature (30°C for *A. ferrooxidans* and *L. ferrooxidans*) in a Ratek rotary shaker maintaining 155 rpm. Media controls were conducted in the same conditions, without the presence of bacteria.

Pure mineral sections were prepared by shaping mineral pieces with silicon carbide sandpaper of different grades and polished using a Trident polishing cloth and diamond paste (1 µm and 0.25 µm) [1]. The surface of the mineral sections was cleaned through sonication in ultrapure Milli-Q water and sterilized using ultraviolet light. Once sterilised, mineral sections were exposed to bacterial cells as described above.

Sample preparation for SEM imaging is as described in Bleeze, et al. [1]. Aliquots of approximately 1 mL, containing mineral, were removed, and preserved in 1 mL of electron microscopy (EM) fixative solution containing 3% glutaraldehyde. The samples were removed from the EM fixative and washed with PBS buffer (phosphate buffered saline containing 4% sucrose) before being saturated with 2% osmium tetroxide. Samples were then dehydrated through a stepwise dehydration process using a series of ethanol concentrations (70%, 90% and 100%). The dehydration process is completed with two washes of 1-1-3-3-3 Hexamethyldisilazane (HMDS). The first wash is 50:50 with 100% ethanol: HMDS, and the second wash 100% HMDS and left to air dry. When dry, the samples are attached to a SEM stub using carbon tape and sputter coated with platinum ($\sim 2\mu\text{m}$) to increase the conductivity of the sample and reduce charging during the imaging process.

3.3.1.3 Data Collection

Samples were analysed using an FEI Inspect F50 Scanning Electron Microscope with an Everhart-Thornley secondary electron detector and a solid-state backscattered electron detector. Images were captured with a spot size of 4 micron and range of accelerating voltage (5kV – 20kV). TEAM EDX software (version 4.1) was used to process the elemental quantification data. An eZAF matrix calculation and corrections were applied to the scan for quantification of elements based on atomic number (Z), adsorption X-rays (A), and secondary X-rays (F) [7].

ImageJ Processing and Analysis software was used to analyse images for particle size and cell concentration [8,9]. An average of 10 images/particles were used for each calculation.

3.3.2 Bio-Flotation Studies

3.3.2.1 Background

Background for the bio-flotation technique was covered in Section 2.3.4. The efficiency of flotation and separation is dependent on three factors: particle size, bubble size and flow rate. As the mineral particle size is set at $-38 +75 \mu\text{m}$, the modified Hallimond tube is optimised for this mineral size. Therefore, the parameters for bubble size and flow rate are dependent on this. If the bubble size is not large enough to support the weight of the mineral particles, either the bubble bursts or the particles are dropped [10]. An increase in flow rate increases the number of bubbles produced and in-turn the bubble size increases through the

coalescence phenomenon [11]. Coalescence of bubbles occurs upon collision of multiple bubbles, forming bubbles with greater volume. As the number of bubbles within the flotation chamber increases, so does the possibility of interactions and coalescence of bubbles. Therefore, the coalescence effect needs to be considered when optimizing the micro-flotation cell.

Due to the relationship between flow rate and bubble size, optimising the flow rate is imperative to optimising the efficiency of the flotation cell. The optimal bubble size for the fraction size of +38 – 75 μ m is 0.6 – 1.0 cm [11], therefore the flow rate is optimal when the average bubble size is within this range. The optimal flow rate was determined through a series of baseline recovery tests.

3.3.2.2 Experimental Procedure

Mineral samples were prepared by weighing out the required amount of pure sample (1 g for single mineral, 0.5 g or 0.3 g for differential mineral) and sterilized via ultraviolet light for a total of 20 minutes, with the sample shaken occasionally. The mineral fractions for differential flotation tests are sterilised as single mineral fractions. Once sterilised, mineral fractions are transferred to 100 mL Erlenmeyer flask and solutions for pre-conditioning are added. Pre-conditioning of samples occurred at a volume of 20 mL with exposure time of 2 h, 12 h, 24 h, 36 h, 48 h, 60 h or 72 h. Baseline flotation tests were pre-conditioned in modified HH media solution A, pre-conditioning to EPS occurred with EPS supernatant, and cell pre-conditioning occurred at a starting cell concentration of 1.5×10^7 cells/mL. Samples were maintained at 155 rpm and 30°C (*L. ferrooxidans* and *A. ferrooxidans*) for the duration of exposure.

After conditioning, samples were transferred to a modified Hallimond tube and the total volume increased to 50 mL with the respective media. Micro-flotation tests were conducted for five minutes with a flow rate on 0.4 Lmin^{-1} with instrument grade compressed air. Both floated fractions and tailings were collected and analysed through quantitative XRD and recoveries calculated using TOPAS [1,12]. Flotation tests were conducted as collector-free flotation tests and in the presence of potassium isopropyl xanthate (PIPX) collector (10^{-4} M).

3.3.3 X-Ray Diffraction

3.3.3.1 Background

X-Ray Diffraction (XRD) is a technique used to determine the composition and crystallinity of a compound and has the ability to determine the difference between polymorphic substances. XRD uses a cobalt radiation source (Co $K\alpha_1$ [$\lambda = 1.78892 \text{ \AA}$]) at -35 kilovolts and 30 milliamperes, where the incident x-rays are monochromatic and interact with the surface of the crystalline structure. The resulting signal from the emitted x-rays can be interpreted using Bragg's law.

Bragg's law analyses the angular difference between the incidence x-rays and the diffracted fluorescent photons, which can be used to determine the crystalline lattice structure. The Bragg's law Equation 3.4, where: d represents interplanar spacing of the crystal, θ represents the Bragg angle (X-ray incident angle) and λ represents the wavelength of the characteristic X-ray.

$$2d(\sin\theta) = \lambda_0 \quad (3.4)$$

3.3.3.2 Experimental procedure

The air-dried and weighed flotation tests fractions were ground with a mortar and pestle to less than 50 μm and transferred to the zero-background sample holder. The samples of pure mineral for quantification of purity were micro milled with 15% corundum prior to analysis. Analysis of data collected is assisted through programs such as Jade [13] to calculate the lattice parameters, Find it [14] determine a literature comparison and TOPAS [12] to quantitatively analyse the data.

XRD analysis was conducted at room-temperature using a powder XRD Bruker D8 Advanced Eco Bragg-Brentano geometry X-ray Diffractometer with a Co $K\alpha$ ($\lambda = 1.789 \text{ \AA}$) irradiation source at 35 kV and 28 mA. Samples patterns were scanned over the 2θ range of 10 to 90° for either 15 minutes (flotation fractions) or 55 minutes (mineral quantification). Diffraction patterns were quantitatively analysed by Rietveld quantitative phase analysis (QPA) of powder X-ray diffraction data using TOPAS [12]. The peak shapes were modelled using a pseudo-Voigt function, with a sixth-order Chebychev polynomial used to model the background [1]. For each diffraction pattern, the zero shift and scale factors for identified phases were refined.

3.3.4 Photoemission Electron Microscopy

3.3.4.1 Background

Photoemission Electron Microscopy (PEEM) is a type of emission microscopy which utilizes local variation in electron emission to generate a contrast image. This technique is capable of showing the spatial distribution of chemical species on the sample surface as well as morphology. The excitation of electrons can be produced by a photon source, such as UV light, synchrotron radiation or an X-ray source. The photon source illuminates the sample, and the photons are absorbed, causing core holes to be formed. The emitted electrons are passed through a series of electrostatic lenses and focused onto a fluorescent screen, as shown in Figure 3.4.

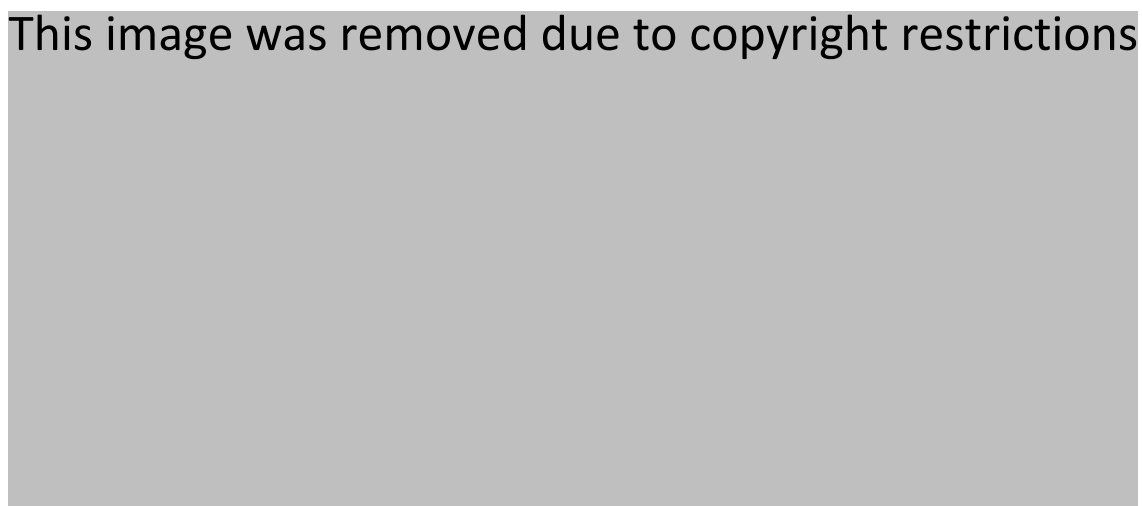


Figure 3.4: Optics schematic for the photoemission electron microscopy (PEEM) end-station, from [<http://efd.nsrc.org.tw/EFD.php?num=242>]

PEEM is surface sensitive as the emitted electrons originate from a very shallow layer of the sample. The images collected are full field images which allows for fast imaging with high resolution, with the resolution being better than 10 nm. The corresponding spectra can be gathered by measuring the drain current of the sample over a range of incident photon energies. Measuring the drain current results in the collection of Near Edge X-ray Absorption Fine Structure (NEXAFS) spectra allowing a high chemical sensitivity. Therefore, PEEM can be operated in three modes: spectra only – a NEXAFS spectrum is taken from a fixed area; image only – an image is taken at a fixed photon incident energy; and 3D imaging – spectra and imaging combined, where images of a fixed area are collected over a desired photon incident range and stacked on top of one another resulting in each pixel obtaining its own NEXAFS spectrum. These three modes allow a high degree of chemical information to be recorded

which allows detailed spatial and chemical analysis of the sample. This technique has been employed for the characterisation of heterogeneous and complex environmental carbon materials [15].

Near Edge X-ray Absorption Fine Structure (NEXAFS) spectroscopy is a chemical and local coordination specific technique which is complimentary to X-ray photoelectron spectroscopy (XPS) [15,16]. Unlike other techniques, NEXAFS measures the intensity and energy of the incident electrons which are absorbed by the sample, rather than measuring the energy of electrons which are ejected. Collection of spectra requires an incident photon source which can be varied across the element absorption edge. Excitation of electrons occur when incident photons are absorbed, leading to the core level electrons shifting to unoccupied energy levels. This usually occurs just prior to the main absorption peak [16]. As the electrons shift from core levels to unoccupied energy levels, NEXAFS gives information about the unoccupied energy levels of the sample. NEXAFS spectra can be collected by measuring different interactions that are occurring. The total electron yield mode (TEY) measures all electrons off the sample and is often used for conventional samples. The TEY cascade involves multiple scattering events which originate from an average sample depth, which is typically a few nanometres. As electrons from different elements contain different energies, NEXAFS is considered to be element specific and sensitive to the binding environment.

As fluctuations can occur within the photon current at the beamline, an I_0 is collected simultaneously to the NEXAFS spectrum. This is done by measuring the photon current that is passed through a gold mesh. This I_0 is used to correct the spectrum by dividing the measured intensity of the spectrum by the I_0 . Fluctuations within the beam can cause the spectra to shift, this is corrected by taking the spectrum of known standards of interested elements at the same time. Thus, giving a point of reference for the analysis. Once the energy shift has been corrected, the spectra are then normalised. This is done so the pre-edge region is at an intensity of 0, while the post edge region is set as an intensity of 1.

For analysis of images and the spatial distribution, topography effects must be removed. Images that are acquired at a peak absorption energy contain both chemical and topographical effects. This is done by subtracting one image (background) from another (adsorption peak). The background image is acquired at the pre-edge energy, as no excitation

of elements should occur in this region. Therefore, the image should only contain topographical effects such as sharp surface features and shadowing [17]. Subtracting this image removes the pixel intensity attributed to topography effects and leaves the spatial distribution of chemical states. Equation 3.5 represents the equation used for the counteraction of topographical effects.

$$\frac{MM_1+MM_2}{MM_1-MM_2} \quad (3.5)$$

Where the intensity of each pixel taken at the peak energy is represented by M_1 and the intensity of each pixel at the pre-edge is represented by M_2 . It is important to note that for images to be directly comparable, they must have the same parameters such as dwell time, so removal of the background leaves an accurate representation of the surface chemistry.

3.3.4.2 Sample Preparation

Mineral sections with mixed mineral phases were prepared similar to the mineral sections used for SEM, as discussed in Section 3.3.1.2. The mineral sections were shaped and polished using silicon carbide sandpaper of varying grit sizes (80, 180, 240, 400, 600, 800 and 1200) and polished to a mirror finish using a Trident polishing cloth with diamond paste (1 μm and 0.25 μm). The mineral sections were cleaned via ultrasonication in ultrapure Milli-Q water, prior to UV sterilisation.

Exposure of the mineral sections to both HH media and the EPS supernatant occurred using a volume of 300 mL and maintained at 30°C in a Ratek rotary shaker maintaining 155 rpm for the duration of exposure. After exposure, samples were transferred to DNase and RNase free 15 mL centrifuge tubes and snap frozen in liquid nitrogen. Samples were maintained at -80°C and transported on dry ice until analysis could be conducted. Exposure for the fresh EPS sample occurred in the wet lab at the National Synchrotron Radiation Research Centre (NSRRC). After exposure to the EPS supernatant, the excess solution was wicked away using a KimWipe before being mounted on the sample holder. This occurred directly prior to analysis. Samples were mounted to a conductive sample holder using conductive carbon tape.

3.3.4.3 Data Collection and Data Processing

Images and spectra were collected at the BL05B2 beamline at the National Synchrotron Radiation Research Centre (NSRRC) in Hsinchu, Taiwan [18]. The BL05B2 beamline uses an

elliptically polarised undulator (EPU5) with a spherical-grating monochromator, yielding very high photon flux (2×10^{12} photons S^{-1} at 800eV in a 0.4 mm x 0.2 mm spot) with spatial resolution better than 50 nm [19,20]. The beamline maintained a pressure of 10^{-9} torr throughout the duration of experiments. The Near Edge X-ray Adsorption Fine Structure (NEXAFS) spectra were collected with a step size of 0.1 eV and a dwell of 2-3 seconds. The I_0 was simultaneously collected using a gold mesh grid. Images were generated on a phosphor screen mounted on a CCD detector through the collection of the total electron yield (TEY) [20], with a field of view (FOV) of 450 μm with 1000 pixels per image.

The images, spectra, and stack images were analysed using the IDL package aXis2000 [21]. Topographical effects were removed from images through background subtraction to illustrate the distribution of chemical states. NEXAFS spectra were collected from FOV analysis and 3D images. All spectra were pre- and post-edge corrected using a linear fit using Athena [22]. Peak fitting of the carbon K-edge was performed using the Athena package in Demeter Version 0.9.18 [22-24]. The carbon K-edge spectra had an arctangent background applied at 290.0 eV so deconvolution could occur with a series of Gaussian peaks for the main C 1s transitions up to 290.5 eV. The full width half maximum (FWHM) was constrained to ~ 0.5 eV for peaks before the ionization step. Transitions after the ionization step were not fit with Gaussian peaks as these transitions overlap, creating large potential error in assignments [23]. The C 1s transitions were assigned using the assignments in Table 3.2.

Table 3.2: C 1s K-edge NEXAFS transitions

Energy (eV)	C 1s Transition
283.7 – 284.3	Unsaturated aromatic C–H, low energy π^* states, quinone [25,26]
284.9 – 285.5	π^* protonated/alkylated aromatic [26] π^* C–C, C=C [23,25,27-30]
285.8 – 286.4	π^* carbonyl substituted aromatic [26]
286.0	Aromatic bound aldehyde [25]
286.2 – 286.4	π^* C=N, C \equiv N, π^* aldehyde, aromatic C–N, aromatic C–O, aromatic C–ketone [25]
286.5	π^* ketone/aldehyde, crosslinking polysaccharide [25,26,31]
286.8 – 286.9	π^* amine [25]

287.1 – 287.4	π^* ketone C=O, aromatic C–OH [26] HARDIE
287.6 – 288.2	C 1s – 3p/ σ^* CH ₃ , CH ₂ , CH [26]
287.8 – 288.2	Amide [25]
288.1 – 288.6	π^* resonance of carboxylic C=O, acetic/acetate, polysaccharide [26-28,31] Aliphatic COOH [25]
288.2	π^* carboxyl group associated with protein [32]
288.6	π^* carboxyl group associated with polysaccharide [28]
289.2 – 289.6	π^* aliphatic C–OH [25] C 1s – 3p/ σ^* C–OH [26]
289.9 – 290.1	Carbamate [25]
290	Carboxyl bound to iron [31]
290.2 – 290.6	π^* carbonate [25]

3.3.5 X-Ray Photoelectron Spectroscopy

3.3.5.1 Background

X-ray photoelectron spectroscopy (XPS) is a well-known chemically sensitive spectroscopic technique. The fundamentals of this technique include the excitation of a core electron using an X-ray source. When the energy transferred to an electron is greater than the binding energy (E_b) of that electron, the electron is ejected from the electron shell and measured [33]. This interaction is similar to the production of secondary electrons shown in

Figure 3.3 above. Changes in the initial and final state of an atom after excitation are due to the environment the atom is in, with the chemical state also influencing the kinetic energy (E_k) of the ejected electron [33]. The kinetic energy of the ejected electron is used to calculate the binding energy using Equation 3.6 [34], where $h\nu$ is the incident photon energy and ϕ is the work function of the system.

$$h\nu = E_b + E_k + \phi \quad (3.6)$$

The spectra obtained is a convolution of peaks arising from the different kinetic energies of ejected electrons [33], offering chemical information of the surface. As the peaks

representing different chemical states are convoluted, peak fitting is required to derive the information.

3.3.5.2 Sample preparation

Single mineral particles of fraction size +38 – 75 μm were sterilized using ultra-violet light prior to experimental set up. Control samples were conducted by the addition of pyrite (20 g) to HH Media Solution A (200 mL) at an approximate pH of 1.8. Bacterial exposures were conducted on pyrite (20 g) at a starting cell concentration of 1.5×10^7 cell/mL and a total volume of 200 mL. Aliquots of 1 mL were taken at 24, 48, 72 and 168 hours and placed in sterile RNase and DNase free 10 mL centrifuge tubes with a nitrogen atmosphere and snap frozen in liquid nitrogen, similar to the method presented in Harmer, et al. [35]. Samples were stored in a freezer at -80°C until immediately before surface analysis. Directly prior to analysis, samples were defrosted rapidly, and the sample was mounted as a slurry on carbon tape. Excess moisture was wicked away using a Kimwipe before being spread evenly over the sample holder with a spatula. Gentle pressure was applied to ensure the sample was attached to the carbon tape. Finally, the top layer of the mineral particles was removed using the spatula, to remove any potentially contaminated particles as depicted below in Figure 3.5. Samples were transferred into the pre-cooled introduction chamber.

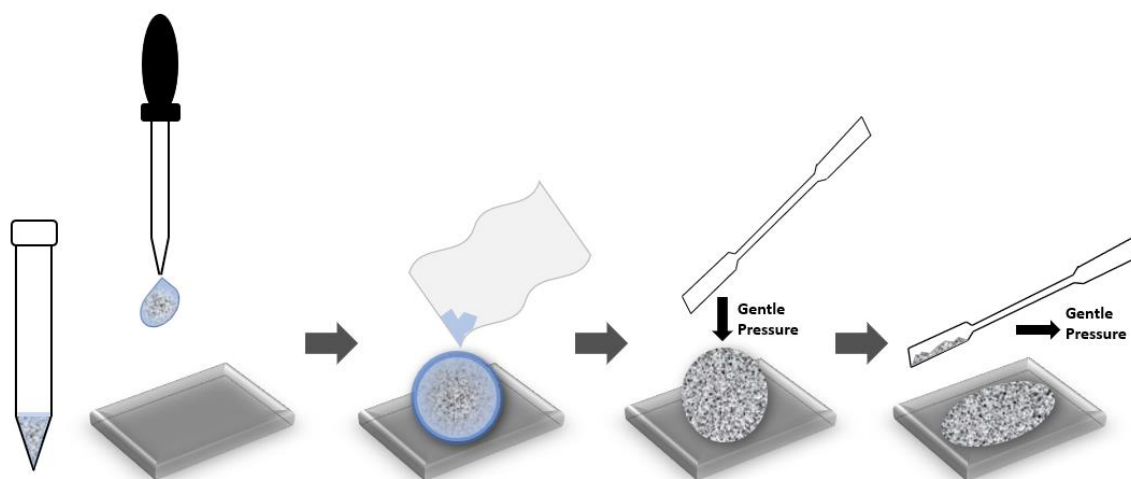


Figure 3.5: Schematic of XPS sample preparation process

3.3.5.3 Experimental Setting

Measurements were obtained using a Kratos Axis Ultra spectrometer using a monochromated Al $K\alpha$ X-ray source with a photon energy of 1487 eV. A pressure of 10^{-9} Torr was maintained

in the analysis chamber, with the sample holder cooled using liquid nitrogen for the duration of analysis maintaining a temperature of approximately -155°C . Pre-cooling of the introduction chamber and sample holder with liquid nitrogen occurred to reduce the likelihood of volatile compounds being removed. The thermo couple was disconnected and the stage was floating during analysis due to charging effects. The Kratos charge neutralisation system was employed during analysis. Spectra were obtained using a step size of 0.05 and a pass energy of 10 eV, with 10 sweeps used to collect high resolution spectra. Ambient scans were obtained at an approximate temperature of 22°C , this was done by allowing the analysis chamber to slowly increase in temperature overnight to remove volatile elemental sulphur species.

3.3.5.4 Data Analysis and Peak Fitting

CasaXPS software [36] was used for processing of both survey and high resolution spectra. The survey spectra were energy corrected using adventitious carbon at 248.8 eV [37-39], while the high resolution scans were energy corrected using the bulk disulfide contribution at 162.5 eV [40]. As electrons from different sub shells can be ejected, in the survey spectra the electrons ejected from the *s*-sub shell are considered to be the primary peak.

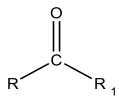
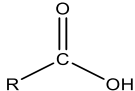
For improved accuracy of interpretation and line shape fitting, the background of the spectra needs to be considered. Changes in the background can occur over the spectra through processes such as energy loss, therefore complex interpolations of the background may be required. There are three common interpolations used for background removal, these are Shirley, linear and Tougaard [33]. The background used is dependent on the samples. The Shirley background was applied to the high-resolution spectra. Fits of the high-resolution spectra is guided by the chemical formula and constraints can be placed on the fit parameters, such as peak width and intensity, to obey chemistry [33]. These constraints are appropriate for fitting spectra that is obtained from non *s*-sub shell electrons (*p*, *d*, *f*) as these electrons are ejected in pairs with related intensities [33].

The spectra were fit using a Voight function with a 50:50 ratio of Gaussian and Lorentzian line shapes. Each spectrum was first fit with a symmetric line shape on the leading adsorption edge. This initial line shape was used as a guide for subsequent line shapes used in the fit.

Each fit was obtained using the least number of peaks possible, with all peaks justified transitions by literature as shown in Table 3.3 and Table 3.4 below.

The carbon and oxygen components were fit as single contributions, while the sulfur $2p$ was fit as a doublet. This doublet is an expected feature of the $2p$ sub shell due to the spin orbit coupling and is attributed to $2p_{3/2}$ and $2p_{1/2}$ components [41]. As the $2p_{3/2}$ peak has the lowest energy of the two it was fit to the spectrum and the fit parameters used to place constraints on the $2p_{1/2}$ peak. The $2p_{1/2}$ peak is expected to have the same width, half the area and a fixed energy of $2p_{3/2}+1.19$ eV.

Table 3.3: Binding Energy Reference Table for C 1s, N 1s, O 1s and Fe 2p

Species	Binding Energy (eV)				Reference
	C 1s	N 1s	O 1s	Fe 2p	
C – C C – H	284.8	--	--	--	[37-39]
CH ₃ CH ₂ Aromatic	284.81– 285.03	--	--	--	[15,42,43]
<u>C</u> – COO	285.7	--	--	--	[43]
C – N	285– 287	399.92– 400.22	--	--	[44,45]
C – O – C	286	--	532.8	--	[42,43]
C – OH Aromatic C	286.3 – 286.73	--	532.8	--	[15,39,42,43]
Nitrile $\text{---C}\equiv\text{N}$	286.73	399.57	--	--	[44]
C=O O–C–O	287.5 – 288.03	--	531.2 – 532.6	--	[15,39,42,43]
Ketone 	287.81 – 288.03	--	533.6	--	[15]
Carboxylic 	288.6 – 289.55	--	=O 532.2 –O 533.7	--	[15,39,42,43]

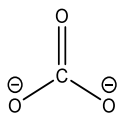
Carbonate  FeCO ₃	289	--	535.0	710.5*	[43,46-48]
Oxide O ²⁻ Fe–O	--	--	530.1	710.9	[19,49]
Fe ₂ O ₃	--	--	530.0 – 530.1	709 – 711.0	[49-51]
FeO ^{(1)O⁽²⁾H}	--	--	(1) 530.1 (2) 531.3	711.3 – 711.8	[49,50]
Iron oxide – hydroxide	--	--	--	711 – 712	[19]
Bulk Fe ²⁺	--	--	--	Fe ²⁺ 707* Fe ³⁺ 707– 708^	[50]^ [52]*
Fe(III)–S Cp	--	--	--	707.7 ± 0.2	[19]
Fe ³⁺ multiplets in Py	--	--	--	708.5 – 712	[52]
Hydroxide –OH	--	--	530.8 – 531.5	--	[19,50,53]
Chemisorbed H ₂ O	--	--	532.1 – 532.6 533.2 – 533.5	--	[50]
Adsorbed H ₂ O	--	--	533 – 536	--	[19,48,53]
Physisorbed H ₂ O	--	--	535.1	--	[50]

Table 3.4: Binding energy reference table for sulfur species

Species	Location	Binding Energy (eV) S 2p	Reference
Unoxidised bulk monosulfide	Chalcopyrite + NaEX	161.2 ± 0.2	[19]
Surface state disulfide (S ₂ ²⁻)	Pyrite	162.0	[52]
Mono sulfide (S ²⁻) (Relaxation through oxidation)	Pyrite	161.3	[52]

Monosulfide (fully coordinated in bulk)	Chalcopyrite	161.3	[50,54]
Disulfide and the presence of S in absorbed xanthate	Chalcopyrite + NaEX	161.9	[19]
Surface state disulfide (surface most sulfur atom of surface disulfide)	Pyrite	162.0	[52]
Surface disulfide	Chalcopyrite	162.3 – 162.4	[50]
Bulk disulfide / bulk contribution	Pyrite	162.6	[52]
Metal deficient sulfides / polysulfide	Chalcopyrite + NaEX	163 ± 0.2	[19]
Polysulfides	Chalcopyrite	163.0 – 163.4	[50]
Elemental sulfur (S ⁰)	Chalcopyrite; Pyrite	164.0 – 164.4	[35,55]
Energy loss feature	Chalcopyrite	164.5	[50]

3.3.6 Extracellular Polymeric Substance (EPS) Extraction and analysis

The EPS extraction method can be dependent on the bacterial strain, therefore multiple extraction methods exist and have previously been trialled [56-63]. Some extraction methods are more taxing on the cells such as sonication, formaldehyde, sulfuric acid and formaldehyde with sodium hydroxide, can cause the cells to lyse, expelling intracellular materials such as single strand DNA [64]. When extraction methods include these extra steps are often used to determine the concentration of membrane fragments and DNA from lysed cells. DNA 2-keto-3-deoxyoctonate (Kdo) is a component found in the membrane of a Gram-negative bacteria and is used for Gram-negative cells [64,65]. Before extraction can take place, first the cells need to be removed. The two most common ways this occurs is through centrifugation and filtration [56,57,62,65]. The following methods of extraction are commonly used and attempted for the studies presented and discussed in Chapter 7. Other methods employed include the use of a cation exchange resin (CER) for EPS extraction [66]. Analysis techniques are component dependent and is dependent on which component is being characterised.

3.3.6.1 Weaver and Hicks [56] Extraction Method

Weaver and Hicks [56] extracted EPS from cultures of *A. vinelandii* and *S. bijugatus*. The cultures were grown at 28 °C until cell concentration reached the exponential phase, with

glucose being added to the culture after 54 hours. Once maximum turbidity was reached, 0.5% formaldehyde was added as a fixative along with 0.04M of EDTA. The pH was adjusted to 6.5 before the removal of the exopolymer. The exopolymer was removed from the cells through centrifugation (twice at 12,100xg, 10 minutes with resuspension in the supernatant followed by 12,100xg, 40 minutes). Supernatant was then frozen at -20°C before precipitation (12 hours, 70% ethanol) and resuspended in Milli-Q water, with this process being repeated a total of three times. The final precipitation was then washed with 3 aliquots of ice-cold 70% ethanol. Proteins and lipids were extracted from the filtrate through the addition of 5:1:0.2 solution of water:chloroform:n-butanol. The chloroform was added and removed until no further precipitate was formed.

3.3.6.2 Lima, et al. [57] Extraction Method

Lima et al. [57] used cultures of *mycelia* grown for 6 days at 29°C. Cells were removed from the medium through low-pressure filtration and the supernatant concentrated to one fourth of the original volume using a rotary evaporator at 45°C and reduced pressure. Precipitation was conducted through two different methods for comparison.

Ethanol precipitation: A 4:1 ratio of ethanol (96°GL) was added to the supernatant and maintained at 4°C over night. The precipitate was recovered through centrifugation, redissolved in distilled water and dialyzed in the membrane with a cut off at 8,000 Da then freeze dried.

Trichloroacetic acid (TCA) treatment combined with ethanol precipitation: A 1:6 ratio of TCA (80%) was added to the supernatant and homogenized using a vortex, followed by centrifugation (10,000 x g, 10 minutes). The supernatant was recovered, and ethanol precipitation was carried out with two parts ethanol (96°GL; 4°C for 18 hours) centrifuged and dialyzed with the final product being freeze dried. It was reported that the addition of TCA reduced the contaminants in the precipitate.

3.3.6.3 Jiao, et al. [62] Extraction Method

Biofilm samples were collected and immediately frozen and stored at -80°C until extraction occurred. Samples were thawed on ice and centrifuged at 15,000 x g for 20 minutes with the supernatant being saved for further analysis. The biofilm pellets were resuspended in cold sulphuric acid (0.2 M, pH 11) and broken up. The cell suspension was stirred for 3 hours at

4°C and centrifuged again at 15,000 x g for 20 minutes. The supernatant was then referred to as the EPS solution with both the colloidal and capsular fragments.

3.3.6.4 Patra and Natarajan [63] Extraction Method

Patra and Natarajan [63] investigated EPS extraction from a culture of *Bacillus polymyxa*, cells were removed from the culture through centrifugation and the supernatant filtered through a 0.2µm Millipore filter. Polysaccharides and proteins were isolated using different methods.

Protein isolation occurred through the slow addition of analytical grade, powdered ammonium sulfate to a saturation of 90% while at 4°C with constant shaking. Precipitate was dissolved in 1M tris hydrochloride buffer at pH7 and dialyzed for over 18 hours at 4°C. Precipitates that were formed during the dialysis was separated through centrifugation and discarded, with the supernatant being lyophilised.

Polysaccharides were isolated through the use of Virtis Freezemobile 12EL lyophiliser at -80°C. Double distilled ethanol was added and kept stationary at 4°C for 8 hours. The resulting precipitate was washed with double distilled water. Purification was done through repeated ethanol precipitations. Dialysis then occurred with double distilled water.

3.3.6.5 Protein Concentration – Bradford Assay

The most common protein quantification methods are the Bradford Assay and the Lowry Protein Assay [2,57,63,65,67]. Both methods are spectroscopic methods relying on the binding of protein to a reagent before absorbance can be detected. The Bradford Assay uses Coomassie blue G-250 assay reagent which gives an absorbance at 595 nm (for 1 mm path length) when bound to protein. The absorbance at 595 nm is then used to quantify the protein concentration [68]. The Lowry Protein Assay is similar, using a Folin-Ciocalteu reagent giving an absorbance at 660 nm. The colour change, and cause of absorbance, is due to the reduction of the Folin-Ciocalteu reagent. However, this reagent has also been noted to interact with other components such as thiols and nucleotides with phenol reactivity increased in the presence of copper [69]. For this reason, the Bradford Assay is more suitable and reliable.

The Bradford Assay was conducted using the Coomassie blue G-250 assay reagent obtained from ThermoFisher Scientific. Measurements were conducted on a Thermo Scientific Nanodrop 1000 Spectrophotometer V3.8 using the Protein Bradford module. For accuracy in

quantification of the protein content, a standard curve using known concentrations of Bovine serum albumin (BSA) is required. The Protein Bradford module uses the standard curve to calculate the protein content within the sample through linear interpolation and polynomial fitting. A full step by step guide for conducting Bradford Assay analysis is presented in Appendix II below.

3.3.6.6 Polysaccharide and Monosaccharide Content

The phenol – sulfuric acid assay is a common technique used to analyse the saccharide concentration within EPS. This is an Ultra Violet method of determining the carbon content of carbohydrates in solution and depends on the dehydration of hydrolysed saccharides to furfural derivatives with concentrated sulfuric acid [70]. The furfural derivatives react with phenol to produce a coloured complex which absorbs light from the visible spectrum at 490 nm [70]. The absorbance of the solution is related to the concentration and can be described mathematically by the Beer Lambert law, shown in Equation 3.7 [70]; A represents the absorbance, ϵ represents the molar adsorption coefficient, c represents the molar concentration and l represents the optical path length.

$$A = \epsilon cl \quad (3.7)$$

As the results are presented as glucose equivalents, this may produce some limitations when it comes to complex carbohydrates [70]. The nature of the carbohydrates within the EPS can also influence the reactivity with the sulfuric acid. Interference can also occur with phenol – sulfuric acid assays, so this method is only employed to solutions which do not have an absorbance at 490 nm prior to treatment. Absorbance at this wavelength prior to treatment can indicate the presence of proteins and/or flavonoid impurities [70].

Measurements for the phenol – sulfuric acid assay were conducted a Thermo Scientific Nanodrop 1000 Spectrophotometer V3.8 using the UV-Vis module with absorbance of 220 – 750 nm. The wavelength for analysis was selected as 490 nm. A full procedure for phenol – sulfuric acid assay is presented in Appendix II.

Quantitative and qualitative analysis of fatty acids and monosaccharides has also been conducted through techniques such as gas-liquid chromatography, gas chromatography and

gas chromatography mass spectrometry [57,65,71]. These chromatography techniques often require adapted methods of extraction and/or further treatment prior to analysis.

3.3.7 Fourier Transform Infrared Spectroscopy

3.3.7.1 Background

Fourier Transform Infrared (FTIR) spectroscopy is a configurational and conformational analysis technique, commonly used for the study of polymers and proteins [72]. The infrared absorption spectrum is the most unique physical property of a compound, providing a chemical fingerprint of compounds through the detection of infra-red active functional groups [72,73]. This spectroscopic technique can become quantitative with the addition of chemometric methods which has the same precision as other techniques but is faster and requires less sample manipulation [72,74]. Absorption involves a transition between vibrational and rotational energies, with mid infrared spectroscopy measuring the absorption in the frequency range of $4000 - 400 \text{ cm}^{-1}$ [72]. However, there is a selective rule that applies to the absorption and transition of infrared light. The absorption and transitions can only occur if there is a change in the dipole moment of the molecule caused by the vibration [72].

Attenuated Total Reflection – Fourier Transform Infrared (FTIR-ATR), is a technique which uses an infrared beam passed through a crystal with a high refractive index. When the infrared beam is passed through the crystal and interacts with the sample, an evanescent wave is produced which is altered by the infrared vibrations of the sample. The quality of the resulting spectrum is dependent on the contact between the sample and the crystal. ATR allows analysis of samples which may be difficult to analyse in other FTIR techniques such as liquid samples and complex solid samples. A schematic of the ATR set up is seen in Figure 3.6 below.

Image removed due to copyright restriction

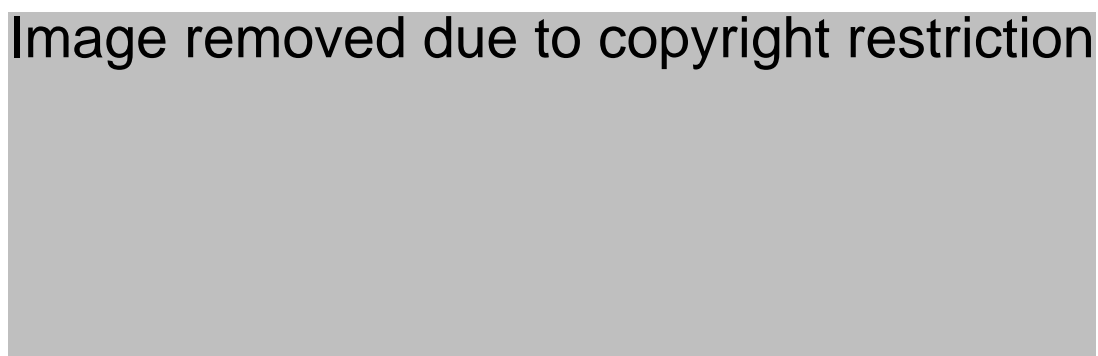


Figure 3.6: Schematic of an ATR-FTIR system from Ausili, et al. [75]

FTIR-ATR has been used for EPS analysis by Jiao, et al. [62], Kacuráková and Wilson [72] and Fang, et al. [73]. With a spectral range of 950-750 cm^{-1} , the structural study of sugars in aqueous solutions was conducted by Kacuráková and Wilson [72] and the changes in conformation and constraints by hydrogen bonding was recorded [62,72]. While Fang, et al. [73] used the technique to prove the phosphodiester groups of nucleic acids mediate the binding of EPS to a mineral surface [73]. Structural information can be gained from the spectra with carbohydrates showing high absorbance in the 950 – 1200 cm^{-1} [72,76,77]. The shape of the spectrum influenced by both the backbone structure and the side chain constituents [76].

3.3.7.2 Data Collection and Analysis

Samples were prepared as stated in Section 3.3.1.2, where the aliquots of 1 mL are placed in a 1.5 mL Eppendorf tube with analysis proceeding immediately. Approximately 100 μL of the aliquot sample (as a slurry) was placed on the FTIR-ATR crystal ensuring the crystal was completely covered. Adequate pressure was steadily applied through the duration of analysis. Once analysis was complete, the sample was removed, and the ATR crystal was cleaned with ethanol. Data acquisition was conducted on a Perkin Elmer Frontier FTIR over the range of 600 – 4000 cm^{-1} with each sample being analysed over 10 scans.

Table 3.5: Reference table for FTIR peak absorbance

Wavenumber (cm^{-1})	Assignment	Reference
950 – 1250	C–O–C stretch	[42]
1052	C–O, C–O–C from polysaccharides	[78,79]
1080	C–O stretch (vibrational modes) of carbohydrates and alcohols	[80]
1082	CH ₂ twisting from carbohydrates	[81]
1085	Ring vibrations	[78,79]
1114	C–O–P, P–O–P, ring vibrations	[78,79]
1140	S containing functional group	[82]
1155	CH ₃ wagging from carbohydrates	[81]
1222	P=O	[78,79]
1240	P=O stretching from phosphate	[78,79,81]
1250	Phenolic OH	[78]

1259	S containing functional group	[82]
1303	Amide II (C–N)	[78,79]
1380 – 1400	C–H bending vibration	[82]
1398 – 1402	C–O bend from carboxylate ions	[78-80]
1399	CH ₂ bending group of proteins	[81]
1445	CH ₃ bending groups of proteins	[81]
1454 – 1460	C–H bend from CH ₂	[78,79]
1452 – 1456	CH ₂ scissor	[80]
1548 – 1550	Amide II N–H, C–N structure of proteins	[78-80]
1515 – 1550	NH bending of secondary amide group –CONH	[81]
1648 – 1652	Amide I C=O different conformations Folded and helical structures of proteins	[78-80]
1661	NH ₂ bending – primary amide	[81]
1700	Carbonyl C=O stretch	[42]
1705	>C=O stretch, Ester, carboxylic groups	[78,79]
1735	> C=O stretch, Ester, fatty acids	[78]
1738	C=O stretch	[80]
1745 1750 – 1620	> C=O stretch, Ester, fatty acids	[78,79,81]
2800 – 3000	CH ₃ > CH ₂ > CH stretching modes	[83]
2850 – 2854	CH ₂ symmetric stretch	[78,79,82]
2870	CH ₃ symmetric stretch	[42,78,79]
2920 – 2924	CH ₂ asymmetric stretch	[42,78,79,82]
2926	CH ₂ asymmetric stretch from fatty acids	[81]
2956	CH ₃ asymmetric stretch	[78,79]
3340	OH Stretch	[42]
3400	OH of water	[78,79,82]
3448	OH stretching	[82]

3.3.8 Contact Angle Measurements

3.3.8.1 Background

Contact angle measurements are used to determine the degree of wettability of a surface. The wettability of a surface refers to how well a surface attracts or repels water. The wettability of a mineral phase is an important factor in the relationship between the floatability and recovery of the mineral of interest [84].

There are three possible contact angle calculations due to the reproducibility issues in different systems. These calculations are: the Young equation (homogeneous three phase systems), the Wenzel equation (homogeneous, rough surfaces), and the Cassie equation (heterogeneous, rough surfaces) [85]. The contact angle is measured at the interaction point of the solid, liquid and gas phases, which is also referred to as the three phase contact line [84]. The equilibrium at the three phase contact line is shown in the Young's equation, presented below in Equation 3.8 [11,84], which is best suited to these systems as the samples are polished, single mineral segments. A schematic representation of the three phase contact line illustrated in Figure 3.7. The notation of γ_{SG} , γ_{SL} , and γ_{LG} represents the interfacial tension for solid-gas, solid-liquid, and liquid-gas phases. The resulting contact angle (θ) can be influenced by surface roughness and porosity of the mineral surface [84].

$$\gamma_{SG} = \gamma_{SL} + \gamma_{LG} \cos \theta \quad (3.8)$$

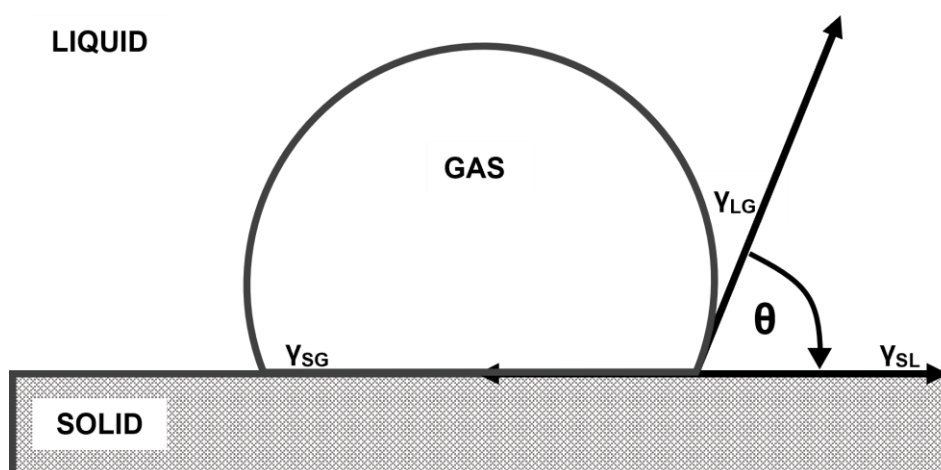


Figure 3.7: Schematic representation of the three phase contact line at equilibrium, adapted from Abaka-Wood, et al. [84]

3.3.8.2 Sample Preparation

Pure mineral coupons were prepared as outlined in Section 3.3.4.2.

3.3.8.3 Data Analysis

Captive bubble measurements were conducted on a Sinterface Profile Analysis Tensiometer PAT1, Version 8 with a CCD camera. The contact angle was calculated from the images captured by the CCD camera using ImageJ Processing and Analysis software with the Contact Angle plugin. The Contact Angle plugin calculates the contact angle using both the sphere and ellipse approximation ($\theta = 2\arctan(2h/l)$) [9]. This method of contact angle determination takes into account influences such as gravity and volume of the bubble.

3.4 References

1. Bleeze, B.; Zhao, J.; Harmer, S.L. Selective Attachment of *Leptospirillum ferrooxidans* for Separation of Chalcopyrite and Pyrite through Bio-Flotation. *Minerals* **2018**, *8*, 86.
2. Bastias, M.; Gentina, J.C. Variables affecting the growth and ferrous oxidation capacity of *L. Ferrooxidans* in continuous culture. *Hydrometallurgy* **2010**, *104*, 351-355, doi:10.1016/j.hydromet.2010.04.015.
3. Freund, M.; Carol, B. Factors Affecting Haemocytometer Counts of Sperm Concentration in Human Semen. *J Reprod Fertil* **1964**, *8*, 149-155.
4. Monod, J. The Growth of Bacterial Cultures. *Annu Rev Microbiol* **1949**, *3*, 371-394, doi:10.1146/annurev.mi.03.100149.002103.
5. Dhau, J.S.; Singh, A.; Singh, A.; Sook, B.S.; Brandao, P.; Felix, V. Synthesis and antibacterial activity of pyridylselenium compounds: Self-assembly of bis(3-bromo-2-pyridyl)diselenide via intermolecular secondary and pi center dot center dot center dot pi stacking interactions. *J Organomet Chem* **2014**, *766*, 57-66, doi:10.1016/j.jorganchem.2014.05.009.
6. Swapp, S. Geochemical Instrument Analysis: Scanning Electron Microscopy. Available online: http://serc.carleton.edu/research_education/geochemsheets/techniques/SEM.html (accessed on 19th July).
7. Horny, P.; Lifshin, E.; Campbell, H.; Gauvin, R. Development of a new quantitative X-ray microanalysis method for electron microscopy. *Microscopy and Microanalysis* **2010**, *16*, 821-830.
8. Image Processing and Analysis in Java. Analyze Menu. Available online: <https://imagej.nih.gov/ij/docs/menus/analyze.html> (accessed on 19 March).
9. Brugnara, M. Contact Angle. Available online: <https://imagej.nih.gov/ij/plugins/contact-angle.html> (accessed on 19 March).
10. Napier-Munn, T.; Wills, B.A. *Wills' mineral processing technology: an introduction to the practical aspects of ore treatment and mineral recovery*; Butterworth-Heinemann: 2011.
11. Wills, B.A. *Mineral processing technology: an introduction to the practical aspects of ore treatment and mineral recovery*, 4th ed.; Pergamon Press: New South Wales, Australia, 1988.
12. Coelho, A.A. *TOPAS Academic: General Profile and Structure Analysis Software for Powder Diffraction Data*, 2007. Available from
13. McCready, D.E.; Balmer, M.L.; Keefer, K.D. Experimental and calculated X-ray powder diffraction data for cesium titanium silicate, CsTiSi₂O_{6.5}: A new zeolite. *Powder Diffraction* **1997**, *12*, 40-46, doi:10.1017/S0885715600009416.
14. Hellenbrandt, M. The inorganic crystal structure database (ICSD)-present and future. *Crystallography Reviews* **2004**, *10*, 17-22.
15. Singh, B.; Fang, Y.Y.; Cowie, B.C.C.; Thomsen, L. NEXAFS and XPS characterisation of carbon functional groups of fresh and aged biochars. *Org Geochem* **2014**, *77*, 1-10, doi:10.1016/j.orggeochem.2014.09.006.
16. Stanford University. NEXAFS Spectroscopy. Available online: <https://www-ssrl.slac.stanford.edu/stohr/nexafs.htm> (accessed on 6 December).

17. Günther, S.; Kaulich, B.; Gregoratti, L.; Kiskinova, M. Photoelectron microscopy and applications in surface and materials science. *Progress in surface science* **2002**, *70*, 187-260.
18. Wei, D.H.; Chan, Y.-L.; Hsu, Y.-J. Exploring the magnetic and organic microstructures with photoemission electron microscope. *Journal of Electron Spectroscopy and Related Phenomena* **2012**, *185*, 429-435.
19. Kalegowda, Y.; Chan, Y.L.; Wei, D.H.; Harmer, S.L. X-PEEM, XPS and ToF-SIMS characterisation of xanthate induced chalcopyrite flotation: Effect of pulp potential. *Surf Sci* **2015**, *635*, 70-77, doi:10.1016/j.susc.2014.12.012.
20. Acres, R.G.; Harmer, S.L.; Beattie, D.A. Synchrotron PEEM and ToF-SIMS study of oxidized heterogeneous pentlandite, pyrrhotite and chalcopyrite. *J Synchrotron Radiat* **2010**, *17*, 606-615, doi:10.1107/S0909049510026749.
21. Hitchcock, A.P. *aXis2000*, 2009. Available from <http://unicorn.mcmaster.ca/aXis2000.html/>
22. Ravel, B.; Newville, M. ATHENA, ARTEMIS, HEPHAESTUS: data analysis for X-ray absorption spectroscopy using IFEFFIT. *Journal of Synchrotron Radiation* **2005**, *12*, 537-541, doi:10.1107/S0909049505012719.
23. Latham, K.G.; Simone, M.I.; Dose, W.M.; Allen, J.A.; Donne, S.W. Synchrotron based NEXAFS study on nitrogen doped hydrothermal carbon: Insights into surface functionalities and formation mechanisms. *Carbon* **2017**, *114*, 566-578, doi:10.1016/j.carbon.2016.12.057.
24. Singh, B.; Fang, Y.; Cowie, B.; Thomsen, L. NEXAFS and XPS characterisation of carbon functional groups of fresh and aged biochars. *Org Geochem* **2014**, *77*, 1-10, doi:10.1016/j.orggeochem.2014.09.006.
25. Hardie, A.G.; Dynes, J.J.; Kozak, L.M.; Huang, P.M. The role of glucose in abiotic humification pathways as catalyzed by birnessite. *J Mol Catal a-Chem* **2009**, *308*, 114-126, doi:10.1016/j.molcata.2009.03.035.
26. Cody, G.D.; Ade, H.; Wirick, S.; Mitchell, G.D.; Davis, A. Determination of chemical-structural changes in vitrinite accompanying luminescence alteration using C-NEXAFS analysis. *Org Geochem* **1998**, *28*, 441-455, doi:10.1016/S0146-6380(98)00010-2.
27. Boese, J.; Osanna, A.; Jacobsen, C.; Kirz, J. Carbon edge XANES spectroscopy of amino acids and peptides. *Journal of Electron Spectroscopy and Related Phenomena* **1997**, *85*, 9-15, doi:10.1016/S0368-2048(97)00032-7.
28. Coker, V.; Byrne, J.; Telling, N.; Van der Laan, G.; Lloyd, J.; Hitchcock, A.; Wang, J.; Patrick, R. Characterisation of the dissimilatory reduction of Fe (III)-oxyhydroxide at the microbe–mineral interface: the application of STXM–XMCD. *Geobiology* **2012**, *10*, 347-354.
29. Ade, H.; Hitchcock, A.P. NEXAFS microscopy and resonant scattering: Composition and orientation probed in real and reciprocal space. *Polymer* **2008**, *49*, 643-675, doi:10.1016/j.polymer.2007.10.030.
30. La Vars, S.; Newton, K.; Quinton, J.; Cheng, P.-Y.; Wei, D.-H.; Chan, Y.-L.; Harmer, S. Surface chemical characterisation of pyrite Exposed to *Acidithiobacillus ferrooxidans* and associated extracellular polymeric substances. *Minerals* **2018**, *8*, 132.
31. Chan, C.S.; Fakra, S.C.; Edwards, D.C.; Emerson, D.; Banfield, J.F. Iron oxyhydroxide mineralization on microbial extracellular polysaccharides. *Geochimica Et Cosmochimica Acta* **2009**, *73*, 3807-3818, doi:10.1016/j.gca.2009.02.036.

32. Chandra, A.P.; Puskar, L.; Simpson, D.J.; Gerson, A.R. Copper and xanthate adsorption onto pyrite surfaces: Implications for mineral separation through flotation. *International Journal of Mineral Processing* **2012**, *114*, 16-26, doi:10.1016/j.minpro.2012.08.003.
33. Casa Software Ltd. Peak Fitting in XPS. Available online: http://www.casaxps.com/help_manual/manual_updates/peak_fitting_in_xps.pdf (accessed on
34. Hagström, S.; Nordling, C.; Siegbahn, K. Electron spectroscopy for chemical analyses. *Physics Letters* **1964**, *9*, 235-236, doi:[https://doi.org/10.1016/0031-9163\(64\)90062-9](https://doi.org/10.1016/0031-9163(64)90062-9).
35. Harmer, S.L.; Thomas, J.E.; Fornasiero, D.; Gerson, A.R. The evolution of surface layers formed during chalcopyrite leaching. *Geochimica Et Cosmochimica Acta* **2006**, *70*, 4392-4402, doi:10.1016/j.gca.2006.06.1555.
36. Casa Software Ltd. *CasaXPS*, 2.3.19PR1.0; 2000. Available from
37. Moulder, J.F.; Stickle, W.F.; Sobol, P.E.; Bomben, K.D. *Handbook of X-ray photoelectron spectroscopy*; Physical Electronics Inc.: Minnesota, USA, 1992.
38. Crist, B.V. A review of XPS data-banks. *XPS Reports* **2007**, *1*.
39. Ahimou, F.; Boonaert, C.J.; Adriaensen, Y.; Jacques, P.; Thonart, P.; Paquot, M.; Rouxhet, P.G. XPS analysis of chemical functions at the surface of *Bacillus subtilis*. *J Colloid Interface Sci* **2007**, *309*, 49-55, doi:10.1016/j.jcis.2007.01.055.
40. Nesbitt, H.W.; Muir, I.J. X-Ray Photoelectron Spectroscopic Study of a Pristine Pyrite Surface Reacted with Water-Vapor and Air. *Geochimica Et Cosmochimica Acta* **1994**, *58*, 4667-4679, doi:10.1016/0016-7037(94)90199-6.
41. Smart, R.S.C.; Skinner, W.M.; Gerson, A.R. XPS of sulphide mineral surfaces: metal-deficient, polysulphides, defects and elemental sulphur. *Surface and Interface Analysis: An International Journal devoted to the development and application of techniques for the analysis of surfaces, interfaces and thin films* **1999**, *28*, 101-105.
42. Akhter, S.; Allan, K.; Buchanan, D.; Cook, J.A.; Campion, A.; White, J.M. XPS and IR study of X-ray induced degradation of PVA polymer film. *Applied Surface Science* **1988**, *35*, 241-258, doi:[https://doi.org/10.1016/0169-4332\(88\)90053-0](https://doi.org/10.1016/0169-4332(88)90053-0).
43. López, G.P.; Castner, D.G.; Ratner, B.D. XPS O 1s binding energies for polymers containing hydroxyl, ether, ketone and ester groups. *Surface and interface analysis* **1991**, *17*, 267-272.
44. Le Normand, F.; Hommet, J.; Szörényi, T.; Fuchs, C.; Fogarassy, E. XPS study of pulsed laser deposited CN x films. *Phys Rev B* **2001**, *64*, 235416.
45. Zubavichus, Y.; Fuchs, O.; Weinhardt, L.; Heske, C.; Umbach, E.; Denlinger, J.D.; Grunze, M. Soft X-ray-induced decomposition of amino acids: an XPS, mass spectrometry, and NEXAFS study. *Radiation Research* **2004**, *161*, 346-358.
46. Campbell, C.T. An XPS study of molecularly chemisorbed oxygen on Ag (111). *Surface Science Letters* **1986**, *173*, L641-L646.
47. Descostes, M.; Mercier, F.; Thromat, N.; Beaucaire, C.; Gautier-Soyer, M. Use of XPS in the determination of chemical environment and oxidation state of iron and sulfur samples: constitution of a data basis in binding energies for Fe and S reference compounds and applications to the evidence of surface species of an oxidized pyrite in a carbonate medium. *Applied Surface Science* **2000**, *165*, 288-302, doi:10.1016/S0169-4332(00)00443-8.

48. Jones, C.F.; LeCount, S.; Smart, R.S.C.; White, T.J. Compositional and structural alteration of pyrrhotite surfaces in solution: XPS and XRD studies. *Applied surface science* **1992**, *55*, 65-85.
49. Suzuki, S.; Yanagihara, K.; Hirokawa, K. XPS study of oxides formed on the surface of high-purity iron exposed to air. *Surface and Interface Analysis: An International Journal devoted to the development and application of techniques for the analysis of surfaces, interfaces and thin films* **2000**, *30*, 372-376.
50. Acres, R.G.; Harmer, S.L.; Beattie, D.A. Synchrotron XPS, NEXAFS, and ToF-SIMS studies of solution exposed chalcopyrite and heterogeneous chalcopyrite with pyrite. *Minerals Engineering* **2010**, *23*, 928-936, doi:10.1016/j.mineng.2010.03.007.
51. McIntyre, N.; Zetaruk, D. X-ray photoelectron spectroscopic studies of iron oxides. *Analytical Chemistry* **1977**, *49*, 1521-1529.
52. Nesbitt, H.W.; Bancroft, G.M.; Pratt, A.R.; Scaini, M.J. Sulfur and iron surface states on fractured pyrite surfaces. *Am Mineral* **1998**, *83*, 1067-1076.
53. Comans, R.N.; Eighmy, T.T.; Shaw, E.L. Reference Spectra for Environmentally Important Secondary Minerals: Ettringite (Ca₆Al₂(SO₄)₃(OH)₁₂·26H₂O) by XPS. *Surface Science Spectra* **1996**, *4*, 150-156.
54. Harmer, S.L.; Pratt, A.R.; Nesbitt, W.H.; Fleet, M.E. Sulfur species at chalcopyrite (CuFeS₂) fracture surfaces. *Am Mineral* **2004**, *89*, 1026-1032, doi:10.2138/am-2004-0713.
55. Nelson, N. A photometric adaptation of the Somogyi method for the determination of glucose. *Journal of Biological Chemistry* **1944**, *153*, 375-380.
56. Weaver, D.T.; Hicks, R.E. Biodegradation of Azotobacter vinehni & exopolymer by Lake Superior microbes. *Limnol. Oceanogr* **1995**, *40*, 1035-1041.
57. Lima, L.F.; Habu, S.; Gern, J.C.; Nascimento, B.M.; Parada, J.L.; Nosedá, M.D.; Gonçalves, A.G.; Nisha, V.R.; Pandey, A.; Soccol, V.T., et al. Production and characterization of the exopolysaccharides produced by *Agaricus brasiliensis* in submerged fermentation. *Appl Biochem Biotechnol* **2008**, *151*, 283-294, doi:10.1007/s12010-008-8187-2.
58. Li, X.Y.; Yang, S.F. Influence of loosely bound extracellular polymeric substances (EPS) on the flocculation, sedimentation and dewaterability of activated sludge. *Water Res* **2007**, *41*, 1022-1030, doi:10.1016/j.watres.2006.06.037.
59. Liu, H.; Fang, H.H. Extraction of extracellular polymeric substances (EPS) of sludges. *J Biotechnol* **2002**, *95*, 249-256, doi:[https://doi.org/10.1016/S0168-1656\(02\)00025-1](https://doi.org/10.1016/S0168-1656(02)00025-1).
60. Meng, L.; Xi, J.; Yeung, M. Degradation of extracellular polymeric substances (EPS) extracted from activated sludge by low-concentration ozonation. *Chemosphere* **2016**, *147*, 248-255, doi:10.1016/j.chemosphere.2015.12.060.
61. Ravella, S.R.; Quinones, T.S.; Retter, A.; Heiermann, M.; Amon, T.; Hobbs, P.J. Extracellular polysaccharide (EPS) production by a novel strain of yeast-like fungus *Aureobasidium pullulans*. *Carbohydr Polym* **2010**, *82*, 728-732, doi:10.1016/j.carbpol.2010.05.039.
62. Jiao, Y.; Cody, G.D.; Harding, A.K.; Wilmes, P.; Schrenk, M.; Wheeler, K.E.; Banfield, J.F.; Thelen, M.P. Characterization of extracellular polymeric substances from acidophilic microbial biofilms. *Appl Environ Microb* **2010**, *76*, 2916-2922, doi:10.1128/AEM.02289-09.

63. Patra, P.; Natarajan, K.A. Microbially induced flocculation and flotation for separation of chalcopyrite from quartz and calcite. *International Journal of Mineral Processing* **2004**, *74*, 143-155, doi:10.1016/j.minpro.2003.10.006.
64. He, Z.G.; Yang, Y.P.; Zhou, S.; Hu, Y.H.; Zhong, H. Effect of pyrite, elemental sulfur and ferrous ions on EPS production by metal sulfide bioleaching microbes. *Transactions of Nonferrous Metals Society of China* **2014**, *24*, 1171-1178, doi:10.1016/S1003-6326(14)63176-9.
65. Harneit, K.; Göksel, A.; Kock, D.; Klock, J.-H.; Gehrke, T.; Sand, W. Adhesion to metal sulfide surfaces by cells of *Acidithiobacillus ferrooxidans*, *Acidithiobacillus thiooxidans* and *Leptospirillum ferrooxidans*. *Hydrometallurgy* **2006**, *83*, 245-254.
66. Sheng, G.P.; Xu, J.; Luo, H.W.; Li, W.W.; Li, W.H.; Yu, H.Q.; Xie, Z.; Wei, S.Q.; Hu, F.C. Thermodynamic analysis on the binding of heavy metals onto extracellular polymeric substances (EPS) of activated sludge. *Water Res* **2013**, *47*, 607-614, doi:10.1016/j.watres.2012.10.037.
67. Stoytcheva, M.; Zlatev, R.; Magnin, J.-P.; Ovalle, M.; Valdez, B. *Leptospirillum ferrooxidans* based Fe²⁺ sensor. *Biosensors and Bioelectronics* **2009**, *25*, 482-487.
68. Thermo Scientific. Coomassie (Bradford) Protein Assay Kit. ThermoFisher Scientific: 2013; Vol. 23200, p 7.
69. Everette, J.D.; Bryant, Q.M.; Green, A.M.; Abbey, Y.A.; Wangila, G.W.; Walker, R.B. Thorough Study of Reactivity of Various Compound Classes toward the Folin–Ciocalteu Reagent. *Journal of Agricultural and Food Chemistry* **2010**, *58*, 8139-8144, doi:10.1021/jf1005935.
70. Albalasmeh, A.A.; Berhe, A.A.; Ghezzehei, T.A. A new method for rapid determination of carbohydrate and total carbon concentrations using UV spectrophotometry. *Carbohydr Polym* **2013**, *97*, 253-261, doi:10.1016/j.carbpol.2013.04.072.
71. Aires, C.P.; Koo, H.; Sassaki, G.L.; Iacomini, M.; Cury, J.A. A procedure for characterizing glucans synthesized by purified enzymes of cariogenic *Streptococcus mutans*. *International Journal of Biological Macromolecules* **2010**, *46*, 551-554, doi:<https://doi.org/10.1016/j.ijbiomac.2010.01.018>.
72. Kacuráková, M.; Wilson, R.H. Developments in mid-infrared FT-IR spectroscopy of selected carbohydrates. *Carbohydr Polym* **2001**, *44*, 291-303, doi:10.1016/S0144-8617(00)00245-9.
73. Fang, L.; Huang, Q.; Wei, X.; Liang, W.; Rong, X.; Chen, W.; Cai, P. Microcalorimetric and potentiometric titration studies on the adsorption of copper by extracellular polymeric substances (EPS), minerals and their composites. *Bioresource Technol* **2010**, *101*, 5774-5779, doi:10.1016/j.biortech.2010.02.075.
74. Dupuy, N.; Ruckebush, C.; Duponchel, L.; BeurdeleySaudou, P.; Amram, B.; Huvenne, J.P.; Legrand, P. Quantitative determination of polymer and mineral content in paper coatings by infrared spectroscopy. Improvements by non-linear treatments. *Analytica Chimica Acta* **1996**, *335*, 79-85, doi:10.1016/S0003-2670(96)00328-5.
75. Ausili, A.; Sánchez, M.; Gómez-Fernández, J. Attenuated total reflectance infrared spectroscopy: A powerful method for the simultaneous study of structure and spatial orientation of lipids and membrane proteins. *Biomedical Spectroscopy and Imaging* **2015**, *4*, 159-170, doi:10.3233/BSI-150104.
76. Kacuráková, M. FT-IR study of plant cell wall model compounds: pectic polysaccharides and hemicelluloses. *Carbohydr Polym* **2000**, *43*, 195-203, doi:10.1016/s0144-8617(00)00151-x.

77. Coimbra, M.A.; Barros, A.; Barros, M.; Rutledge, D.N.; Delgadillo, I. Multivariate analysis of uronic acid and neutral sugars in whole pectic samples by FT-IR spectroscopy. *Carbohydr Polym* **1998**, *37*, 241-248, doi:10.1016/S0144-8617(98)00066-6.
78. Schmitt, J.; Flemming, H.C. FTIR-spectroscopy in microbial and material analysis. *International Biodeterioration & Biodegradation* **1998**, *41*, 1-11, doi:10.1016/S0964-8305(98)80002-4.
79. Schmitt, J.; Nivens, D.; White, D.C.; Flemming, H.C. Changes of biofilm properties in response to sorbed substances - An FTIR-ATR study. *Water Science and Technology* **1995**, *32*, 149-155, doi:10.1016/0273-1223(96)00019-4.
80. Wuertz, S.; Spaeth, R.; Hinderberger, A.; Griebe, T.; Flemming, H.C.; Wilderer, P.A. A new method for extraction of extracellular polymeric substances from biofilms and activated sludge suitable for direct quantification of sorbed metals. *Water Sci Technol* **2001**, *43*, 25-31.
81. Li, Q.; Wang, Q.F.; Zhu, J.Y.; Zhou, S.; Gan, M.; Jiang, H.; Sand, W. Effect of Extracellular Polymeric Substances on Surface Properties and Attachment Behavior of *Acidithiobacillus ferrooxidans*. *Minerals* **2016**, *6*, 100, doi:ARTN 100.10.3390/min6040100.
82. Parikh, A.; Madamwar, D. Partial characterization of extracellular polysaccharides from cyanobacteria. *Bioresource Technol* **2006**, *97*, 1822-1827, doi:10.1016/j.biortech.2005.09.008.
83. Naumann, D.; Fijala, V.; Labischinski, H.; Giesbrecht, P. The Rapid Differentiation and Identification of Pathogenic Bacteria Using Fourier-Transform Infrared Spectroscopic and Multivariate Statistical-Analysis. *J Mol Struct* **1988**, *174*, 165-170, doi:10.1016/0022-2860(88)80152-2.
84. Abaka-Wood, G.B.; Addai-Mensah, J.; Skinner, W. A study of flotation characteristics of monazite, hematite, and quartz using anionic collectors. *International Journal of Mineral Processing* **2017**, *158*, 55-62, doi:<https://doi.org/10.1016/j.minpro.2016.11.012>.
85. Chau, T.T.; Bruckard, W.J.; Koh, P.T.; Nguyen, A.V. A review of factors that affect contact angle and implications for flotation practice. *Adv Colloid Interfac* **2009**, *150*, 106-115, doi:10.1016/j.cis.2009.07.003.

4 SELECTIVE ATTACHMENT OF *LEPTOSPIRILLUM FERROOXIDANS* FOR THE SEPARATION OF CHALCOPYRITE AND PYRITE THROUGH BIO-FLOTATION

The following chapter is based in part on the paper; Bleeze, B., Zhao, J., & Harmer, S. L. (2018). *Selective Attachment of Leptospirillum ferrooxidans for Separation of Chalcopyrite and Pyrite through Bio-Flotation. Minerals, 8(3), 86.* While this chapter presents the ideas and concepts present in the paper, all data presented is an extension to the publication and has not been published. This publication has been appropriately referenced in text where required.

4.1 Introduction

Bio-leach microbes such as *Acidithiobacillus ferrooxidans* (*A. f* formally *T. ferrooxidans*), *Acidithiobacillus thiooxidans* (*A. t*), and *Leptospirillum ferrooxidans* (*L. f*) have been thoroughly investigated for the use in leaching processes. The focus has primarily been sulfide minerals due to the iron and/or sulfur oxidising capabilities [1-10]. More recently the application for *A. f* and *L. f* in bio-leaching has been investigated, with the focus on the selective attachment and EPS expression [11].

L. ferrooxidans exhibit a favourability in binding to iron, which has been capitalised for the use in sulfide mineral studies [12]. It is predicted that the oxidation state of the iron within the minerals contributes to the selective attachment of *L. f*, showing potential selective attachment for the Py/Cp system as the oxidation state of iron in Py (Fe^{2+}) and Cp (Fe^{3+}) differs [13,14]. Previous studies investigating the use of *L. f* and metabolites for the bio-modulation of pyrite, chalcopyrite, sphalerite and pyrrhotite (Po) have been reported with conflicting results [12,15]. However, these studies suggest that *L. f* and/or EPS may have the ability to act as a depressant. The study by Pecina, et al. [12] reports superficial surface changes causing a weak depressive effect on Po, while Vilinska and Rao [15] reported a depressive effect on Cp in a Cp/Py mixed system. This was determined as there was an increased amount of surface defects and an increase of iron availability for the Cp, leading to greater cell adsorption. Questions can be raised over the exact cause of the surface changes, as the cell adsorption was determined through cell counts of the solution over exposure time, with the difference in the cell number being taken as the number of cells attached [11]. Without visualisation of

the cells and the EPS on the surface it is difficult to determine the cause of surface chemistry changes. As EPS is known to mediate the microbe-mineral interaction, cell counts alone are not enough to determine the impact of cells [11].

The interactions and implications of *L. f* and their metabolites on the separation of Py and Cp is still not fully understood. Previous studies have focused on various exposure conditions including pH, exposure time and collector concentration, yet the effect of selective attachment of cells and metabolites has not been specifically investigated [1,11,15,16]. This chapter investigates the use of *Leptospirillum ferrooxidans* under different growth conditions, and their respective EPS supernatant, for the selective separation of Cp from Py. The objective of this chapter is to determine the effect of growth conditions on the flotation effect of *L. ferrooxidans*.

4.2 Experimental

4.2.1 Mineral Samples

Two natural mineral sources of both pyrite and chalcopyrite were used in the studies conducted in this chapter. All mineral samples were sourced from GeoDiscoveries (The Willyama Group, New South Wales, Australia). Culture growth, bio-flotation tests and attachment studies were conducted on a combination of these mineral samples, with preparation of the +38 – 75 μ m size fraction covered in Section 3.2.1.1 above.

The natural mineral samples use for attachment studies on mineral coupons originated from Peru (pyrite) and Moonta Mines, Australia (chalcopyrite). The composition and purity were determined through Quantitative Evaluation on Minerals by Scanning electron microscopy (QEMSCAN, FEI, Hillsboro, OR, USA) [17]. The results indicate a purity of 88% for pyrite, with the remaining 12% as pyrrhotite; while the purity of chalcopyrite was approximately 83% with bornite being the most predominant impurity [11,17].

The second source of pyrite (Huanzala mine, Peru) and chalcopyrite (China) were characterised using quantitative XRD (QXRD) and inductively coupled plasma mass spectrometry (ICPMS) to confirm purity. Analysis, shown in Section 3.2.1, indicates a purity of 96.4% for pyrite and 83.5% for chalcopyrite.

4.2.2 Bacterial Culture and Adjustment to Mineral

Bacterial cultures of *L. ferrooxidans* were obtained and maintained according to Section 3.2.2.1. Cultures were monitored for the total cell concentration using a haemocytometer, as outlined in Section 3.2.2.2. As *L. ferrooxidans* are iron oxidising bacteria, the ferrous iron concentration of the cultures was monitored through cerium sulfate oxidation – reduction titrations as described in Section 3.2.2.3.

4.2.2.1 Free Extracellular Polymeric Supernatant (EPS)

EPS supernatant was harvested from mature cultures in the late exponential phase. The process of extraction is outlined in Section 3.2.2.4.

4.2.2.2 FTIR-ATR Analysis

Samples were prepared as stated in Section 3.3.1.2 and aliquots of 1 mL were taken and placed in a 1.5 mL Eppendorf tube with analysis proceeding immediately. Approximately 100 μL of the aliquot sample (as a slurry) was placed on the Perkin Elmer Frontier FTIR-ATR crystal, ensuring it was completely covered. Adequate pressure was steadily applied through the duration of analysis. Data acquisition was conducted over the range of 600 – 4000 cm^{-1} with each sample being analysed over 10 scans.

4.2.3 Scanning Electron Microscopy (SEM)

Scanning Electron Microscopy was conducted on both pure mineral sections and mineral particles (+38 -75 μm). Samples were prepared and fixed as described in Section 3.3.1.2, with a starting cell concentration of 1.5×10^7 cells per mL.

Images were collected using an Inspect FEI F50 SEM, with an accelerating voltage of 5 – 10 kV and varying spot size. The secondary electron (SE) and back scattered electron (BSE) modes were used to obtain information about bacterial attachment and topographical changes, while chemical information was gathered using high Energy Dispersive Analysis by X-ray (EDAX). The particle size distribution and cell attachment concentration was assessed using the ImageJ software [18]. The particle size of 20 random particles was used to determine the average particle size.

4.2.4 Micro-Flotation Studies

Single mineral and differential mineral micro-flotation tests were conducted as collector-free flotation tests and in the presence of potassium isopropyl xanthate (PIPX) collector (10^{-4} M). Single mineral flotation tests were conducted on 1g high purity natural mineral, with a fraction size of +38 – 75 μ m. Differential mineral micro-flotation tests were conducted on 1g synthetic mix of chalcopyrite and pyrite with an approximate ratio of 1:1. All micro-flotation tests were performed at ambient temperature with the parameters as previously outlined in Section 3.3.2.2.

Conditioning environments for flotation tests are shown in Table 4.1 below. Conditioning environments are characterised into three variables: baseline, growth conditions, and EPS conditions. Control flotation tests (0 h) were conducted without preconditioning of the sample for both Milli-Q adjusted to pH 9 using NaOH and modified *Leptospirillum* HH medium at pH 1.8 [11]. Baseline flotations in modified *Leptospirillum* HH medium were also completed in the presence of sodium bisulfite (NaHSO_3) depressant (1.9×10^{-3} M), for a comparison to industrial processes [19]. NaHSO_3 can enhance the selectivity of the collector in Py and Cp separation [20].

Table 4.1: Conditioning of samples at an exposure time of 12 h, 24 h, 36h, 48 h, 60 h and 72 h

Conditions	
Baseline	M.Q water adjusted to pH 9 with NaOH Modified <i>Leptospirillum</i> HH Media
Food source	<i>L. f</i> grown on HH media (Fe^{2+})
	<i>L. f</i> grown on Py
	<i>L. f</i> grown on Cp
	<i>L. f</i> grown on Asp
EPS	EPS supernatant extracted from <i>L. f</i> grown on Py
	EPS supernatant extracted from <i>L. f</i> grown on Cp
	EPS supernatant extracted from <i>L. f</i> grown on Asp

4.2.4.1 X-Ray Diffraction Analysis

Flotation test fractions were analysed using a Bruker D8 Advance Eco Bragg-Brentano geometry X-ray Diffractometer (XRD), with a cobalt X-ray source. The quantitative analysis was determined by Rietveld quantitative phase analysis (QPA) of powder X-ray diffraction data using TOPAS [21]. For each diffractogram, the zero shift and scale factors for chalcopyrite (Inorganic Crystal Structure Database (ICSD) no. 94554) and pyrite (ICSD no. 15012) were refined. Refer to Section 3.3.3.2 for XRD sample preparation and procedure.

4.3 Results and Discussion

4.3.1 Culture Growth and Monitoring

Monitoring of the growth cycle of the *L. f* cultures was conducted through cell counts, using a haemocytometer as described in Section 3.2.2.2, and the iron content was monitored through a redox titration of cerium sulfate and ferrous iron as described in Section 3.2.2.3.

The growth curves obtained are assessed for the six distinct and key growth phases expected throughout the bacterial growth cycle [22], as discussed in Section 3.2.2.2. The analysis of the distinct growth phases can help determine the differences between the growth conditions, as growth conditions are known to have a direct influence on these growth phases [22].

4.3.1.1 *L. f* grown in Modified HH Media

The culture of *L. f* on modified HH media with iron (Fe^{2+}) sulfate was monitored over 240 h, to capture all growth phases of the culture, as shown in Figure 4.1. The growth curve indicates six distinct growth phases, starting with an acceleration phase immediately following inoculation until 8 h. Between 8 h and 18 h, the culture exhibits a lag phase with declined growth observed. At the end of the lag phase, the culture enters directly into the exponential growth phase, until approximately 60 h. The retardation phase is observed until approximately 98 h, where the linear stationary phase starts. The linear stationary phase is maintained until 168 h, where the culture enters the decline growth phase. Although the growth curve of the culture exceeds 240 h, re-inoculation of the culture occurs at 96 h to ensure aliquots are taken from a healthy culture, where the cell growth rate is greater than the cell death rate.

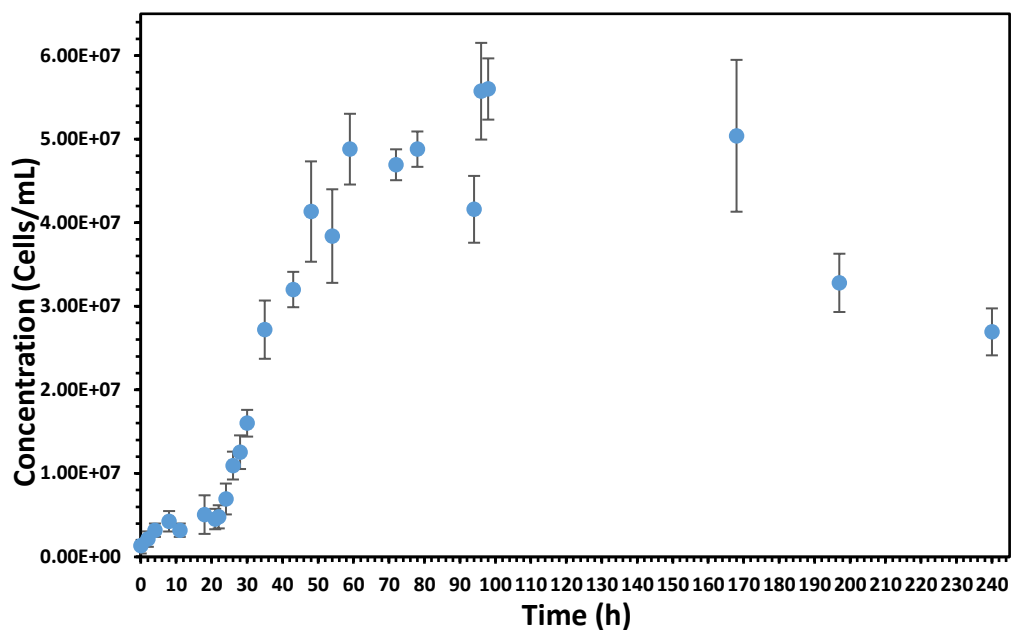


Figure 4.1: Growth curve of *L. ferrooxidans* in HH media with soluble Fe^{2+} monitored over 240 h

As *L. f* bacteria have the ability to oxidise iron, the change in oxidation state can also act as an indicator of culture growth. Therefore, the change in iron oxidation was monitored through a cerium sulfate redox titration over 180 h, shown in Figure 4.2 below. The initial change in concentration is slow, with gradual decreases occurring until 16 h – corresponding with the lag phase and acceleration phase of the culture. There is a rapid decrease in ferrous iron concentration observed between 16 and 48 h. This sudden decrease in the concentration corresponds with the exponential growth phase of the culture. At this point, the ferrous iron concentration is seen to stabilise for approximately 30 h, before slowly reducing again. Comparison of the cell concentration with ferrous iron concentration indicates that the end of the exponential phase and the start of the retardation phase correspond with this window of stability. After 88 h of growth, there is negligible amounts of ferrous iron detected, with slight fluctuations observed. This corresponds with the linear stationary phase, indicating that cell replication is still occurring. This suggests that there is a mechanism in the system allowing for the reduction of ferric iron to ferrous iron, allowing the culture to maintain growth.

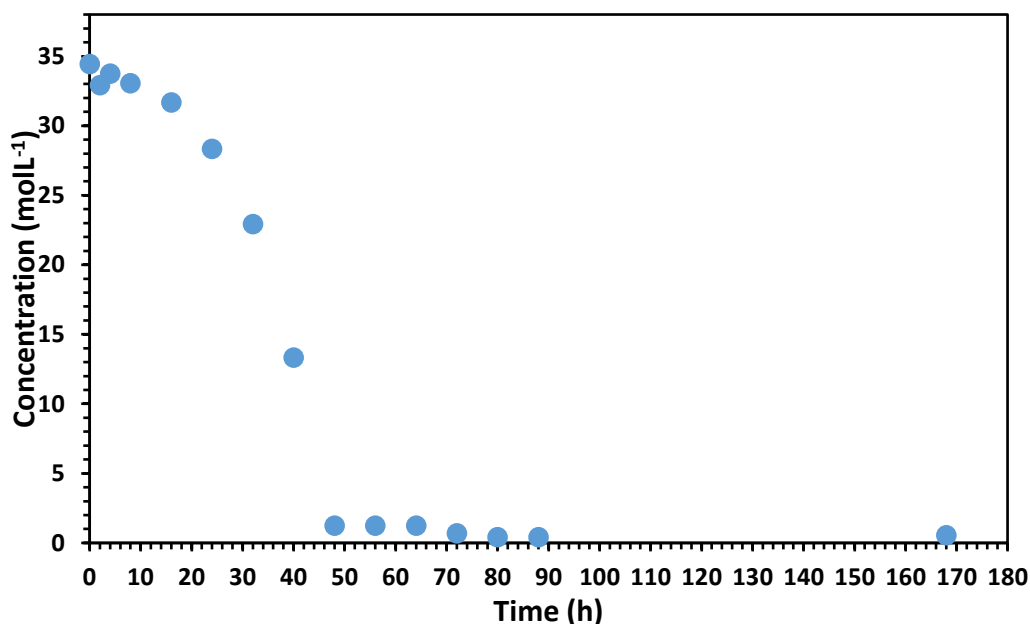


Figure 4.2: Fe²⁺ iron concentration of *L. ferrooxidans* grown on HH media with iron sulfate heptahydrate solution

4.3.1.2 *L. f* Adapted to Pyrite

L. ferrooxidans cultures grown on modified HH media with iron (Fe²⁺) sulfate were slowly adapted to grow on pyrite. Adaption was conducted through slow and subtle replacement of iron (Fe²⁺) sulfate heptahydrate solution with ground pyrite (-38 +75 μ m).

The growth cycle was monitored over 1,200 h (50 days) to capture all growth phases, with a representative growth curve shown in Figure 4.3. Overall, the growth of the culture is increased in comparison to the culture grown on iron (Fe²⁺) sulfate heptahydrate solution, however the growth phases exhibited are different. The growth curve indicates the presence of the exponential growth phase, retardation phase, stationary linear phase, and decline growth phase. The growth curve enters an acceleration phase directly after re-inoculation, until approximately 72 h (3 days) where the culture enters the first retardation phase. This retardation phase occurs until 168 h (7 days), where the culture enters a second acceleration phase, this second acceleration phase is much shorter than the first, lasting only 48 h. The exponential phase of the culture is observed from 216 h (9 days) until 456 h (19 days), where the second retardation phase and the stationary linear is observed at 552 h (23 days). The culture maintains the stationary linear phase until 1,128 h (47 days), where the decline growth phase starts.

The lack of lag phase suggests the growth conditions of the culture are favourable for *L. f* bacteria [22]. This is also supported by the length of the growth curve and the maximum cell concentration of 1.45×10^8 cells/mL.

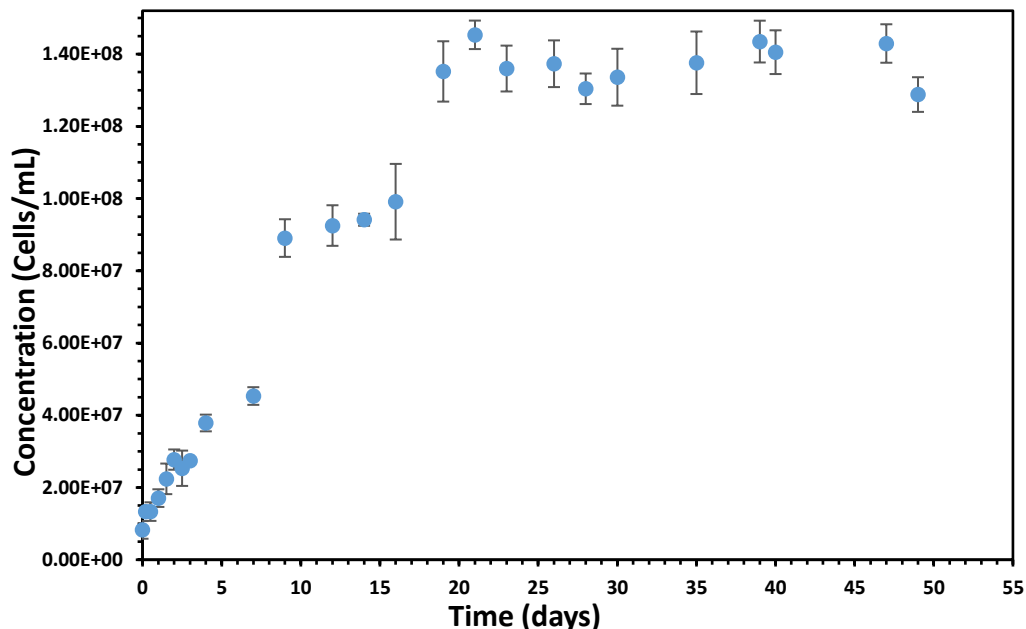


Figure 4.3: Growth curve of *L. ferrooxidans* adapted to pyrite in HH media, monitored over 55 days

4.3.1.3 *L. f* Adapted to Chalcopyrite

Adaption of *L. f* to chalcopyrite was achieved using successfully adapted *L. f* on pyrite cultures. The ground pyrite ($-38 + 75 \mu\text{m}$) was slowly replaced (5 grams per re-inoculation) with ground chalcopyrite ($-38 + 75 \mu\text{m}$). Culture growth over 1,320 h (55 days) was monitored with a representative growth curve illustrated in Figure 4.4 below.

The growth curve is considerably different to what is observed for the culture grown on pyrite. There are 8 growth phases identified over the monitoring period including multiple lag, exponential and stationary linear phases. After inoculation the culture enters a short lag phase and a short exponential phase before entering a second and longer lag phase at 48 h. This lag phase lasts 72 h before the culture enters a second exponential phase. This exponential phase is observed up to 288 h (12 days) where the growth enters a stationary linear phase until 432 h (18 days). This is followed by a longer exponential phase, retardation phase and stationary linear phase until the end of the observation time. The decrease in cell concentration observed at the end of the 55-day monitoring period is determined to be the

beginning of the decline growth phase, as the reduction in cell concentration was observed to be 3×10^7 cells/mL.

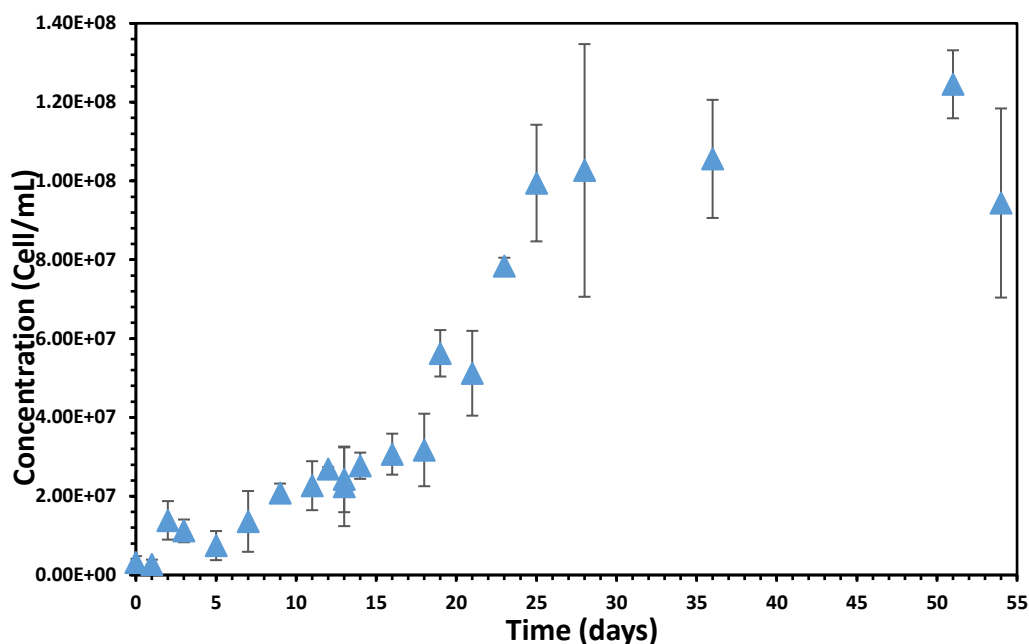


Figure 4.4: Growth curve of *L. ferrooxidans* adapted to chalcopyrite in HH media, monitored over 55 days

The presence of multiple lag phases and stationary linear phases suggest that while growth of *L. f* bacteria is sustainable on chalcopyrite, the conditions are less favourable than those produced by growth on pyrite [22]. This is attributed to a combination of readily available Fe^{2+} ions and the presence of copper/copper toxicity [23]. The maximum cell concentration observed was 1.24×10^8 cells/mL, which is considerably less than what was observed in the pyrite culture.

4.3.1.4 *L. f* Adapted to Arsenopyrite

Adaption of *L. f* to arsenopyrite was achieved through the same methods as chalcopyrite adaption described above. The adaption process for arsenopyrite cultures was longer in comparison to both pyrite and chalcopyrite. Culture growth over 1,200 h (50 days) was monitored with a representative growth curve illustrated in Figure 4.5.

The growth curve of *L. f* adapted to arsenopyrite exhibits four distinct phases, stationary linear phase, lag phase, acceleration phase and exponential phase. Interestingly, there is a rapid increase in cell concentration observed at 24 h. However, the culture then enters a short lag phase, with the cell concentration plateauing by 72 h. This stationary linear phase is observed

until approximately 168 h (7 days), where the culture enters a second lag phase. This second lag phase is slightly longer than the lag phase observed at 24 h, with the cell concentration dipping below the inoculation concentration (1.5×10^7 cell/mL) to an approximate concentration of 8.5×10^6 cells/mL. At 288 h (12 days), the culture enters a short acceleration phase, with the cell concentration recovering before entering a second stationary linear phase at 336 h (14 days). At 696 h (29 days) the culture enters a second acceleration phase, shifting into an exponential phase by 984 h (41 days). The maximum cell concentration is observed at 1,104 h (46 days) with a concentration of 7.5×10^7 cells/mL.

As the exponential phase is the last phase observed in the monitoring period, it is anticipated that the overall growth cycle of cultures grown on arsenopyrite is longer than that of both pyrite and chalcopyrite cultures. Similar to the chalcopyrite culture, the multiple lag phases present in the growth curve also suggest that the conditions produced by growth on arsenopyrite are less favourable than those of pyrite [22]. The less favourable conditions are contributed by arsenic toxicity of the cells as well as the potential lack of readily available Fe^{2+} irons for metabolic processes; as the oxidation state of iron in arsenopyrite has been previously assigned both Fe (II) and Fe (III) [24-26].

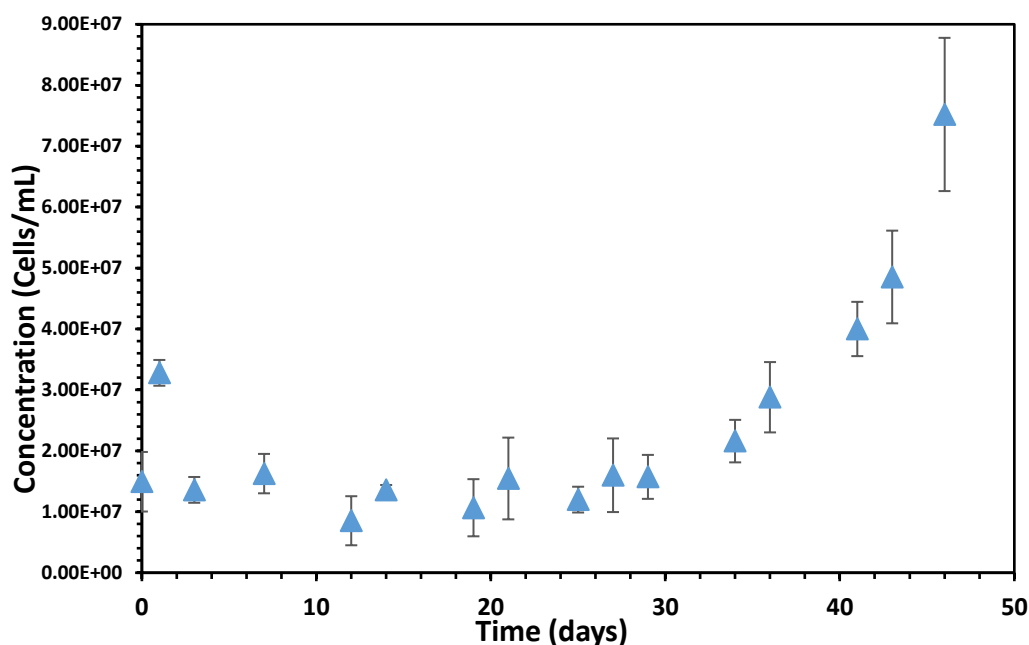


Figure 4.5: Growth curve of *L. ferrooxidans* adapted to arsenopyrite in HH media, monitored over 50 days

4.3.2 Attachment Studies

Bacterial attachment to pure mineral sections and pure mineral fractions (-38 +75 μ m) were analysed through SEM. The works by Chandraprabha, et al. [16], Chandraprabha, et al. [27], Harneit, et al. [2], Ohmura, et al. [28], Patra and Natarajan [29], and Zhu, et al. [10] have previously investigated bacterial adsorption through centrifugation and changes in planktonic cell concentration of a solution rather than interactions on the surface of the mineral. This method allows visual representation of the changing surface to include morphology, cell attachment and density as a function of time [11,30].

4.3.2.1 Mineral Sections

L. ferrooxidans attachment to mineral sections of pure pyrite and chalcopyrite was analysed at 2, 24, 48, 72 and 168 h exposures. Attachment to pyrite occurred within the first 2 h of exposure, with attachment to chalcopyrite observed at 168 h [11]. Attachment is initially observed around surface defects and pre-existing voids. Morphology changes, surface roughening and pitting was observed to increase as a function of time, with a greater effect observed on the pyrite surface than the chalcopyrite surface. These changes are contributed by both dissolution and sedimentation/precipitation on the surface. The dissolution of the mineral is a result of both bacterial and chemical leaching. A comparison to HH media control indicates that the leaching effect is increase in the presence of bacteria for both pyrite and chalcopyrite. Precipitation of media salts was observed on all samples, which was confirmed through energy dispersive analysis by X-ray (EDAX) spectroscopy. The precipitation was more prominent on the chalcopyrite, increasing with exposure time. The sedimentation observed on the pyrite surface includes the early stages of EPS/biofilm, with this first sign of EPS/biofilm observed at 48 h exposure. This structure has previously been observed in literature and has been described as a macromolecular 'honey comb' structure [31] and is shown below in Figure 4.6 (a). Interestingly, EPS/biofilm formation was not detected on the surface of chalcopyrite over the exposure times examined. However, the speckled appearance observed on the surface being attributed to cellular products such as polyphosphate (polyP) [32], shown in Figure 4.6 (b).

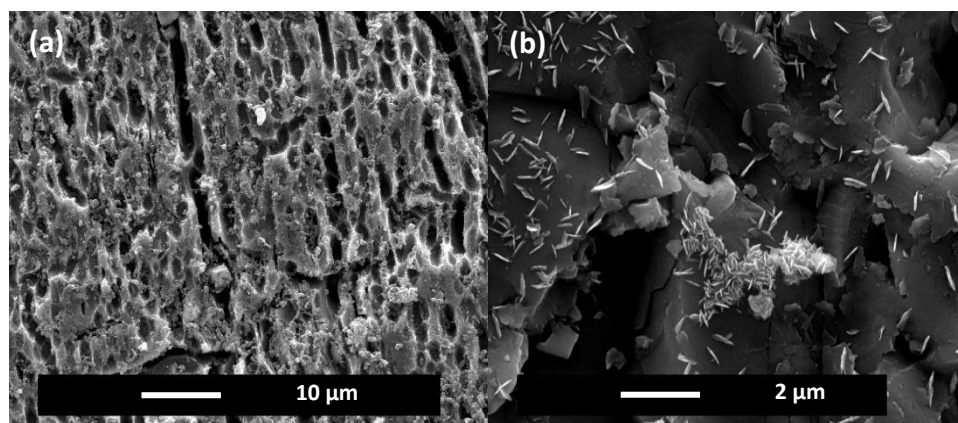


Figure 4.6: SEM images of the 'honey comb' structure observed on pyrite at 48 h (a), and PolyP and media salt precipitation observed on chalcopyrite at 24 h (b); imaged at an accelerating voltage of 20 kV, spot size of 3 (a) and 4 (b), with a magnification of 5000x (a) and 25000x (b)

4.3.2.2 Mineral Fraction -38 + 75 µm

The SEM images presented in this section are representative images from each exposure time and exposure condition. These images represent observational trends across the entire sample, with atypical observations clearly noted.

HH Media Control

Pure pyrite and chalcopyrite mineral fractions (38 – 75 µm) were exposed to HH media solution A (pH 1.8). Samples were analysed at exposure times of 0, 2, 12, 24, 36, 48, 60 and 72 hours. Particles which visually appeared to be impurities were detected in both pyrite and chalcopyrite samples, for all time frames. EDAX spectroscopy was used to determine the chemical composition of these particles. The different impurities are presented in Figure 4.7, which shows a particle with multiple faces/cleavages (Figure 4.7 a) observed in the pyrite sample; a particle with multiple thin layers (Figure 4.7 b) observed in both pyrite and chalcopyrite; a cubic particle with strong cleavages (Figure 4.7 c) observed in the chalcopyrite samples; and needle like structures (Figure 4.7 d). These particles were observed to charge more than the pyrite and chalcopyrite particles.

EDAX analysis (shown in Figure 0.1, Appendix IV) of the particle presented in Figure 4.7 (a) confirmed the presence of Fe, Na, Al, Si, P, S, O and Ca, confirming these particles are impurities. Similar to the particles represented by Figure 4.7 (b) which contains K, Si, Al, Ca, O and Mg (representative EDAX shown in Figure 0.2, Appendix IV). This suggests a clay like mineral, such as kaolinite ($\text{Al}_2(\text{Si}_2\text{O}_5)(\text{OH})$) which can have multiple impurities such as Fe, Mg,

Na, K, Ca and Ti [33]. This is also supported by the visual nature of the particles, with the multiple layers seen in previous studies of clay minerals [34,35]. The cubic structure, shown in Figure 4.7 (c), and the needle like structures, shown in Figure 4.7 (d), indicates the presence of galena. Galena is a lead sulfide (PbS) and is often found with chalcopyrite [36-38]. The EDAX spectrum (shown in Figure 0.3, Appendix IV) indicates lead and sulfur in ratios expected for galena [36,37]. Small amounts of C, O, Na, K, Fe, Cu and Ag we also detected. Visually, these particles are similar to what is expected of galena, with strong cleavages, which has been observed in previous studies [36-39]. These particles are observed with precipitates on the surface, so it is expected that the presence of C, O, Na, K and Fe arises from precipitated media salts and leached components. The silver and copper components detected are likely impurities within the galena crystal structure, as these are common impurities [36-38].

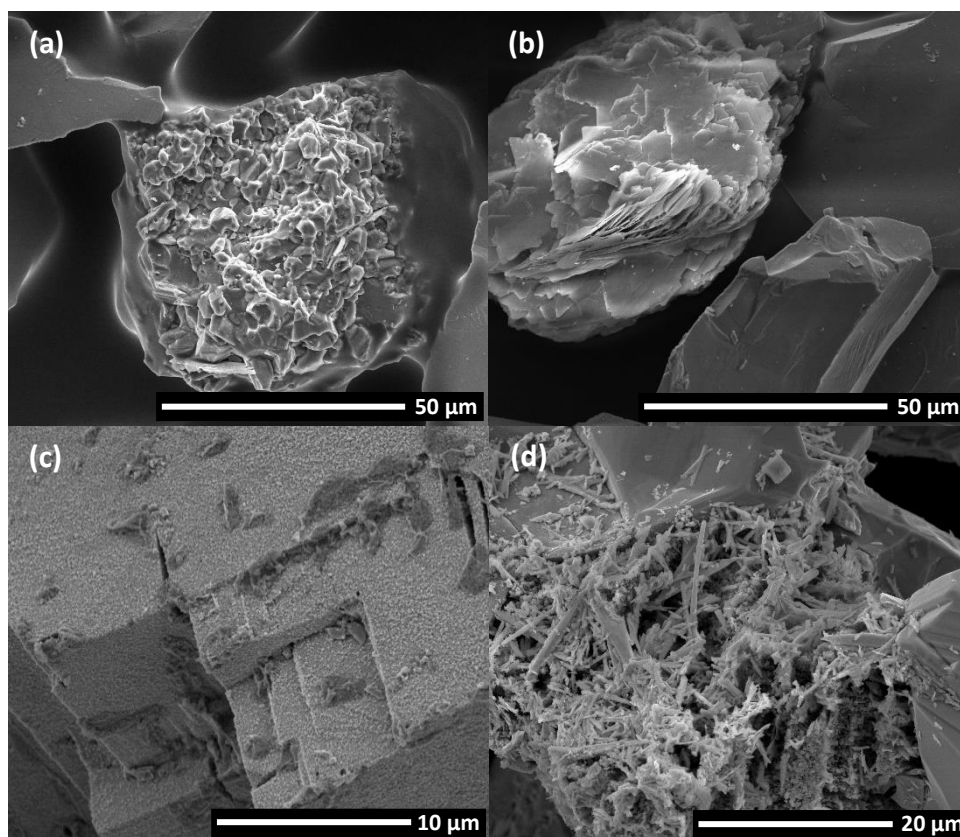


Figure 4.7: SEM images of impurities observed in the HH media controls for pyrite (a and b) and chalcopyrite (c and d); imaged at a magnification of 3000x (a and b), 12000x (c) and 6000x (d) and an accelerating voltage of 10kV (a, b and d) and 5kV (c)

The unreacted (0 h) pyrite, displayed in Figure 4.8 (a) and (b), show particles with sharp edges and smooth surfaces, with some particles exhibiting evidence of conchoidal fractures. The conchoidal fractures are expected to be an artifact of the crushing and grinding process. There

are some holes and voids present, but these are observed sporadically across particles. Small amounts of debris is observed on the surface, which EDAX confirmed as smaller mineral fragments. Although there are smaller mineral particles present, the particle size distribution appears reasonable, as shown in Table 4.2 below.

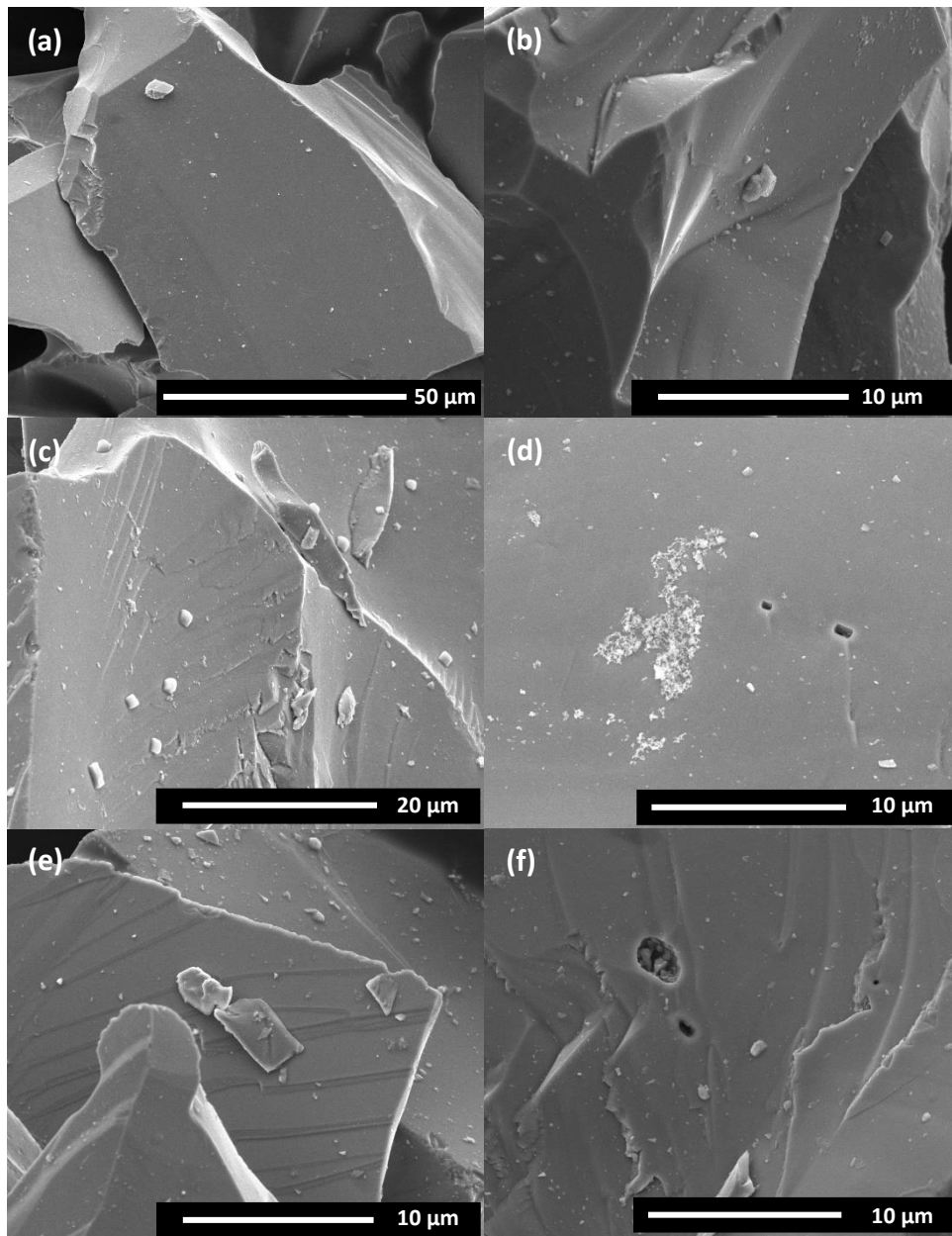


Figure 4.8: SEM image of pyrite particles exposed to HH media at exposure times 0 h (a – b), 2 h (c – d) and 12 h (e – f); imaged at a magnification of 1200x (b, d and f), 3000x (a), and 6000x (c and e), with an accelerating voltage of 10 kV

Pyrite at 2 h is shown in Figure 4.8 (e) and (d), where little difference is observed in comparison to 0 h. The debris on the surface is more dispersed than what was previously observed. It is expected that the edges round with the occurrence of leaching, therefore

leaching is not evident at 2 h, but is noticeable at 12 h. At 12 h, shown in Figure 4.8 (e) and (f), the surface of the pyrite particles still appears smooth although some debris is still observed. However, the conchoidal fracture marks are starting to soften. Surface defects, such as holes and voids, are observed infrequently and the particles of impurities are still easily distinguishable.

This is similar to what is observed for chalcopyrite at 0 h, 2 h, and 12 h, as shown by the images in Figure 4.9, however less debris is observed on the surface. The conchoidal fracture marks and cracks from the crushing and grinding processes are more prominent, shown in Figure 4.9 (d). This is expected due to the difference in physical properties. Singular crystal like structures, pictured in Figure 4.9 (c), were observed over these earlier time frames. EDAX analysis indicates these are singular crystals of chalcopyrite with an aluminium impurity.

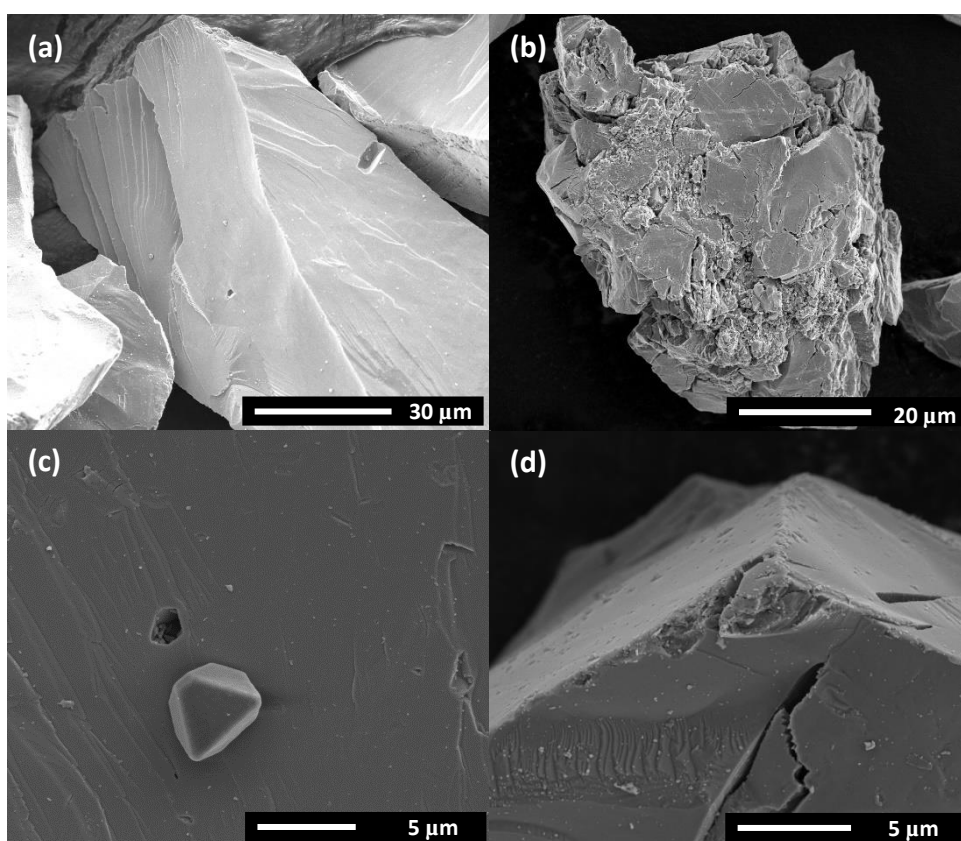


Figure 4.9: SEM image of chalcopyrite particles exposed to HH media at exposure times 0 h (a), 2 h (b – c) and 12 h (d), imaged at a magnification of 3000x (a), 4000x (b), 12000x (c) and 14000x (d), with an accelerating voltage of 5 kV

The leaching effect of pyrite continues to increase at 24 h, indicated by the increased rounding of the particle edges and the softening of the conchoidal fracture marks, as shown in Figure

4.10 (a-c). Structured debris is now observed on the surface, as shown in Figure 4.10 (b), with EDAX suggesting a combination of media salts and iron oxide. The leaching effect continues to increase at 36 h, with the frequency and size of holes and voids increasing as shown in Figure 4.10 (d). Fine, hairline fractures are also starting to appear, although more commonly observed on impurities. Debris is still observed, with the cubic debris, pictured in Figure 4.10 (e), becoming more frequent with EDAX (shown in Figure 0.4, Appendix IV) indicating media salt precipitation. Figure 4.10 (f) illustrates an atypical particle that exhibits acicular crystals within a void on the surface. EDAX analysis of these crystals indicates the presence of Fe, S, Ca, O and N.

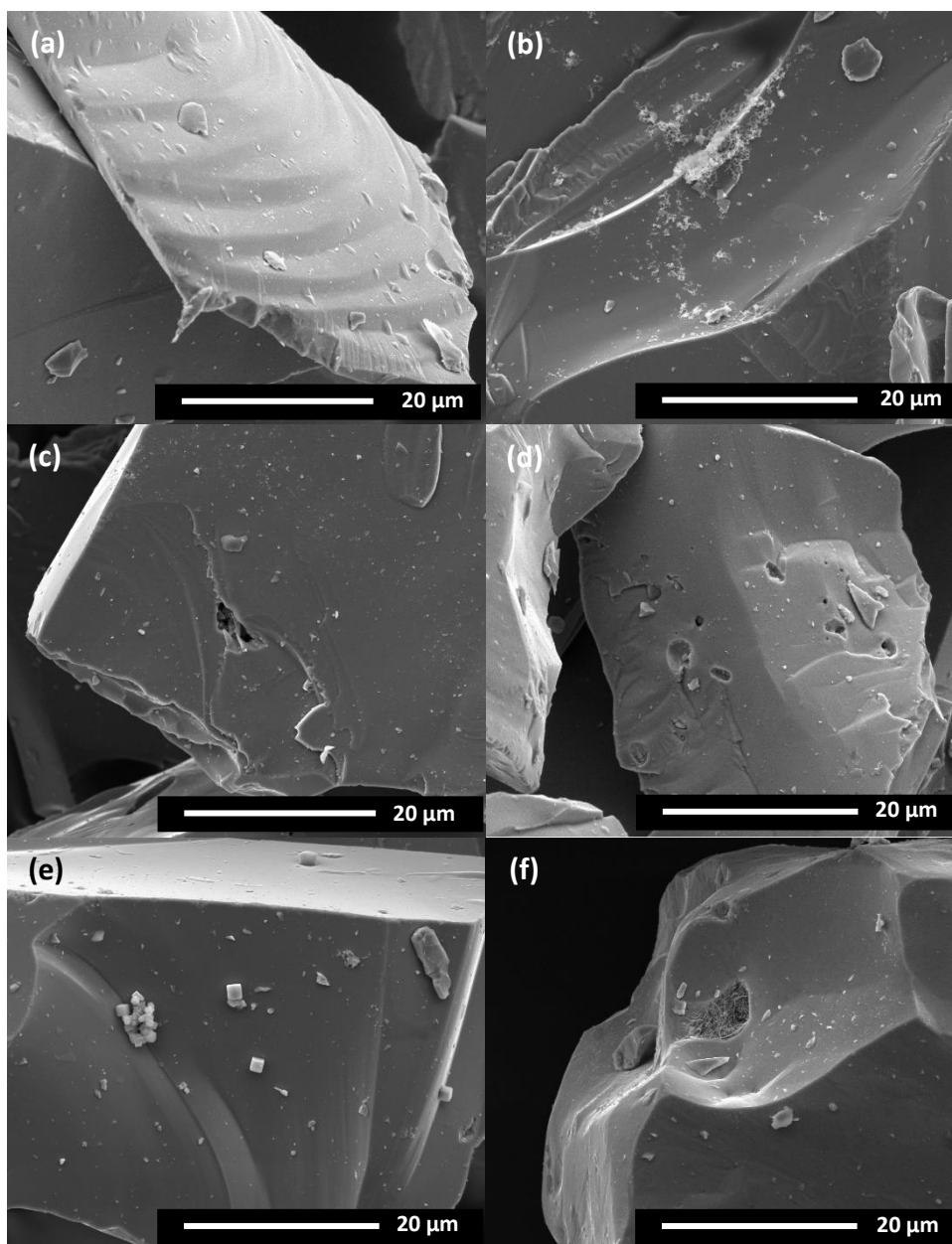


Figure 4.10: SEM image of pyrite particles exposed to HH media at exposure times 24 h (a – c) and 36 h (d – f); imaged at a magnification of 3000x (a) and 6000x (b – f), with an accelerating voltage of 10 kV

Figure 4.11 below shows chalcopyrite particles at 24 h (a and b), 36 h (e) and 48 h (d) exposure. In comparison to pyrite, the leaching effect is less evident. Cracks are present on majority of the particles, however as their edges appear sharp it is expected that the cracks originate from the crushing and grinding process. Figure 4.11 (b) shows polyhedral microcrystals as debris along the edge of a particle. This was observed sporadically throughout the sample but was not observed in the unreacted sample. EDAX indicates these polyhedral microcrystals are primarily copper sulfide with small amounts of iron. Visually, these are similar to the covellite microcrystals observed by Tezuka, et al. [40]. However, the ratio of copper to sulfur suggests chalcocite, which is a known product of chalcopyrite oxidation [41]. The presence of these microcrystals is indicative of leaching due to the removal of iron [41,42].

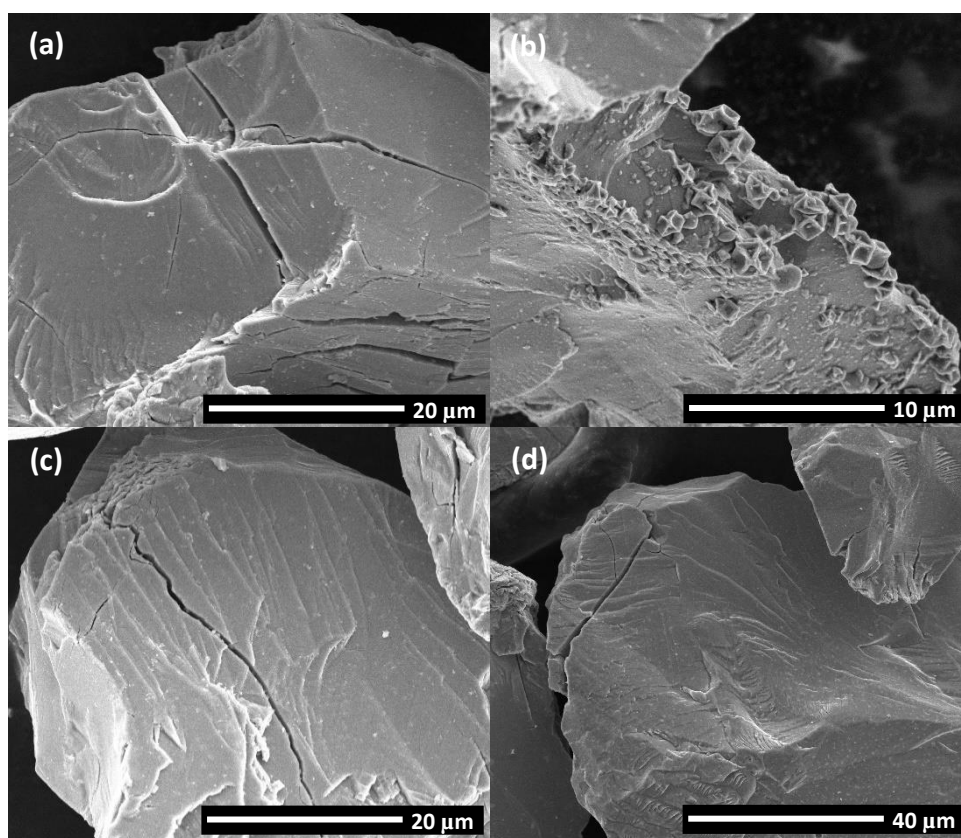


Figure 4.11: SEM image of chalcopyrite particles exposed to HH media at exposure times 24 h (a – b), 36 h (e) and 48 h (d), imaged at a magnification of 3000x (d), 6000x (a and c) and 12000x (b), with an accelerating voltage of 5 kV (b) and 10 kV (a, c and d)

Pyrite, at 48 h exposure, continues to exhibit greater leaching effects, with the conchoidal fracture marks no longer clearly distinguishable. The presence of voids has increased, with multiple voids now observed on some particles. Hairline fractures are more noticeable on both pyrite particles and impurities, with the impurities still easily distinguishable. Small fragments of impurities is observed to for some of the debris on the pyrite, as shown in Figure 4.12 (b). The features affected by leaching continue to deteriorate further between 48 h and 60 h exposure. The cubic debris is becoming larger, as shown in Figure 4.12 (d), with EDAX (representative spectra shown in Figure 0.5, Appendix IV) indicating these are small framboid structures of jarosite rather than salt precipitate [43,44].

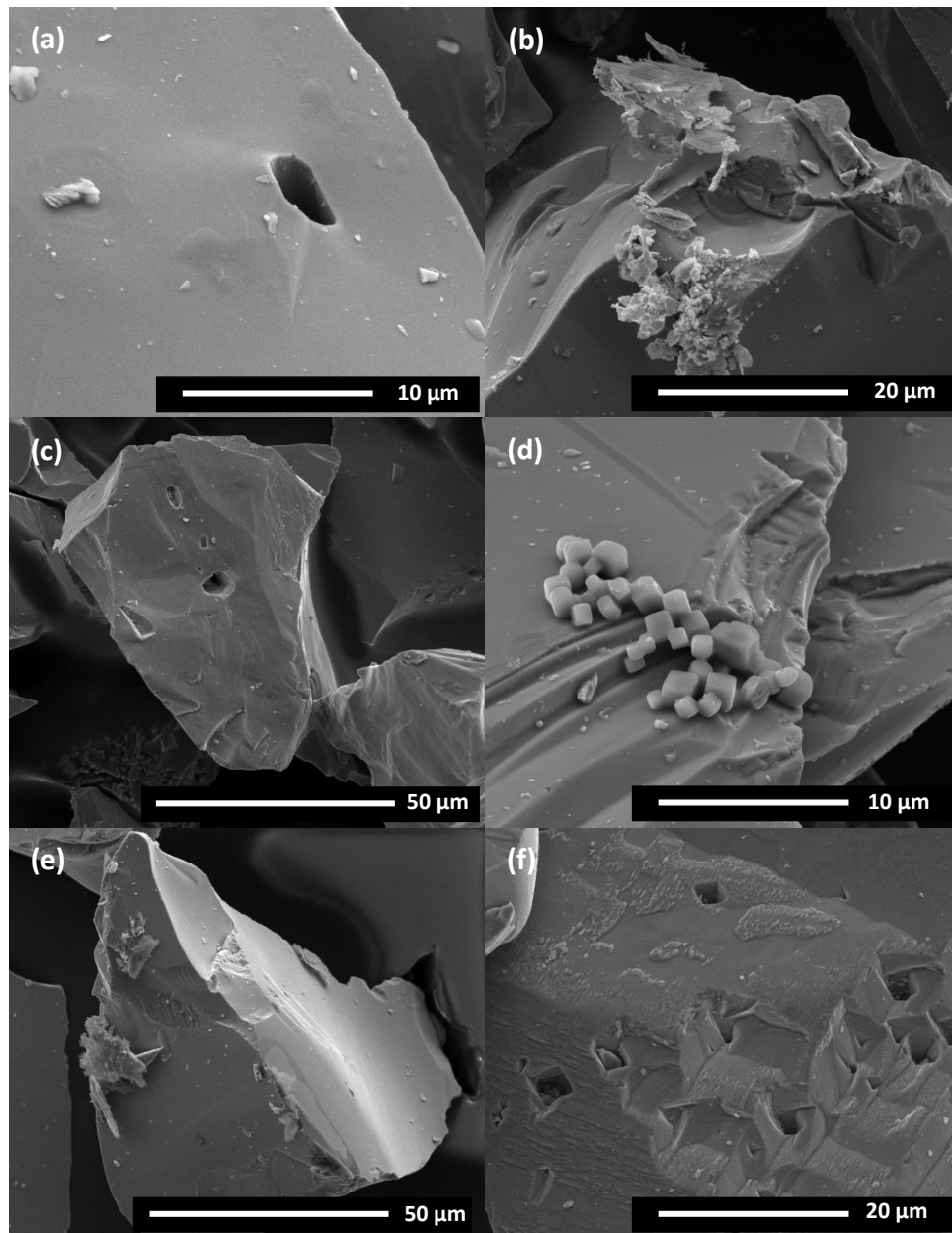


Figure 4.12: SEM image of pyrite particles exposed to HH media at exposure times 48 h (a – b), 60 h (c – d) and 72 h (e – f); imaged at a magnification of 3000x (c and e), 6000x (a, b and f) and 12000x (d), with an accelerating voltage of 10 kV

These leaching effects are observed to continue and increase at 72 h. This increase in leaching has caused cubic shaped voids to become a common occurrence, as shown in Figure 4.12 (f). At these later exposure times, the particles of impurity are still easily distinguishable, partly because they charge during analysis. This charging is a result of a change in conductivity from an increase in surface roughness or a change in the chemical composition [45].

Interestingly, minimal change is observed for the longer exposure times of chalcopyrite. Figure 4.13 below shows the chalcopyrite surface at 60 h, 72 h and 168 h exposures to HH

media. These images show a softening of the particle edges and the conchoidal fracture marks. At 60 h, Figure 4.13 (a), small amounts of debris is seen on the surface and fine hairline cracks are starting to appear on some particles. The occurrence and size of both debris and cracks is increased at both 72 h and 168 h, as shown in Figure 4.13 (b – d). The increase presence of precipitates at 168 h is expected to be the start of a passivation layer forming. This is supported by EDAX, which indicates the presence of Fe, S, Cu, Na, K, O and occasionally Pb and Ag. The passivating species of chalcopyrite have previously been identified as polysulfides, metal-deficient sulfides, jarosite and elemental sulfur [46,47].

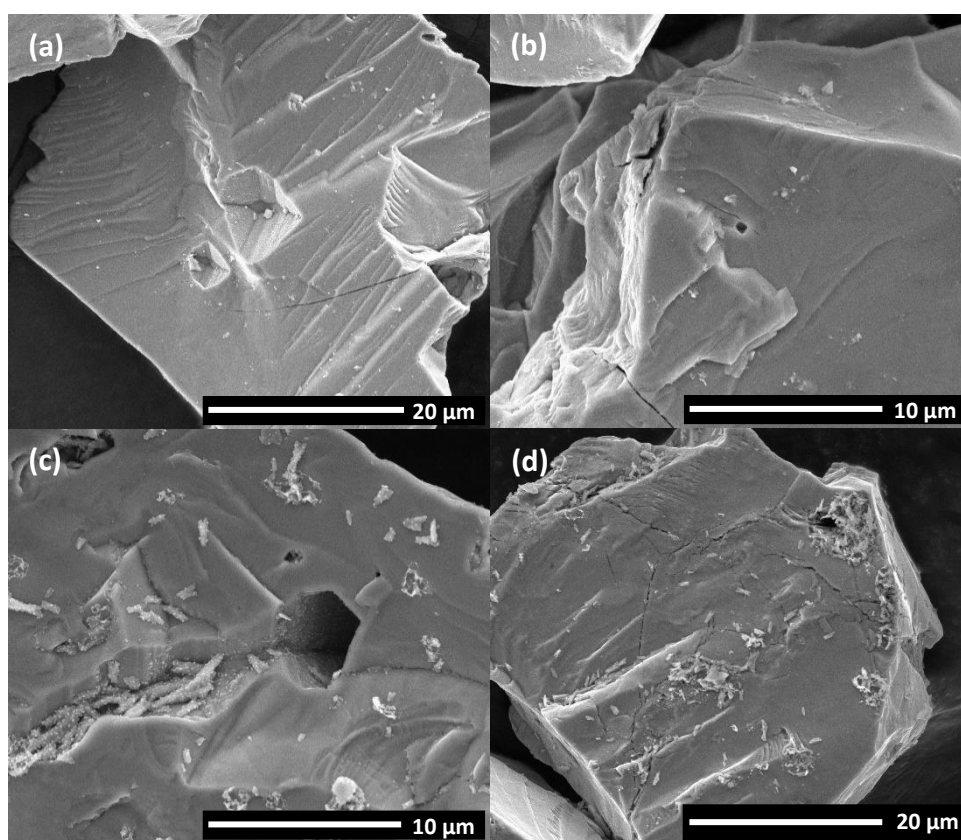


Figure 4.13: SEM image of chalcopyrite particles exposed to HH media at exposure times 60 h (a), 72 h (b) and 168 h (c and d), imaged at a magnification of 6000x (a and d) and 12000x (b and c), with an accelerating voltage of 10 kV

The particle size distribution for both pyrite and chalcopyrite over the exposure times to HH media solution A are shown below in Table 4.2. The average particle size at all exposure times is calculated to be in the +38 -75µm range. This indicates that the leaching effect of the media, over the 72 h exposure, does not impact the required flotation set up. The average particle size and standard deviation is seen to decrease as a function of time for both minerals, indicating the variation in particle size decreases with exposure time. At 72 h exposure the

average size and standard deviation for both minerals are approximately equal. This is slightly unexpected as visually the pyrite particles appear to be more affected by leaching.

Table 4.2: Calculated particle size distribution of pyrite and chalcopyrite +38 -75 μm fraction

Exposure Time (h)	Pyrite		Chalcopyrite	
	Mean (μm)	Std. Dev.	Mean (μm)	Std. Dev
0	64.88	26.01	56.11	15.32
2	56.19	17.64	62.77	17.86
12	60.11	13.84	62.51	19.51
24	59.71	23.15	65.18	14.48
36	61.41	19.72	45.91	9.31
48	58.53	15.55	52.39	10.03
60	50.61	13.97	57.31	14.00
72	47.26	8.53	47.73	9.72

4.3.2.3 *L. f* Adapted to Pyrite

Pure pyrite mineral fractions of 38 – 75 μm were exposed to *L. ferrooxidans* adapted to pyrite. Samples were analysed at exposure times of 0, 2, 12, 24, 36, 48, 60 and 72 hours, to assess the attachment and growth on the mineral surface. Impurities, discussed above in Section 4.3.2.2, were observed throughout all exposure times.

The *L. ferrooxidans* strain used is non-motile, therefore the 0 h exposure time was analysed to determine the ‘settling effect’ of cells. This can also be used to determine if the fixing and dehydration procedure disrupts cells on the mineral surface. At 0 h, Figure 4.14 (a and b), minimal debris is present on the surface, with singular cells (identified by white arrows) are present sporadically across the surface. The mineral particles exhibit no significant difference to the unreacted and control sample. At 2 h, Figure 4.14 (c – f), the particle edges start to round, indicating the presence of leaching, which is faster than the HH media control. The number of cells present also increased, with majority of cells still present as single cells and do not appear near surface defects. The debris/precipitate on the surface has increased in comparison to both the 0 h sample and the HH media control. The ‘holes’ shown in Figure 4.14 (d) are observed infrequently among particles and was not observed in the HH media

control and are expected to be bacterial induced pitting [48,49]. Due to the degree of pitting, this particle is expected to have originated from the parent culture used for inoculation.

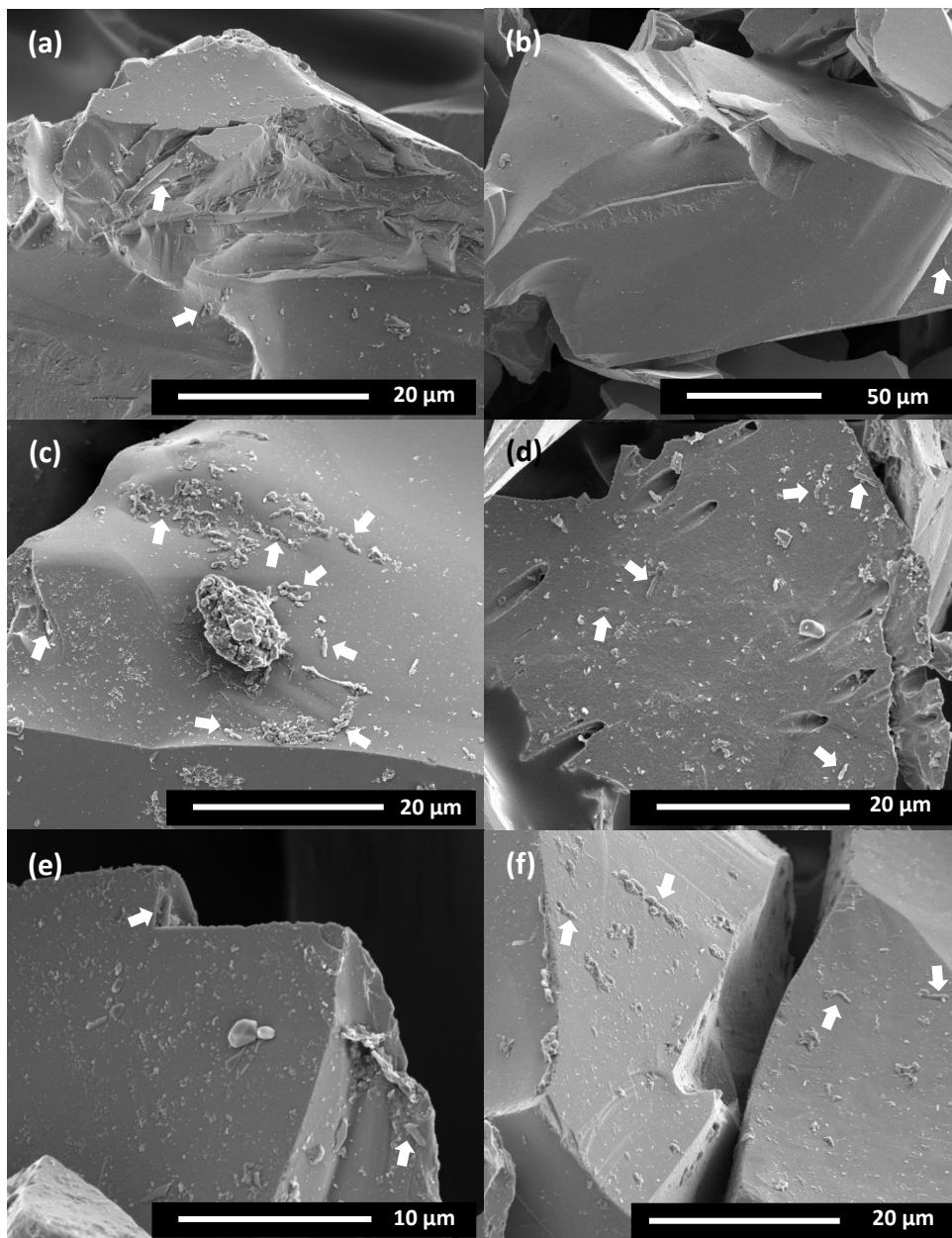


Figure 4.14: SEM image of *L. f* adjusted to pyrite exposed to pyrite particles in HH media at exposure times 0 h (a – b) and 2 h (c – f); imaged at a magnification of 6000x (a, c, d and f), 1600x (b) and 12000x (e), with an accelerating voltage of 5 kV

At 12 h exposure, the number of cells observed on the surface continues to increase along with the amount of debris. The conchoidal fracture marks and particle edges are softening further, similar to the HH media control. Some particles are starting to exhibit fine hairline fractures. These hairline fractures are shown in Figure 4.15 (c) and are indicated by the blue

arrows. These hairline cracks were first observed at 24 h exposure in the HH media control, suggesting that the presence of bacteria increases the leaching effect at earlier time frames.

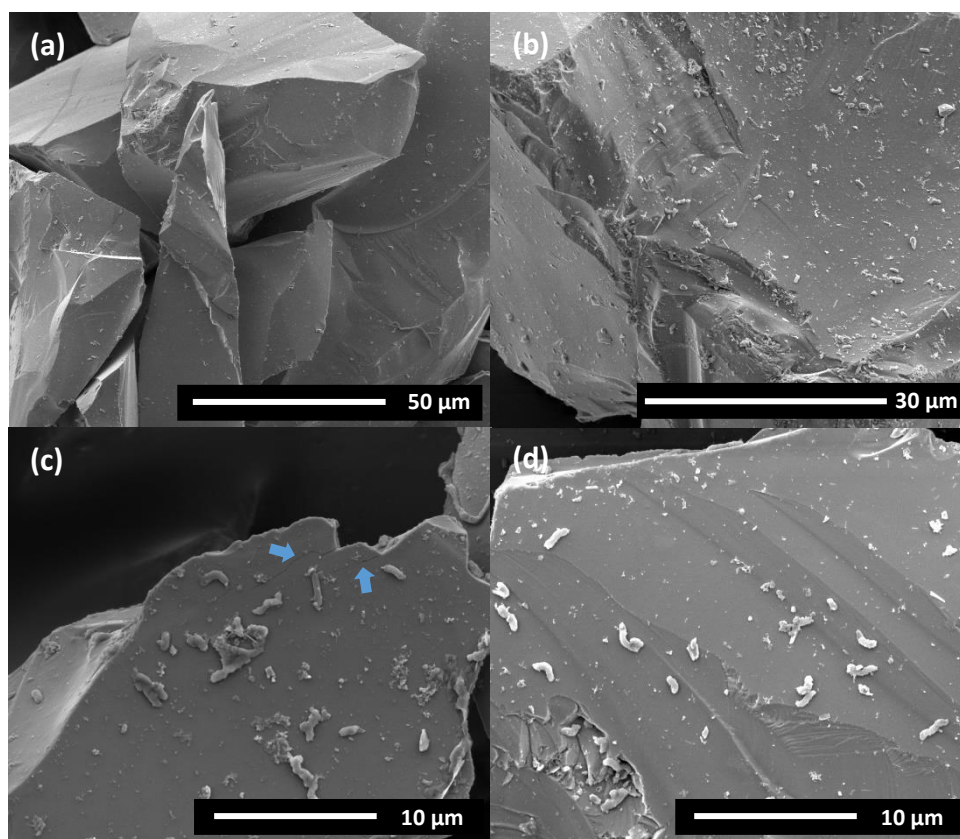


Figure 4.15: SEM image of *L. f* adjusted to pyrite exposed to pyrite particles in HH media at an exposure time of 12 h; imaged at a magnification of 2400x (a), 5000x (b), and 10000x (c and d), with an accelerating voltage of 5 kV

At 24 h exposure, the features attributed to leaching continue to increase. The hairline cracks (indicated by the blue arrows) are more distinguishable with small voids on the surface are now observed, as shown in Figure 4.16 (b) (indicated by the orange arrow). The *L. ferrooxidans* cells are starting to appear on the surface in small clusters. These clusters are indicated by the white arrows in Figure 4.16. As these cells are non-motile, this is indicative of cell division and early colonisation on the surface. At this exposure time, more debris is observed than previous time frames. This debris includes clusters of a scaffold like structure, expected to be iron oxides, such as ferrihydrite [50], are shown in Figure 4.16 (d) and indicated by the red arrow. This is a result of the bacterial presence, as this was not observed in the HH media control samples. The cubed precipitate is also observed at this exposure time. As mentioned above, this precipitate has the potential to be a framboid structure, however some of these appear as singular structures rather than a cluster as expected [43].

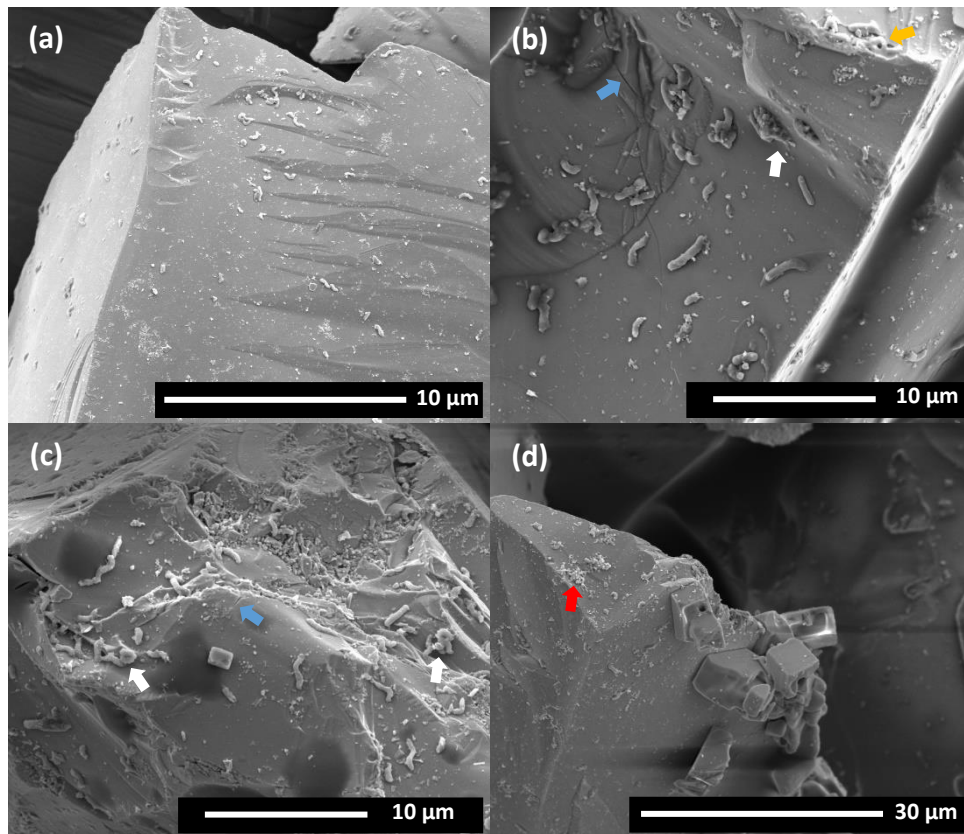


Figure 4.16: SEM image of *L. f* adjusted to pyrite exposed to pyrite particles in HH media at an exposure time of 24 h; imaged at a magnification of 5000x (a and d), and 10000x (b and c), with an accelerating voltage of 5 kV

As the exposure time increases to 36 h, debris and the size of cell clusters on the surface increases. The image in Figure 4.17 (a) shows the start of a microcolony, while the image in Figure 4.17 (b) shows a cluster of cells on the surface. A thin film like feature is present in Figure 4.17 (c). EDAX analysis of these features indicates a high amount of carbon and oxygen suggesting this is organic residue, such as EPS, created by the bacteria. These features were not observed at the earlier exposure times, therefore EPS/biofilm of *L. ferrooxidans* adjusted to pyrite forms on the surface between 24 h and 36 h. At this time frame pitting is continuing and more evident on the mineral surface, as shown in Figure 4.17 (d).

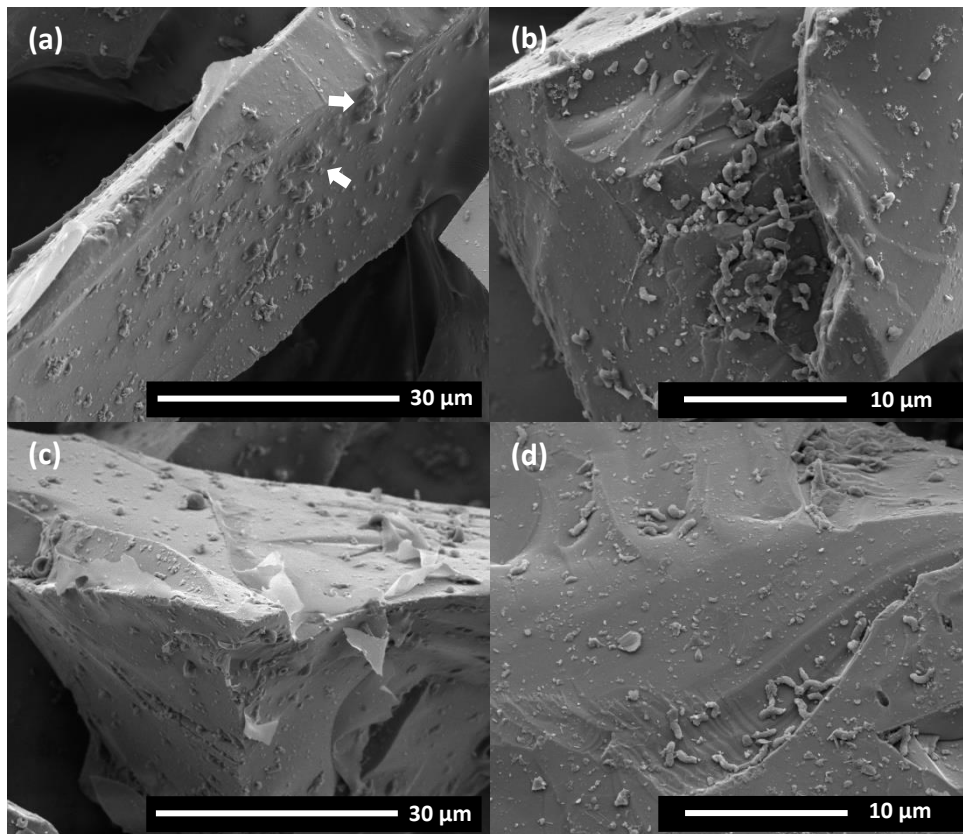


Figure 4.17: SEM image of *L. f* adjusted to pyrite exposed to pyrite particles in HH media at an exposure time of 36 h; imaged at a magnification of 5000x (a and c), and 10000x (b and d), with an accelerating voltage of 5 kV

The clustering of cells on the mineral surface increases at both 48 h and 60 h, as shown in Figure 4.18 (a). At 48 h the leaching effect on the mineral continues to increase, with the particle edges appearing coarse. Debris is still observed on the surface, with the iron oxide debris covering the surface of some particles as shown in Figure 4.18 (c). Organic residue is also observed on the surface, appearing as a transparent sheet-like object, as shown in Figure 4.18 (c).

At 60 h exposure, microcolonies are observed on the surface, as shown in Figure 4.18 (f). The frequency and size of the organic residue, determined to be EPS/biofilm, is increased in comparison to earlier exposure times. Clustering of this residue is shown in Figure 4.18 (d), with the structure shown more clearly in Figure 4.18 (e). At 60 h, the organic residue is no longer transparent. The difference observed between the organic residue present at 48 h and 60 h exposure, indicates that biofilm formation starts to occur between the two exposure times.

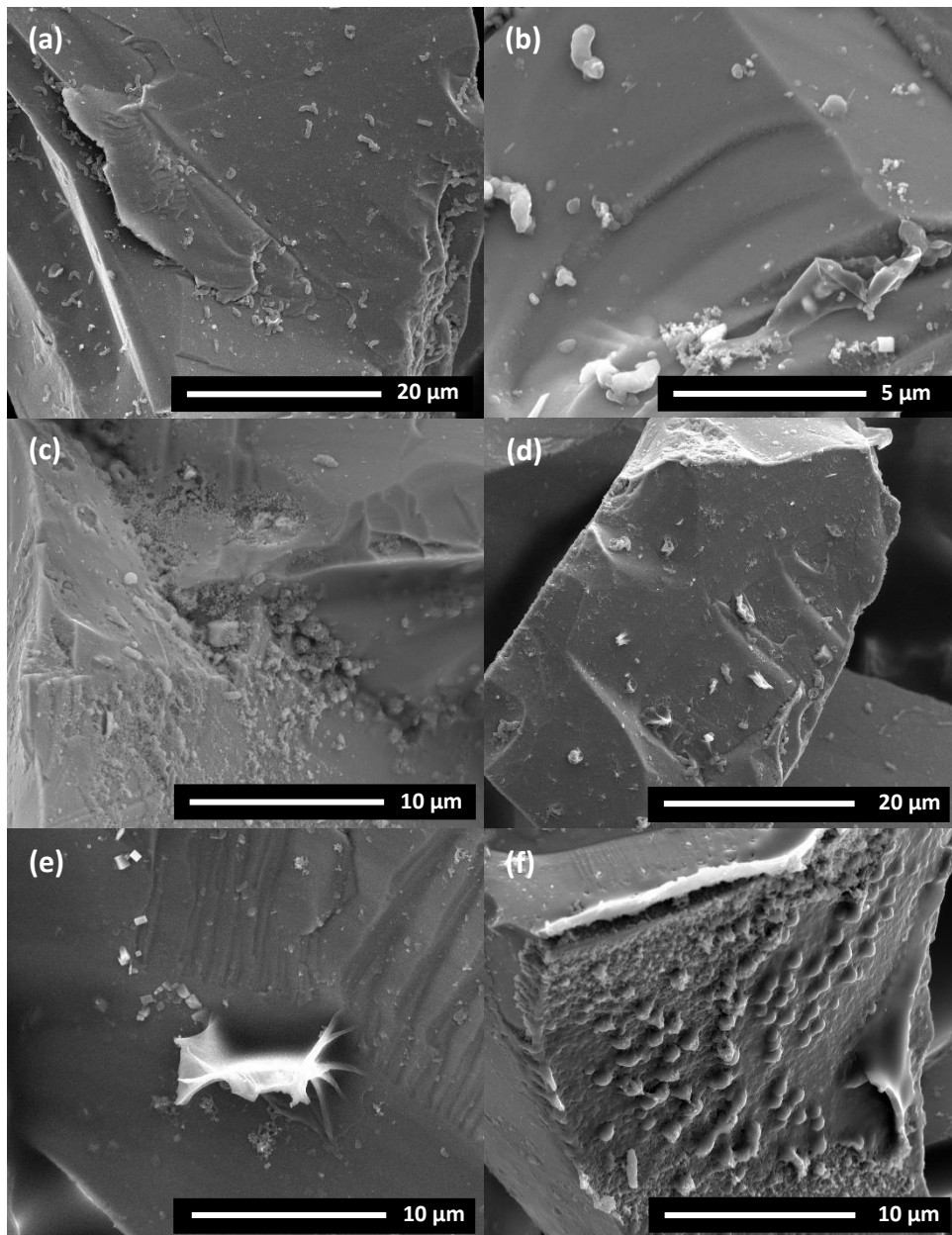


Figure 4.18: SEM image of *L. f* adjusted to pyrite exposed to pyrite particles in HH media at an exposure of 48 h (a – c) and 60 h (d – f); imaged at a magnification of 6000x (a, d and f), 12000x (c and e), and 24000x (b) with an accelerating voltage of 10 kV

At 72 h and 168 h exposure, leach pits/tunnels are present on the pyrite surface, as shown in Figure 4.19 (a) and (d). The size and presence of these leach pits increases with exposure time, with clusters of cells observed in the pits/tunnels at 168 h exposure. These leach pits are a result of bacterial oxidation and dissolution [48,49]. Biofilm is also present at both exposure times, with the structure of the biofilm changing visually between the two exposure times. The different structure, shown in Figure 4.19 (c), appears more ridged than what is observed at the earlier exposure times.

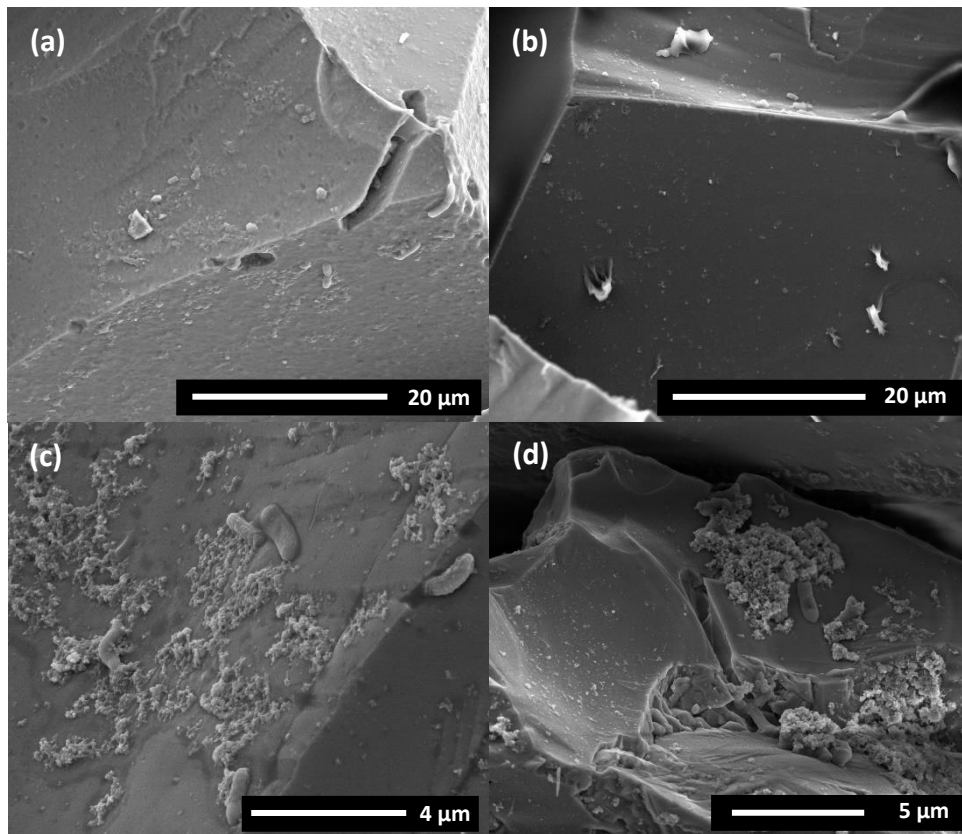


Figure 4.19: SEM image of *L. f* adjusted to pyrite exposed to pyrite particles in HH media at an exposure time of 72 h (a and b) and 168 h (c and d); imaged at a magnification of 6000x (a and b), 16000x (d) and 24000x (e) with an accelerating voltage of 10 kV (a and b) and 5 kV (c and d)

Cell attachment was also observed on the impurities, as illustrated in Figure 4.20. Attachment to the clay impurity was observed from 60 h and attachment to the second impurity was first observed at 168 h exposure. At this exposure time, leach pits were also observed on these particles of impurity. This delayed attachment to the impurities indicates a preferential attachment of *L. ferrooxidans* adjusted to pyrite. This also indicates that the window of selective attachment differs depending on the substrates involved.

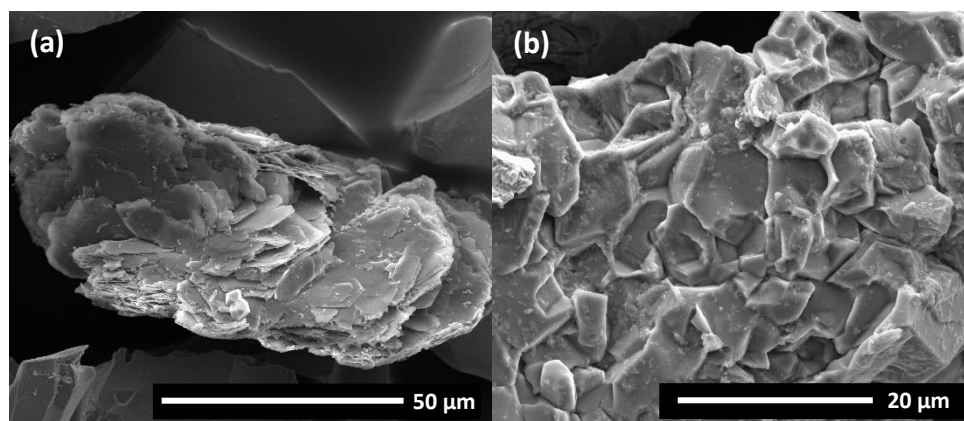


Figure 4.20: SEM image illustrating attachment of *L. f* adjusted to pyrite to impurities at 60 h (a) and leaching at 168 h (b); imaged at a magnification 3000x (a) and 6000x (b) with an accelerating voltage of 10 kV

4.3.2.4 *L. f* Adapted to Chalcopyrite

Pure pyrite mineral fractions of 38 – 75 μm were exposed to *L. ferrooxidans* adapted to pyrite. Samples were analysed at exposure times of 0, 2, 12, 24, 36, 48, 60, 72 and 168 hours, to assess the attachment and growth on the mineral surface. Impurities, discussed above in Section 4.3.2.2, were observed throughout all exposure times. Representative images of each exposure time are shown below in Figure 4.21, Figure 4.22 and Figure 4.23.

At 0 h, Figure 4.21 (a and b), there is little to no debris observed on the surface, similar to what was observed for the HH media control. Single cells, although infrequent and identified by white arrows, are present on the surface. The single cells are expected to be present due to the ‘settling’ effect of the bacteria, which was also observed in the 0 h exposure to pyrite. There is an increase in debris observed on the surface at 2 h (Figure 4.21 c and d), with single cells still sporadically distributed across the surface. The distribution of the cells does not correspond with any morphological features, such as surface defects, supporting the idea of the settling effect and suggesting cells are reversibly attached [51]. The image shown in Figure 4.21 (d) exhibits some cracks and stress marks. These are similar to what was observed in the HH media control and are considered artefacts of the crushing and grinding process. The edges of the cracks and particles at 2 h are still clearly defined and crisp, indicating that there is minimal to no leaching occurring at this exposure time. This is also consistent for the 12 h exposure, shown in Figure 4.21 (e) and (f), where the features of the mineral particles are still sharp indicating no visible effects of leaching. There is also minimal change in the occurrence of debris on the surface between 2 h and 12 h. However, the physical appearance of the debris

has changed with elongated flecks, similar to those previously assigned to polyphosphate (PolyP) precipitate [11,32], present on the mineral surface which are indicated by orange arrows. While the frequency of cells does not appear to increase, cells are starting to appear closer together especially around areas where cracks and voids are present. According to Harneit, et al. [2], this indicates selective and primary attachment of cells to the mineral surface.

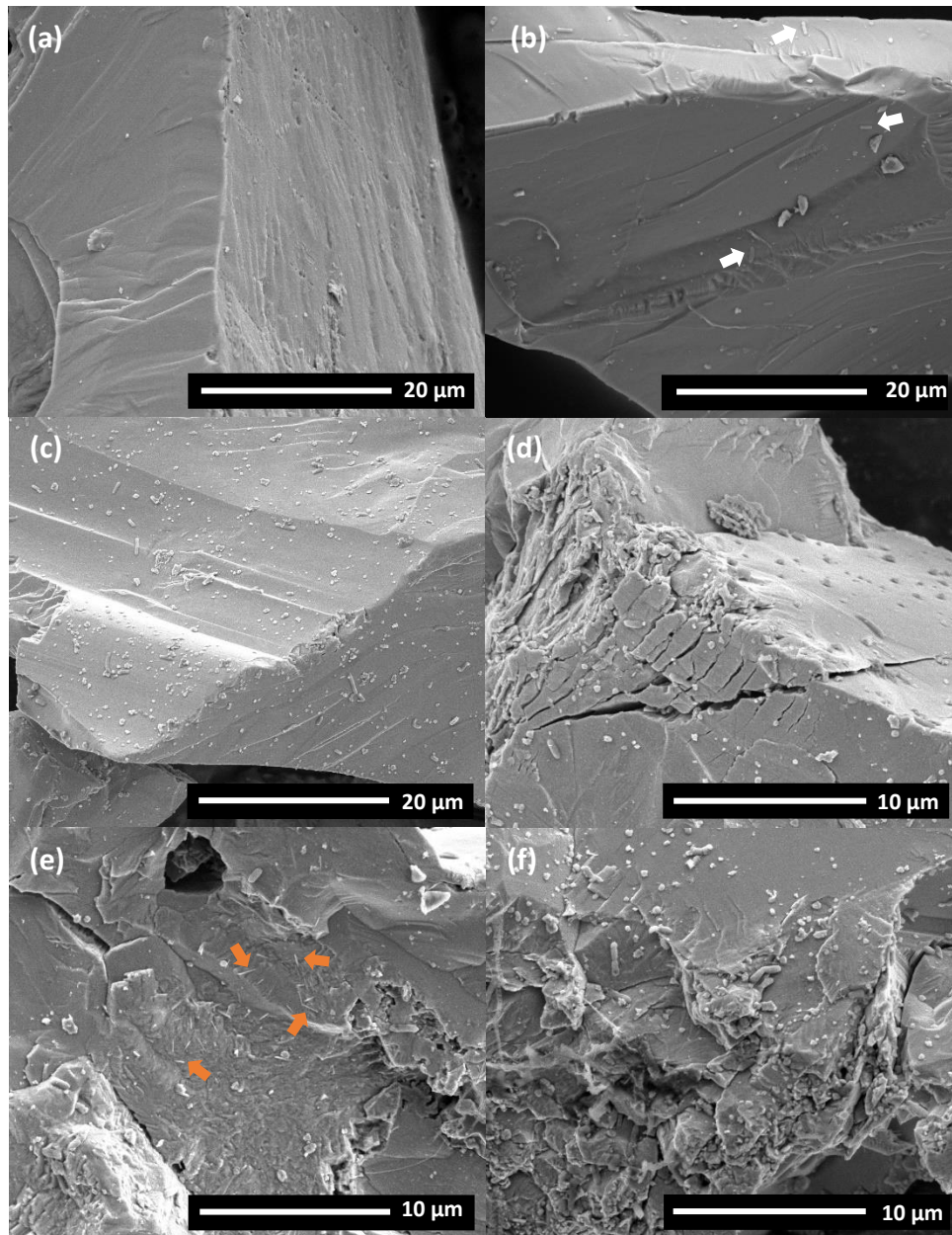


Figure 4.21: SEM image of *L. f* adjusted to chalcopyrite exposed to chalcopyrite in HH media at exposure time of 0 h (a – b), 2 h (c – d) and 12 h (e – f); imaged at a magnification of 6000x (a – c) and 12000x (d – f) with an accelerating voltage of 10 kV (a – b) and 5 kV (c – f)

Leaching of the chalcopyrite particles becomes visible at 24 h (Figure 4.22 a) with the hard crisp features, such as particle edges, start to soften and round. This softening and rounding of sharp edges was first observed at 48 h in the HH media control, indicating the presence of bacteria increases the rate of leaching. PolyP (indicated by the orange arrow) is still present, with larger particulates of debris (indicated by the blue arrow) also observed. EDAX indicates these larger particles are small fractions of mineral. These smaller particles of mineral either originate from the break down of larger particles in the sample or an error in the process of fraction size separation. As there is no evidence of extreme damage to particles, in either the *L. f* exposed and HH media samples, it is unlikely that the small (< 35µm) particles arise from leaching or bacterial action on the mineral. Cells (indicated by white arrows) are still present on the surface as single cells.

At 36 h exposure (Figure 4.22 b) cells start to appear in clusters of two or three on the surface, highlighted by the white arrow. Organic matter, confirmed by EDAX and indicated by the orange arrow, is observed in small quantities around some of the small cell clusters. The presence of this organic matter indicates that by 36 h some cells start to irreversibly bind to the mineral surface [2,52-54]. The softening and rounding of the mineral particles is still observed, with the conchoidal fracture marks still easily distinguished. This is similar to what is observed at 48 h, as shown in Figure 4.22 (c and d). Again, cells are observed closer together with the frequency of small cell clusters (2 – 3 cells) increasing, these are represented by white arrows. This increase in cell presence on the surface correlates with an increase in organic matter observed on the surface. Similar to the 36 h exposure, the organic matter is only located in small quantities around some cells, these are identified by orange arrows. However, particles of impurity exhibit greater cell attachment and an increase in organic matter, as shown in Figure 4.22 (d).

The debris and cell presence does not change significantly between 48 h and 60 h exposures. However, signs of leaching have increase with some particles exhibiting multiple voids on the surface as represented by the image in Figure 4.22 (e). This increase in surface roughness may also be contributed to by the formation of a passivation layer [42]. Interestingly, at this exposure time the organic matter is still only observed around cells, even with the increase in cells on the surface there is no evidence of biofilm formation or cell colonisation.

Likewise the 72 h exposure does not provide evidence of cell colonisation or biofilm formation. Cell colonisation may be impacted by the copper content of the mineral, with the surface becoming copper rich in the presence of a passivation layer [23,42]. The representative image, shown in Figure 4.22 (f), shows individual cells on the mineral surface which appears rough. This surface roughness is most likely a combination of leaching, formation of a passivation layer and the presence of debris which now includes iron oxide clusters (indicated by the red arrows) [50].

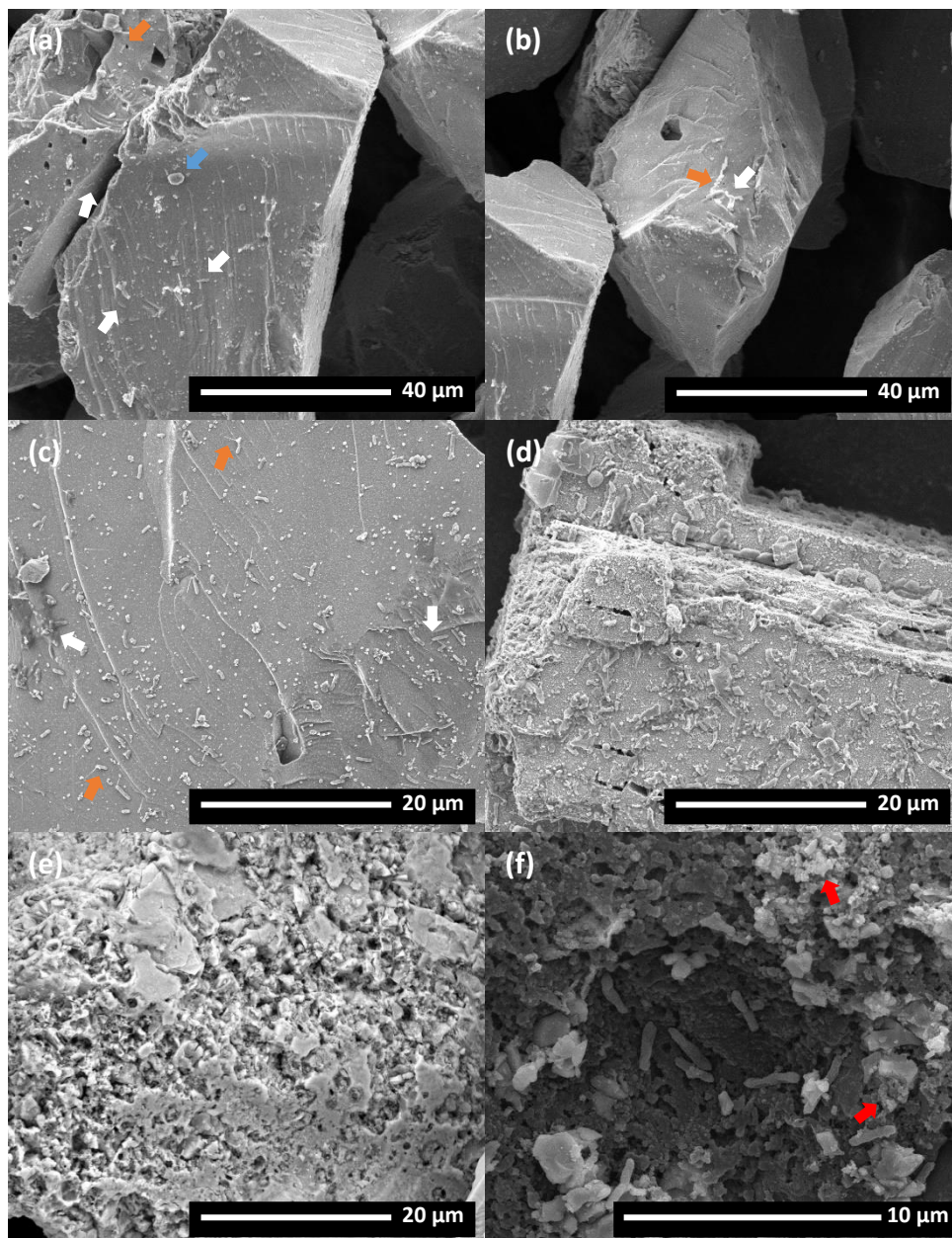


Figure 4.22: SEM image of *L. f* adjusted to chalcopyrite exposed to chalcopyrite in HH media at exposure time of 24 h (a), 36 h (b), 48 h (c and d), 60 h (e) and 72 h (f); imaged at a magnification of 3000x (a and b), 6000x (c – e) and 16000x (f) with an accelerating voltage of 10 kV (a, b, e and f) and 5 kV (c and d)

The images presented in Figure 4.23 are representations of what is observed after 168 h exposure. At 168 h the surface of the chalcopyrite mineral is almost completely covered in a combination of cells and debris, as shown in Figure 4.23 (a). The increase in cell cluster size (clusters marked by white arrows) suggests that colonisation of cells has started. This is also supported by the increase in organic matter. EDAX point analysis confirms that the web-like structures, identified by red arrows, are organic with strong C, O and N peaks. These features are presumed to be EPS or the starting structure of biofilm. Interestingly, these organic complexes coexist on the surface with iron oxide clusters (red arrows). Figure 4.23 (b) shows a chalcopyrite particle with a face covered in leach pits. While the extent of leaching can not be completely derived from this image, this does provide evidence for *L. ferrooxidans* induced leaching of chalcopyrite at 168 h as leach pits were not observed in the HH media control.

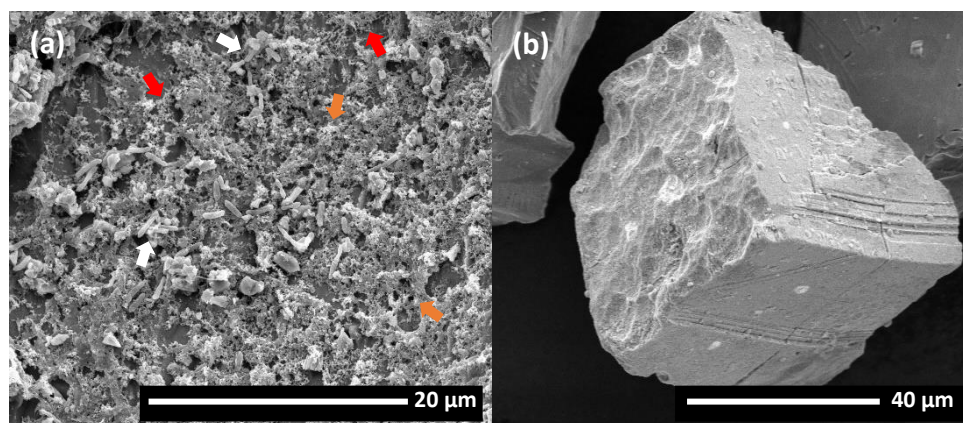


Figure 4.23: SEM image of *L. f* adjusted to chalcopyrite exposed to chalcopyrite in HH media at exposure time of 168 h; imaged at a magnification of 8000x (a) and 3000 (b) with an accelerating voltage of 10 kV

Overall, cells were observed on the surface from the point of inoculation. This is believed to be due to the 'settling' effect up until approximately 12 h where the cell(s) location is an indication of selective attachment. Organic matter, expected to be EPS, is first observed at 36 h, with no evidence of biofilm formations until 168 h. Leaching is first observed at 24 h, which is faster than that of the HH media control, and leach pits observed at 168 h. As leaching is observed without large numbers of cells present on the surface, these results indicate that *L. ferrooxidans* adjusted to chalcopyrite use an indirect non-contact mechanism as their primary source of energy production.

4.3.2.5 Comparison of attachment behaviour

Attachment of *L. ferrooxidans* to pyrite was observed to occur by 2 h exposure for both mineral section and mineral fraction, with the initial attachment occurring around surface imperfections. This result is unsurprising due to the favourable environment pyrite produces for the growth of *L. ferrooxidans*. On the other hand, the chalcopyrite fraction exhibited faster cell attachment at 12 h rather than the 168 h for the mineral section. This change in adaption behaviour could be influenced by the change in surface area to volume ration of the chalcopyrite or better adaption to the growth conditions. EPS and biofilm production was observed to be different for both pyrite and chalcopyrite, with EPS observed at earlier exposure times for both minerals. This indicates there are some changes in the growth behaviour between the different cultures of the same strain and growth conditions. This is not unexpected as the adaptability of the bacteria increases with each growth cycle. Interestingly, the culture of *L. ferrooxidans* adapted to chalcopyrite used for the fractions study was multiple generations younger than the culture used for the sections study. This is because the culture required readaptation from *L. f* adapted to pyrite due to unforeseen and unavoidable complications.

Leaching was more easily identified on the mineral fractions than mineral sections, as there were more features to assess for changes. Both pyrite and chalcopyrite exhibited leaching effects across the exposure times monitored, with the presence of bacteria increasing the leaching. Pyrite was observed to leach at earlier exposure times, both in the presence of bacteria and the media control. According to Hackl, et al. [42], this is expected due to the nature of the minerals and the HH media. Overall, the greatest difference observed was the attachment mechanism used by the different growth conditions. It was ascertained that the *L. ferrooxidans* adapted to pyrite attach via an indirect contact mechanism, while the chalcopyrite adapted *L. ferrooxidans* interact primarily by an indirect non-contact mechanism.

4.3.2.6 FTIR-ATR Analysis

FTIR-ATR was used to analyse the surface chemistry changes of pyrite and chalcopyrite over these exposure times. Parikh and Chorover [55] suggest that the surface chemistry changes, which occur with cell attachment, are detectable through ATR-FTIR. Figure 4.24 and Figure 4.25 illustrates the changes which occurred on the pyrite surface and chalcopyrite surface, respectively. The spectra presented in (a) of both figures represents unreacted pyrite and

chalcopyrite, respectively. This illustrates there are spectral differences between 700 cm^{-1} and 1300 cm^{-1} for the pyrite and the chalcopyrite prior to interaction with the HH media and *L. ferrooxidans* cells. This could be attributed to the different sulfur functional groups on the mineral surface [56]. The change from image a and image b (measured at 0 h), in both Figure 4.24 and Figure 4.25, is due to the addition of HH media and this is needed for comparisons to be drawn. When comparing pyrite exposed to HH media at 0 h and 168 h, and pyrite exposed to *L. ferrooxidans* at 168 h, there are minimal changes observed. Some variation is observed in the region of $1000\text{ cm}^{-1} - 1300\text{ cm}^{-1}$ for the pyrite exposed to *L. ferrooxidans* at 168 h, shown in Figure 4.24 (d). Transmittance in this region corresponds with C-O functionalities of polysaccharides, carbohydrates and alcohols, sulfur containing functional groups and amides [56-60]. However, these variations are on a scale which could be difficult to differentiate between changes in background. This is also the case with the chalcopyrite.

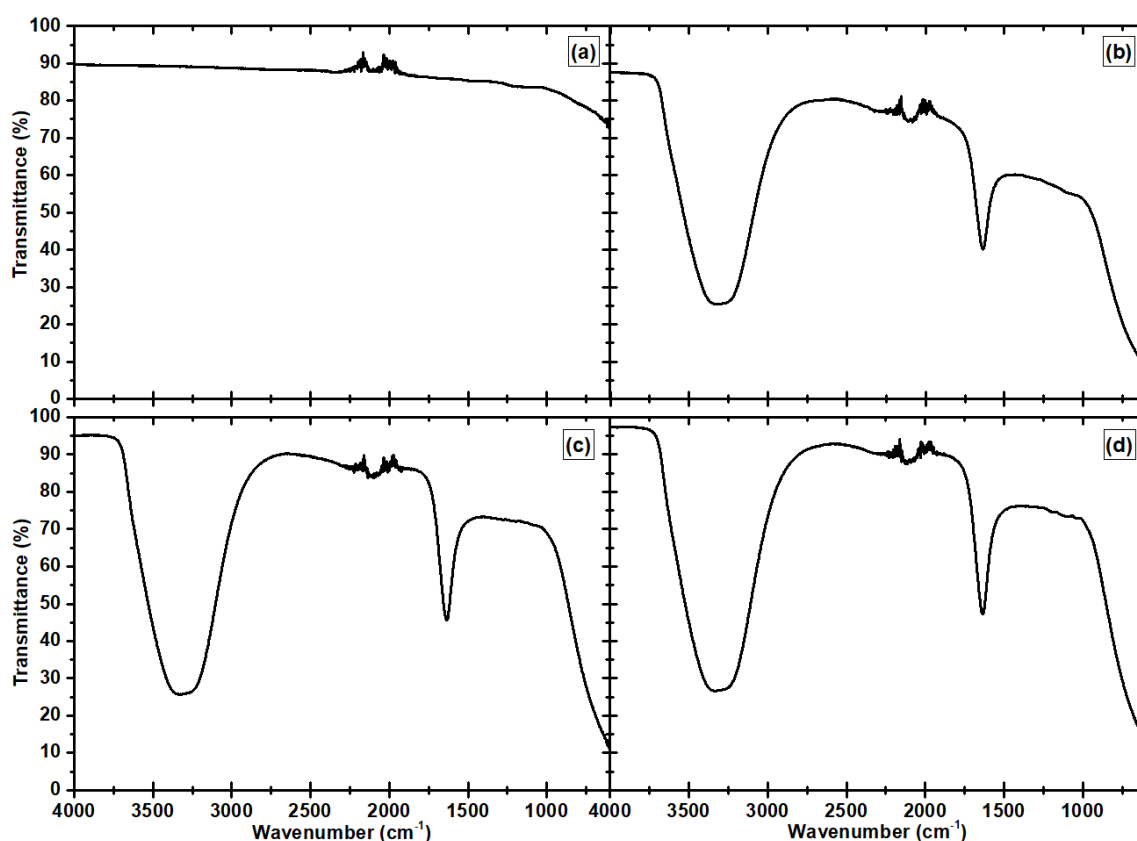


Figure 4.24: FTIR-ATR of pyrite showing unreacted pyrite (a), pyrite in HH media at 0 h (b), pyrite in HH media at 168 h (c), and pyrite exposed to *L. f* at 168 h (d)

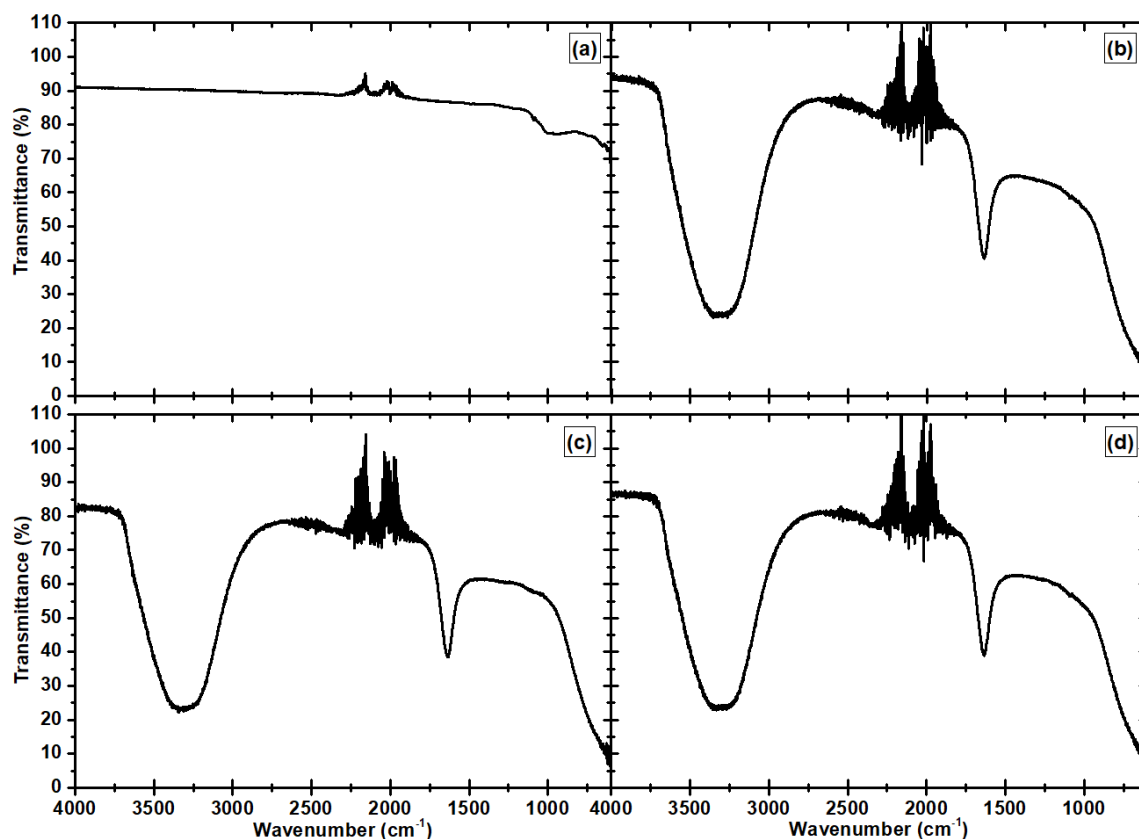


Figure 4.25: FTIR-ATR of chalcopyrite showing unreacted chalcopyrite (a), chalcopyrite in HH media at 0 h exposure (b), chalcopyrite in HH media at 168 h (c), and chalcopyrite exposed to *L. f* at 168 h (d)

As these samples were analysed as a slurry, the intensity of the peaks may have been altered through the presence of the media. However, as these samples contain bacteria and possibly EPS/biofilm, dehydrating the sample prior to the analysis will not present a true representation of surface chemistry and changes. The lack of intensity can also be related to the concentration. Therefore, these results indicate that some changes do occur, however no strong conclusions can be drawn.

4.3.3 Micro-Flotation Studies

4.3.3.1 Baseline

The recovery recorded for the baseline differential flotation tests in HH media are shown in Figure 4.26. The collector-free baseline flotation test shows adequate recovery of the chalcopyrite for all exposure times. However, it is seen that the exposure times of 36 h, 60 h and 72 h exhibit the lowest recovery out of the exposure times investigated with a recovery of 65.6%, 87.2% and 83.4%, respectively. These exposure times also present a large error value (calculated using the replicates), with an error of 27.1%, 26.4% and 26.7 %, respectively.

This suggests the reproducibility of recoveries for these exposure conditions is low at an exposure time of 36 h, 60 h and 72 h. The pyrite recovery remained under 12% for all exposure times, with the 72 h exposure resulting in the greatest recovery of 11.8%. This suggests that the HH media at a pH of approximately 1.8 supports the separation of chalcopyrite from pyrite, with the greatest separation observed at 48 h exposure.

Interestingly, the addition of the PIPX collector decreases the recovery of chalcopyrite for all exposure times except 60 h. This is expected to be due to galvanic interactions present between the pyrite and the chalcopyrite. The addition of collector also increases the recovery of pyrite. Pyrite recovery is seen to increase as a function of time, with the greatest recovery of 24.1% at 72 h. The greatest separation is observed at 60 h exposure.

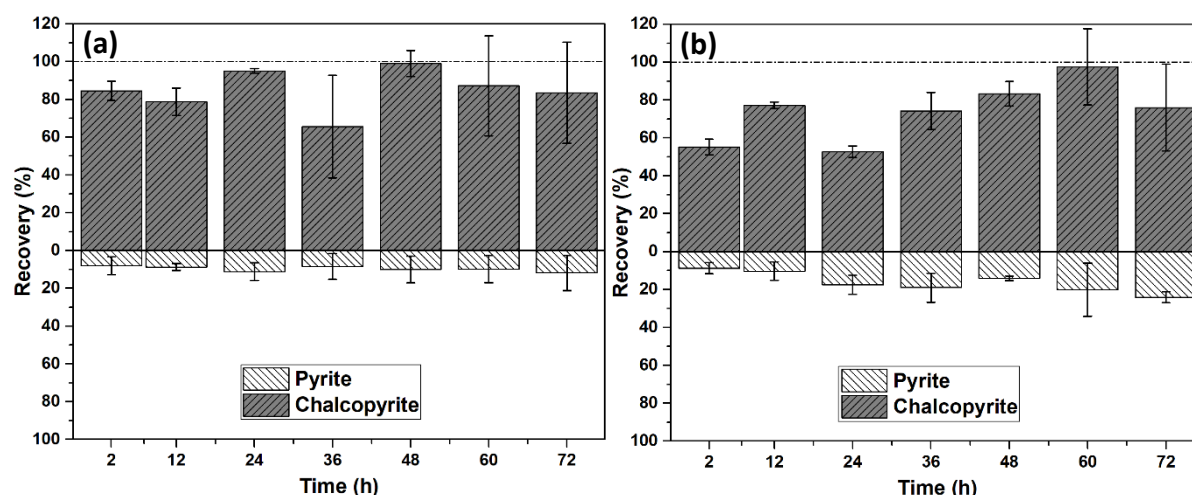


Figure 4.26: Differential flotation test recovery for HH Media control pH 1.8 as collector-free flotation tests (a); in the presence of PIPX collector (b)

Baseline differential flotation tests were also conducted in the presence of sodium bisulfite depressor, with the recoveries shown in Figure 4.27 below. These conditions were investigated so a comparison of effectiveness could be drawn between bio-flotation conditions and industrial conditions.

Both collector-free flotation tests, Figure 4.27 (a), and flotation tests conducted in the presence of PIPX collector, Figure 4.27 (b), show the same trends. Almost total suppression of pyrite is observed between 12 h and 60 h conditioning, with recovery increasing to 58.9% and 30.5%, respectively. The recovery of chalcopyrite fluctuates over all conditioning times with the greatest recovery recorded at 72 h. Conditioning times of 12 h, 24 h and 48 h resulted

in a recovery below 4%. Collector-free flotation tests at 36 h, 60 h, and 72 h resulted in a recovery of 9.4%, 11.4% and 92.4%, respectively. Interestingly, the recovery decreased with addition of PIPX collector at 60 h and 72 h to 7.2% and 61.2 %, respectively. At 36 h, the recovery increased to 18.7%. These results indicate that there is no preferential attachment of the sodium bisulfite depressor, hindering the separation of chalcopyrite from pyrite.

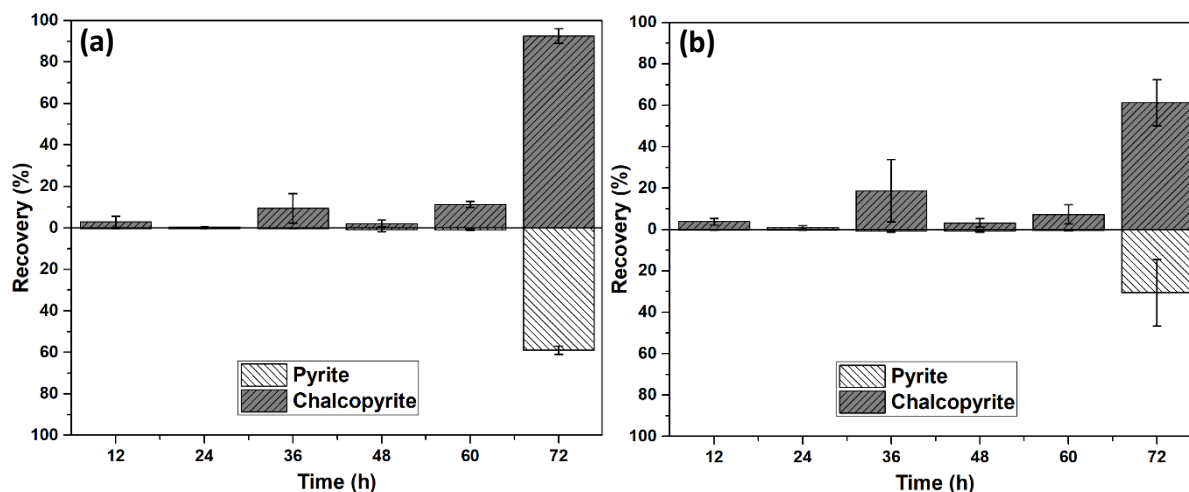


Figure 4.27: Differential flotation test recovery from HH Media control pH 1.8 in the presence of NaHSO_3 depressor as collector-free flotations flotation tests (a); in the presence of PIPX collector (b)

Although the iron hydroxides produced through the oxidation process for both pyrite and chalcopyrite are more soluble at lower pH [16], industrial processes for chalcopyrite/pyrite separation occurs basic levels (\sim pH 9) [61]. Therefore, separation of pyrite and chalcopyrite were conducted in these conditions so accurate comparisons and conclusions could be drawn. Recoveries from basic conditions (Milli-Q water, pH 9) are shown in Figure 4.28.

The results indicate that both minerals exhibit hydrophobic properties at pH 9, indicating there are iron hydroxides on the surface. While the recovery of chalcopyrite is greater than that of the pyrite, recovery of both minerals overall is observed to decrease with increasing exposure time. The lowest recovery of both minerals is obtained at 48 h and 72 h, with 12.6% and 13.6% chalcopyrite, and 0.9% and 1.2% pyrite recovered at this exposure times, respectively. The best separation is observed at 48 h, with 96.7% chalcopyrite recovered and only 9.9% pyrite.

Interestingly, the addition of PIPX collector changes the recovery trend for chalcopyrite, with the recovery increasing with exposure time. Unlike the collector-free flotation tests, the error

values calculated are more uniform across the data set indicating less variation was observed and recoveries measured from 73.5% (12 h) and 96.1% (60 h). The overall trend for pyrite is similar to the collector-free flotation tests, with recovery decreased with an increase of exposure time, from 25.3% (12 h) to 6.3% (72 h). There is an exception of 60 h exposure, with a recovery of 53.6%. It is expected that copper activation of the pyrite contributes to this increase in recovery [16,19]. This recovery impacts the separation efficiency of the 60 h exposure. While the greatest recovery of chalcopyrite, in the presence of PIPX, is 96.1% at 60 h exposure, the best separation is obtained at 72 h with a chalcopyrite recovery of 86.4% and pyrite recover of 6.3%.

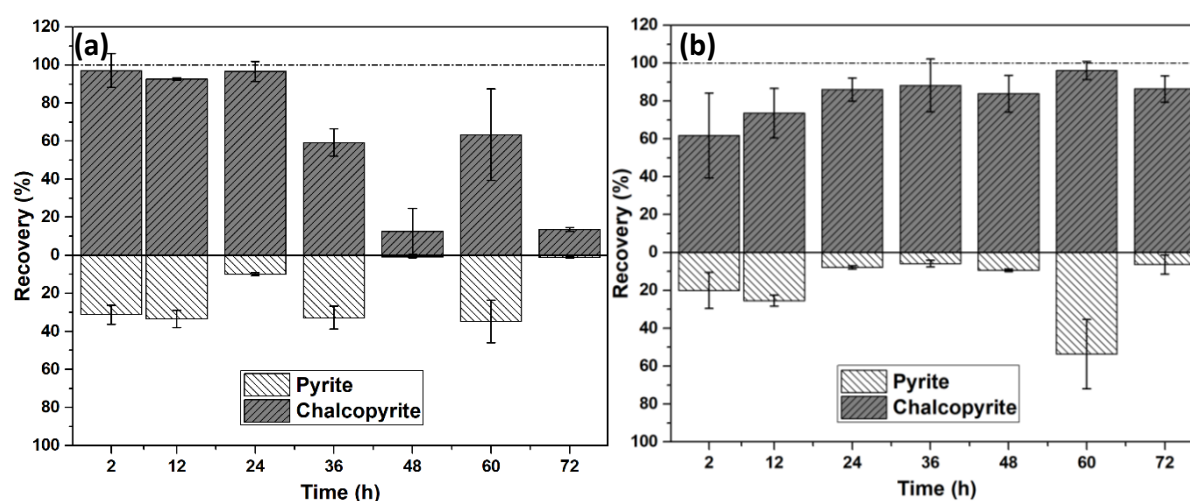


Figure 4.28: Differential flotation test recovery from Milli-Q pH 9 as collector-free flotation tests (a); in the presence of PIPX collector (b)

These baseline results differ slightly from those previously reported [11]. This variation can arise from variations within the mineral samples. With these variations taken into consideration, the results still indicate that the floatability of both minerals is greater in the HH media than M.Q pH 9 and that copper activation of pyrite does occur with the addition of PIPX.

4.3.3.2 Food Source

The recoveries of chalcopyrite and pyrite as a function of cell growth conditions are shown in Figure 4.29, Figure 4.30, Figure 4.31, and Figure 4.32. The introduction of *L. ferrooxidans* and their metabolites greatly affects the recovery and separation of chalcopyrite from pyrite. This impact does change depending on the growth condition of the cells.

The recoveries from *L. f* grown on HH media is shown in Figure 4.29. These results show that the introduction of *L. f* cells decreases the recovery of both chalcopyrite and pyrite in comparison to the baseline flotation tests. Collector-free flotations, presented in Figure 4.29 (a), shows that the recovery of chalcopyrite increases as a function of exposure time to a maximum recovery of 7% (72h); with pyrite almost being completely suppressed and a recovery between 0.2% (12 h) and 1.6% (48 h). This excludes the recovery observed at 24 h, where 49.9% chalcopyrite and 26.9% pyrite is recovered, giving the best recovery and separation. The increased recovery at this exposure time is accompanied by an increase in the error value of 21.1% and 15.5% for chalcopyrite and pyrite, respectively. This indicates that the recovery obtained at 24 h is less reproducible than the other exposure times. The only variable that is different for this exposure time than the others is the expected growth phase of the bacteria. This indicates that the growth phase of the bacteria may influence flotation results.

Addition of PIPX collector increases the recovery of both pyrite and chalcopyrite at 12 h, 48 h, and 60 h. For these exposure times, chalcopyrite was observed to increase by a minimum of 22.6% (12 h) and a maximum of 47.3% (60 h), while pyrite was increased by a minimum of 5.1% (48 h) and a maximum of 25.3% (60 h). Chalcopyrite recovery was also observed to increase at 72 h by 7.2%, while the pyrite recovery decreased by 0.1%. The increase in recovery indicates that the presence of cells did not completely inhibit the adsorption of PIPX collector. The recovery at 24 h and 36 h decreased with the PIPX addition, which was also observed in the baseline flotation tests. At these exposure times, chalcopyrite was decreased by 7.4% and 1.1%, respectively. While pyrite recovery decreased by 16.1% at 24 h and 0.7% and 36 h. The best recovery and separation for these experimental conditions is obtained at 48 h.

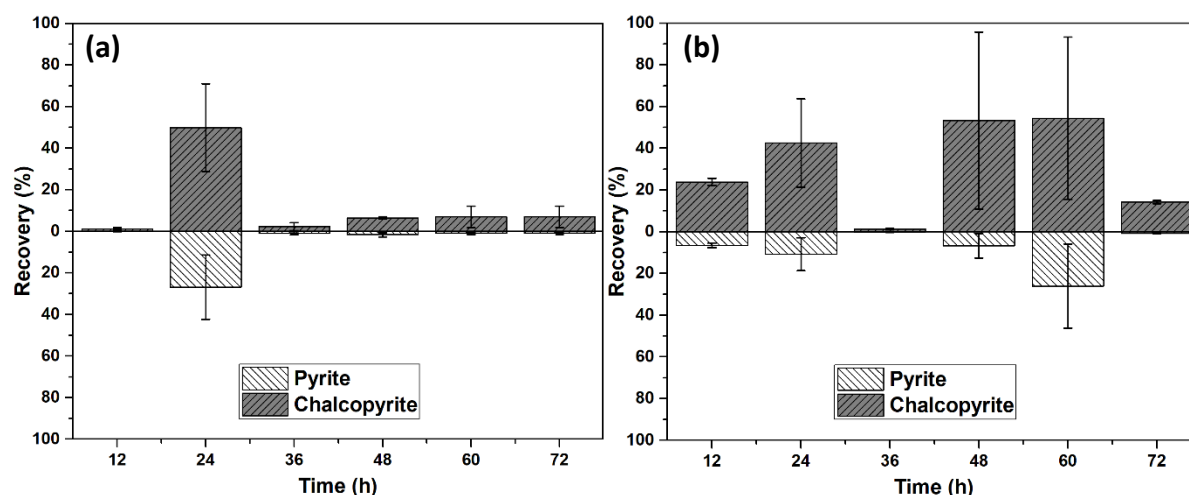


Figure 4.29: Differential flotation test recovery from *L. f* grown in HH media with iron sulfate as collector-free flotation tests (a); in the presence of PIPX collector (b)

Similar to the HH media grown cells, the addition of *L. f* adapted to pyrite decreases the recovery of both minerals in comparison to the HH media control. These flotation test recoveries are shown in Figure 4.30, with collector-free recoveries shown in (a) and recoveries in the presence of PIPX shown in (b). The recovery of both pyrite and chalcopyrite is reduced to below 0.5% for 12 h and 36 h exposures. In comparison to the *L. f* grown on HH media flotation tests recovery of chalcopyrite is increase by 1.7%, 26.4 % and 7.5% for 48 h, 60 h and 70 h, respectively; while the recovery of pyrite increased by 1.2%, 2.7% and 4.2%, respectively. However, the 24 h exposure time exhibits a 16.4% decrease of chalcopyrite recovery and a 18.6% decrease in pyrite recover. The greatest separation was achieved at 60 h, however the recovery of chalcopyrite (33.4%) indicates that the bio-flotation system is not optimised.

Addition of PIPX collector reduced the recovery of pyrite to below 1.5% for all exposure times. This suppression of pyrite over all exposure times suggests preferential attachment of the *L. f* cells to pyrite inhibits the attachment of PIPX to the mineral [11]. Upon addition of PIPX collector the chalcopyrite recovery fluctuates, with an increase in recovery observed at 12 h, 36 h and 48 h, and a decrease in recovery observed at 24 h, 60 h and 72 h. While the addition of PIPX does increase the recovery of chalcopyrite at some exposure times, the recovery does not exceed 25%. The greatest separation efficiency is observed at 24 h, however the chalcopyrite recovery is only 24.3% and therefore not economical.

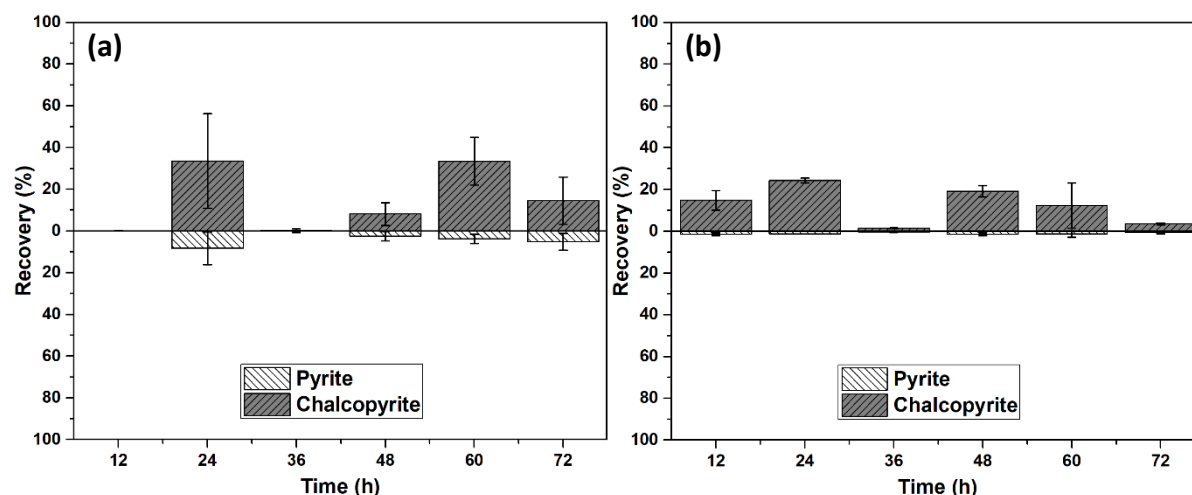


Figure 4.30: Differential flotation test recovery from *L. f* adapted to pyrite as collector-free flotation tests (a); in the presence of PIPX collector (b)

In comparison to the HH media baseline the addition of cells adapted to chalcopyrite also decreases the recovery of both minerals. However, the recovery is far greater than that observed for the HH media grown cells and the cells adapted to pyrite. The chalcopyrite recovery fluctuates between 10.2% (60h) and 54.6% (48 h) with no clear trend observed between exposure time and recovery. This is also observed with the pyrite recovery, with almost complete suppression (1.5% or less) of pyrite observed at 12 h, 24 h, 48 h, and 72 h exposure. This suppression of pyrite may be occurring due to the cells and/or their metabolite showing preferential attachment to the pyrite, as seen in the pyrite adapted cells above. Interestingly, at 60 h exposure the chalcopyrite recovery drops to 10.2% while the pyrite recovery increases to 17.2%. This means the best separation and recovery of *L. f* cells adapted to chalcopyrite occurs at 48 h.

The addition of PIPX appears to have differing effects on the minerals. Overall, the recovery of chalcopyrite is observed to decrease between 0.2% and 27.5%. On the other hand, pyrite recovery is seen to increase by 6.6%, 39.1%, 7.7%, and 9.1% for 12 h, 24 h, 48 h, and 72 h, respectively; and decrease by 4.8% (36 h) and 17.2% (60 h). The best separation and recovery, in the presence of PIPX, is observed at 36 h.

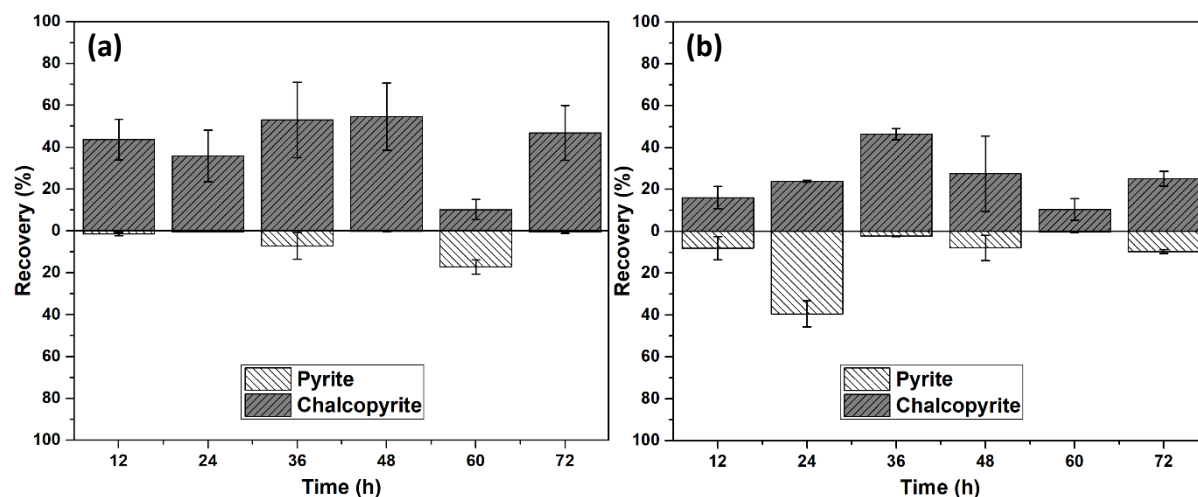


Figure 4.31: Differential flotation test recovery from *L. f* adapted to chalcopyrite as collector-free flotation tests (a); in the presence of PIPX collector (b)

Surprisingly, the *L. f* cells adapted to grow on arsenopyrite give recoveries closest to what was observed in the HH media control. These recoveries are shown in Figure 4.32. Interestingly, the pyrite is not suppressed as much as previously observed with the HH media grown cells, pyrite adapted cells and the chalcopyrite adapted cells. Likewise, the chalcopyrite recoveries are also greater than what was observed for the other growth conditions. This indicates that growth conditions of the cells can alter its effectiveness and interactions with other minerals.

Collector-free flotations tests, shown in Figure 4.32 (a), demonstrates no clear trend between chalcopyrite recovery and exposure time. The smallest chalcopyrite recovery (16%) was obtained at 12 h exposure and the greatest recovery of 88.1% was achieved at 48 h exposure. This is similar for pyrite, although overall the recovery of pyrite was considerably lower than chalcopyrite recovery; the 12 h exposure resulted in a recovery of 2.8% and the 60 h exposure recovered 68.6% of pyrite. The greatest separation was observed at 48 h, where 88.1% of chalcopyrite and only 15.2% of pyrite was recovered.

Flotation tests in the presence of PIPX collector are shown in Figure 4.32 (b), which shows an increase in pyrite recovery across exposure times and a slight decrease in chalcopyrite recovery between 12 h and 48 h but a slight increase at 60 h and 72 h. Without analysing the surface chemistry of the minerals, it is difficult to determine what has led to the increase in pyrite recovery upon the addition of PIPX without drawing assumptions. The increase in recovery may be due to copper activation of the pyrite or it may be from microbial interactions. The change in chalcopyrite recovery is also perplexing, as it indicates the PIPX is

not acting effectively on the chalcopyrite in these conditions. Due to the increase in pyrite recovery poor separation was achieved for all exposure times.

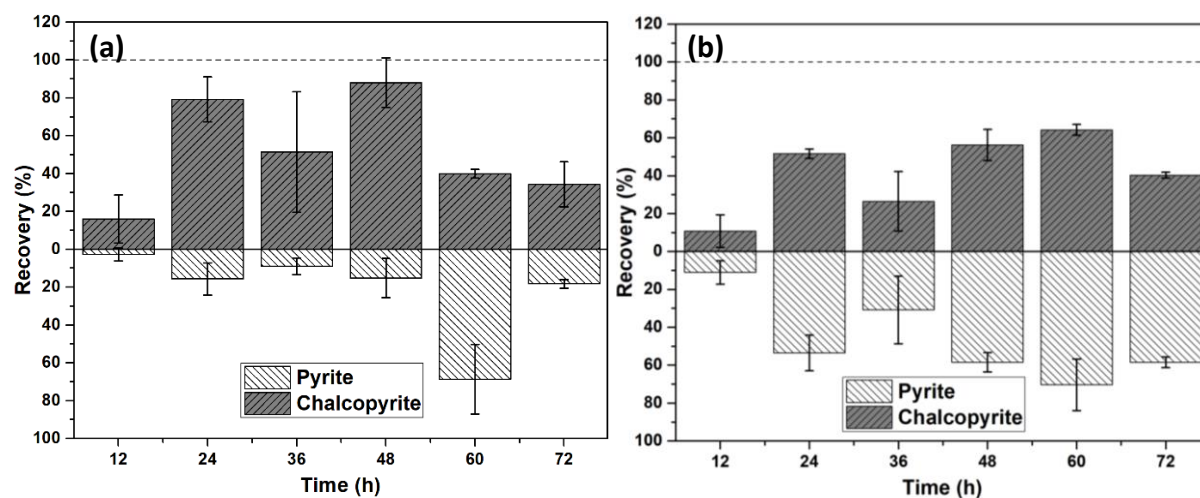


Figure 4.32: Differential flotation test recovery from *L. f* adapted to arsenopyrite as collector-free flotation tests (a); in the presence of PIPX collector (b)

Overall, addition of cells resulted in a decrease in recovery for collector-free flotation tests. Addition of PIPX was seen to increase the recovery of mineral. However, the selectiveness and effectiveness of the collector was not optimised in these systems.

4.3.3.3 Extracellular Polymeric Substance Supernatant

The EPS supernatants of *L. ferrooxidans* adapted to different growth material (pyrite, chalcopyrite and arsenopyrite) was investigated for their effectiveness in the separation of chalcopyrite from pyrite. Section 4.3.3.2 above indicates that the presence of cells in the bio-flotation system contributes to the suppression of pyrite and chalcopyrite, which is supported by studies conducted by Vilinska and Rao [15], and Chandraprabha and Natarajan [62]. However, cell metabolites may be able to alter the surface chemistry of the minerals in the absence of cells. The recoveries of the EPS supernatant flotation tests are shown in Figure 4.33, Figure 4.34 and Figure 4.35.

4.3.3.3.1 EPS Supernatant from *L. ferrooxidans* Adapted to Pyrite

The EPS supernatant of *L. ferrooxidans* adjusted to pyrite does not have the same suppressive effect on pyrite and chalcopyrite as the cells adapted to pyrite. The collector-free recovery of both minerals, shown in Figure 4.33 (a), fluctuates with exposure time. Chalcopyrite recovery is adequate (+80%) for 12 h, 48 h and 60 h exposure, with the recovery of 24 h, 36 h and 72 h

only 4.8%, 6.5% and 41.6%, respectively. The recovery of pyrite exhibits the same trend, with exposure times 12 h, 48 h, and 60 h having the highest recovery at 13.1%, 38.2% and 31.6% respectively. The 12 h exposure time returned the best separation.

Addition of PIPX increased the chalcopyrite recovery at 12 h, 24 h, 36 h and 72 h by 7.6%, 4.8%, 1.3 % and 44.3% respectively. The decrease in recovery at 48 h and 60 h was 37.1% and 16.9%, respectively. The pyrite recovery decreased between 24 h and 60 h by a minimum of 0.7% (24 h) and a maximum of 13.9% (48 h), while recovery of pyrite increased by 3.1% at 12 h and 7.8% at 72 h. Even with the addition of PIPX, the greatest recovery and separation of chalcopyrite occurred at 12 h exposure.

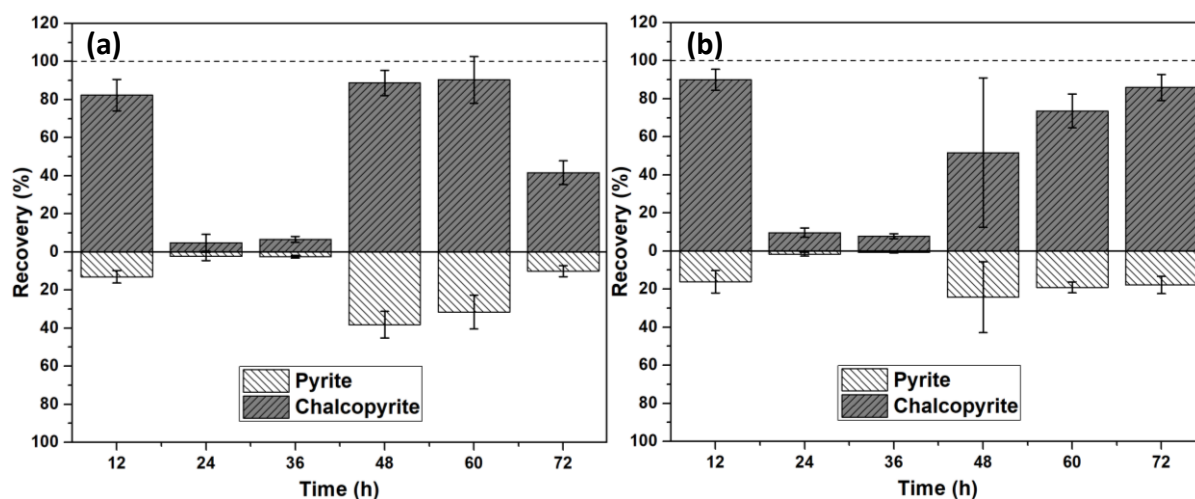


Figure 4.33: Differential flotation test recovery from EPS supernatant of *L. f* adapted to pyrite as collector-free flotation tests (a); in the presence of PIPX collector (b)

4.3.3.3.2 EPS Supernatant from *L. ferrooxidans* Adapted to Chalcopyrite

The EPS supernatant of *L. f* adapted to chalcopyrite is shown in Figure 4.34, which shows a decrease in recovery of both pyrite and chalcopyrite in comparison to the cells adapted to chalcopyrite. While the recovery of chalcopyrite is not as high as the EPS from pyrite adapted cells or the HH media baseline, pyrite recovery is suppressed to below 6.5% across the exposure times. This means the maximum recovery of 61.8%, at 48 h, is achieved with good separation. This separation, without the use of inorganic chemicals, could be a result of the oxidative stress the microbes are under when grown on chalcopyrite [23]. Addition of the PIPX collector increases the recovery of both pyrite and chalcopyrite. The increase in recovery of pyrite is seen to occur between 5.8% (36 h) and 34.6% (12h); while the recovery of chalcopyrite was between 17.2% (48 h) and 83.8% (60 h) with the exception of 36 h, which decreased by 16.5%.

Even with this increase in chalcopyrite recovery, adequate separation of chalcopyrite is achieved with the best separation occurring at 60 h exposure.

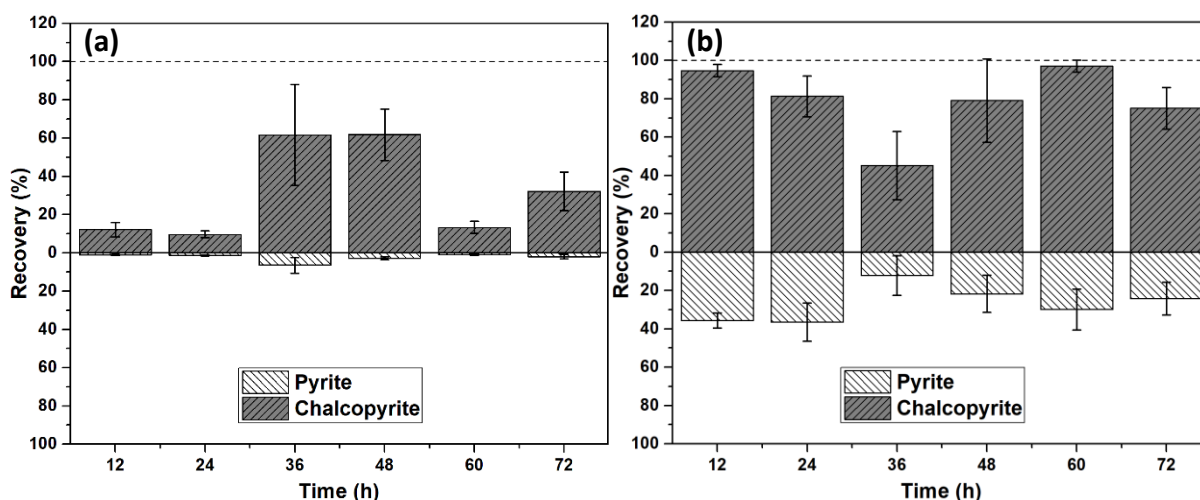


Figure 4.34: Differential flotation test recovery from EPS supernatant of *L. f* adapted to chalcopyrite as collector-free flotation tests (a); in the presence of PIPX collector

4.3.3.3.3 EPS Supernatant from *L. ferrooxidans* Adapted to Arsenopyrite

Similar flotation test results are observed for EPS supernatant of *L. f* grown on arsenopyrite shown in Figure 4.35. The collector-free flotation recoveries are similar to what was observed for the *L. f* grown on chalcopyrite, with suppression of pyrite between 12 h and 48 h. However, the pyrite recovery increases to 30.5% and 34.9% at 60 h and 72 h, respectively. This is a similar trend to what was observed for *L. f* grown on arsenopyrite. Chalcopyrite recovery is more consistent with only 12 h and 36 h exposures recording a recovery less than 58%, which is greater than what was obtained when the cells were included in the system. The greatest separation is retrieved from 24 h exposure, which recorded a chalcopyrite recovery of 66% and a pyrite recovery of 5.2%. The addition of PIPX collector increased the recovery of both minerals. In the presence of collector, the recovery of chalcopyrite is observed between 98.4% (12 h) and 83.6% (72 h), while the recovery of pyrite is between 10.7% (12h) and 41% (72 h). This high recovery of chalcopyrite gives reasonable separation over exposure times, with the best separation observed at 12 h.

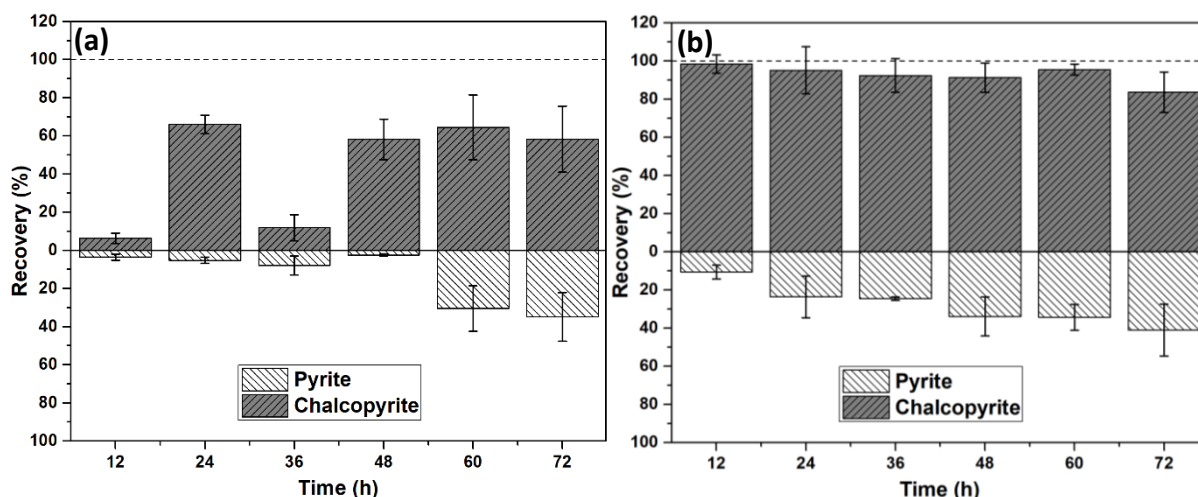


Figure 4.35: Differential flotation test recovery from EPS supernatant of *L. f* adapted to arsenopyrite as collector-free flotation tests (a); in the presence of PIPX collector

The similarities in flotation behaviour between the different EPS supernatants may indicate a similarity in the EPS composition. However, these results do signify that the EPS components have the ability to alter the mineral surface chemistry in the absence of cells.

4.4 Conclusions

Leptospirillum ferrooxidans exhibit different growth curves when adapted to grow in different growth conditions, as indicated by the different growth curves obtained. *L. f* grown in an iron sulfate solution has a rapid growth curve, achieving a maximum cell concentration of 5.6×10^6 cells/mL. Pyrite produces a stable growth environment for *L. f*, which is supported by the lack of lag phase and maximum cell concentration of 1.45×10^8 cells/mL. Although chalcopyrite can produce a culture with the same magnitude of cells, 1.24×10^8 cells/mL, the growth curve indicates the environment to be sub-optimal. This is also the case for cells adjusted to arsenopyrite, which exhibit the longest growth curve and a maximum cell concentration of only 7.5×10^7 cells/mL. This is also replicated with the attachment studies, with attachment to pyrite almost instantaneously to both mineral sections and mineral fractions. Initial attachment is observed around areas that contain imperfections such as crack and voids. Attachment of cells to chalcopyrite is observed at 12 h (mineral fractions) and 168 h (mineral sections). Interestingly, EPS and biofilm production was observed on both pyrite and chalcopyrite samples. With the earliest signs of EPS/biofilm observed at 36 h for both pyrite and chalcopyrite. It was noted that the clusters of organic matter on pyrite was observed more frequently than the organic matter observed on the chalcopyrite.

Adaption studies also identified that the presence of bacteria increases the leaching of both minerals. Pyrite exhibited more drastic changes due to the presence of bacteria, while the leaching on chalcopyrite was observed at earlier time frames. The attachment mechanism for *L. f* adaption to pyrite and chalcopyrite was also confirmed using SEM. *L. ferrooxidans* adapted to pyrite attach via an indirect contact mechanism, while the chalcopyrite adapted *L. ferrooxidans* interact primarily by an indirect non-contact mechanism. Both indirect contact and indirect non-contact mechanisms utilise metabolic products, such as EPS, to absorb and react with the mineral surface.

The difference in growth conditions, and the cells metabolic processes, directly impacts the outcome of the micro-flotation tests. The presence of cell within the bio-flotation system decreases the recovery of both minerals, even in the presence of PIPX collector. The use of only EPS supernatant indicates selective suppression of pyrite under acidic conditions. The EPS supernatant of *L. f* grown on chalcopyrite gives the best separation, closely followed by *L. f* grown on arsenopyrite. The addition of PIPX collector increases the recovery for all three EPS conditions with selected exposure times giving good separation efficiency.

4.5 References

1. Govender, Y.; Gericke, M. Extracellular polymeric substances (EPS) from bioleaching systems and its application in bioflotation. *Minerals Engineering* **2011**, *24*, 1122-1127, doi:10.1016/j.mineng.2011.02.016.
2. Harneit, K.; Göksel, A.; Kock, D.; Klock, J.-H.; Gehrke, T.; Sand, W. Adhesion to metal sulfide surfaces by cells of *Acidithiobacillus ferrooxidans*, *Acidithiobacillus thiooxidans* and *Leptospirillum ferrooxidans*. *Hydrometallurgy* **2006**, *83*, 245-254.
3. Lavallo, L.; Giaveno, A.; Pogliani, C.; Donati, E. Bioleaching of a polymetallic sulphide mineral by native strains of *Leptospirillum ferrooxidans* from Patagonia Argentina. *Process Biochem* **2008**, *43*, 445-450, doi:10.1016/j.procbio.2007.10.019.
4. Olson, G.J. Rate of Pyrite Bioleaching by *Thiobacillus ferrooxidans*: Results of an Interlaboratory Comparison. *Appl Environ Microbiol* **1991**, *57*, 642-644.
5. Sand, W.; Gehrke, T. Extracellular polymeric substances mediate bioleaching/biocorrosion via interfacial processes involving iron(III) ions and acidophilic bacteria. *Res Microbiol* **2006**, *157*, 49-56, doi:10.1016/j.resmic.2005.07.012.
6. Sand, W.; Gerke, T.; Hallmann, R.; Schippers, A. Sulfur chemistry, biofilm, and the (in) direct attack mechanism—a critical evaluation of bacterial leaching. *Applied Microbiology and Biotechnology* **1995**, *43*, 961-966.
7. Sand, W.; Rohde, K.; Sobotke, B.; Zenneck, C. Evaluation of *Leptospirillum ferrooxidans* for Leaching. *Appl Environ Microbiol* **1992**, *58*, 85-92.
8. Schippers, A.; Jozsa, P.; Sand, W. Sulfur chemistry in bacterial leaching of pyrite. *Appl Environ Microbiol* **1996**, *62*, 3424-3431.
9. Sharma, P.K.; Das, A.; Rao, K.H.; Forssberg, K.S.E. Surface characterization of *Acidithiobacillus ferrooxidans* cells grown under different conditions. *Hydrometallurgy* **2003**, *71*, 285-292, doi:10.1016/S0304-386x(03)00167-1.
10. Zhu, J.; Li, Q.; Jiao, W.; Jiang, H.; Sand, W.; Xia, J.; Liu, X.; Qin, W.; Qiu, G.; Hu, Y. Adhesion forces between cells of *Acidithiobacillus ferrooxidans*, *Acidithiobacillus thiooxidans* or *Leptospirillum ferrooxidans* and chalcopyrite. *Colloids and Surfaces B: Biointerfaces* **2012**, *94*, 95-100.
11. Bleeze, B.; Zhao, J.; Harmer, S.L. Selective Attachment of *Leptospirillum ferrooxidans* for Separation of Chalcopyrite and Pyrite through Bio-Flotation. *Minerals* **2018**, *8*, 86.
12. Pecina, E.T.; Rodriguez, M.; Castillo, P.; Diaz, V.; Orrantia, E. Effect of *Leptospirillum ferrooxidans* on the flotation kinetics of sulphide ores. *Minerals Engineering* **2009**, *22*, 462-468, doi:10.1016/j.mineng.2008.12.008.
13. Goh, S.W.; Buckley, A.N.; Lamb, R.N.; Rosenberg, R.A.; Moran, D. The oxidation states of copper and iron in mineral sulfides, and the oxides formed on initial exposure of chalcopyrite and bornite to air. *Geochimica Et Cosmochimica Acta* **2006**, *70*, 2210-2228, doi:10.1016/j.gca.2006.02.007.
14. Pearce, C.I.; Patrick, R.A.D.; Vaughan, D.J.; Henderson, C.M.B.; van der Laan, G. Copper oxidation state in chalcopyrite: Mixed Cu d9 and d10 characteristics. *Geochimica et Cosmochimica Acta* **2006**, *70*, 4635-4642, doi:10.1016/j.gca.2006.05.017.
15. Vilinska, A.; Rao, K.H. *Leptospirillum ferrooxidans*-sulfide mineral interactions with reference to bioflotation nad bioflocculation. *Transactions of Nonferrous Metals Society of China* **2008**, *18*, 1403-1409.

16. Chandraprabha, M.N.; Natarajan, K.A.; Modak, J.M. Selective separation of pyrite and chalcopyrite by biomodulation. *Colloids Surf B Biointerfaces* **2004**, *37*, 93-100, doi:10.1016/j.colsurfb.2004.06.011.
17. Kalegowda, Y.; Chan, Y.L.; Wei, D.H.; Harmer, S.L. X-PEEM, XPS and ToF-SIMS characterisation of xanthate induced chalcopyrite flotation: Effect of pulp potential. *Surf Sci* **2015**, *635*, 70-77, doi:10.1016/j.susc.2014.12.012.
18. Image Processing and Analysis in Java. Analyze Menu. Available online: <https://imagej.nih.gov/ij/docs/menus/analyze.html> (accessed on 19 March).
19. Khmeleva, T.N.; Beattie, D.A.; Georgiev, T.V.; Skinner, W.M. Surface study of the effect of sulphite ions on copper-activated pyrite pre-treated with xanthate. *Minerals Engineering* **2003**, *16*, 601-608, doi:10.1016/S0892-6875(03)00133-X.
20. Houot, R.; Duhamet, D. Floatability of Chalcopyrite in the Presence of Dialkyl-Thionocarbamate and Sodium-Sulfite. *International Journal of Mineral Processing* **1993**, *37*, 273-282, doi:10.1016/0301-7516(93)90031-5.
21. Coelho, A.A. *TOPAS Academic: General Profile and Structure Analysis Software for Powder Diffraction Data*, 2007. Available from
22. Monod, J. The Growth of Bacterial Cultures. *Annu Rev Microbiol* **1949**, *3*, 371-394, doi:10.1146/annurev.mi.03.100149.002103.
23. Orell, A.; Navarro, C.A.; Arancibia, R.; Mobarec, J.C.; Jerez, C.A. Life in blue: copper resistance mechanisms of bacteria and archaea used in industrial biomining of minerals. *Biotechnol Adv* **2010**, *28*, 839-848, doi:10.1016/j.biotechadv.2010.07.003.
24. Silva, J.C.M.; De Abreu, H.A.; Duarte, H.A. Electronic and structural properties of bulk arsenopyrite and its cleavage surfaces – a DFT study. *RSC Advances* **2015**, *5*, 2013-2023, doi:10.1039/C4RA13807D.
25. Vaughan, D.J.; Craig, J.R. *Mineral chemistry of metal sulfides*; Cambridge University Press Cambridge: 1978; Vol. 493.
26. Bindi, L.; MOËLO, Y.; Léone, P.; Suchaud, M. Stoichiometric arsenopyrite, FeAsS, from La Roche-Balue quarry, Loire-Atlantique, France: Crystal structure and mossbauer study. *The Canadian Mineralogist* **2012**, *50*, 471-479, doi:10.3749/canmin.50.2.471.
27. Chandraprabha, M.N.; Natarajan, K.A.; Somasundaran, P. Selective separation of arsenopyrite from pyrite by biomodulation in the presence of Acidithiobacillus ferrooxidans. *J Colloid Interf Sci* **2004**, *276*, 323-332, doi:10.1016/j.jcis.2004.03.047.
28. Ohmura, N.; Kitamura, K.; Saiki, H. Selective Adhesion of Thiobacillus ferrooxidans to Pyrite. *Appl Environ Microbiol* **1993**, *59*, 4044-4050.
29. Patra, P.; Natarajan, K.A. Microbially induced flocculation and flotation for separation of chalcopyrite from quartz and calcite. *International Journal of Mineral Processing* **2004**, *74*, 143-155, doi:10.1016/j.minpro.2003.10.006.
30. Chandraprabha, M.N.; Natarajan, K.A. Microbially induced mineral beneficiation. *Mineral Processing and Extractive Metallurgy Review* **2009**, *31*, 1-29.
31. Flemming, H.-C.; Neu, T.R.; Wozniak, D.J. The EPS matrix: the “house of biofilm cells”. *Journal of bacteriology* **2007**, *189*, 7945-7947.
32. Usher, K.M.; Shaw, J.A.; Kaksonen, A.H.; Saunders, M. Elemental analysis of extracellular polymeric substances and granules in chalcopyrite bioleaching microbes. *Hydrometallurgy* **2010**, *104*, 376-381, doi:10.1016/j.hydromet.2010.02.028.
33. Hudson Institute of Mineralogy. Kaolinite. Available online: <https://www.mindat.org/min-2156.html> (accessed on

34. Shahwan, T.; Zünbül, B.; Tunusoğlu, Ö.; Eroğlu, A.E. AAS, XRPD, SEM/EDS, and FTIR characterization of Zn²⁺ retention by calcite, calcite–kaolinite, and calcite–clinoptilolite minerals. *J Colloid Interf Sci* **2005**, *286*, 471-478, doi:<https://doi.org/10.1016/j.jcis.2005.02.047>.
35. Frost, R.L.; Van Der Gaast, S.J.; Zbik, M.; Kloprogge, J.T.; Paroz, G.N. Birdwood kaolinite: a highly ordered kaolinite that is difficult to intercalate—an XRD, SEM and Raman spectroscopic study. *Applied Clay Science* **2002**, *20*, 177-187, doi:[https://doi.org/10.1016/S0169-1317\(01\)00071-0](https://doi.org/10.1016/S0169-1317(01)00071-0).
36. King, H.M. Galena. Available online: <https://geology.com/minerals/galena.shtml> (accessed on
37. Nnanwube, I.A.; Onukwuli, O.D. Hydrometallurgical processing of a Nigerian galena ore in nitric acid: Characterization and dissolution kinetics. *Journal of Minerals and Materials Characterization and Engineering* **2018**, *6*, 271.
38. Vidale, M.; Craig, O.; Desset, F.; Guida, G.; Bianchetti, P.; Sidoti, G.; Mariottini, M.; Battistella, E. A Chlorite Container Found on the Surface of Shahdad (Kerman, Iran) and its Cosmetic Content. *Journal of the British Institute of Persian Studies* **2012**, *50*, 27-44, doi:10.1080/05786967.2012.11834711.
39. Budzyń, B.; Harlov, D.E.; Kozub-Budzyń, G.A.; Majka, J. Experimental constraints on the relative stabilities of the two systems monazite-(Ce)–allanite-(Ce)–fluorapatite and xenotime-(Y)–(Y, HREE)-rich epidote–(Y, HREE)-rich fluorapatite, in high Ca and Na-Ca environments under PT conditions of 200–1000 MPa and 450–750° C. *Mineralogy and Petrology* **2017**, *111*, 183-217.
40. Tezuka, K.; Sheets, W.C.; Kurihara, R.; Shan, Y.J.; Imoto, H.; Marks, T.J.; Poepelmeier, K.R. Synthesis of covellite (CuS) from the elements. *Solid State Sciences* **2007**, *9*, 95-99, doi:<https://doi.org/10.1016/j.solidstatesciences.2006.10.002>.
41. Zhu, W.; Xia, J.-l.; Yang, Y.; Nie, Z.-y.; Zheng, L.; Ma, C.-y.; Zhang, R.-y.; Peng, A.-a.; Tang, L.; Qiu, G.-z. Sulfur oxidation activities of pure and mixed thermophiles and sulfur speciation in bioleaching of chalcopyrite. *Bioresource Technology* **2011**, *102*, 3877-3882, doi:<https://doi.org/10.1016/j.biortech.2010.11.090>.
42. Hackl, R.P.; Dreisinger, D.B.; Peters, E.; King, J.A. Passivation of Chalcopyrite during Oxidative Leaching in Sulfate Media. *Hydrometallurgy* **1995**, *39*, 25-48, doi:10.1016/0304-386x(95)00023-A.
43. Wang, Q.; Morse, J.W. Pyrite formation under conditions approximating those in anoxic sediments I. Pathway and morphology. *Marine Chemistry* **1996**, *52*, 99-121, doi:[https://doi.org/10.1016/0304-4203\(95\)00082-8](https://doi.org/10.1016/0304-4203(95)00082-8).
44. Potter-McIntyre, S.; McCollom, T. Jarosite in Ancient Terrestrial Rocks: Implications for Understanding Mars Diagenesis and Habitability. In Proceedings of Lunar and Planetary Science Conference; p. 1237.
45. Abraitis, P.K.; Pattrick, R.A.D.; Vaughan, D.J. Variations in the compositional, textural and electrical properties of natural pyrite: a review. *International Journal of Mineral Processing* **2004**, *74*, 41-59, doi:10.1016/j.minpro.2003.09.002.
46. Khoshkhoo, M.; Dopson, M.; Shchukarev, A.; Sandstrom, A. Chalcopyrite leaching and bioleaching: An X-ray photoelectron spectroscopic (XPS) investigation on the nature of hindered dissolution. *Hydrometallurgy* **2014**, *149*, 220-227, doi:10.1016/j.hydromet.2014.08.012.
47. Bevilaqua, D.; Lahti-Tommila, H.; Garcia, O.; Puhakka, J.A.; Tuovinen, O.H. Bacterial and chemical leaching of chalcopyrite concentrates as affected by the redox potential

- and ferric/ferrous iron ratio at 22°C. *International Journal of Mineral Processing* **2014**, *132*, 1-7, doi:10.1016/j.minpro.2014.08.008.
48. Mitsunobu, S.; Zhu, M.; Takeichi, Y.; Ohigashi, T.; Suga, H.; Jinno, M.; Makita, H.; Sakata, M.; Ono, K.; Mase, K., et al. Direct Detection of Fe(II) in Extracellular Polymeric Substances (EPS) at the Mineral-Microbe Interface in Bacterial Pyrite Leaching. *Microbes Environ* **2016**, *31*, 63-69, doi:10.1264/jsme2.ME15137.
 49. Tributsch, H. Direct versus indirect bioleaching. *Hydrometallurgy* **2001**, *59*, 177-185, doi:[https://doi.org/10.1016/S0304-386X\(00\)00181-X](https://doi.org/10.1016/S0304-386X(00)00181-X).
 50. Chan, C.S.; Fakra, S.C.; Edwards, D.C.; Emerson, D.; Banfield, J.F. Iron oxyhydroxide mineralization on microbial extracellular polysaccharides. *Geochimica Et Cosmochimica Acta* **2009**, *73*, 3807-3818, doi:10.1016/j.gca.2009.02.036.
 51. Pinto, A.; Cerqueira, M.; Bañobre-López, M.; Pastrana, L.; Sillankorva, S. Bacteriophages for Chronic Wound Treatment: From Traditional to Novel Delivery Systems. *Viruses* **2020**, *12*, 235, doi:10.3390/v12020235.
 52. Li, Q.; Yang, B.; Zhu, J.; Jiang, H.; Li, J.; Zhang, R.; Sand, W. Comparative Analysis of Attachment to Chalcopyrite of Three Mesophilic Iron and/or Sulfur-Oxidizing Acidophiles. *Minerals* **2018**, *8*, 406, doi:10.3390/min8090406.
 53. Jiao, Y.; Cody, G.D.; Harding, A.K.; Wilmes, P.; Schrenk, M.; Wheeler, K.E.; Banfield, J.F.; Thelen, M.P. Characterization of extracellular polymeric substances from acidophilic microbial biofilms. *Appl Environ Microb* **2010**, *76*, 2916-2922, doi:10.1128/AEM.02289-09.
 54. He, Z.G.; Yang, Y.P.; Zhou, S.; Hu, Y.H.; Zhong, H. Effect of pyrite, elemental sulfur and ferrous ions on EPS production by metal sulfide bioleaching microbes. *Transactions of Nonferrous Metals Society of China* **2014**, *24*, 1171-1178, doi:10.1016/S1003-6326(14)63176-9.
 55. Parikh, S.J.; Chorover, J. ATR-FTIR Spectroscopy Reveals Bond Formation During Bacterial Adhesion to Iron Oxide. *Langmuir* **2006**, *22*, 8492-8500, doi:10.1021/la061359p.
 56. Parikh, A.; Madamwar, D. Partial characterization of extracellular polysaccharides from cyanobacteria. *Bioresource Technol* **2006**, *97*, 1822-1827, doi:10.1016/j.biortech.2005.09.008.
 57. Schmitt, J.; Flemming, H.C. FTIR-spectroscopy in microbial and material analysis. *International Biodeterioration & Biodegradation* **1998**, *41*, 1-11, doi:10.1016/S0964-8305(98)80002-4.
 58. Schmitt, J.; Nivens, D.; White, D.C.; Flemming, H.C. Changes of biofilm properties in response to sorbed substances - An FTIR-ATR study. *Water Science and Technology* **1995**, *32*, 149-155, doi:10.1016/0273-1223(96)00019-4.
 59. Li, Q.; Wang, Q.F.; Zhu, J.Y.; Zhou, S.; Gan, M.; Jiang, H.; Sand, W. Effect of Extracellular Polymeric Substances on Surface Properties and Attachment Behavior of *Acidithiobacillus ferrooxidans*. *Minerals* **2016**, *6*, 100, doi:ARTN 100.10.3390/min6040100.
 60. Wuertz, S.; Spaeth, R.; Hinderberger, A.; Griebe, T.; Flemming, H.C.; Wilderer, P.A. A new method for extraction of extracellular polymeric substances from biofilms and activated sludge suitable for direct quantification of sorbed metals. *Water Sci Technol* **2001**, *43*, 25-31.

61. Wills, B.A. *Mineral processing technology: an introduction to the practical aspects of ore treatment and mineral recovery*, 4th ed.; Pergamon Press: New South Wales, Australia, 1988.
62. Chandraprabha, M.N.; Natarajan, K.A. Surface chemical and flotation behaviour of chalcopyrite and pyrite in the presence of *Acidithiobacillus thiooxidans*. *Hydrometallurgy* **2006**, *83*, 146-152, doi:10.1016/j.hydromet.2006.03.021.

5 LEPTOSPIRILLUM FERROOXIDANS INTERACTION WITH CHALCOPYRITE, PYRITE AND HAEMATITE FOR SEPARATION THROUGH BIO-FLOTATION

5.1 Introduction

The investigation in Chapter 4, which is an expansion of previous work, indicates that the replacement of inorganic chemicals with biological alternatives is plausible. The results show the presence of bacterial cells in the flotation system increases the suppression of minerals, regardless of any selective attachment which occurs. However, it was discovered that the use of the bacterial extracellular polymeric substances (EPS) alone aided in the separation and recovery of chalcopyrite from pyrite.

The attachment behaviour of EPS supernatant extracted from *L. ferrooxidans* adjusted to chalcopyrite is investigated to understand the implications and use in bio-flotation practices. To optimise the recovery of chalcopyrite from mixed mineral systems using EPS supernatants as a bioreagent, it is imperative to understand how the supernatant interacts with the mineral surface. Surface analysis of the chalcopyrite mineral and the gangue minerals are important to understand how the EPS components interact in the system. As the beneficiation of low purity ore is becoming more of a requirement, due to the depletion of high purity ore [1], understanding the flotation behaviour of common gangue minerals is required. While pyrite and chalcopyrite are sulfide minerals, haematite is classed as an insoluble oxide [2]. Sulfide minerals have been thoroughly investigated for froth flotation applications, however insoluble oxides are not as well studied [2].

This chapter investigates the surface chemistry of pyrite, chalcopyrite and haematite after exposure to EPS from *L. ferrooxidans* grown on chalcopyrite. The surface chemistry changes and the resulting flotation effect of the interaction between EPS supernatant and mineral surface was investigated through bio-flotation studies, contact angle measurements and synchrotron-based photoemission electron microscopy (PEEM).

5.2 Experimental

5.2.1 Extracellular Polymeric Substance Supernatant

L. f adjusted to chalcopyrite was cultured as a 30% inoculation in modified HH media, at pH 1.8 and 30°C on a rotary shaker maintaining 155 rpm. The culture was maintained until late exponential phase, where the culture was harvested. Mineral particles were removed from the culture through filtration with a 5µm Millipore SMWP mixed cellulose membrane and vacuum filter. Once the mineral was removed, the culture was filtered through a 0.2µm Isopore hydrophilic membrane to remove cells, producing the free EPS supernatant solution.

5.2.2 Mineral Preparation

Pyrite (Peru), chalcopyrite (Moonta Mines, Australia), and haematite (unknown origin) mineral samples used in this chapter were sourced through GEO Discovery (The Willyama Group, New South Wales). To evaluate the composition and purity of each sample, samples were characterised using Quantitative Evaluation on Minerals by Scanning electron microscopy (QEMSCAN, FEI, Hillsboro, OR, USA) [3]. The samples were found to have a purity of 88% (pyrite), 83% (chalcopyrite), and 77% (haematite).

5.2.2.1 Micro-Flotation Studies

Single mineral and mixed mineral micro-flotation tests were conducted as collector-free flotation tests and in the presence of PIPX collector (10^{-4} M). Single mineral flotation tests were conducted on 1g high purity natural mineral, with a fraction size of +38 – 75µm. Mixed mineral micro-flotation tests were conducted on 1g synthetic mix of chalcopyrite, pyrite and haematite with an approximate ratio of 1:1:1. All micro-flotation tests were performed at ambient temperature with the parameters as previously outlined in Section 2.5.2.

5.2.2.2 Contact Angle and Photoemission Electron Microscopy

Single mineral sections were used for contact angle analysis, while mineral sections with mixed mineral phases were used for PEEM analysis. The mineral sections were prepared similar to the method outlined in Section 3.3.4.2. The mineral sections were shaped and polished using varying grit sizes of silicon carbide sandpaper and polished to a mirror finish using a Trident polishing cloth with diamond paste (1 µm and 0.25 µm). The mineral sections were cleaned via ultrasonication in ultrapure Milli-Q water, prior to UV sterilisation.

Exposure of the mineral sections to both HH media and the EPS supernatant occurred using a volume of 300 mL and maintained at 30°C in a Ratek rotary shaker maintaining 155 rpm for the duration of exposure. After exposure, samples were removed and preserved for analysis. Samples analysed via captive bubble contact angle were transferred to sterile HH media to avoid the drying out of the sample prior to analysis. Samples required for PEEM analysis were transferred to DNase and RNase free 15 mL centrifuge tubes and snap frozen in liquid nitrogen. Samples were maintained at -80°C and transported on dry ice until PEEM analysis could be conducted. Exposure for the fresh EPS sample occurred in the wet lab at the National Synchrotron Radiation Research Centre (NSRRC). After exposure to the EPS supernatant, the excess solution was wicked away using a KimWipe before being mounted on the sample holder. This occurred directly prior to analysis.

5.2.3 Captive Bubble Contact Angle

The change in surface wettability of the samples was conducted via captive bubble contact angle measurements. The captive bubble method is preferred to the Sessile drop method, as it allows the surface to remain hydrated, which is important for maintain the structural integrity of biofilms. This provides a more accurate measure of the surface wettability changes induced by adsorption of EPS components [4].

Samples were removed from exposure flask and transferred into scintillation vial with 5mL sterile HH media to prevent drying out. Samples were held face down in the sample holder and immersed in HH media, with the J-shaped needle positioned under the centre of the sample. The volume of the air bubble was increased slowly, with images taken to capture the advancing and receding angles [5,6]. Measurements were taken in triplicate and measured on a Sinterface Profile Analysis Tensiometer PAT1 Version 8 (Sinterface, Berlin, Germany). Images were captured by a Sinterface PAT1 Charge Coupled Device (CCD) camera and contact angles were analysed using the Contact Angle plugin of the ImageJ software [7-9].

5.2.4 FTIR-ATR Analysis

Samples were prepared similar to the method outlined in Section 3.3.1.2, where mineral fractions (+38 – 75µm) of pyrite and chalcopyrite were exposed to EPS supernatant from *L. ferrooxidans* adapted to chalcopyrite. Aliquots of 1 mL were taken at differing exposure times

and placed in a 1.5 mL Eppendorf tube with analysis proceeding immediately. Analysis was conducted as described in Section 4.2.2.2.

5.2.5 Photoemission Electron Microscopy

Photoemission Electron Microscopy (PEEM) was conducted on beamline BL05B2 at the NSRRC in Hsinchu, Taiwan. The BL05B2 beamline uses an elliptically polarised undulator (EPU5) with a spherical-grating monochromator, yielding very high photon flux (2×10^{12} photons S^{-1} at 800eV in a 0.4 mm x 0.2 mm spot) with spatial resolution better than 50 nm [3,10]. The Near Edge X-ray Adsorption Fine Structure (NEXAFS) spectra were collected with a step size of 0.1 eV and a dwell of 2-3 seconds. Images were generated on a phosphor screen mounted on a CCD detector through the collection of the total electron yield [10], with a field of view (FOV) of 450 μm .

5.2.5.1 Near Edge X-ray Fine Structure analysis and peak fitting

PEEM data was collected via three different modes; field of view (FOV) imaging at a fixed photon energy, FOV collection of spectra over an adsorption edge, and stacked images collected over an adsorption edge. Stacked images create a 3-dimensional image, where each pixel contains an adsorption spectrum. The images, spectra, and stack images were analysed using the IDL package aXis2000 [11]. Morphological effects were removed from images through background subtraction to illustrate the distribution of chemical states. NEXAFS spectra were collected from FOV analysis and 3D images. All spectra were pre- and post-edge corrected using a linear fit using Athena [12].

Peak fitting of the carbon K-edge was performed using the Athena package in Demeter Version 0.9.18 [12-14]. The carbon K-edge spectra were deconvoluted using the arctangent function at 290.0 eV and a series of Gaussian peaks for the main C 1s transitions up to 290.5 eV. The full width half maximum (FWHM) was constrained to ~ 0.5 eV for peaks before the ionization step. Transitions after the ionization step were not fit with Gaussian peaks as these transitions overlap, creating large potential error in assignments [13].

5.3 Results and Discussion

5.3.1 Micro-Flotation Studies

Single mineral flotation tests allow the physicochemical properties and the flotation behaviour of the individual minerals to be assessed for each flotation condition. This is important as effects such as galvanic interactions can influence the flotation behaviour of certain minerals in a mixed mineral system [15].

The results of the single mineral flotation tests of pyrite, chalcopyrite and haematite in baseline conditions with and without potassium isopropyl xanthate (PIPX) collector are displayed in Figure 5.1. The results of the collector-free flotation tests indicate poor recovery for all three minerals at both exposure times. A study conducted by Ahlberg, et al. [16] supports this observation, as it has been noted that pyrite floatability is minimal in acidic conditions. Likewise, this was also observed for haematite single mineral flotation tests [17]. However, the floatability of chalcopyrite in acidic conditions is dependant on the reduction/oxidation potential of the solution. In acidic solutions, chalcopyrite flotation is observed under oxidising conditions but is not achievable under reducing conditions [18]. As the recovery for chalcopyrite at 48 h and 72 h was 3.0% and 8.1%, respectively, this is an indication that the collector-free baseline conditions are reductive.

The addition of PIPX collector to single mineral flotation tests increased the recovery of all three minerals. Both chalcopyrite and pyrite show an increase in recovery of at least 55% and 40%, respectively, however the increase in haematite is negligible. The greatest recovery of chalcopyrite is observed at 48 h exposure, whilst the greatest recovery of pyrite and chalcopyrite is observed at the 72 h exposure. The increase in recovery of chalcopyrite is expected, as PIPX is a common collector used in the recovery of chalcopyrite. Previous studies have also indicated an increase in pyrite recovery in the presence of this collector [19,20]. However, previous studies have indicated that the addition of a collector to haematite can result in an increased recovery in acidic conditions [17]. Although not all collectors are suitable for haematite collection [17]. The limited recovery of haematite at both the 48 h and 72 h exposure in the presence of PIPX confirms that PIPX is a suitable collector to use in the recovery of chalcopyrite from systems which have a reasonable amount of haematite present.

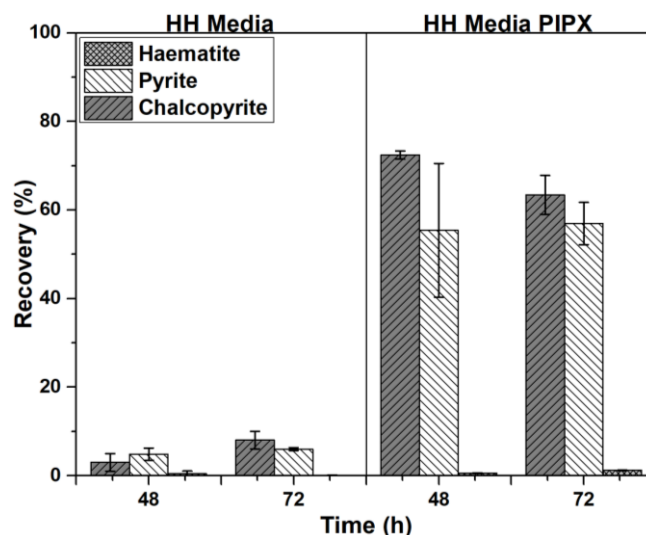


Figure 5.1: Single mineral micro-flotation for baseline conditions as a collector-free and in the presence of collector at 48 h and 72 h exposures

Analysing the Eh in conjunction with the pH measurements with the assistance of a Pourbaix diagram can help determine the surface chemistry present. These surface chemistry and oxidation states present impact the minerals flotation behaviour. According to the chalcopyrite Pourbaix diagram, presented in Section **Error! Reference source not found.** Figure 2.4 (b), the aqueous speciation predicts a combination of Fe^{2+} , CuS , and FeS_2 present on the surface [21]. The pyrite Pourbaix diagram, presented in Figure 2.4 (a) of Section **Error! Reference source not found.**, indicates that the aqueous species present in these conditions are FeS_2 , Fe^{2+} and H_2S [22]. While haematite is expected to have Fe^{2+} present [23], as shown by the haematite Pourbaix diagram in Figure 2.4 (c) of Section **Error! Reference source not found.**

Identifying the potential surface chemistry can help explain some of the results observed for the single mineral flotation tests. The Eh and pH measurements for the baseline single mineral flotation tests are shown in Figure 5.2 below. From Figure 5.2 (a), it is observed that both the chalcopyrite and pyrite flotation tests have a greater pH than the haematite flotation tests. This could be due to the changes in dissolution of the different mineral phases in acidic conditions, as the dissolution of haematite is minimal in the presence of sulfuric acid [24]. The addition of PIPX collector is seen to reduce the pH of the solution by 0.1 – 0.2 degrees of acidity.

The redox potential of the flotation tests was recorded, and the results are shown in Figure 5.2 (b). The collector-free conditions record higher potentials than the systems in the presence of PIPX. At 48 h exposure, the difference in potential is slight. However, at 72 h exposure, this decrease in potential is greater for all three minerals, with a difference of 51.9 mV (Cp), 157.6 mV (Py) and 213.4 (Hm) observed. The decrease in potential for flotation tests in the presence of PIPX corresponds with a decrease in recovery. At this exposure time the chalcopyrite is the only mineral that retains a positive potential, as both pyrite and haematite experience a negative potential. As the potential of the system can also provide an insight into how well the collector is expected to work. Therefore, the decrease in recovery is attributed to the decrease in activation of the collector due to the change in potential. As the redox potential of the baseline conditions with PIPX are less than the reduction potential of +0.13 V for disulfide and dixanthogen production, this explains why the recovery is increased to a reasonable value but optimal recovery is not achieved [2].

An unexplainable result is the 57.0% recovery of pyrite obtained at 72 h exposure in the presence of PIPX collector. This is unexpected as the recovery occurred at a redox potential of -123 mV. In these conditions, both disulfide and dixanthogens are not expected to be forming on the surface of the mineral [2], and therefore it is unlikely that the recovery observed is completely due to the influence of collector. The hydrophobicity of pyrite exhibited in these conditions could be an indication of sulfur states on the surface. The presence of elemental sulfur (S_8) and/or sulfate (SO_4^{2-}) increases the hydrophobicity of the surface, both sulfur states have previously been noted to occur on the pyrite surface throughout the pyrite oxidation pathways [25,26].

Qualitative X-Ray Diffraction (QXRD) of the pyrite fraction indicated the presence of impurities. It is expected that the dissolution of these impurities has contributed to the reduction in the redox potential observed, as noted in the study conducted by Descostes, et al. [27].

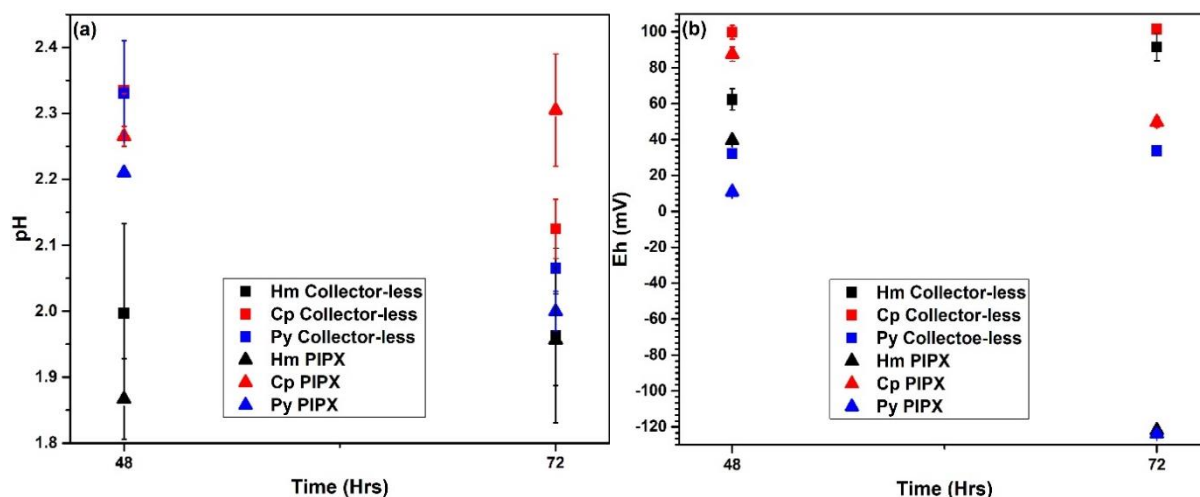


Figure 5.2: pH (a) and Eh (b) measurements for baseline single mineral flotation tests

The single mineral flotation tests of pyrite, chalcopyrite and haematite conducted in EPS supernatant from *L. f* adjusted to chalcopyrite, as collector-free flotation tests and in the presence of PIPX, are illustrated in Figure 5.3 below. The collector-free flotation tests in Figure 5.3 illustrates a greater recovery of all three minerals at 48 h exposure (Cp 3.2%, Py 24.3%, Hm 0.5%) in comparison to 72 h exposure (Cp 1.2%, Py 7.9%, Hm 0.4%). This is the opposite to what was observed in the baseline collector-free flotation tests, where the 72 h exposure produced the highest recovery. The low recovery of chalcopyrite at both exposure times can be an indication of the redox potential of the EPS supernatant, as low recovery rates of chalcopyrite in acidic conditions indicates reductive conditions [18]. With the addition of collector the recovery at 48 h of exposure was observed to be 79.0% for chalcopyrite, 81.1% for pyrite and 3.5% for haematite, while the recovery obtained from the 72 h exposure was 79.8% chalcopyrite, 76.8% pyrite and 1.1% haematite. This indicates that the best exposure time for pyrite and haematite is 48 h, while 72 h exposure is optimal for chalcopyrite.

In comparison to the baseline conditions, the collector-free flotation tests of EPS supernatant show an increase in recovery for all minerals at 48 h. At 72 h exposure, an increased recovery is only observed for pyrite and haematite. At 48 h exposure, the increase in recovery observed for chalcopyrite and haematite was less than 1%. However, the increase observed for pyrite was far greater at an increase of 19.3% and a total recovery of 24.3%. The increase in recovery for 72 h is minimal, with a 1.8% increase observed for pyrite and 0.2% increase for haematite. The chalcopyrite recovery was seen to decrease by 6.9%. A similar trend was seen with the addition of PIPX collector. At 48 h the recovery observed for chalcopyrite is 79%, which is a

6.6% increase, haematite flotation tests resulted in a 2.9% increase for a recovery of 3.5%. The increase in recovery observed for pyrite was far greater at 26.8%, resulting in a recovery of 81.1%. The recoveries for pyrite (76.8%) and chalcopyrite (79.5%) are also seen to increase at 72 h exposure, by 19.8% and 16.1%, respectively. Haematite on the other hand resulted in a decrease of 0.1% and a total recovery of 1.1%.

The increase in pyrite recovery in the EPS supernatant is an interesting observation, as pyrite has been noted to have low floatability is acidic conditions [16]. This increase in recovery is an indication of a change on the pyrite surface, induced by the changes between the HH media and the EPS supernatant solutions. The interactions between the biomolecules present in the EPS supernatant and the mineral surfaces is still under investigation, with a focus on the early stages of biofilm formation and attachment [28,29].

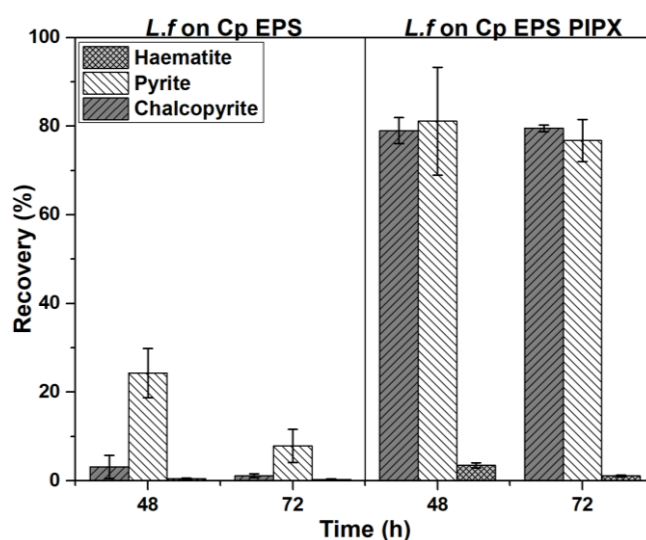


Figure 5.3: Single mineral micro-flotation tests as collector-free and in the presence of collector for mineral exposed to EPS supernatant at an exposure of 48 h and 72 h exposures

Some of the differences observed in the recoveries could be attributed to the different Eh and pH conditions. The pH and Eh of the EPS supernatant systems are present in Figure 5.4 below. The pH conditions shown in Figure 5.4 (a) are similar to those observed in Figure 5.2 (a). The collector-free samples of chalcopyrite and pyrite at 48 h exposure are 0.2 and 0.3 degrees of acidity lower than those observed for baseline conditions, while the pH for haematite was the same in both conditions. At 72 h exposure there is a decrease for chalcopyrite and pyrite, in comparison to the 48 h exposure and the baseline conditions, was observed; the haematite was shown to have a slight increase. The addition of PIPX collector

resulted in a decrease in pH for chalcopyrite, pyrite and haematite at 48 h exposure, as observed in the baseline conditions. At 72 h exposure, both chalcopyrite and haematite exhibit an increase of 0.15 and 0.7, respectively. Pyrite was observed to have a decrease of 0.05 degrees of acidity. This trend was also seen in the baseline conditions.

The potential of the single minerals in the EPS supernatant is higher (+395 mV to +595 mV) than what was recorded for the baseline conditions, both with and without collector. This change in potential also changes the expected surface speciation of the minerals. The expected surface speciation for chalcopyrite are Cu(II) and Fe(II) [21]; the surface speciation expected for pyrite are Fe(II) + 2S and SO_4^{2-} [22]. However, in the conditions of the EPS supernatant the haematite surface is expected to remain as Fe_2O_3 [23]. These predicted surface species can help explain the results recorded.

In the collector-free EPS supernatant flotations tests, chalcopyrite is seen to have low recovery. The conditions support the presence of Cu(II) and Fe(II) on the surface, these states can oxidise in aqueous environments, producing metal hydroxides and increasing the hydrophilicity of the surface [30]. The presence of Cu(II) on the surface aids xanthate adsorption, increasing the recovery which is reflected in the flotation tests in the presence of collector. Likewise, the surface states predicted by the pyrite pourbaix diagram support the results of the single mineral flotation tests. The Eh and pH conditions indicate the presence of sulfate on the surface, producing a hydrophobic surface. This can explain the recovery observed in the collector-free flotation tests. According to Klimpel [2], and Chandra, et al. [30] these conditions also support the formation of disulfide and dixanthogen on the addition of collector. Both disulfide and dixanthogen are hydrophobic, increasing the floatability of the mineral leading to the recoveries observed.

The low levels of haematite recovery observed for all flotation tests can be explained by the expected surface species. As the surface speciation of haematite is expected to remain as Fe_2O_3 , with Fe^{2+} , in the conditions produced by the EPS supernatant, the surface is anticipated to maintain hydrophilic properties, therefore leading to low recovery rates. As stated above, the conditions also support the formation of dixanthogen, which could account for the 3.5% recovery observed at 48 h. While the conditions are in favour for the formation of

dixanthogen, the likelihood of it adsorbing to the surface is minimal [31], thus the recovery seen is reasonable.

Overall, the EPS supernatant is observed to increase the floatability of the individual minerals. It is observed that the 48 h exposure time produces the greatest recovery of chalcopyrite, pyrite and haematite for base line conditions and EPS supernatant in the presence of PIPX collector and as collector-free flotation tests.

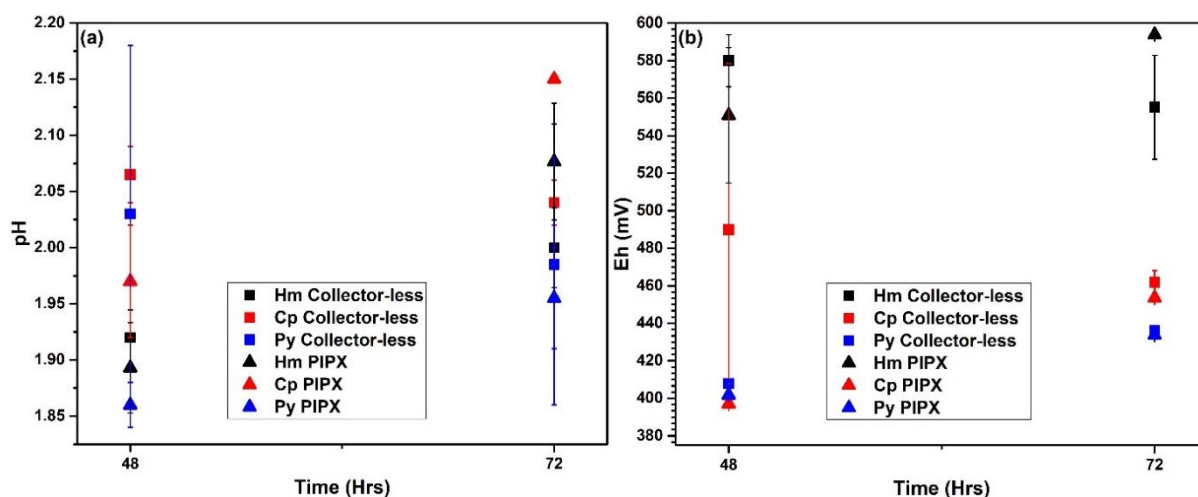


Figure 5.4: pH (a) and Eh (b) measurement for EPS supernatant single mineral flotation tests

While single mineral flotation tests can indicate the flotation behaviour of individual mineral phases, but this is not a trustworthy representation of a mixed mineral system. As pyrite and chalcopyrite are both sulfide minerals, galvanic interactions can occur between the two phases, altering their flotation behaviour [32]. The effect of these galvanic interactions can be seen through a comparison of the single mineral recovery of the pyrite, chalcopyrite and haematite with the mixed mineral flotation tests.

The mixed mineral flotation tests of pyrite, chalcopyrite and haematite for both baseline conditions and EPS supernatant conditions are shown below in Figure 5.5 and Figure 5.6, respectively. Baseline collector-free flotation test show a recovery for chalcopyrite of 39.5% and 49.8% for 48 h and 72 h exposure, respectively. This recovery is significantly greater than pyrite (1.3% and 4.9%) and haematite (1.5% and 2.5%). This shows that 72 h exposure results in a greater recovery of all three minerals and produces a slightly better separation than the 48 h exposure. In comparison to the single mineral flotation tests, the recovery of chalcopyrite

and haematite has increased, while the recovery of pyrite decreased. This change in flotation behaviour can be attributed to the galvanic interactions occurring within the flotation cell.

In the presence of other sulfide minerals, pyrite can act as a cathode creating galvanic cell like conditions [32]. In cathodic conditions the pyrite phase attract electrons from the other sulfide mineral phase present, creating reducing conditions on the pyrite surface [32]. These reducing conditions increase the probability of hydroxides forming on the surface of pyrite, increasing the hydrophilic conditions of the phase [32]. In a pyrite/chalcopyrite system, in the case where the pyrite is acting as a cathode, oxidative conditions are expected to occur at the chalcopyrite surface. As mentioned above, oxidative conditions in acidic solutions are preferable for chalcopyrite flotation [18]. The increase in recovery of chalcopyrite between the single mineral flotation tests and the mixed mineral flotation tests is 36.5% and 41.8% for the 48 h and 72 h exposure, respectively. As this increase in recovery is significant and the conditions were the same as the single mineral flotation tests, the increase in chalcopyrite recovery observed is an indication of the effects of potential galvanic interactions occurring. The presence of potential galvanic interactions is also reflected in the difference of pyrite recovery between the single mineral flotation tests and the mixed mineral flotation tests. The pyrite recovery is observed to reduce by 3.5% for 48 h exposure and 1.1% at 72 h exposure. While haematite is not expected to partake in galvanic interactions, as it is not a sulfide mineral, the recovery can still be influenced. Haematite recovery is observed to increase by 1.1% at 48 h exposure and 2.3% at 72 h exposure in mixed mineral flotation tests. These results indicate that the galvanic interactions between the mineral phases is favourable to chalcopyrite recovery, with the best recovery and separation occurring at 72 h exposure.

The addition of PIPX collector is observed to increase the recovery of all mineral phases, as seen in the baseline single mineral flotation tests. Chalcopyrite recovery is seen to increase to 93.8% and 93.5% for 48 h and 72 h, respectively. This is an increase of 54.3% and 43.6% in comparison to the collector-free flotation tests. Pyrite recovery was also seen to increase in the presence of collector; however, the recovery is still noticeably less than the recovery of chalcopyrite. The recovery was observed at 31.5% for 48 h exposure and 23.8% at 72 h exposure, this is an increase of 30.2% and 18.8%, respectively. Likewise, the haematite recovery was also increased by 24.9% at 48 h and 8.7% at 72 h exposure. These results indicate that the best recovery of chalcopyrite occurs at 48 h exposure, however the best separation

of chalcopyrite from gangue minerals occurs at 72 h exposure due to the higher recovery rates of both pyrite and chalcopyrite at 48 h. While the addition of PIPX collector is expected to increase the recovery of mineral, the increase of pyrite and haematite recovery can be an artifact of copper activation [20,33].

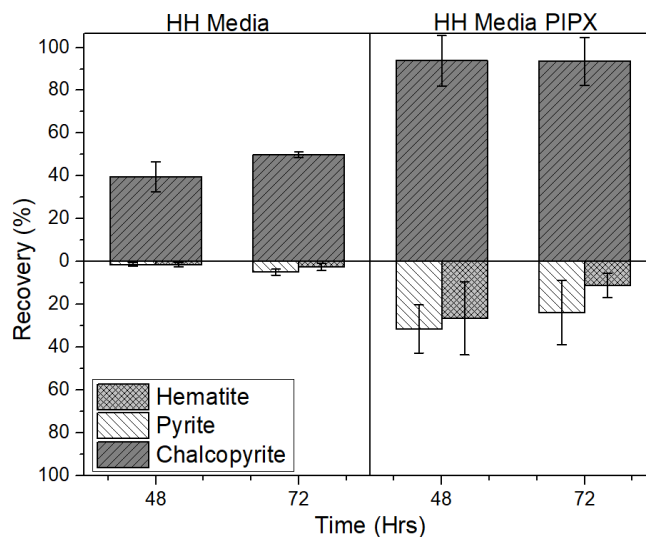


Figure 5.5: Recovery of Cp, Py and Hm differential micro-flotation tests as a function of time in baseline conditions as collector-free flotation tests and in the presence of PIPX collector

The results from the mixed mineral floatation tests conducted in EPS supernatant are shown in Figure 5.6. The collector-free flotation tests indicate a recovery for chalcopyrite of 57.6% and 11.3% for 48 h and 72 h, respectively. This is an increase in recovery of 18.3% at 48 h and a decrease in recovery of 38.6% at 72 h in comparison to the baseline conditions. The recovery of pyrite is observed to be far less than chalcopyrite recovery, with a recovery of 2.5% at 48 h exposure and 0.3% at 72 h exposure. In comparison to the baseline conditions, this recovery follows the same trend as the chalcopyrite recovery with an increase of 1.2% at 48 h and a decrease of 4.6% at 72 h exposure. This trend is also observed with the haematite recovery. At 48 h a recovery of 5.7% is observed, this is an increase of 4.1% from the baseline flotation tests. The 72 h exposure results in a recovery of 0.9%, which is a decrease of 1.6% from the baseline conditions. These results indicate that the best recovery and separation of chalcopyrite for EPS supernatant conditions is recorded for 48 h exposure. While the recovery of the gangue mineral phases is negligible at the 72 h exposure, the recovery of chalcopyrite is not optimised.

Similar to the baseline conditions, the addition of the PIPX collector increases the recovery of all three minerals. The chalcopyrite is observed to be at 103.4% at 48 h exposure and 95.9% at 72 h exposure. The pyrite and haematite recovery increased to 14.3% and 17.4%, respectively, for the 48 h exposure with 16.2% and 8.7% observed for the 72 h sample. The EPS supernatant samples at both exposure times, in the presence of PIPX collector result in a better separation efficiency. Although the PIPX addition does increase the recovery of the gangue minerals, the recovery is greater in the baseline conditions than the EPS supernatant conditions.

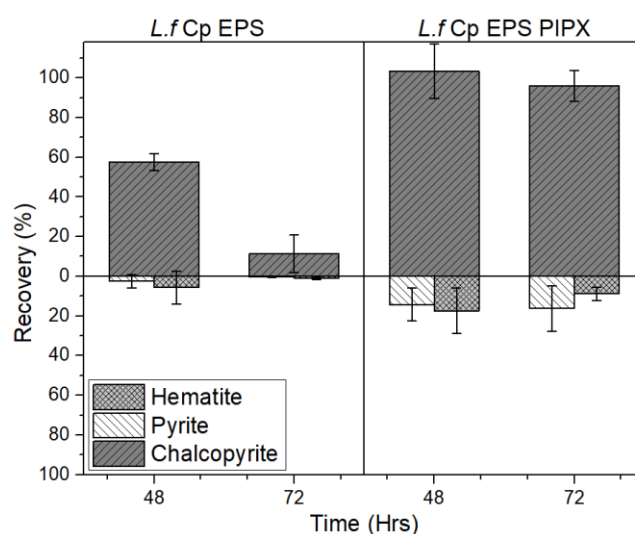


Figure 5.6: Recovery of Cp, Py and Hm differential micro-flotation tests as a function of time exposed to EPS supernatant as collector-free and in the presence of PIPX collector

An interesting observation from the mixed mineral flotation tests is the phases present for QXRD and TOPAS refinement. QXRD indicated the presence of troilite (FeS) and marcasite (FeS₂) in the samples obtained for mixed mineral flotation tests. While the percentage of these phases are negligible, they are required to acquire a satisfactory refinement. A study conducted by Schoonen and Barnes [34] suggests the precipitation of pyrite and marcasite is probable in solutions containing Fe²⁺ and H₂S. Likewise, Blowes, et al. [15] notes marcasite as an oxidation product of pyrrhotite, which was identified as a minor impurity in the pyrite samples. The Eh and pH measurements obtained from the samples, shown in Figure 5.7, and the Pourbaix diagrams of each mineral indicates that the states expected to occur in these conditions are Cu²⁺, Fe²⁺, 2S, SO₄²⁻, and Fe₂O₃ [21-23]. The precipitation of pyrite and marcasite is expected to occur through a nucleation pathway or through the formation of a FeS precursor [34]. These phases were not observed in the single mineral flotation tests or

the mixed mineral baseline flotation tests. Therefore, it is assumed that a mixed system and the conditions produced by the EPS supernatant are required for the formation and detection of these phases. Precipitation of these phases is expected to create an error in the recovery calculations due to the added weight to the recovered fraction.

In comparison to the single mineral samples, the mixed mineral samples show less variance in the pH and Eh. The pH results illustrated in Figure 5.7 (a) show an increase of 0.21 to 0.28 acidity units upon the addition of PIPX for the 48 h exposures, while the change in the 72 h samples is negligible. Figure 5.7 (b) indicates the redox potential of the samples exposed to the EPS supernatant is greater than HH media samples.

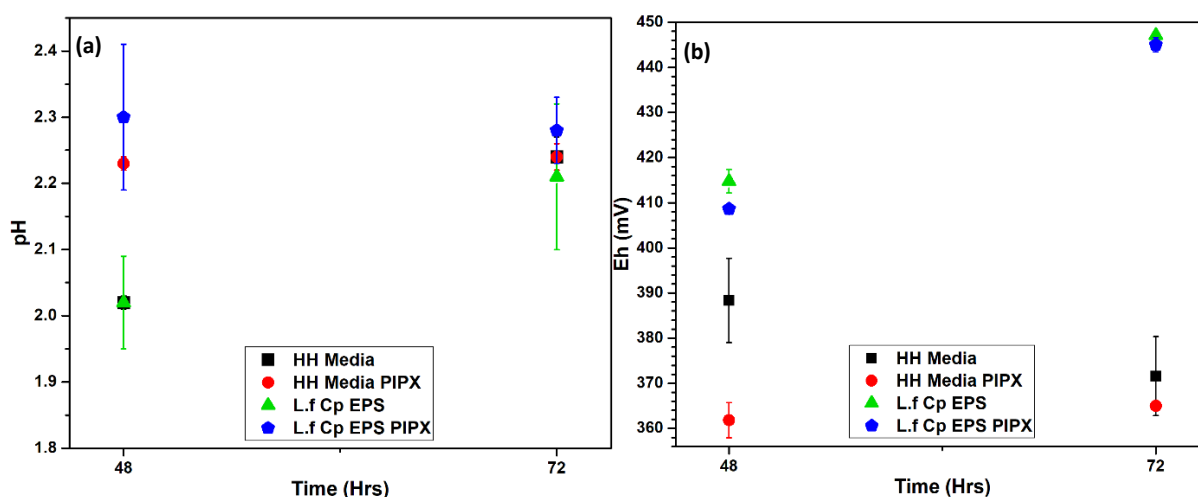


Figure 5.7: pH (a) and Eh (b) measurement for the mixed mineral flotation tests with HH media and EPS supernatant

5.3.2 Contact Angle

The wettability of the pyrite and chalcopyrite surface was assessed through captive bubble contact angle. Measurements were taken at the advancing contact angle (ϑ_A) and the receding contact angle (ϑ_R). From these measurements the contact angle hysteresis was calculated. The results are displayed in Table 5.1 below. It is important to note that the contact angle can be impacted by particle size, surface roughness and heterogeneity [4,35], therefore these results are only an indication of what is occurring in the flotation system.

The advancing and receding contact angles for pyrite in HH media are seen to decrease with a function of time. This indicates that with increasing exposure time, the wettability of the pyrite surface increases. Over the exposure time, the advancing and receding contact angle

for chalcopyrite fluctuates, with the difference between the unreacted (0 h) and 72 h sample being 4.3° and 3.4° , respectively. This suggests the chalcopyrite surface has a higher affinity to air than media in the control conditions. This is similar to what is observed when pyrite and chalcopyrite are exposed to EPS supernatant. Pyrite exhibits a decrease in both advancing and receding contact angles with increasing exposure. The difference observed between the unreacted (0 h) and 72 h is 22.1° and 48.2° , respectively. This indicates that interactions between the pyrite surface and the EPS supernatant is creating a hydrophilic surface. This is similar to what was observed for the chalcopyrite samples. However, the decrease in the contact angle is not as great as what is observed in the pyrite samples. The change observed from 0 h to 72 h is 16.1° and 12° for the advancing and receding angle, respectively. The larger receding contact angle indicates the surface is exhibiting hydrophobic/aerophilic properties [33].

Assessing the contact angle hysteresis can indicate the heterogeneity of the surface; a lower hysteresis value indicates greater homogeneity [35]. The hysteresis for the pyrite control samples indicates that the sample surface is heterogeneous, even at 0 h. The hysteresis is minimised at 48 h at 7.8, indicating the surface is more homogeneous at this exposure time. Interestingly, the hysteresis of chalcopyrite is minimised at 0 h exposure than all other exposure times, indicating that the polished surface is more homogeneous prior to exposure to HH media. As surface roughness can impact the contact angle, the increase in hysteresis observed may be influenced by both topographical changes and surface speciation.

Exposure of pyrite to the EPS supernatant is seen to decrease the contact angle hysteresis gradually as a function of time. The hysteresis is minimised to 0.5 at 72 h exposure, this indicates that the homogeneity of the surface is increasing as a function of exposure time. Chalcopyrite, on the other hand, does not demonstrate the same relationship between exposure time and contact angle hysteresis as the pyrite samples. The contact angle hysteresis for the chalcopyrite samples exposed to EPS supernatant fluctuates and follows

the same trend which is observed in the HH media control. The smallest hysteresis value obtained, of 15.8, was observed at 48 h exposure.

Table 5.1: Change in contact angle (°) of mineral tiles of pyrite and chalcopyrite showing the static contact angle (ϑ), advancing contact angle (ϑ_A), receding contact angle (ϑ_R), and contact angle hysteresis (H_w)

Sample	Time (h)	Pyrite			Chalcopyrite		
		ϑ_A	ϑ_R	H_w	ϑ_A	ϑ_R	H_w
HH Media Control	0	63.0	76.5	13.5	53.0	68.8	15.8
	24	47.2	55.4	8.3	48.2	78.3	30.1
	48	38.3	46.2	7.8	46.7	70.9	24.3
	72	27.8	48.8	21.0	48.7	65.4	16.7
EPS Supernatant	0	38.7	65.3	26.6	50.5	72.1	21.7
	24	21.3	40.9	19.5	44.5	66.6	22.1
	48	25.1	27.4	2.2	42.6	58.4	15.8
	72	16.6	17.1	0.5	34.4	60.1	25.7

Overall, these results indicate an increase in the wetting behaviour of pyrite in both the HH media control and the EPS supernatant. The EPS supernatant was observed to create a surface which is less heterogeneous than samples exposed to HH media. There is minimal change observed between the HH media control and EPS supernatant exposures for the chalcopyrite samples.

5.3.2.1 FTIR-ATR Analysis

The surface chemistry changes were also observed through FTIR-ATR analysis, with the resulting spectra shown in Figure 5.8. Unreacted pyrite and chalcopyrite, shown in Figure 5.8 a and b respectively, show some differences between 700 cm^{-1} and 1300 cm^{-1} which is expected to be due to the different sulfur functional groups on the surface [36].

When pyrite is exposed to EPS supernatant from *L. ferrooxidans* adapted to chalcopyrite, there is little to no change observed between the 48 h exposure and the 72 h exposure, as shown in Figure 5.8. The 72 h exposure (Figure 5.8 e) shows a lower baseline transmittance, but otherwise similar features as the 48 h exposure (Figure 5.8 c) in the 700 cm^{-1} and 1300 cm^{-1} region.

The chalcopyrite samples show some variations in comparison to the unreacted sample. At 48 h exposure, changes in transmittance peaks observed between 700 cm^{-1} and 1300 cm^{-1} . Unlike the pyrite, the change observed is more than a change in baseline transmittance, which correspond to ring vibrations and C–O–C stretch [37-39]. More variation is seen for the 72 h exposure, these variations are seen between 2300 cm^{-1} and 3000 cm^{-1} , and 700 cm^{-1} and 1300 cm^{-1} . These changes indicate an increase in the presence of the CH_2 , CH_3 asymmetric stretch, including that of fatty acids [36-41], and C–O–C stretch [37-39].

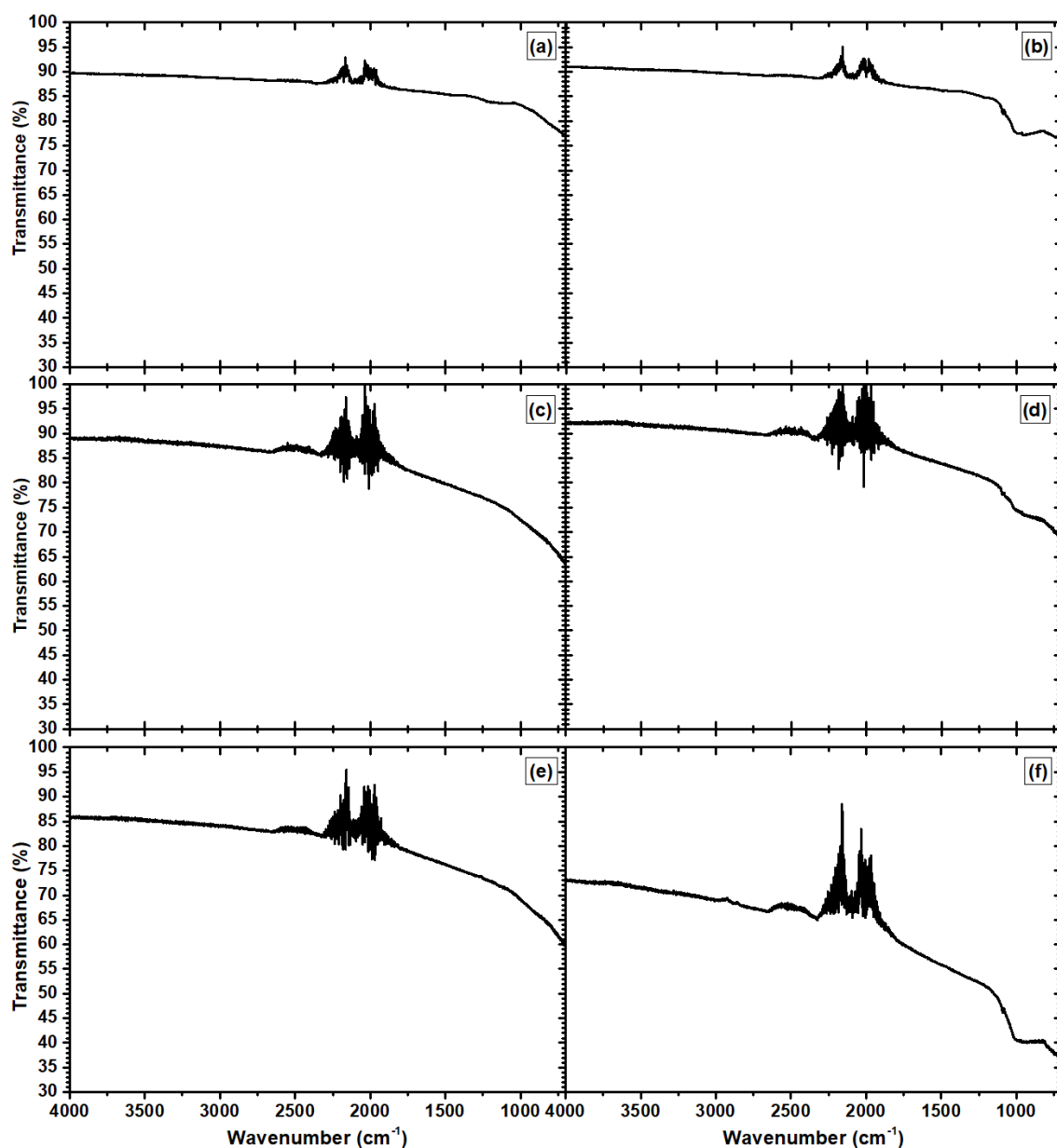


Figure 5.8: FTIR-ATR Analysis of pyrite and chalcopyrite exposed to EPS supernatant of *L. ferrooxidans* adapted to chalcopyrite showing unreacted pyrite (a), unreacted chalcopyrite (b), pyrite at 48 h (c), chalcopyrite at 48 h (d), pyrite at 72 h (e) and chalcopyrite at 72 h (f)

These results suggest greater interaction occurs between the chalcopyrite and the EPS supernatant than pyrite and the EPS supernatant. However, these samples, unlike the samples analysed in Chapter 4 which were analysed as a slurry, these samples were dried before being analysed. This means that any organic matter would not exist in its original hydrated state, and therefore there may be some variation in measurements. However, these results do provide a quick snapshot the surface chemistry and can be used to guide further investigations.

5.3.3 Photoelectron Emission Microscopy Analysis

Photoelectron Emission Microscopy (PEEM) analysis was conducted with total electron yield (TEY). TEY analysis was used to analysed the samples to an approximate analysis depth up to 15nm, therefore near surface oxidation states can be detected [42].

5.3.3.1 Copper L-edge Analysis

Copper is the differentiating element between the mineral phases and was used to determine an area for analysis. The region of interest contained both a copper containing region and a copper deficient region. This was achieved by acquiring quick Cu L_{2,3} NEXAFS scans and images of the surface at a fixed energy of 933 eV.

The NEXAFS Cu L-edges obtained from field of view (FOV) analysis are illustrated in Figure 5.10. These spectra are qualitatively similar to the Cu L_{2,3} NEXAFS spectra for chalcopyrite previously observed [43,44]. However, the leading adsorption peak for all spectra, except the spectrum obtained from EPS supernatant 48 h fresh, was observed at 932.9 eV (feature ii), which is suggested to be indicative of Cu (I) sulfide like chalcopyrite [42,44]. The energy of this adsorption peak is 0.3 eV higher than that Goh, et al. [43] reported, however chalcopyrite NEXAFS has previously been reported to occur in an energy range of 932.4 – 932.7 eV [43], with XRD confirming the presence of chalcopyrite.

The 48 h and 72 h HH media baseline samples, shown in Figure 5.10 (a) and (b) respectively, are qualitatively similar. This indicates that there is little change detected with the copper between the 48 h and 72 h exposure in HH media. Changes are observed in the Cu L_{2,3} spectra for samples exposed to the EPS supernatant. At 48 h exposure changes are observed around the leading adsorption peak. For the frozen EPS supernatant sample at this exposure time,

there is a slight inflection present on the leading adsorption peak at 931.2 eV (feature i). This slight inflection is suggested to be a contribution of Cu (II) states [45]. The Cu (II) on the surface giving rise to this feature can be either CuO and Cu(OH)₂ [30,45], both are reasonable for the conditions and an indication of oxidation of the chalcopyrite phase [46]. The redox potential for the system supports the formation of Cu(OH)₂ on the surface [21].

For the 48 h EPS fresh sample, the inflection is observed as a fully resolved peak with the same energy. The change in intensity between the fresh and frozen sample is expected to come from the sample preparation differences. The frozen sample was prepared prior to analysis and snap-frozen and kept at – 80°C while the fresh sample was prepared directly prior to analysis. Having the sample frozen and then placed into a vacuum, sublimation can occur. This means the sample could be partially hydrated. The hydration could be in the form of EPS supernatant present on the surface, or it could be hydrated biofilm. Therefore, the increased intensity is an indication of an increase concentration of CuO and Cu(OH)₂ species, however, it cannot be determined if these species are attached to the surface or sitting on the surface in a hydrated state. While the spectra have indicated the presence of these surface states, the corresponding PEEM images illustrates the spatial distribution of these states. For the 48 h frozen sample, there is very little to no spatial distributions observed, this could be due to the smaller concentration of Cu (II) states. However, differences were observed for the 48 h fresh sample, as pictured in Figure 5.9. At 931.2 eV, Figure 5.9 (a), the overall contrast of the surface is similar with only some mildly bright spots. This indicates that the Cu (II) is present over most of the surface, with higher concentrations observed throughout the centre of the sample. However, at 932.9 eV there are specific regions of the sample which indicate the presence of Cu (I) and regions which do not. As the leading adsorption edge of chalcopyrite is expected at 932.9 eV [42], the regions which are excited at this energy are determined to be chalcopyrite. When comparing these two images, there are two regions which are of interest; these are indicated with arrows. The region to the top left-hand corner of the sample indicates the presence of Cu (II) in an area where Cu (I) is not. The second region is the bottom middle section of the sample. Here the images indicate the presence of Cu (I) without the strong presence of Cu (II). As there is a lack in consistency between the areas where the Cu (I) and Cu (II) states are present in these two regions, it is suggested that the presence of Cu (II) is not simply present due to the oxidation of the chalcopyrite phase. It also suggests that the

Cu (II) states observed on the surface are a factor of deposition through either the growth of copper containing biofilm on the surface or attachment of copper compounds from the leachate. This deposition of copper observed on the surface explains the increase of recovery for both pyrite and haematite in the mixed mineral flotation tests with the addition of PIPX. The deposition of copper onto the pyrite and haematite can cause copper activation of the collector, increasing the recovery [20,33].

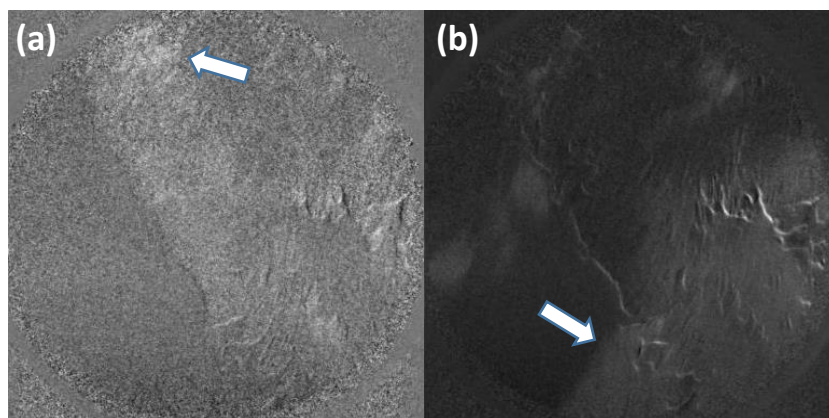


Figure 5.9: Corresponding PEEM image (background removed) of the leading adsorption edge for the EPS supernatant 48 h fresh at (a) 931.2 eV and (b) 932.9 eV. FOV = 450 μ m

Another difference observed between the HH media and EPS supernatant for the 48 h exposure is the trough between the adsorption peak at 932.9 eV (feature ii) and the adsorption peak at 936.7 eV (feature iii). For the samples exposed to the EPS supernatant, this trough is shallower and not as well resolved. This is likely due to the convolution of the Cu (II) contributions from CuO and Cu(OH)₂, as this is not observed in the samples where the feature at 931.2 eV is absent.

At longer exposures to the EPS supernatant the shape of the Cu L_{2,3} spectrum changes slightly at approximately 940eV. The change in shape is where the broad adsorption peak present at 936.7 eV (feature iii) is resolved further to show a second adsorption peak at 941.9 eV (feature iv). This feature is observed at both the L₃ and L₂ edge, with the feature at the L₂ edge occurring at 961.6 eV. It is important to note that this change only occurs when the sample is exposed to the EPS supernatant for 72 h or longer and is not present in the 72 h HH media baseline sample, indicating that this feature is a result of exposure to the EPS supernatant for extended periods of time.

This shape has previously been predicted by Goh, et al. [42] in ab initio calculations. These calculations used WIEN2k modelling to look at the Cu-S 3-coordinate and 4-coordinate bonding. This feature is only observed in simulations where a ratio between the 3-coordinate and 4-coordinate states is used. This suggests that at longer exposure times to the EPS supernatant, both 3-coordinate and 4-coordinate Cu-S bonds are present. As TEY is surface sensitive, the presence of this shape indicates that the changes in the Cu-S bonding is occurring at the surface rather than through the bulk of the sample. As the conditions produced by the EPS supernatant favour the leaching of both copper and iron into solution, the change in ratio between the 3-coordinate and 4-coordinate Cu-S bonds could be through both the breaking and/or forming of the Cu-S bonds. The removal of iron from the surface through leaching causes the formation of a metal deficient surface layer. Chander [47] suggests that a metal deficient surface can contribute to higher recoveries in collector-free flotation. When metal deficiency occurs in chalcopyrite surface states such as CuO and Cu(OH)₂ are expected to occur, increasing the hydrophobicity [47]. Although the spectra collected from the samples exposed to the EPS supernatant for 72 h and 7-days indicates there is a change in the coordination of the Cu-S bond, there is no evidence of the presence of CuO or Cu(OH)₂. The lack of CuO and Cu(OH)₂ at these exposure times is also reflected in the lack of recovery of collector-free flotation tests for the EPS supernatant at 72 h exposure.

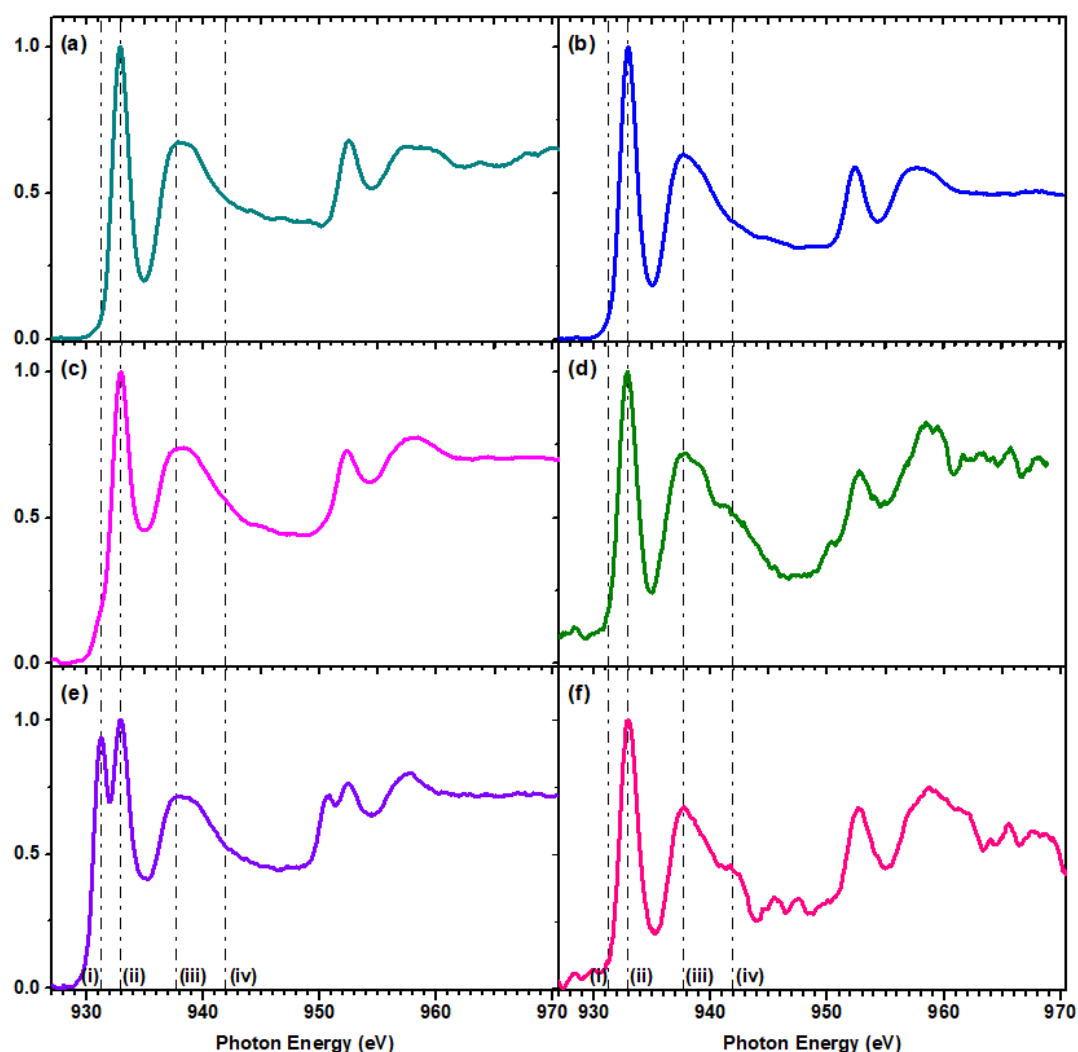


Figure 5.10: TEY Cu $L_{2,3}$ -edge NEXAFS spectrum for mixed mineral coupon exposed to (a) HH media control 48 h; (b) HH media control 72 h; (c) EPS supernatant 48 h – frozen; (d) EPS supernatant 72 h; (e) EPS supernatant 48 h – fresh; (f) EPS supernatant 7 days

5.3.3.2 Iron L-edge Analysis

Iron $L_{2,3}$ -edge spectra presented in Figure 5.11 were collected from the field of view (FOV) of the sample. As these samples are a known natural mix of pyrite, chalcopyrite and haematite, the resulting FOV spectra is expected to be a convolution of all three phases. Although the iron present in pyrite is Fe (II), with both chalcopyrite and haematite composing of Fe (III) [43], the adsorption peaks present in the $L_{2,3}$ -edge cannot confidently assign the oxidation state of iron as each oxidation state has a range of energies [43]. There are specific characteristic features to each mineral phase which can be used to identify the presence of these phases. These features include the splitting of the main adsorption peak, a change in the energy separation of features, and a change in the intensity ratio of adsorption peaks.

The spectra presented in Figure 5.11 illustrate subtle changes between samples, all indicating the presence pyrite through the adsorption feature at 712.5 eV (feature iii) [4,48]. The presence of chalcopyrite and haematite are harder to identify in the FOV spectra. The spectra illustrate a leading adsorption peak at approximately 707.3 eV which appears to be split. The splitting of this main adsorption peak, indicated as peak i and ii in Figure 5.11, has been noted in literature to be influenced by valance states and can also be an indication of oxidation [43,49]. The splitting of this absorbance peak is due to the overlapping energies of the Fe 3d eg transitions (i) and Fe 3d hybridisation with the S 3p [4,48,50]. Therefore, the splitting of this adsorption peak cannot be used to assume the presence of Fe (III) nor can it be used to identify the presence of pyrite as the splitting is also intrinsic to pyrite [43]. The spectrum collected from the EPS supernatant 7-day sample exhibits the greatest change in the adsorption peak at 708.6 eV. Although using the energy of the adsorption peak is not the most infallible way to determine the oxidation. The spectrum observed is quantitatively similar to the Fe (III) spectrum obtained by Bhattacharyya, et al. [51], through organic matter oxidation of iron.

Information can be gained by analysing the energy difference between the peaks and their intensity ratio. These peaks are identified as peaks i and ii in Figure 5.11 and the parameters are shown in Table 5.2 below. The parameters presented in Table 5.2 indicate subtle changes between the samples. These changes can arise from compositional changes due to leaching and/or oxidation of the surface, or from a difference in the ratio of which the pyrite, chalcopyrite and haematite phases present. The expected energy split between peak i and peak ii for pyrite is 1.29 eV with a ratio of 1.08. The change in energy for iron oxides is greater, with haematite expected to have an energy difference of 1.46 eV and goethite, FeOOH an expected hydroxylation product to have a difference of 1.60 eV. The ratio of these peaks are expected to be 0.57 and 0.51, respectively [49]. These values, along with the well resolved doublet of the L₃ and L₂ edge are used to identify the haematite phase [52]. The leading adsorption peak of the L₃ edge doublet is expected at approximately 705.5 eV, with the second adsorption peak is expected at approximately 706.9 eV [49]. The leading adsorption edge for the spectra present in Figure 5.11 is observed at a higher energy than what is expected for haematite. This is expected to be a result of the mixed phase sample, as not all the iron present is from the haematite phase. As noted above, haematite is expected to have

a specific peak ratio, with the intensity of the adsorption peak at 706.9 eV greater than the leading adsorption peak at 705.5 eV. The spectra shown in Figure 5.11 (d – g) show a greater intensity of the second adsorption peak than the leading adsorption peak. However, the energy difference and the calculated ratio does not clearly identify haematite. Although, the ratio is observed to decrease with the expected increase of oxidation.

Table 5.2: ΔE and intensity ratio parameters for the Fe $L_{2,3}$ -edge spectra illustrated in Figure 5.11

Parameter	Sample						
	(a)	(b)	(c)	(d)	(e)	(f)	(g)
ΔE (eV)	1.2	0.9	1.2	1.2	1.3	1.4	1.3
Intensity ratio (i/ii)	1.05	1.06	1.10	0.93	0.97	0.94	0.62

Pyrite has a characteristic minor peak at 712.5 eV, which is commonly used as an identifier. This minor peak arises from the Fe 4s and 4p states hybridising with the S 3p states [4,48-50]. This characteristic peak is observed in the spectra displayed in Figure 5.11 and labelled as feature iii. Using this feature as an identifier, pyrite can be confirmed to be present in the samples for HH media controls for 48 h and 72 h, samples exposed to EPS supernatant for 48 h (frozen and fresh), and the sample exposed to *L. f* adjusted to chalcopyrite for 72 h. There are two samples where this feature is not clearly identified, these are samples that have been exposed the EPS supernatant for extended period of times of 72 h and 7 days.

Chalcopyrite exhibits a strong, asymmetric Fe L_3 adsorption peak at 706.8 eV, with a pre-edge feature present at 705.5 eV [3,10]. This feature is expected to arise from the hybridisation of S 3p and Fe 3d states, with transition of the Fe L_3 to unoccupied electron states below the ionisation threshold [10]. This feature is observed as broadening on the low energy side of the leading adsorption peak in Figure 5.11. There is a feature on the higher binding energy side of the leading adsorption peak at approximately 708 eV, this is what gives rise to the asymmetric shape. The feature is caused by the presence of iron oxidation products, such as FeOOH, therefore the intensity increases with increasing oxidation [3,10].

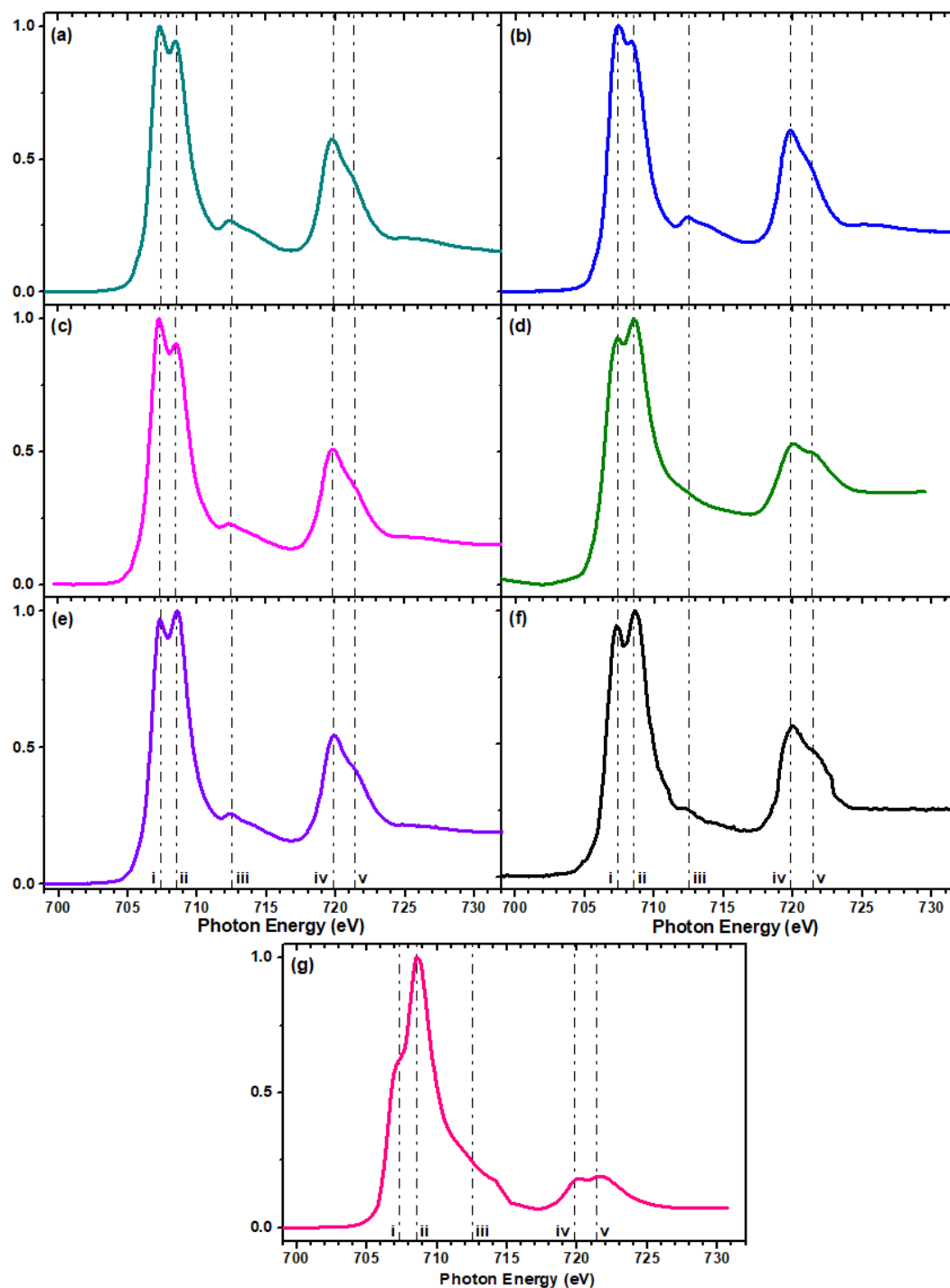


Figure 5.11: TEY Fe $L_{2,3}$ -edge NEXAFS spectrum for mixed mineral coupon exposed to (a) HH media control 48 h; (b) HH media control 72 h; (c) EPS supernatant 48 h – frozen; (d) EPS supernatant 72 h; (e) EPS supernatant 48 h – fresh; (f) *L. f* on Cp 72 h; (g) EPS supernatant 7 days

Although the results presented in Table 5.2 show an indication of increasing oxidation as a function of exposure time, the parameters are inconclusive in determining what exact phases are present. Likewise, the spectra exhibit the characteristic features for all three phases but does not provide in-depth insight into the surface species due to the mixed phased nature of

the sample. This can be seen as a downfall of FOV analysis of mixed phase samples. Analysis of the Fe L_{2,3} edge through the 3D-stack feature allows in depth analysis of all iron containing phases present.

5.3.3.2.1 EPS 48 h Analysis

Analysis of the 3D-stack of the 48 h EPS supernatant sample revealed three distinct iron phases identified as oxidised chalcopyrite, pyrite and haematite. The resulting spectra are shown in Figure 5.12, with the inset images depicting the corresponding regions. Analysis of the stack failed to identify an unoxidized chalcopyrite phase. Although the spectrum (Figure 5.12 a) shows an uncharacteristic splitting of the leading adsorption peak, the leading adsorption peak occurs at 706.8 eV and there is evidence of a pre-edge feature at 705.5 eV, in line with what is expected of chalcopyrite. The feature present at 708.5 eV is expected to be iron oxidation products such as FeOOH [3], therefore indicating an oxidised chalcopyrite phase. This aligns with the Cu L_{2,3}-edge spectrum (shown in Figure 5.10 c) which confirms the presence of chalcopyrite and indicates oxidation. The pyrite phase (Figure 5.12 b) was identified thorough the characteristic adsorption peak at 712.5 eV. Although the spectrum is cut off at approximately 714 eV, the FOV spectrum of the sample (Figure 5.11 c) clearly illustrates the characteristic adsorption peak, which is only exhibited in this phase. The difference in adsorption energy of this phase is 1.35 eV, with a ratio of 1.05, indicating the pyrite phase is oxidised. Oxidation of the pyrite phase is expected when galvanic interactions occur. The haematite phase, Figure 5.12 (e), displays a typical iron oxide shape. While the L₃-edge demonstrates similarities to haematite, goethite and jarosite with the ratio between the first and second adsorption peak being 0.58. However, jarosite typically has a splitting on the second adsorption peak [49], therefore jarosite can be ruled out. The greatest differentiating features between haematite and gothite is the energy of the leading adsorption edge and the difference in energy between the two adsorption peaks. This region has a leading adsorption edge at approximately 706.5 eV with a difference in energy of 1.5 eV. These parameters align with the phase being haematite rather than goethite.

The RGB overlay shown in Figure 5.12 (d) illustrates the special distribution of these regions; chalcopyrite (green), pyrite (red) and haematite (blue). This overlay indicates pyrite as the primary phase and a lack of clear grain boundaries between the phases. This could be an effect caused by the polishing of the sample prior to exposure or leaching due to the acidic

nature of the EPS supernatant. Interestingly, the haematite phase is seen to be surrounded by the oxidised chalcopyrite, and in some cases the phases are superimposed. This indicates a relationship between haematite and the oxidation of the chalcopyrite. As the micro-flotation test results in Figure 5.6 indicate greater recovery of haematite over pyrite in both the collector-free and in the presence of PIPX collector, the areas where the chalcopyrite and haematite phases are superimposed could be an indication of copper attachment to haematite. Copper activation of haematite would explain the increased recovery in the presence of PIPX and the Cu L-edge indicates the presence of small quantities of CuO and/or Cu(OH)₂. It is reasonable to expect the regions where this is happening to overlap with both the haematite and chalcopyrite spectra.

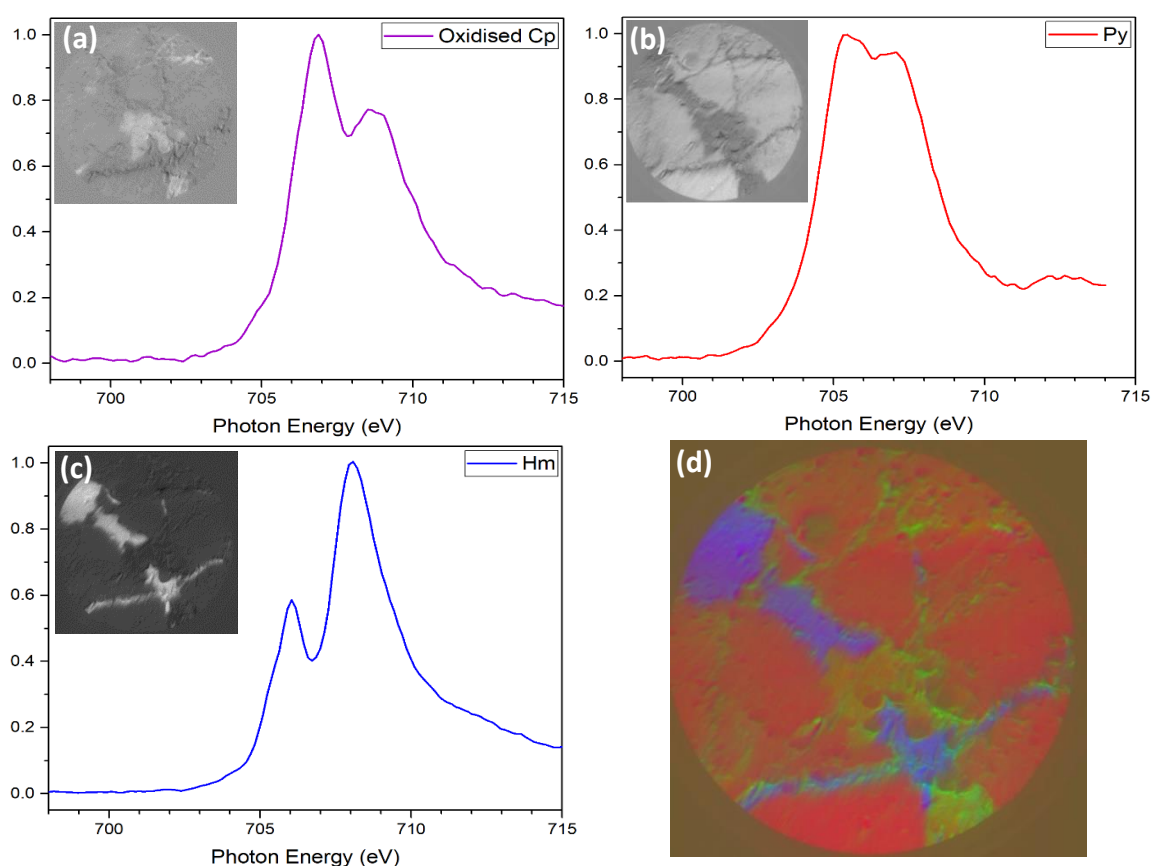


Figure 5.12: Extracted Fe L₃-edge spectra collected from the stack of the 48 h EPS supernatant (frozen) sample identifying (a) oxidised chalcopyrite (b) pyrite (c) haematite and (d) RGB overlay of mapped spectra; inset images illustrate what regions correspond with the spectra. FOV = 450µm

5.3.3.2.2 EPS 72 h Analysis

Similar to the 48 h sample, the Fe 3D-stack of the 72 h exposed EPS supernatant sample was analysed. Analysis indicated three clearly identifiable iron containing phases, these are

illustrated in Figure 5.13; (a) chalcopyrite (slightly oxidised [3,10]), (b) pyrite, and (c) haematite. Figure 5.13 (d) shows the RGB spatial distribution of the corresponding spectra, with green representing chalcopyrite, red representing pyrite and blue representing haematite. The differentiation of the haematite phase was conducted similar to what was described above for the 48 h sample. The Fe L_{2,3}-edge spectra is representative of an iron oxide phases, such as haematite (Fe₂O₃) and goethite (α-FeO(OH)). The two features, indicated by the black arrows and labelled as (i) and (ii), were used to identify the phase as haematite with the presence of oxy-hydroxides. The presence of oxy-hydroxides can change the intensity ratio and give rise to an additional feature in the L₂ edge [24,49]. A study by Bath [24] indicates these surface species are present in the dissolution process of haematite in acidic conditions, therefore implying the occurrence of leaching in these conditions.

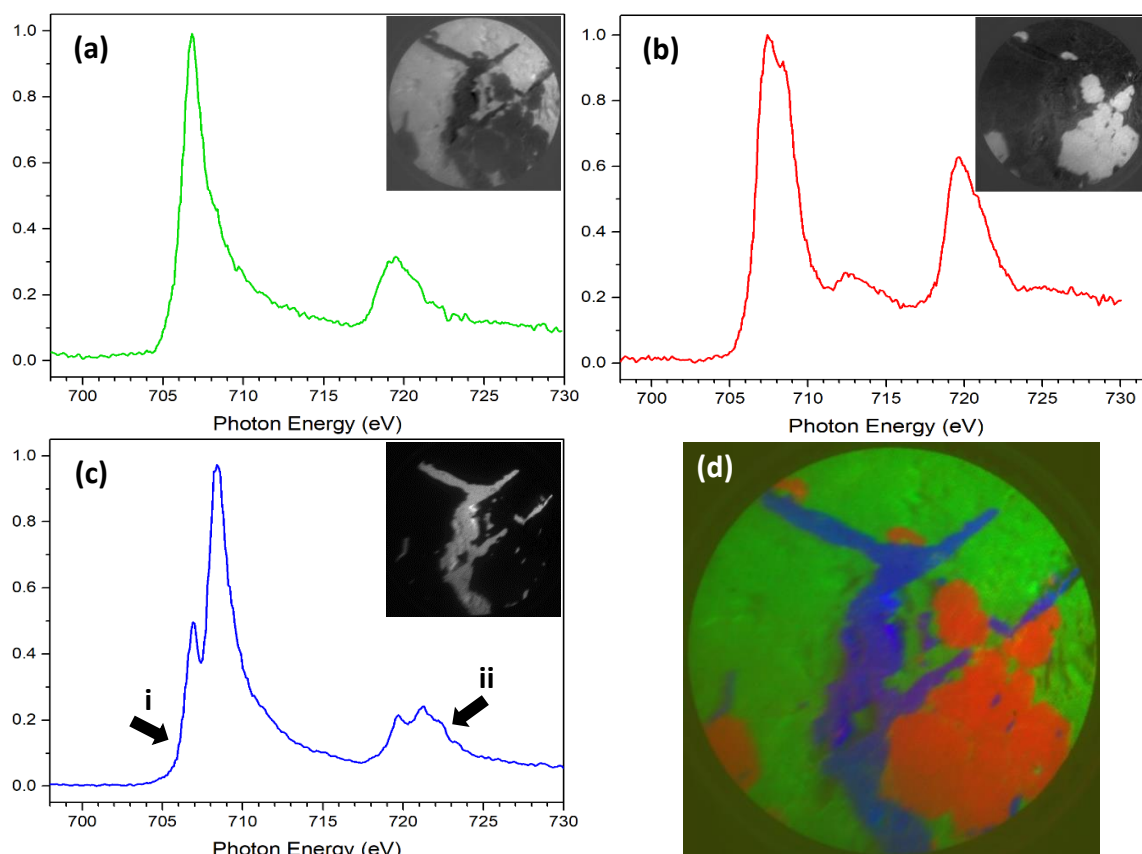


Figure 5.13: Extracted Fe L_{2,3} – edge spectra collected from the stack of the 72 h EPS supernatant sample identifying (a) chalcopyrite (b) pyrite (c) haematite and (d) RGB overlay of mapped spectra; inset images illustrate which regions correspond to the respective spectrum. FOV = 450µm

The RGB overlay shown in Figure 5.13 (d) indicates chalcopyrite as the primary phase. Unlike the 48 h sample, the phase boundaries in this sample are clearly defined. Interestingly, this correlates with the absence of Cu (II) observed in the Cu L-edge. There are some regions that

overlap; however, this is only observed around some of the grain boundaries. The residual of the three-component fit was analysed and resulted in the detection of a fourth phase. This phase was identified as oxidised chalcopyrite and the corresponding spectra and spatial distribution are shown in Figure 5.14. The distribution of this phase matches the areas in the RGB composite which show overlapping phases. It is interesting to note that this phase is only observed around the phase boundaries, unlike the 48 h samples where unoxidised chalcopyrite was not observed. This is of interests as the decrease in oxidation of the chalcopyrite phase correlates with a decrease in the micro-flotation tests recovery.

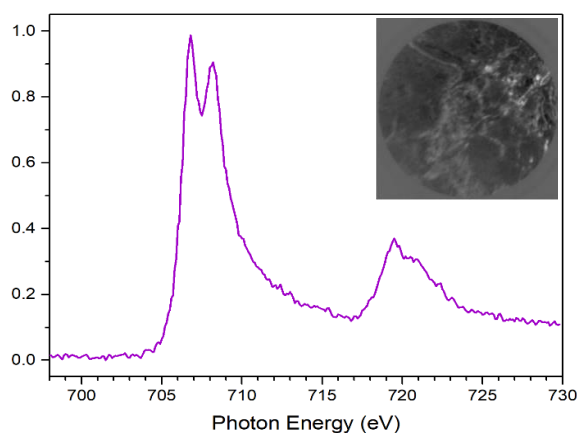


Figure 5.14: Extracted Fe spectra from the residual of the three-component fit for 72 h EPS supernatant sample, the inset image illustrates the region where the spectrum is found. FOV = 450 μ m

5.3.3.2.3 EPS 168 h (7 day) Analysis

The Fe 3D-stack of the sample exposed to the EPS supernatant for 7-days was analysed to investigate the changes that occur over extended periods of time. Analysis of the stack identified three phases, none of which were a pyrite phase. Due to the acidic nature of the EPS supernatant, it is expected that the absence of a pyrite phase may be caused by the oxidation and leaching effects. Pyrite dissolution in acidic environments has been well studied. At exposure times of 7-days (168 h) literature suggests that dissolution of pyrite should be occurring, producing Fe (III) – OH states on the surface and SO_4^{2-} -aqueous species [27,53]. The three phases identified were chalcopyrite (green), oxidised chalcopyrite (red) and haematite (blue) and are illustrated in Figure 5.15. Analysis of the images captured over the Cu L-edge indicates the presence of copper within the green and red phases. The second phase, oxidised chalcopyrite, was identified through the well-defined feature present at

708.3 eV, indicative of iron oxide/hydroxide states [3]. Interestingly, there is no distinct evidence of iron oxyhydroxides present as there was with the 72 h sample.

The RGB overlay, shown in Figure 5.15 (d), suggests chalcopyrite is the dominant phase. There is also an indication that there are areas with intergrown chalcopyrite and haematite. The oxidised chalcopyrite is seen to occur throughout the chalcopyrite phase and along the boundary of the haematite phase. While some overlap does occur, the phase boundaries are still quite sharp.

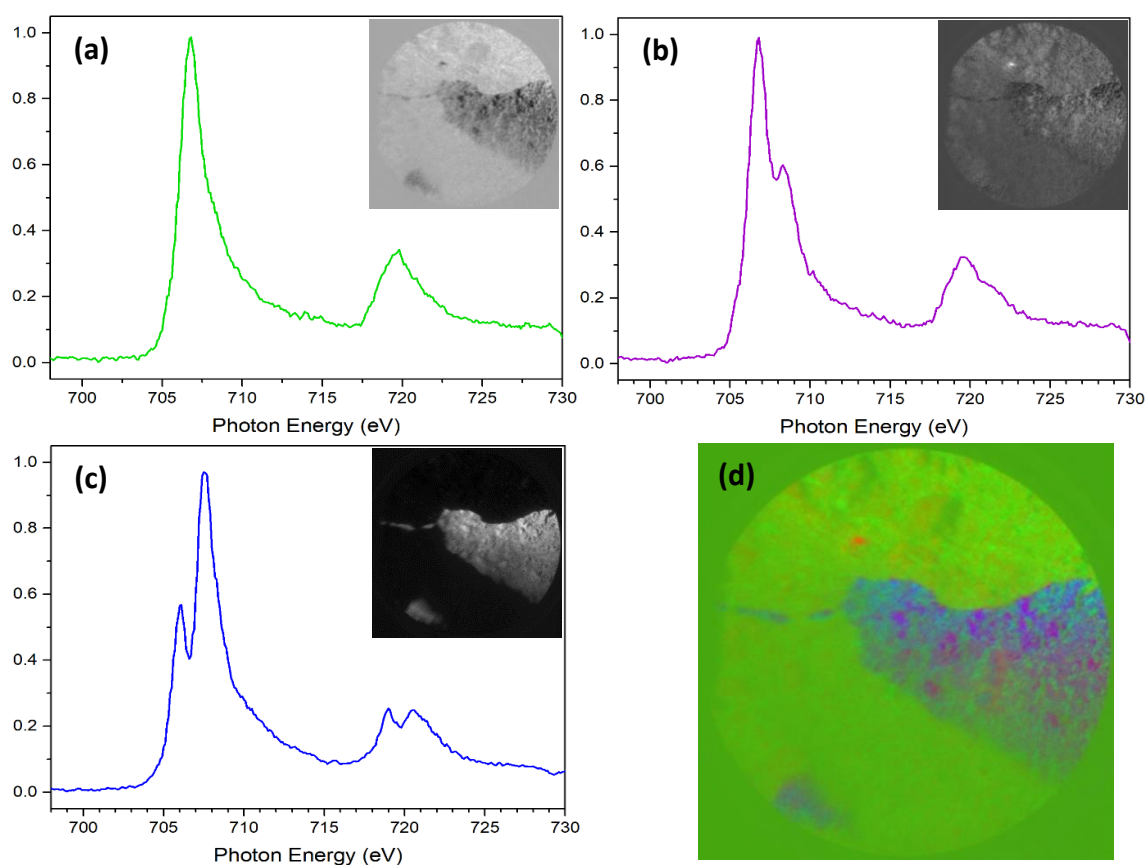


Figure 5.15: Extracted Fe L_{2,3} – edge spectra collected from the stack of the 7-day EPS supernatant sample identifying (a) chalcopyrite (b) pyrite (c) haematite and (d) RGB overlay of mapped spectra; inset images demonstrate the regions where the respective spectrum is identified. FOV = 450 μ m

Overall, analysis of the iron 3D-stacks indicated that the primary phases present are chalcopyrite, pyrite, haematite and oxidised chalcopyrite. Results also indicate that the pyrite phase experiences preferential oxidation to the chalcopyrite phase. This preferential oxidation is an indication of galvanic interactions.

5.3.3.3 Oxygen K-edge Analysis

The leading adsorption edge of the oxygen K-edge spectra presented in Figure 5.16 is approximately 530 eV. The doublet feature observed, indicated by feature (i) and (ii), has previously been observed for FeOOH and Fe₂O₃ states [43,54]. An adsorption peak at this energy indicates the hybridisation between the O 2*p* orbitals and 3*d* orbitals of a transition metal, with metal oxides expected to exhibit adsorption peaks in two distinct regions representing the complexing the 3*d* orbitals and 4*sp* orbitals, and weakly structured metal 4*sp* orbital complexing with O 2*p* orbitals [54]. The doublet which is observed at this energy is indicative of iron oxides with the splitting of the adsorption peak correlating to the octahedral field splitting of the Fe 3*d* orbitals to the t_{2g} and e_g orbitals, respectively [52,54].

All samples exhibit a doublet at the adsorption edge, which is expected due to the presence of haematite. However, there is a noticeable increase in intensity as a factor of time and exposure conditions. This indicates a change in the number of unoccupied Fe 3*d* states interacting with O 2*p* states, and a change in concentration of the iron oxides [54]. These results indicate that greater exposure leads to either a greater concentration of iron oxides and/or more unoccupied 3*d* states, with a decrease in intensity indicating the adsorption of biofilm and/or cells. A change in the intensity ratio of the doublet indicates the presence of other oxygen species which are not assigned to haematite [52]. Other contributing species include Cu (II) oxide [45,55], which has been detected in the Cu L-edge analysis. However, it is important to note that the Cu (II) oxide is not expected to be octahedrally coordinated and does not exhibit t_{2g} and e_g splitting [54], and therefore contributes to only one of the adsorption peaks in the doublet altering the ratio.

A third adsorption peak, shown as feature (iii), is observed in both 48 h EPS supernatant samples. A transition at this energy is attributed to functional groups of OH and NO [52,56]. A study by Frati, et al. [55] suggests this feature arises from organic compounds which contain CO, ON and OH functional groups. Organic compounds which contain these functional groups are also seen to produce adsorption peaks between 542 eV and 549 eV from σ* transitions [55]. The spectra illustrated in Figure 5.16 indicate the presence of subtle features in this region. Therefore, it is concluded that the origin of this slight inflection is indicative of organic molecule attachment. As no broad peak is present at 543 eV, the likelihood of adsorbed H₂O contributing to the OH signal is minimal [56]. Rao and Finch [32] indicate the presence of

nitrogen can decrease the effects of galvanic interactions and the activity of dissolved oxygen. Although a decrease in the intensity of the e_g/t_{2g} feature is observed, the recovery of chalcopyrite remains reasonable and oxidation of the sample is still observed, a strong presence of NO groups on the surface has been ruled out.

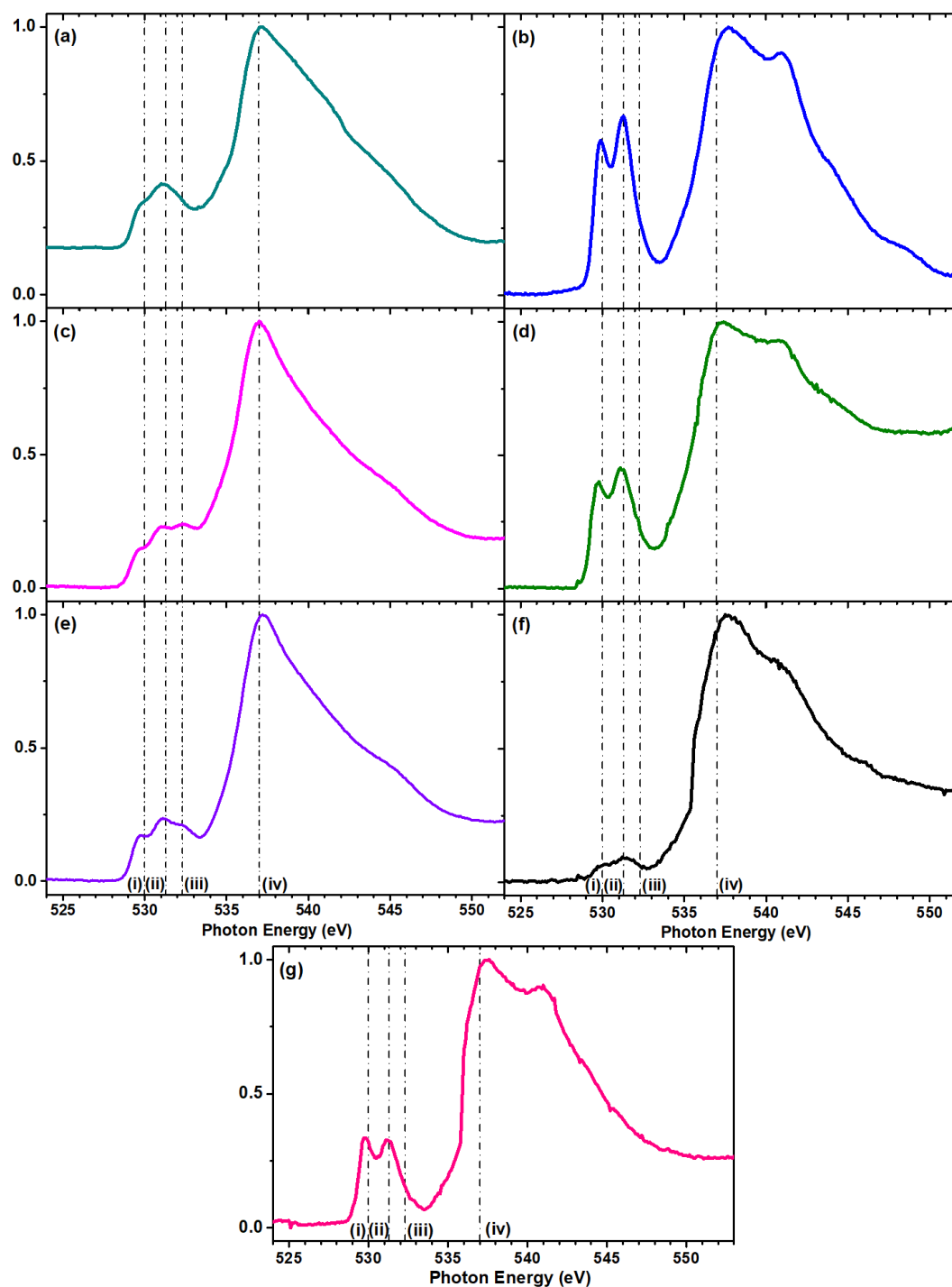


Figure 5.16: TEY O K-edge NEXAFS spectrum for (a) HH media control 48 h; (b) HH media control 72 h; (c) EPS supernatant 48 h – Frozen; (d) EPS supernatant 72 h; (e) EPS supernatant 48 h – Fresh; (f) *L. f* adjusted to Cp 72 h; (g) EPS supernatant 7-days

Interestingly, the images of the surface for the EPS supernatant 48 h sample captured at the energies of 530 eV (peak i), 531.3 eV (peak ii) and 532.3 eV (peak iii), shown in Figure 5.17 a-c, does not show a significant change in the spatial distribution of the oxygen states. This indicates that the components which contribute to the adsorption peak present at 532.3 eV are present in the same area as the iron oxide states, which corresponds to the haematite phase. The lack in the depth of contrast indicates the presence of oxygen species over the surface of the sample. This observation is also supported by the iron analysis, which indicates the presence of oxidised pyrite and chalcopyrite. The image shown in Figure 5.17 (d) illustrates the spatial distribution of the oxygen component corresponding to the main adsorption peak at 537 eV (peak iv), indicating only minor changes in the distribution.

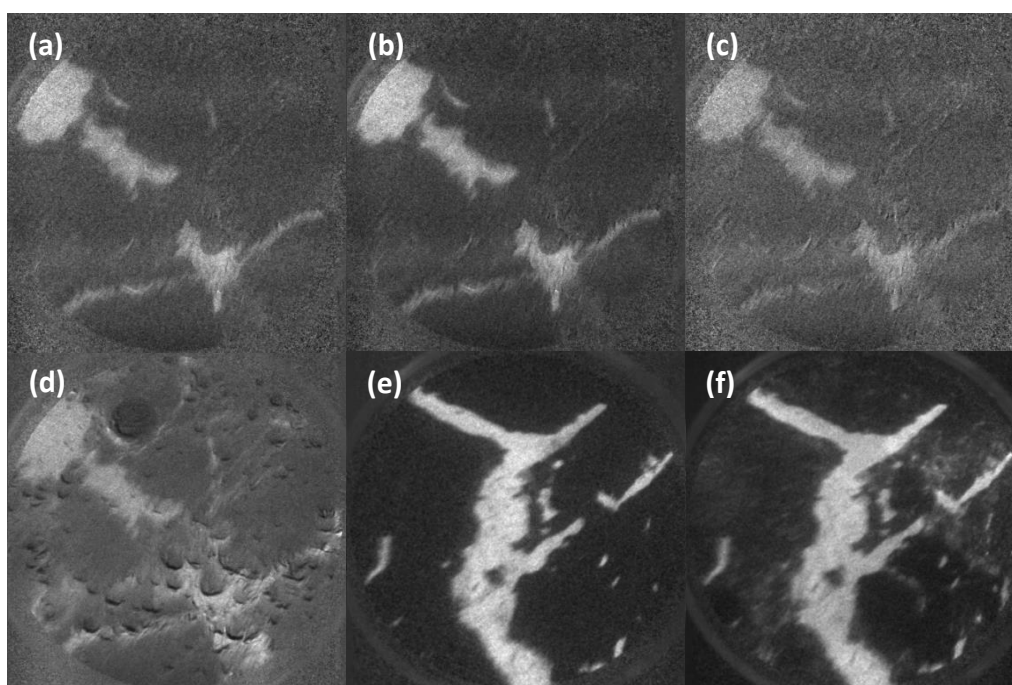


Figure 5.17: O K-edge images of EPS supernatant exposed samples for 48 h (a-d) and 72 h (e-f) at a photon energy of 530 eV (a), 531.3 eV (b and e), 532.3 eV (c) and 537 eV (d and f). FOV = 450 μ m

The images present in Figure 5.17 (e and f) illustrate the difference in the spatial distribution of the oxygen states of the EPS supernatant sample at 72 h exposure. Image (e) corresponds with peak ii (531.5 eV), while image (f) corresponds with peak iii (537 eV). These images indicate a significant change in the spatial distribution. Unlike the 48 h sample, the distribution of the oxygen component at 537 eV is observed on both the haematite phase and the chalcopyrite phase. The iron analysis of this sample indicates the presence of oxidised chalcopyrite, however the spatial distribution of oxidised chalcopyrite does not entirely

overlap with the spatial distribution of the oxygen at 537 eV. This indicates the presence of other oxygen components, such as organic molecules, are present on the chalcopyrite phase.

5.3.3.4 Carbon K-edge Analysis

The carbon K-edge was analysed through field of view (FOV) spectra, displayed in Figure 5.19, and corresponding images. The spectra were energy corrected so the leading adsorption edge is present at 285.1 eV, aligning with the characteristic C 1s transition of π^* C-C/C=C/C-H [4,57-60]. A change in intensity of this leading adsorption peak is observed with an increase in exposure time, correlating with a change in concentration of the functional groups with a transition observed at this energy.

Energies and transitions for the C K-edge is shown in Table 5.3. These values indicate the overlapping energies of transitions for different functional groups. Due to the overlapping of C 1s transitions, differences in the functional groups present may not be observed visually. Deconvoluting the spectra allows for the assignment of functional groups, which was used to determine differences between samples. Ade and Hitchcock [61] discuss the correlation between the excitation energy and oxidation state, allowing the differentiation between a carbonyl group originating from a polysaccharide or a protein. Samples were fit with an arctangent function and Gaussian peaks up to 290.5 eV, as the transitions observed after 295 eV overlap with the potassium L_{2,3} edge [59]. The number of Gaussian peaks used varied between samples, the common Gaussian peaks used illustrated in Figure 5.19, with the energies of 283.8 eV (i), 285.1 eV (ii), 286.8 eV (iii), 287.4 eV (iv), 288.5 eV (v), 289.5 eV (vi), and 290.5 eV (vii).

Table 5.3: C 1s K-edge NEXAFS transitions

Energy (eV)	C 1s Transition
283.7 – 284.3	Unsaturated aromatic C–H, low energy π^* states, quinone [59,60]
284.9 – 285.5	π^* protonated/alkylated aromatic [60] π^* C–C, C=C [4,13,57-59,61]
286.8	π^* ketone/aldehyde, crosslinking polysaccharide [59,60,62]
287.1 – 287.4	π^* ketone C=O, aromatic C–OH [59,60]
287.8 – 288.2	Amide [59]

288.1 – 288.6	π^* resonance of carboxylic C=O, acetic/acetate, polysaccharide [57,58,60,62] Aliphatic COOH [59]
288.6	π^* carboxyl group associated with polysaccharide [57]
289.2 – 289.6	π^* aliphatic C–OH [59] C 1s – 3p/ σ^* C–OH [60]
290	Carboxyl bound to iron [62]
290.2 – 290.6	π^* carbonate [59] σ^* C–C [13,63]

The baseline samples of HH media at 48 h and 72 h exposure are shown in Figure 5.19 (a) and (b), respectively. The 48 h sample was fit with eight gaussian peaks corresponding to unsaturated CH (283.9 eV) [59,60], C-C and C=C (285 eV) [58,61], aromatic aldehydes (286 eV) [59], ketones/amides (286.8 eV) [59,60], ketones (287.5 eV) [59,60], carboxylic acids (288.2 eV)[58,62], 3p/ σ^* COH (289.5 eV) [60], and σ^* C-C (290.5 eV); while the 72 h sample was fit using only six gaussian peaks, excluding the unsaturated CH and aldehyde contributions. The difference between these samples includes a decrease of intensity of the leading adsorption edge at 285 eV, as well as no clearly identified contribution from unsaturated C-H groups and aromatic aldehydes. The decrease in intensity at the leading adsorption edge is determined to be due to an overall decrease in the carbon content, as the 72 h raw spectrum exhibits an overall decrease in intensity. As the HH media is acidic in nature and does not contain a source of carbon, the overall decrease in carbon is suspected to be a result of leaching. The leaching effect of the media has been investigated through scanning electron microscopy and discussed in chapter 4 above.

The samples exposed to the EPS supernatant were all fit with eight gaussian and the sample exposed to *L. f* adapted to chalcopyrite was fit with nine gaussian peaks, six of which were consistent throughout. These six components correspond to the C 1s transitions for C- C/C=C, ketone/amide, ketone, carboxylic acids, 3p/ σ^* C-OH, and carbonate/ σ^* C-C. Interestingly, of the other components fit to the samples, the 48 h EPS supernatant sample shows no similarities to the 72 h and 7-day EPS supernatant samples. The longer exposure times indicate the presence of amines, indicating the presence of proteins. The presence of the

amide contribution in the 72 h EPS supernatant sample correlates with a decrease of recovery for these conditions, as discussed above.

The fits for the 72 h and 7 day EPS supernatant samples also include a component which corresponds to carboxylic acid attached to iron. The Fe stack analysis of these samples also indicates the presence of iron oxyhydroxides. Barco and Edwards [64] suggests that the proteins bind to iron oxyhydroxides. Figure 5.18 illustrates the spatial distribution of carbon transitions for amides at 288 eV (a) and carboxyl bound to iron at 290 eV (b), and iron transition for iron oxyhydroxide at 708.5 eV (c). Similar distribution is observed for the amide component and the carboxyl bound to iron. This supports the idea presented by Barco and Edwards [64]. Comparison to the distribution observed for the iron transition for iron oxyhydroxide indicates that the distribution of the carboxyl is primarily associated with the haematite phase, however, it also shows distribution over the chalcopyrite and pyrite regions. This indicates that at the 72 h time frame there is no preferential attachment of the EPS components to a single mineral phase.

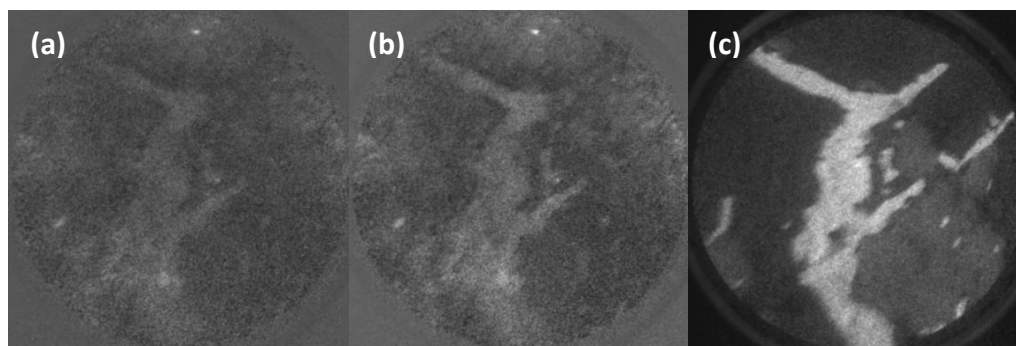


Figure 5.18: Images of the EPS supernatant 72 h samples showing the spatial distribution of carbon at 288 eV (a), 290 eV (b) and iron at 708.5 eV (c). FOV = 450 μm .

While the EPS supernatant samples at 72 h and 7 days indicate a relationship between the distribution of amides with carboxyl groups bound to iron, this is not observed in the *L. f* adapted to Cp sample. This sample exhibited the presence of amides, but the presence of carboxyl bound iron was not detected. This indicates that the bacterial cells are not required in the system for the EPS excreted by the *L. f* adapted to Cp to attach to and/or oxidise the surface.

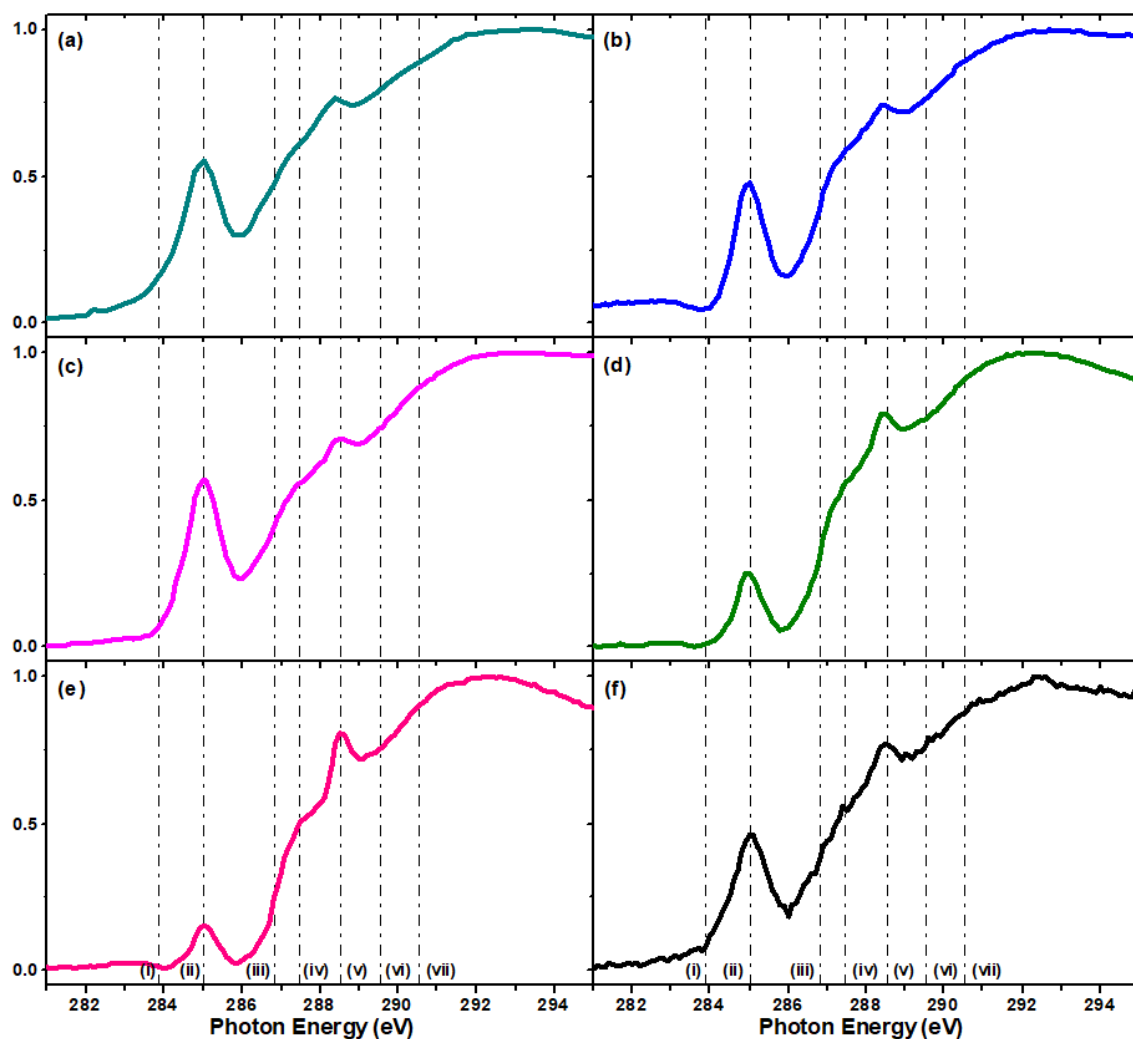


Figure 5.19: TEY C K-edge spectrum for mixed mineral coupons exposed to (a) HH media control 48 h; (b) HH media control 72 h; (c) EPS supernatant 48 h frozen; (d) EPS supernatant 72 h; (e) EPS supernatant 7-day; (f) *L. fCp* 72 h

5.3.4 Spatial Distribution Overlay

RGB composites which illustrate the spatial distribution of different elements can be used to determine differences between samples and exposure times. The RGB composites shown in Figure 5.20 below illustrate the spatial distribution of copper (red), carbon (green) and oxygen (blue). The intensity of each component has been scaled. As iron is not used in the RGB composite, the darker areas of the sample reflect where the pyrite phase is. Interestingly, at the 48 h exposure the carbon is observed over the pyrite and haematite phase but not the chalcopyrite phase (the identification of these phases has been discussed above). However, at 72 h exposure the carbon component is observed to overlap with all three phases, suggesting a potential window of preferential attachment for the EPS components to pyrite and haematite phases. This observation at 72 h correlates with the decrease in recovery of

chalcopyrite in the mixed mineral flotation tests. The increased presence of carbon correlates with a decrease in recovery and a decrease in hydrophobicity, it is predicted that the EPS components are primarily polysaccharides, and are acting as a depressor [65-67].

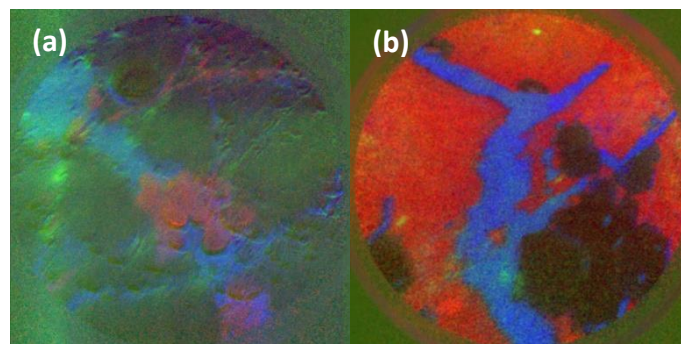


Figure 5.20: RGB overlay for EPS Supernatant samples at 48 h – frozen (a); 72 h (b), where Red = Copper, Green = Carbon, and Blue = Oxygen. FOV = 450 μm .

5.4 Conclusions

This chapter has shown a relationship between the surface chemistry of pyrite, chalcopyrite and haematite and recovery in the presence of EPS supernatant from *L. f* adapted to chalcopyrite. The results presented in this chapter indicate a preferential attachment of EPS to pyrite and haematite at 48 h, which correlates with optimal separation and recovery of chalcopyrite.

The comparison of single mineral flotation test results indicate that recovery of haematite is unfavourable in these conditions, even with the use of PIPX collector (10^{-4} M). Differential flotation tests show the best collector-free flotation was observed at 48 h, with the addition of PIPX collector creating optimal flotation at 72 h. Surface analysis conducted by PEEM indicates the presence of Cu (II) species is only detectable at 48 h exposure, with a change in the coordination of copper states present at longer exposure times. The presence of the Cu (II) species correlates with the presence of oxygen species on the chalcopyrite phase. Exposure to EPS supernatant results in a greater concentration of FeOOH and Fe₂O₃ states than HH media. Comparison of the 48 h and 72 h O K-edge and C K-edge indicate an increase of chalcopyrite oxidation and the presence of amines/proteins and carboxylic acid attached to iron at 72 h. The presence of these correlate with a decrease in recovery in both the single mineral and differential flotation tests. Captive bubble contact angle results also indicate that the surface changes induced by EPS supernatant exposure increase the homogeneity of the

sample, increasing the wettability of pyrite and decreasing the wettability of chalcopyrite. The spatial distribution overlay indicates that there is preferential attachment of the carbon component within the EPS supernatant to both pyrite and haematite phases at 48 h, with no preferential attachment observed at 72 h.

5.5 References

1. Ng, W.S.; Sonsie, R.; Forbes, E.; Franks, G.V. Flocculation/flotation of hematite fines with anionic temperature-responsive polymer acting as a selective flocculant and collector. *Minerals Engineering* **2015**, *77*, 64-71, doi:<https://doi.org/10.1016/j.mineng.2015.02.013>.
2. Klimpel, R.R. Froth Flotation. In *Encyclopedia of Physical Science and Technology (Third Edition)*, Meyers, R.A., Ed. Academic Press: New York, 2003; <https://doi.org/10.1016/B0-12-227410-5/00262-3pp>. 219-234.
3. Kalegowda, Y.; Chan, Y.L.; Wei, D.H.; Harmer, S.L. X-PEEM, XPS and ToF-SIMS characterisation of xanthate induced chalcopyrite flotation: Effect of pulp potential. *Surf Sci* **2015**, *635*, 70-77, doi:10.1016/j.susc.2014.12.012.
4. La Vars, S.; Newton, K.; Quinton, J.; Cheng, P.-Y.; Wei, D.-H.; Chan, Y.-L.; Harmer, S. Surface chemical characterisation of pyrite Exposed to *Acidithiobacillus ferrooxidans* and associated extracellular polymeric substances. *Minerals* **2018**, *8*, 132.
5. Read, M.L.; Morgan, P.B.; Kelly, J.M.; Maldonado-Codina, C. Dynamic Contact Angle Analysis of Silicone Hydrogel Contact Lenses. *Journal of Biomaterials Applications* **2011**, *26*, 85-99, doi:10.1177/0885328210363505.
6. Campbell, D.; Carnell, S.M.; Eden, R.J. Applicability of Contact Angle Techniques Used in the Analysis of Contact Lenses, Part 1: Comparative Methodologies. *Eye & Contact Lens* **2013**, *39*, 254-262, doi:10.1097/ICL.0b013e31828ca174.
7. Brugnara, M. Contact Angle. Available online: <https://imagej.nih.gov/ij/plugins/contact-angle.html> (accessed on 19 March).
8. Lamour, G.; Hamraoui, A.; Buvailo, A.; Xing, Y.; Keuleyan, S.; Prakash, V.; Eftekhari-Bafrooei, A.; Borguet, E. Contact Angle Measurements Using a Simplified Experimental Setup. *Journal of Chemical Education* **2010**, *87*, 1403-1407, doi:10.1021/ed100468u.
9. Image Processing and Analysis in Java. Analyze Menu. Available online: <https://imagej.nih.gov/ij/docs/menus/analyze.html> (accessed on 19 March).
10. Acres, R.G.; Harmer, S.L.; Beattie, D.A. Synchrotron PEEM and ToF-SIMS study of oxidized heterogeneous pentlandite, pyrrhotite and chalcopyrite. *J Synchrotron Radiat* **2010**, *17*, 606-615, doi:10.1107/S0909049510026749.
11. Hitchcock, A.P. *aXis2000*, 2009. Available from <http://unicorn.mcmaster.ca/aXis2000.html/>
12. Ravel, B.; Newville, M. ATHENA, ARTEMIS, HEPHAESTUS: data analysis for X-ray absorption spectroscopy using IFEFFIT. *Journal of Synchrotron Radiation* **2005**, *12*, 537-541, doi:10.1107/S0909049505012719.
13. Latham, K.G.; Simone, M.I.; Dose, W.M.; Allen, J.A.; Donne, S.W. Synchrotron based NEXAFS study on nitrogen doped hydrothermal carbon: Insights into surface functionalities and formation mechanisms. *Carbon* **2017**, *114*, 566-578, doi:10.1016/j.carbon.2016.12.057.
14. Singh, B.; Fang, Y.; Cowie, B.; Thomsen, L. NEXAFS and XPS characterisation of carbon functional groups of fresh and aged biochars. *Org Geochem* **2014**, *77*, 1-10, doi:10.1016/j.orggeochem.2014.09.006.
15. Blowes, D.; Ptacek, C.; Jambor, J.; Weisener, C. The geochemistry of acid mine drainage. *Treatise on geochemistry* **2003**, *9*, 149-204.
16. Ahlberg, E.; Forssberg, K.; Wang, X. The surface oxidation of pyrite in alkaline solution. *Journal of Applied Electrochemistry* **1990**, *20*, 1033-1039.

17. Abaka-Wood, G.B.; Addai-Mensah, J.; Skinner, W. A study of flotation characteristics of monazite, hematite, and quartz using anionic collectors. *International Journal of Mineral Processing* **2017**, *158*, 55-62, doi:<https://doi.org/10.1016/j.minpro.2016.11.012>.
18. Fuerstenau, M.C.; Sabacky, B.J. On the natural floatability of sulfides. *International Journal of Mineral Processing* **1981**, *8*, 79-84, doi:[https://doi.org/10.1016/0301-7516\(81\)90008-9](https://doi.org/10.1016/0301-7516(81)90008-9).
19. Chandraprabha, M.N.; Natarajan, K.A.; Modak, J.M. Selective separation of pyrite and chalcopyrite by biomodulation. *Colloids Surf B Biointerfaces* **2004**, *37*, 93-100, doi:10.1016/j.colsurfb.2004.06.011.
20. Khmeleva, T.N.; Beattie, D.A.; Georgiev, T.V.; Skinner, W.M. Surface study of the effect of sulphite ions on copper-activated pyrite pre-treated with xanthate. *Minerals Engineering* **2003**, *16*, 601-608, doi:10.1016/S0892-6875(03)00133-X.
21. Fairthorne, G.; Fornasiero, D.; Ralston, J. Effect of oxidation on the collectorless flotation of chalcopyrite. *International Journal of Mineral Processing* **1997**, *49*, 31-48, doi:[https://doi.org/10.1016/S0301-7516\(96\)00039-7](https://doi.org/10.1016/S0301-7516(96)00039-7).
22. Kocabag, D.; Shergold, H.L.; Kelsall, G.H. Natural oleophilicity/hydrophobicity of sulphide minerals, II. Pyrite. *International Journal of Mineral Processing* **1990**, *29*, 211-219, doi:[https://doi.org/10.1016/0301-7516\(90\)90054-3](https://doi.org/10.1016/0301-7516(90)90054-3).
23. Shimizu, K.; Tschulik, K.; Compton, R. Exploring the mineral–water interface: reduction and reaction kinetics of single hematite (α -Fe₂O₃) nanoparticles. *Chemical science* **2016**, *7*, 1408-1414.
24. Bath, M.D. Some aspects of the acid dissolution of hematite. University of British Columbia, 1968.
25. Broden, T. Electrochemical characterization of xanthate chemisorption on copper and enargite. University of Montana, 2016.
26. Schippers, A.; Sand, W. Bacterial leaching of metal sulfides proceeds by two indirect mechanisms via thiosulfate or via polysulfides and sulfur. *Appl Environ Microbiol* **1999**, *65*, 319-321.
27. Descostes, M.; Vitorge, P.; Beaucaire, C. Pyrite dissolution in acidic media. *Geochimica et Cosmochimica Acta* **2004**, *68*, 4559-4569, doi:10.1016/j.gca.2004.04.012.
28. Yang, Y.; Tan, S.N.; Glenn, A.M.; Harmer, S.; Bhargava, S.; Chen, M. A direct observation of bacterial coverage and biofilm formation by *Acidithiobacillus ferrooxidans* on chalcopyrite and pyrite surfaces. *Biofouling* **2015**, *31*, 575-586, doi:10.1080/08927014.2015.1073720.
29. Wei, L.; Li, Y.; Noguera, D.R.; Zhao, N.; Song, Y.; Ding, J.; Zhao, Q.; Cui, F. Adsorption of Cu(2+) and Zn(2+) by extracellular polymeric substances (EPS) in different sludges: Effect of EPS fractional polarity on binding mechanism. *J Hazard Mater* **2017**, *321*, 473-483, doi:10.1016/j.jhazmat.2016.05.016.
30. Chandra, A.P.; Puskar, L.; Simpson, D.J.; Gerson, A.R. Copper and xanthate adsorption onto pyrite surfaces: Implications for mineral separation through flotation. *International Journal of Mineral Processing* **2012**, *114*, 16-26, doi:10.1016/j.minpro.2012.08.003.
31. Nguyen, A.V. Froth Flotation☆. In *Reference Module in Chemistry, Molecular Sciences and Chemical Engineering*, Elsevier: 2013; <https://doi.org/10.1016/B978-0-12-409547-2.04401-2>.

32. Rao, S.R.; Finch, J.A. Galvanic Interaction Studies on Sulphide Minerals. *Canadian Metallurgical Quarterly* **1988**, *27*, 253-259, doi:10.1179/cm.1988.27.4.253.
33. Wills, B.A. *Mineral processing technology: an introduction to the practical aspects of ore treatment and mineral recovery*, 4th ed.; Pergamon Press: New South Wales, Australia, 1988.
34. Schoonen, M.A.A.; Barnes, H.L. Mechanisms of pyrite and marcasite formation from solution: III. Hydrothermal processes. *Geochimica et Cosmochimica Acta* **1991**, *55*, 3491-3504, doi:[https://doi.org/10.1016/0016-7037\(91\)90050-F](https://doi.org/10.1016/0016-7037(91)90050-F).
35. Law, K.-Y. Definitions for Hydrophilicity, Hydrophobicity, and Superhydrophobicity: Getting the Basics Right. *The Journal of Physical Chemistry Letters* **2014**, *5*, 686-688, doi:10.1021/jz402762h.
36. Parikh, A.; Madamwar, D. Partial characterization of extracellular polysaccharides from cyanobacteria. *Bioresource Technol* **2006**, *97*, 1822-1827, doi:10.1016/j.biortech.2005.09.008.
37. Akhter, S.; Allan, K.; Buchanan, D.; Cook, J.A.; Campion, A.; White, J.M. XPS and IR study of X-ray induced degradation of PVA polymer film. *Applied Surface Science* **1988**, *35*, 241-258, doi:[https://doi.org/10.1016/0169-4332\(88\)90053-0](https://doi.org/10.1016/0169-4332(88)90053-0).
38. Schmitt, J.; Flemming, H.C. FTIR-spectroscopy in microbial and material analysis. *International Biodeterioration & Biodegradation* **1998**, *41*, 1-11, doi:10.1016/S0964-8305(98)80002-4.
39. Schmitt, J.; Nivens, D.; White, D.C.; Flemming, H.C. Changes of biofilm properties in response to sorbed substances - An FTIR-ATR study. *Water Science and Technology* **1995**, *32*, 149-155, doi:10.1016/0273-1223(96)00019-4.
40. Li, Q.; Wang, Q.F.; Zhu, J.Y.; Zhou, S.; Gan, M.; Jiang, H.; Sand, W. Effect of Extracellular Polymeric Substances on Surface Properties and Attachment Behavior of *Acidithiobacillus ferrooxidans*. *Minerals* **2016**, *6*, 100, doi:ARTN 100.10.3390/min6040100.
41. Naumann, D.; Fijala, V.; Labischinski, H.; Giesbrecht, P. The Rapid Differentiation and Identification of Pathogenic Bacteria Using Fourier-Transform Infrared Spectroscopic and Multivariate Statistical-Analysis. *J Mol Struct* **1988**, *174*, 165-170, doi:10.1016/0022-2860(88)80152-2.
42. Goh, S.W.; Buckley, A.N.; Lamb, R.N. Copper(II) sulfide? *Minerals Engineering* **2006**, *19*, 204-208, doi:10.1016/j.mineng.2005.09.003.
43. Goh, S.W.; Buckley, A.N.; Lamb, R.N.; Rosenberg, R.A.; Moran, D. The oxidation states of copper and iron in mineral sulfides, and the oxides formed on initial exposure of chalcopyrite and bornite to air. *Geochimica Et Cosmochimica Acta* **2006**, *70*, 2210-2228, doi:10.1016/j.gca.2006.02.007.
44. Acres, R.G.; Harmer, S.L.; Beattie, D.A. Synchrotron XPS, NEXAFS, and ToF-SIMS studies of solution exposed chalcopyrite and heterogeneous chalcopyrite with pyrite. *Minerals Engineering* **2010**, *23*, 928-936, doi:10.1016/j.mineng.2010.03.007.
45. Harmer, S.L.; Skinner, W.M.; Buckley, A.N.; Fan, L.-J. Species formed at cuprite fracture surfaces; observation of O 1s surface core level shift. *Surf Sci* **2009**, *603*, 537-545, doi:<https://doi.org/10.1016/j.susc.2008.12.024>.
46. Buckley, A.; Woods, R. An X-ray photoelectron spectroscopic study of the oxidation of chalcopyrite. *Australian Journal of Chemistry* **1984**, *37*, 2403-2413, doi:<https://doi.org/10.1071/CH9842403>.

47. Chander, S. Electrochemistry of sulfide flotation: Growth characteristics of surface coatings and their properties, with special reference to chalcopyrite and pyrite. *International Journal of Mineral Processing* **1991**, *33*, 121-134, doi:[https://doi.org/10.1016/0301-7516\(91\)90047-M](https://doi.org/10.1016/0301-7516(91)90047-M).
48. Fleet, M.E. XANES Spectroscopy of Sulfur in Earth Minerals. *The Canadian Mineralogist* **2005**, *43*, 1811-1838, doi:10.2113/gscanmin.43.6.1811.
49. Qian, G.; Fan, R.; Short, M.D.; Schumann, R.C.; Pring, A.; Gerson, A.R. The Combined Effects of Galvanic Interaction and Silicate Addition on the Oxidative Dissolution of Pyrite: Implications for Acid and Metalliferous Drainage Control. *Environ Sci Technol* **2019**, *53*, 11922-11931.
50. Womes, M.; Karnatak, R.C.; Esteva, J.M.; Lefebvre, I.; Allan, G.; Olivier-Fourcades, J.; Jumas, J.C. Electronic Structures of FeS and FeS₂: X-Ray Absorption Spectroscopy and Band Structure Calculations. *Journal of Physics and Chemistry of Solids* **1997**, *58*, 345-352, doi:[https://doi.org/10.1016/S0022-3697\(96\)00068-6](https://doi.org/10.1016/S0022-3697(96)00068-6).
51. Bhattacharyya, A.; Stavitski, E.; Dvorak, J.; Martínez, C. Redox interactions between Fe and cysteine: Spectroscopic studies and multiplet calculations. *Geochimica et Cosmochimica Acta* **2013**, *122*, 89-100, doi:10.1016/j.gca.2013.08.012.
52. Braun, A.; Chen, Q.; Flak, D.; Fortunato, G.; Gajda-Schranz, K.; Grätzel, M.; Graule, T.; Guo, J.; Huang, T.W.; Liu, Z. Iron resonant photoemission spectroscopy on anodized hematite points to electron hole doping during anodization. *ChemPhysChem* **2012**, *13*, 2937-2944.
53. Dos Santos, E.C.; de Mendonça Silva, J.C.; Duarte, H.A. Pyrite Oxidation Mechanism by Oxygen in Aqueous Medium. *The Journal of Physical Chemistry C* **2016**, *120*, 2760-2768, doi:10.1021/acs.jpcc.5b10949.
54. de Groot, F.; Grioni, M.; Fuggle, J.; Ghijsen, J.; Sawatzky, G.; Petersen, H. Oxygen 1s x-ray-absorption edges of transition-metal oxides. *Phys Rev B* **1989**, *40*, 5715-5723.
55. Frati, F.; Hunault, M.O.J.Y.; de Groot, F.M.F. Oxygen K-edge X-ray Absorption Spectra. *Chemical Reviews* **2020**, *120*, 4056-4110, doi:10.1021/acs.chemrev.9b00439.
56. Křepelová, A.; Newberg, J.; Huthwelker, T.; Bluhm, H.; Ammann, M. The nature of nitrate at the ice surface studied by XPS and NEXAFS. *Physical Chemistry Chemical Physics* **2010**, *12*, 8870-8880.
57. Coker, V.; Byrne, J.; Telling, N.; Van der Laan, G.; Lloyd, J.; Hitchcock, A.; Wang, J.; Patrick, R. Characterisation of the dissimilatory reduction of Fe (III)-oxyhydroxide at the microbe–mineral interface: the application of STXM–XMCD. *Geobiology* **2012**, *10*, 347-354.
58. Boese, J.; Osanna, A.; Jacobsen, C.; Kirz, J. Carbon edge XANES spectroscopy of amino acids and peptides. *Journal of Electron Spectroscopy and Related Phenomena* **1997**, *85*, 9-15, doi:10.1016/S0368-2048(97)00032-7.
59. Hardie, A.G.; Dynes, J.J.; Kozak, L.M.; Huang, P.M. The role of glucose in abiotic humification pathways as catalyzed by birnessite. *J Mol Catal a-Chem* **2009**, *308*, 114-126, doi:10.1016/j.molcata.2009.03.035.
60. Cody, G.D.; Ade, H.; Wirick, S.; Mitchell, G.D.; Davis, A. Determination of chemical-structural changes in vitrinite accompanying luminescence alteration using C-NEXAFS analysis. *Org Geochem* **1998**, *28*, 441-455, doi:10.1016/S0146-6380(98)00010-2.
61. Ade, H.; Hitchcock, A.P. NEXAFS microscopy and resonant scattering: Composition and orientation probed in real and reciprocal space. *Polymer* **2008**, *49*, 643-675, doi:10.1016/j.polymer.2007.10.030.

62. Chan, C.S.; Fakra, S.C.; Edwards, D.C.; Emerson, D.; Banfield, J.F. Iron oxyhydroxide mineralization on microbial extracellular polysaccharides. *Geochimica Et Cosmochimica Acta* **2009**, *73*, 3807-3818, doi:10.1016/j.gca.2009.02.036.
63. Sedlmair, J.; Gleber, S.-C.; Peth, C.; Mann, K.; Niemeyer, J.; Thieme, J. Characterization of refractory organic substances by NEXAFS using a compact X-ray source. *Journal of Soils and Sediments* **2012**, *12*, 24-34, doi:10.1007/s11368-011-0385-9.
64. Barco, R.A.; Edwards, K.J. Interactions of proteins with biogenic iron oxyhydroxides and a new culturing technique to increase biomass yields of neutrophilic, iron-oxidizing bacteria. *Frontiers in Microbiology* **2014**, *5*, doi:10.3389/fmicb.2014.00259.
65. Harneit, K.; Göksel, A.; Kock, D.; Klock, J.-H.; Gehrke, T.; Sand, W. Adhesion to metal sulfide surfaces by cells of *Acidithiobacillus ferrooxidans*, *Acidithiobacillus thiooxidans* and *Leptospirillum ferrooxidans*. *Hydrometallurgy* **2006**, *83*, 245-254.
66. Mahdavi, M.; Ahmad, M.; Haron, M.; Namvar, F.; Nadi, B.; Rahman, M.; Amin, J. Synthesis, surface modification and characterisation of biocompatible magnetic iron oxide nanoparticles for biomedical applications. *Molecules* **2013**, *18*, 7533-7548.
67. Toyofuku, M.; Inaba, T.; Kiyokawa, T.; Obana, N.; Yawata, Y.; Nomura, N. Environmental factors that shape biofilm formation. *Bioscience, biotechnology, and biochemistry* **2015**, *80*, 1-6, doi:10.1080/09168451.2015.1058701.

6 ACIDITHIOBACILLUS FERROOXIDANS APPLICATION IN BIO-FLOTATION SEPARATION OF CHALCOPYRITE AND PYRITE

6.1 Introduction

Acidophilic microorganisms have been extensively studied for their bio-leaching capabilities [1-3]. With advancements in technology and understanding of microbe – mineral interactions, these microorganisms are now being investigated for their use in separation through flotation. *Acidithiobacillus ferrooxidans* (*A. f*) has previously been investigated for its effect on iron sulfide flotation, due to its ability to oxidise iron and inorganic sulfur compounds [4]. Bio-flotation studies of *A. f* have included the separation of pyrite (Py) from chalcopyrite (Cp) and arsenopyrite (Aspy) [5-8]. These studies suggest irreversible attachment of *A. f* to the Py surface occurs within minutes [8], while attachment to Cp was observed after 12 days allowing for successful separation [9]. A similar window of selective attachment has been observed in the previous chapters using *L. f*. Adsorption of *L. f* to Py was found to be greater than both Cp and Aspy [5,6,10]. It is expected that the attachment behaviour and selective attachment of *A. f* will differ to *L. f*, as *A. f* can utilise both iron and sulfur for energy production. Attachment of the cells to Py was also investigated through Atomic Force Microscopy (AFM), with greater dissolution observed for active cells with EPS [10,11]. The attachment of cells to Py resulted in selective depression of Py over Cp and Asp [5,6]. Studies into the use of EPS in bio-modulation of Py and Cp found that an increase in EPS concentration increased the Cp recovery and cells with EPS resulted in a lower recovery than the free extracted EPS [12].

The study in this chapter addresses the use of a single mesophilic, bio-leach microbe, *Acidithiobacillus ferrooxidans*, and its metabolic products for the selective flotation of Cp from Py. The purpose of this study is to determine the individual effect of i) the bacterial cell; ii) the EPS; and iii) different growth condition, to optimise the separation of Cp and Py with bio-flotation. The selective or preferential attachment of the microorganisms is studied through SEM imaging. Surface sensitive techniques such as FTIR-ATR and XPS were used to analyse the surface chemistry changes of the minerals to identify the presence of surface species and compounds assisting with the separation.

6.2 Experimental

6.2.1 Mineral Samples

Mineral samples used in this chapter were sourced through GEO Discovery (The Wilyyama Group, New South Wales, Australia) and characterised using quantitative XRD (QXRD) and ICPMS to confirm the purity. The analysis shows the natural mineral samples of pyrite (Huanzala mine, Peru) has a purity of 96.4%, while the chalcopyrite (China) has a purity of 83.5%. Minerals samples were ground according to the description in Section 3.2.1.1. The fraction size +38 – 75 μm was used for culture growth and all experimental analysis.

6.2.2 Bacterial Culture and Adjustment to Mineral

Bacterial cultures were obtained and maintained according to Section 3.2.2.1. Monitoring of cell concentration was conducted through counts using a haemocytometer and oxidation – reduction titrations, as described in Section 3.2.2.2 and 3.2.2.3, respectively.

6.2.3 Micro-Flotation Studies

Bio-flotation tests were conducted as both single mineral flotation tests and differential (mixed mineral) flotation tests. A summary of the flotation conditions investigated is shown below in **Error! Reference source not found.** Flotation tests were conducted as collector-free condition tests and in the presence of potassium isopropyl xanthate (PIPX) collector. Collected fractions were analysed via XRD, with details of sample preparation and procedure covered in Sections 3.3.3.2. Refinement of each diffractogram using the zero shift and scale factors for chalcopyrite (ICSD no. 94554) and pyrite (ICSD no. 15012).

Table 6.1: Summary of micro-flotation test conditions

Conditions	
Baseline	Modified <i>Leptospirillum</i> HH Media pH 1.8
Food source	<i>A. f</i> grown on iron (Fe^{2+}) sulfate <i>A. f</i> grown on Py <i>A. f</i> grown on Cp <i>A. f</i> grown on Asp
EPS	EPS supernatant extracted from <i>A. f</i> grown on Py EPS supernatant extracted from <i>A. f</i> grown on Cp EPS supernatant extracted from <i>A. f</i> grown on Asp

6.2.4 Analysis

6.2.4.1 FTIR-ATR Analysis

Samples were prepared as outlined by the method in Section 3.3.1.2. Aliquots of 1 mL were taken at differing exposure times and placed in a 1.5 mL Eppendorf tube with analysis proceeding immediately. Analysis was conducted as described in Section 4.2.2.2.

6.2.4.2 Scanning Electron Microscopy

Exposure of *A. f* to single mineral fractions (+38 -75 μm) was conducted at a starting concentration of 1.5×10^7 cells per mL from cultures adapted to the respective mineral. Media controls were conducted in the same conditions but in the absence of cells. Samples were maintained and prepared as described in Section 3.3.1.2. Exposures times of 0, 2, 12, 24, 36, 48, 60, 72 and 168 hours were analysed. Imaging was conducted on an Inspect FEI F50 SEM, with an accelerating voltage of 5-10 kV and varying spot size. The particle size distribution was assessed using the measure tool in the ImageJ software [13].

6.2.4.3 X-Ray Photoelectron Spectroscopy (XPS)

X-ray Photoelectron Spectroscopy (XPS) was used to analyse the surface chemistry changes of pyrite exposed to HH media and *A. f* adjusted to pyrite. Samples for analysis were taken from cultures set up for SEM analysis at exposure times of 24, 48, 72 and 168 hours. Further detail on sample preparation and experimental setting is discussed in Section 3.3.5.

6.3 Results and Discussion

6.3.1 Culture Growth

The growth cycles of the different cultures were monitored over 240 h (base culture) and 55 days (cultures adapted to mineral). The growth curves obtained were assessed for the six distinct growth phases expected throughout the growth cycle, as discussed in Section 3.2.2.2. Observing these growth phases helps to draw conclusions between cultures grown in different conditions [14].

6.3.1.1 *A. f* grown on Modified HH Media

The growth of *A. f* on modified HH media with iron (Fe^{2+}) sulfate was monitored over 240 hours to capture the cell growth up to and including the decline growth phase. The growth curve is represented in Figure 6.1 below. The growth curve resembles a typical growth, with the lag phase observed for approximately 6 h after inoculation. The acceleration phase is short and occurs between 6 and 8 h, which is followed by a longer exponential phase observed between 8 and 52 h. The retardation phase of the culture is observed between 52 and 72 h, leading into the linear stationary phase. The linear stationary phase continues until approximately 196 hours, where the culture enters the decline growth phase.

This growth curve indicates favourable growth conditions for the *A. f* bacteria. This is expected as Fe^{2+} ions are readily available within the media. A sharp decrease in the ferrous iron concentration overlaps with the exponential phase, which is expected. Interestingly, the higher concentration of cells occurs when there is little to no ferrous iron detected. This suggests there is another reaction occurring within these conditions to reduce ferric iron.

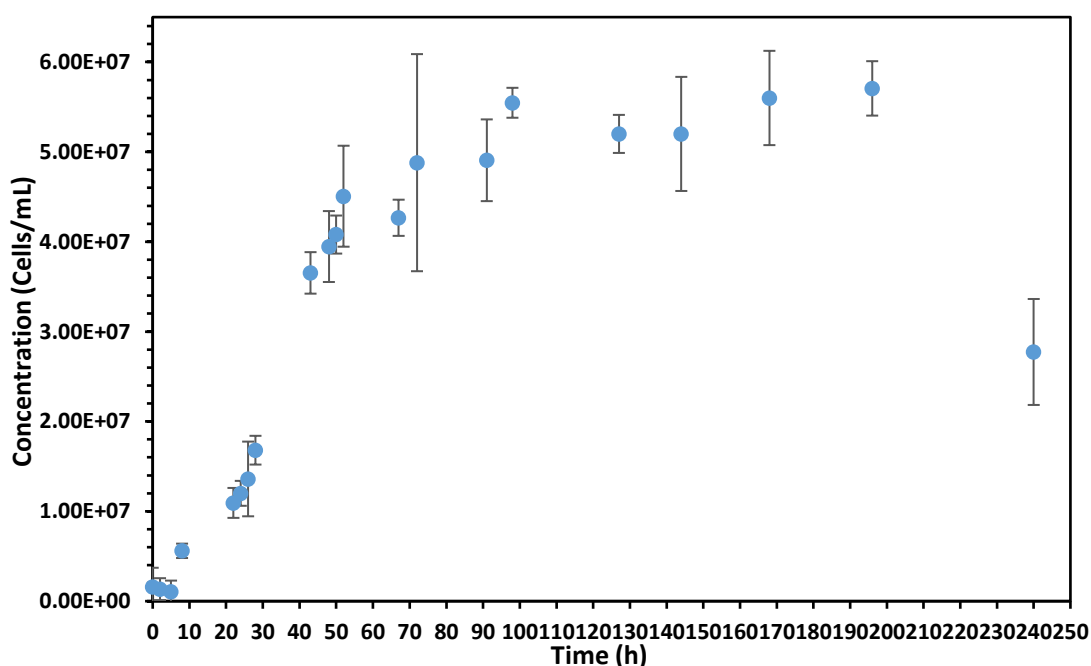


Figure 6.1: Growth of *Acidithiobacillus ferrooxidans* on HH media with iron sulfate over 240 hours

6.3.1.2 *A. f* Adjusted to Pyrite

Cultures of *A. f* adapted to pyrite in modified HH media were originally adjusted to grow on a solid substrate in modified HH media from *A. f* grown on modified HH media with an iron

(Fe²⁺) sulfate. All growth phases, including the decline growth phase, are observed over the 55 days. A representative growth curve is shown in Figure 6.2.

Unlike the growth of *A. f* on iron sulfate solution, the lag phase of *A. f* adapted to pyrite is not observed, with cell concentration increasing from the point of the inoculation. The suppression of the lag phase indicates the growth conditions are suitable to the *A. f* strain [14]. The acceleration phase, however, is seen to be longer, which is observed between 24 and 48 hours. At this point, the total cell concentration is almost equivalent to the maximum cell concentration of the iron sulfate grown culture. Likewise, the exponential phase and the retardation phase are observed to be longer. The maximum cell concentration is observed in the linear stationary phase, with a cell concentration of approximately 2.2×10^8 cells per mL. The linear stationary phase is observed until 696 hours (29 days), where the decline growth phase starts.

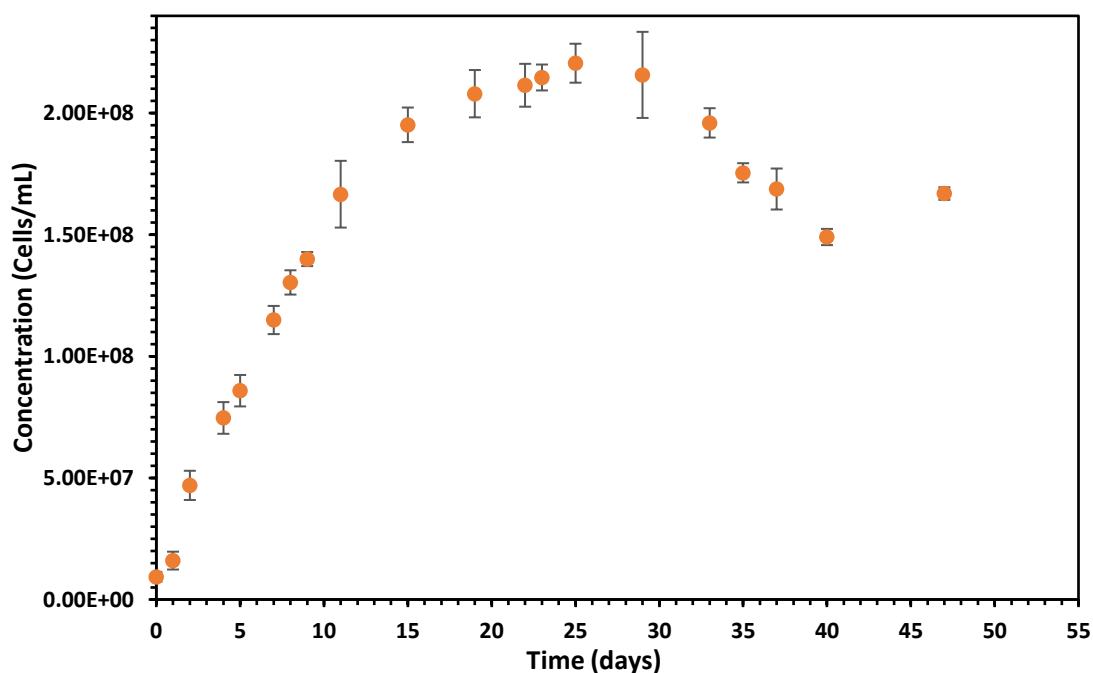


Figure 6.2: Growth of *Acidithiobacillus ferrooxidans* adjusted to pyrite in HH media monitored over 55 days

The increase in both the length of the growth curve and the maximum cell concentration is due to the change in conditions. The presence of pyrite increases the total amount of iron present in the system from approximately 0.1 mol/L (HH media solution B) to approximately 0.56 mol/L. The ferrous iron titrations indicate an initial increase in the concentration of Fe²⁺ up until 72 h, then the concentration fluctuates.

6.3.1.3 *A. f* Adjusted to Chalcopyrite

Cultures of *A. f* adapted to pyrite were slowly adjusted to chalcopyrite, through a series of re-inoculations. The initial inoculation was conducted on a mix (50:50) of pyrite and chalcopyrite. Subsequent inoculations reduced the pyrite content of the culture by 50% each time until the culture was sustainable purely on chalcopyrite. The representative growth curve of *A. f* adapted to chalcopyrite over 55 days is represented in Figure 6.3 below.

The growth cycle of *A. f* adapted to chalcopyrite is longer than 55 days as not all growth phases are observed, with the linear stationary phase and decline growth phase missing. In comparison to the *A. f* on HH media and the *A. f* adapted to pyrite, the lag phase is extended and observed between inoculation and 192 h (8 days). The increased length of the lag phase suggests that the conditions for growth are unfavourable [14]. The unfavourable conditions arise from the natural oxidation state of the iron in chalcopyrite existing as Fe^{3+} and the toxicity caused by the presence of copper [15,16]. Likewise, the length of the acceleration phase is also increased. However, the slope of the curve at this time indicates that the growth rate is slower than what is observed when adapted to pyrite. While the exponential phase is also observed to be longer, the maximum cell concentration is less at approximately 1.45×10^8 cells per mL.

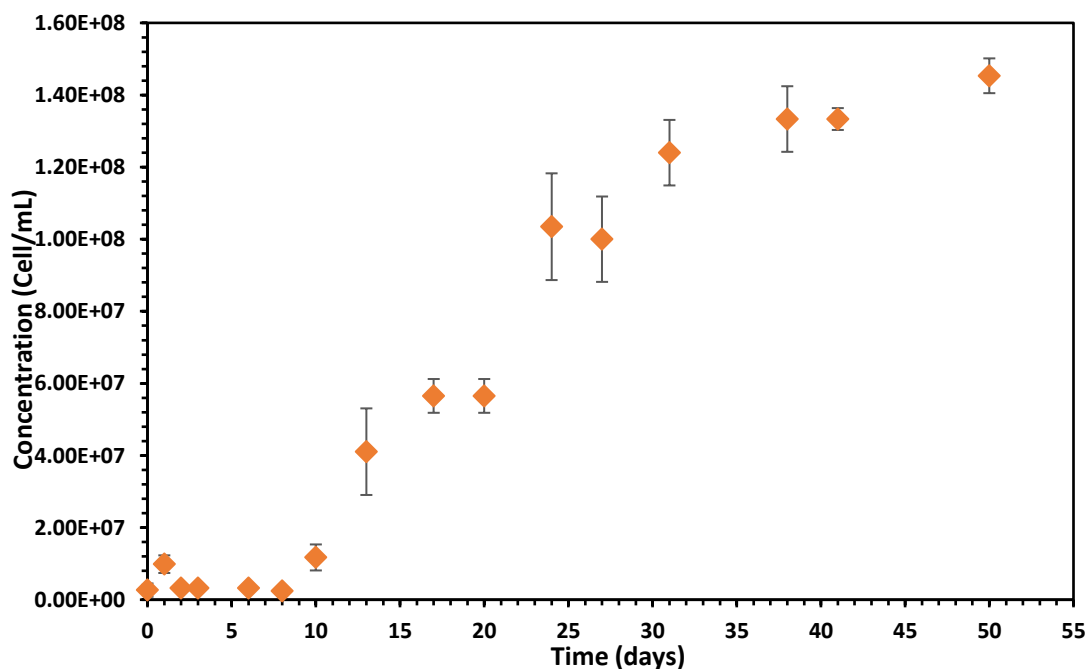


Figure 6.3: Growth of *Acidithiobacillus ferrooxidans* adjusted to chalcopyrite over 55 days

6.3.1.4 *A. f* Adjusted to Arsenopyrite

Cultures of *A. f* adapted to pyrite were slowly adjusted to arsenopyrite, through a series of inoculations. Due to the toxicity of arsenic, in comparison to copper [17], the adaptation to arsenopyrite occurred at a slower rate with the initial inoculation being a 25:75 mix of arsenopyrite to pyrite. The pyrite content was reduced by 25% in subsequent inoculations, until the culture was sustainable on arsenopyrite alone. A representative growth curve for *A. f* adapted to arsenopyrite is illustrated in Figure 6.4 below.

The growth curve of *A. f* adapted to arsenopyrite is dissimilar to what has been observed for the other growth conditions and can be considered a complex growth cycle [14]. Over the 55 days, two exponential phases are observed, indicating a double growth cycle known as a diauxie [14]. A diauxie often indicates a mixture of energy sources, with each cycle corresponding to the utilisation of a source [14,18]. Therefore, this could be an artefact of the *A. f* utilising the iron and sulfur in the system. In acidic environments, arsenopyrite develops a sulfur rich surfaces through the depletion of iron and arsenic [19-21]. This indicates that both iron and sulfur are available for bacterial oxidation.

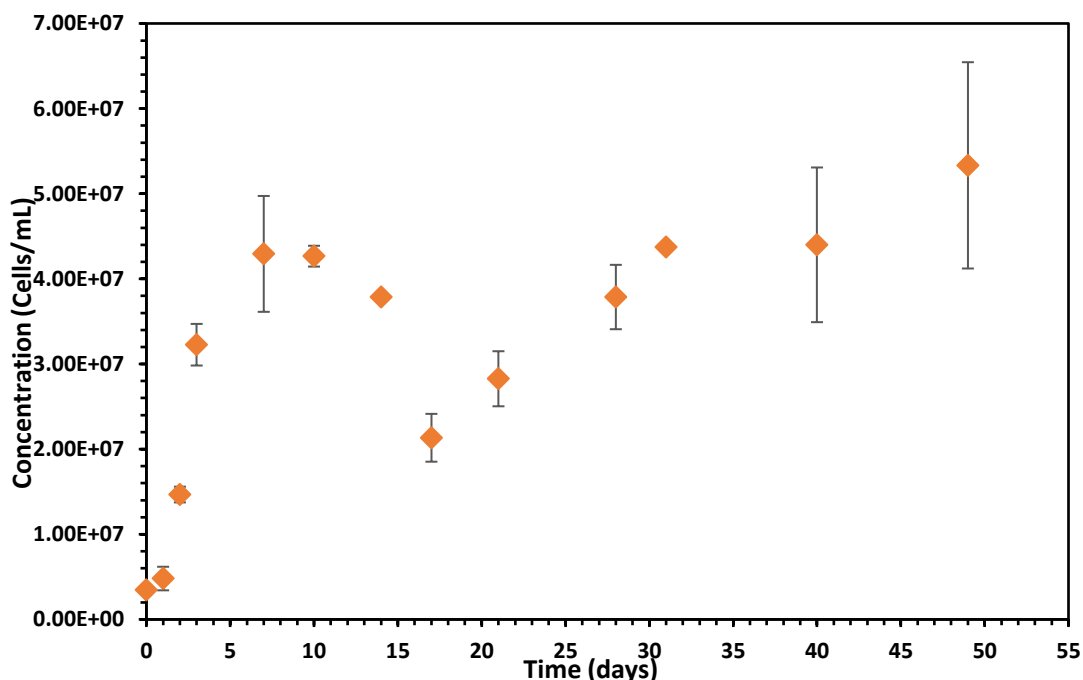


Figure 6.4: Growth of *Acidithiobacillus ferrooxidans* adjusted to arsenopyrite over 55 days

While the growth curve exhibits two exponential phases, only one lag phase is observed between inoculation and 48 hours (2 days). This is surprisingly shorter than the chalcopyrite

culture and is attributed to the natural oxidation state of the iron being predominantly Fe^{2+} [20,22]. The first exponential phase is observed between 48 and 168 hours (2 – 4 days) and is seen to have a greater slope than the second exponential phase, indicating a greater growth rate. This growth cycle also contains a short stationary linear phase and decline growth phase before the second growth cycle starts. The maximum cell concentration is observed in the second growth cycle with approximately 5.3×10^7 cells per mL. This cell concentration is one order of magnitude less than what is observed for the other mineral cultures and is less than what was observed for the cells grown on iron sulfate. This indicates that growth on arsenopyrite is the least favourable environment out of the four.

6.3.2 Attachment Studies

6.3.2.1 HH Media Control

Media controls are analysed to determine the individual effect of the media on the sample, as the media is an acidic environment. These controls can also help determine the presence of contaminants in the sample. Images for HH media controls of pyrite and chalcopyrite fractions have been presented previously in Section 4.3.2.2, a summary of findings is reported here.

Impurities were observed in both samples and throughout all time frames. These impurities are visually distinguishable from the pyrite and chalcopyrite particles, with one impurity showing multiple cleavages, one containing many thin layers and another having strong cubic cleavage. EDX analysis confirms these particles are impurities.

In comparison, the pyrite exhibits evidence of leaching earlier than the chalcopyrite. This is supported by the particle size distribution. The particle size distribution of pyrite and chalcopyrite was assessed over the exposure times. These measurements indicate a larger fluctuation in the average particle size for pyrite than chalcopyrite, as a function of exposure time. This can be explained by the increased leaching and dissolution effect observed for pyrite [23]. Evidence of dissolution/leaching is first observed at 12 h exposure for pyrite and is seen to increase with voids and cracking present at 36 h. However, the observable leaching of chalcopyrite is first identified at 48 h.

Surface defects are observed on both the pyrite and chalcopyrite. Voids and holes are more apparent on the pyrite surface, while cracks are observed at early exposure times for the chalcopyrite and is predicted to be an artefact of the crushing and grinding process. Debris is also present on the surface of both samples throughout the exposure times. Both pyrite and chalcopyrite exhibit debris with a scaffold like structure, which is suspected to be iron oxide products, such as ferrihydrite, as a result of leaching [24]. The pyrite sample also contains a cubic debris, which is seen as individual cubes and as clusters, these are expected to be jarosite formation [25] and is supported by the EDAX results. The charging of some particles is also observed at longer exposure times. The change in surface roughness and/or a change in the chemical composition affecting the conductivity of the particles can lead to the charging effect observed [26].

6.3.2.2 *A. f* Adjusted to Pyrite

Analysis of the 0 h exposure allows for determination of how many cells settle on the surface at the time of re-culture. Similarly, to the HH media control, imaging revealed the presence of impurities which are easily distinguishable from the pyrite particles. These impurities are seen throughout the *A. f* samples and are represented by the images in Figure 6.5 below.

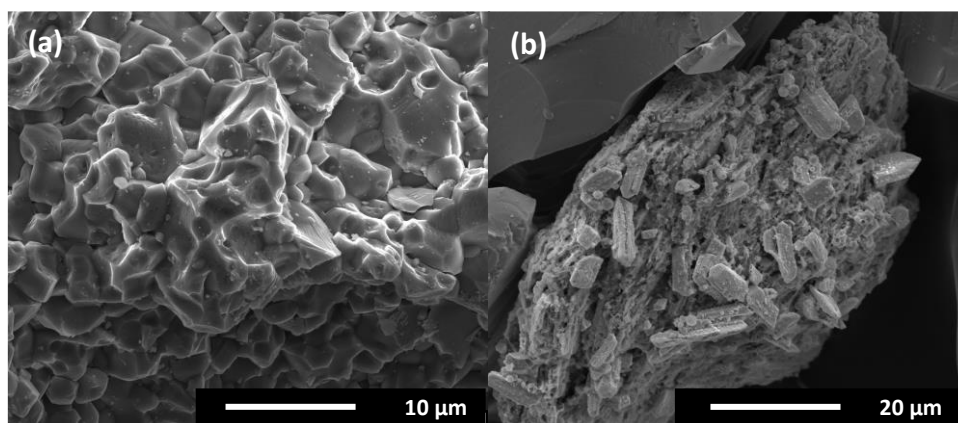


Figure 6.5: SEM image of impurities observed within the pyrite samples, showing a particle with multiple cleavages at 0 h (a) and multiple particles cemented together at 48 h (b); imaged at a magnification of 8000x (a), 4000x (b) and an accelerating voltage of 10 kV

Representative images of *A. f* exposed to pyrite at 0 h and 2 h are shown in Figure 6.6. The presence of cells at 0 h, as shown in Figure 6.6 (a and b), indicate that the SEM sample preparation is gentle enough to not dislodge cells from the mineral surface. At 0 h exposure, particles are observed to have sharp edges and a smooth surface with some particles having

single cells present. However, some particles do appear to have a rougher surface with multiple voids present. These particles are expected to have been transferred from the older culture during the inoculation process. Hair line cracks are also detected on some of the particles, which could be a result of the crushing procedure. There is little debris present on the surface, however this is less than what was observed in the pyrite control.

The sharp fine edges are starting to round at 2 h exposure to *A. f*. This is faster than the leaching effect observed for the HH media control, indicating the presence of the *A. f* bacteria increases the leaching rate [27]. The presence of cells and debris has increased, with the cells showing no preference to morphological differences. This suggests that the cells at this time point are reversibly attached to the surface, as it is known that cells preferentially bind to surface defects in the initial stage of attachment [28].

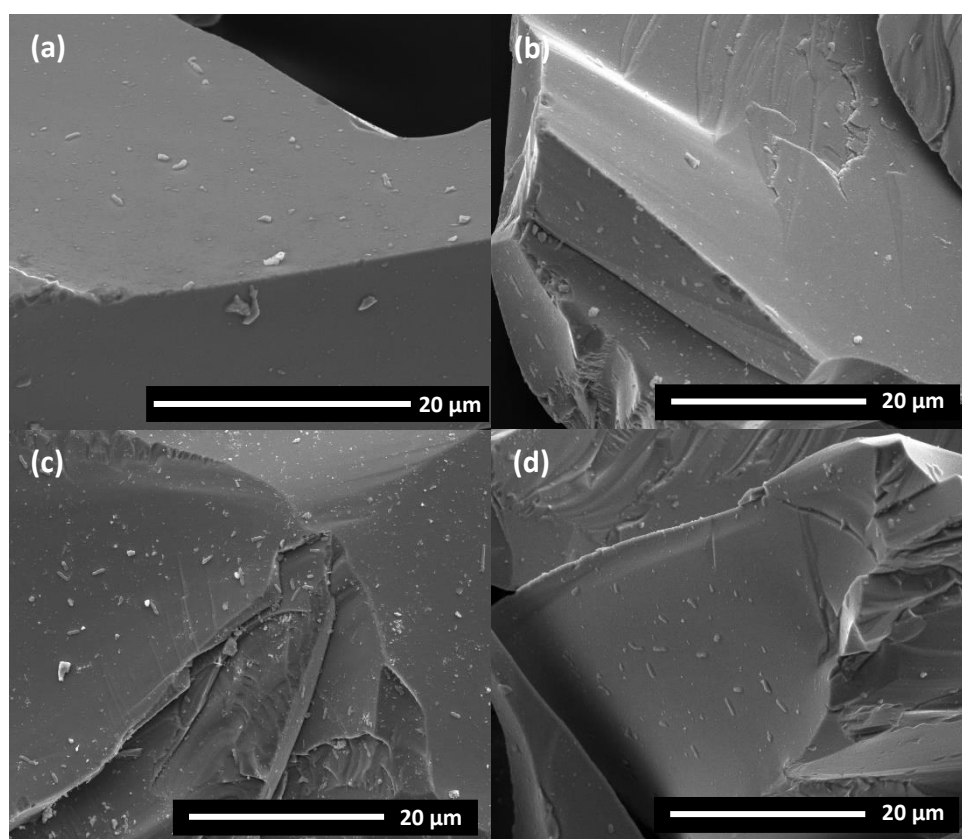


Figure 6.6: SEM image of *A. f* adjusted to pyrite exposed to pyrite particles in HH media at 0 h (a) and 2 h (b-d) imaged at a magnification of 8000 x (a) and 6000 x (b-d) and an accelerating voltage of 10 kV

At 12 h, there is an increase in surface defects is observed (Figure 6.7). These defects include large cracking/tunnelling and voids. The presence of these defects increases the surface roughness, aiding the irreversible attachment of cells. In comparison to the pyrite control,

these features indicate that the leaching has increased in the presence of *A. f* cells, which is supported by a previous study conducted by Hsu, et al. [28]. Scaffold like structures of debris, believed to be iron oxides [24], are present in large clusters as shown in Figure 6.7 (a). Cells are also starting to appear in large clusters among crevasses and surface defects.

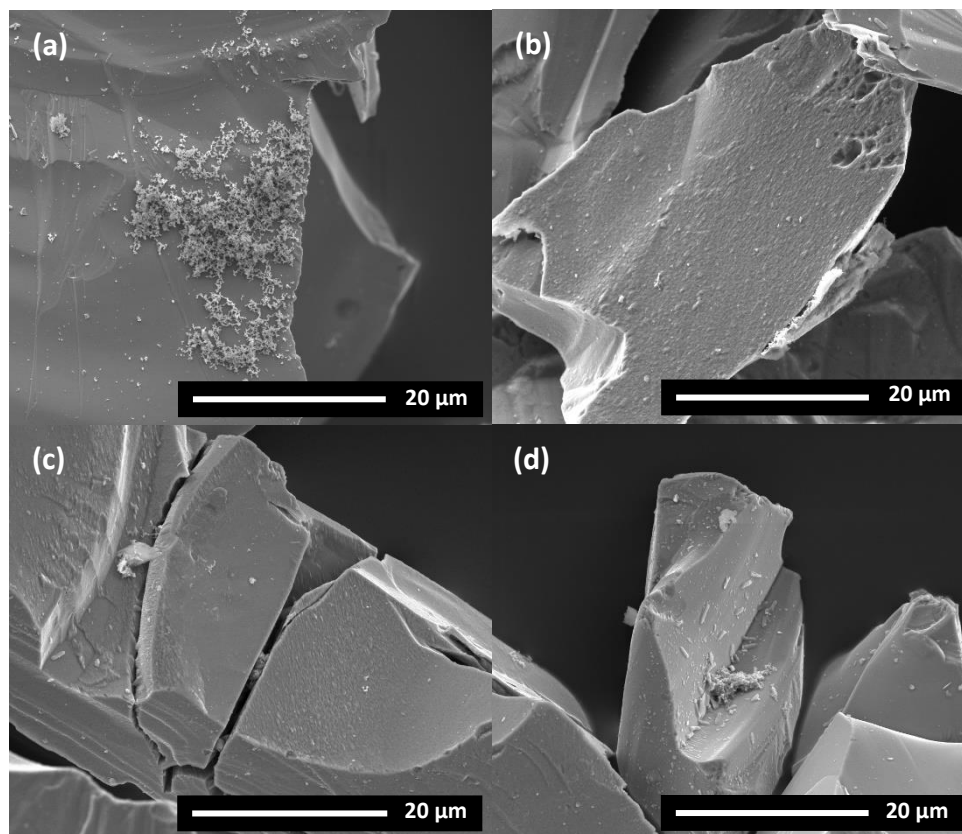


Figure 6.7: SEM image of *A. f* adjusted to pyrite particles at 12 h imaged at a magnification of a 6000x and an accelerating voltage of 5 kV (a) and 10 kV (b-d)

The surface of the pyrite is observed to steadily deteriorate at 24 h exposure. The rounding of edges, presence of debris and surface defects such as voids and cracks are observed to increase. Large clusters of cells or biofilm are not detected at this exposure time. However, by 36 h exposure, small amounts of biofilm are observed on the surface of, some but not all, particles (Figure 6.8 f). At this exposure time, ‘tunnels’ are now observed on some particles, as shown in Figure 6.8 (e). As this phenomenon was not observed in the pyrite control, indicating the presence of *A. f* is responsible for the ‘tunnels’ observed. Interestingly, bacterial cells were not observed around or in these features. As a bioleach microbe, *A. f* has been documented to increase the leaching of pyrite and the lack of cell attachment observed signifies an indirect non-contact mechanism at this time frame.

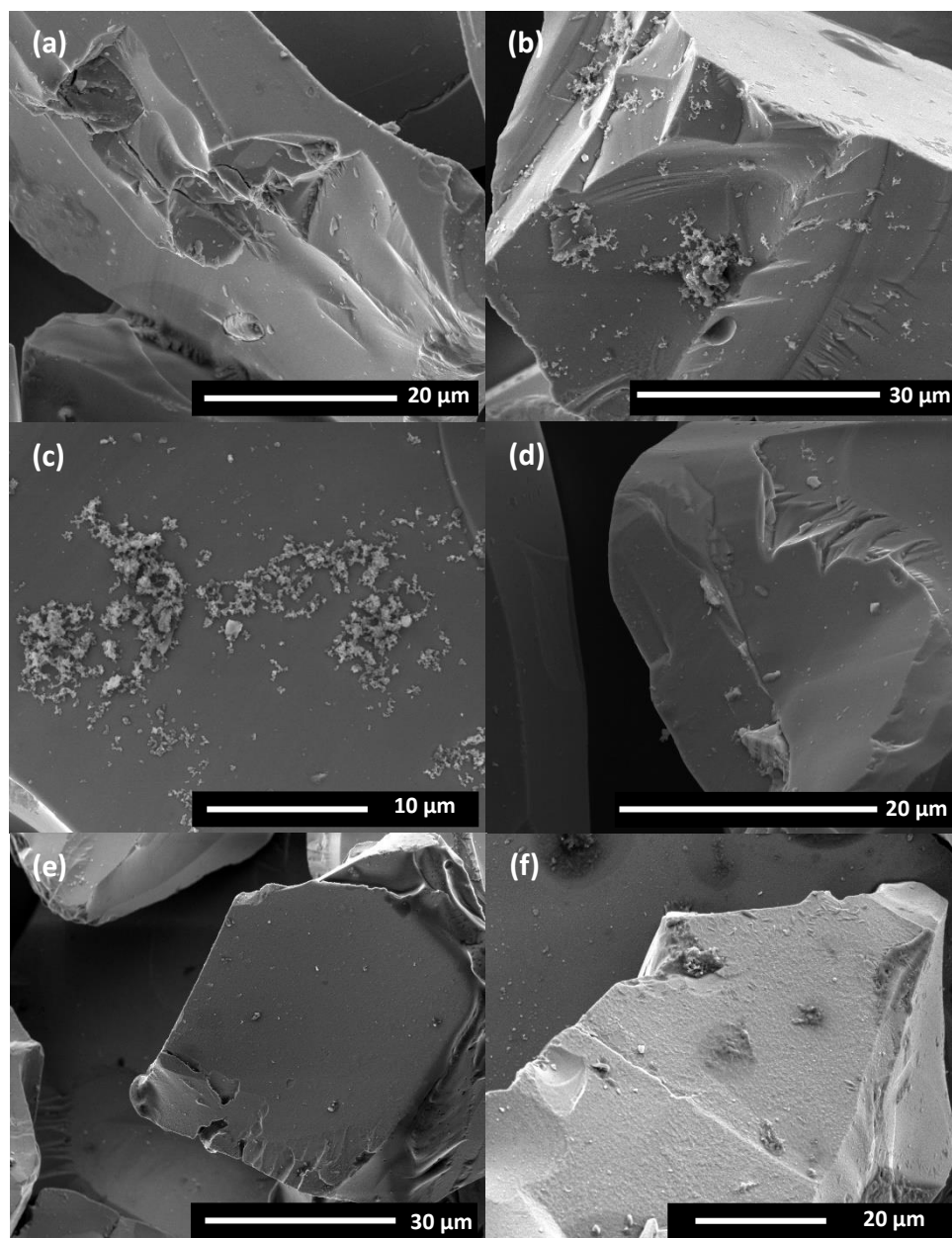


Figure 6.8: SEM image of *A. f* adjusted to pyrite exposed to pyrite particles at 24 h (a – c) and 36 h (d – f) imaged at a magnification of 6000x (a), 5000x (b), 10000x (c), 8000x (d and f), and 4000x (e); and an accelerating voltage of 10 kV (a – d) and 5 kV (e and f)

By 48 h, the presence of cells and biofilm on the surface is increased. However, no large clusters of cells are observed. Figure 6.9 (a) shows the attachment of cells and biofilm between the cracks which have formed on a mineral particle. This indicates that at 48 h exposure the mechanism in which *A. f* is utilising has switched from indirect non-contact to indirect contact mechanism. Figure 6.9 (b and c) illustrate the presence of voids with cells and large biofilms on the surface, while Figure 6.9 (d) demonstrates the presence of debris/biofilm of the surface of impurities.

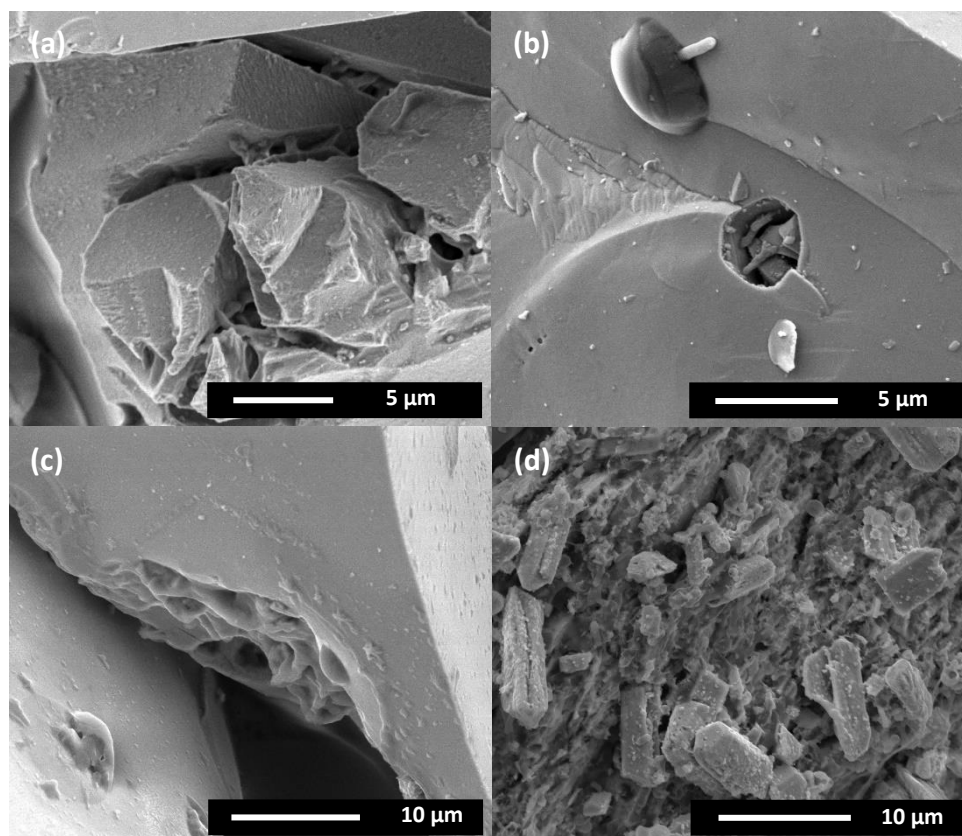


Figure 6.9: SEM image of *A. f* adjusted to pyrite exposed to pyrite particles at 48 h exposure imaged at a magnification of 12000x (a), 15000x (b), and 8000x (c and d); and an accelerating voltage of 5 kV (a and b) and 10 kV (c and d)

At 60 h exposure, there is an increase of biofilm observed on the surface in both large masses (Figure 6.10 a) and smaller fractions (Figure 6.10 b). At this time frame, clusters of cells are more regular. Although they are typically observed around surface defects such as voids and cracks. The presence of debris and biofilm is increased again at 72 h, with Figure 6.10 (d – f) exhibiting large amounts. Image d shows a large cluster of debris, which has been identified as iron oxide products. The presence of large clusters like this signifies substantial leaching has occurred. At this exposure time, some particles are completely covered in biofilm and cells, as shown in image e, while other particles still have cells spread sporadically across the surface (image f).

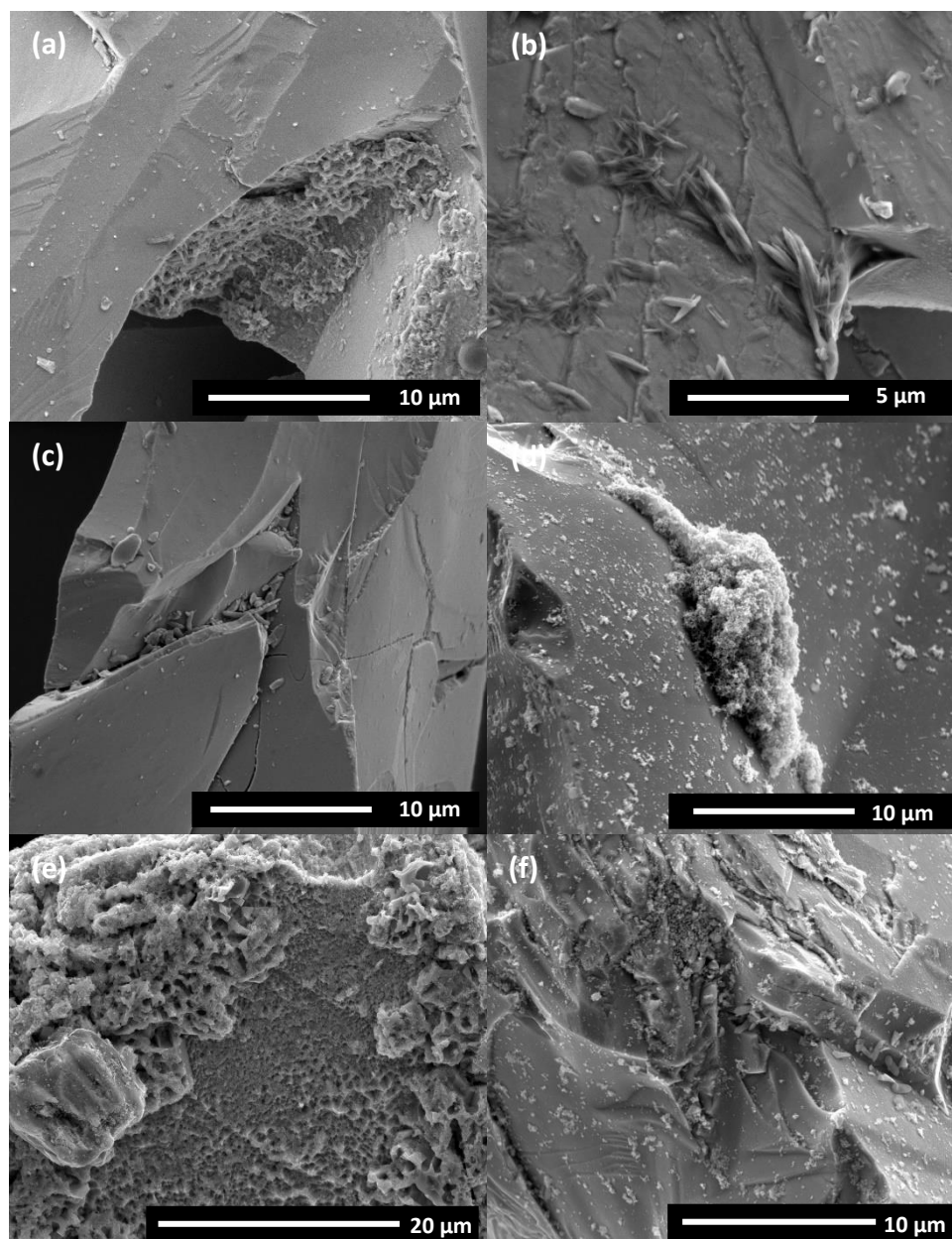


Figure 6.10: SEM image of *A. f* adjusted to pyrite exposed to pyrite particles at 60 h (a-c) and 72 h (d-f) imaged at a magnification of 10000 x (a, c and d), 20000 x (b), 5000 x (e) and 12000 x (f); and an accelerating voltage of 5 kV (a-c), 10 kV (d and f) and 20 kV (e)

Overall, SEM analysis has indicated that *A. f* adjusted to pyrite exhibits both indirect non-contact and indirect contact mechanisms. The leaching effect is observed to be increased in the presence of *A. f*, with visible leaching effects observed at as little as 2 h exposure. Biofilm formation is observed from 12 h exposure and iron oxide precipitates present from 2h.

Figure 6.11 below illustrates the attachment of cells and biofilm on particles of impurity at 72 h exposure. Interestingly, the biofilm is observed to attach to the impurity that was determined, through EDAX, to contain lead; while cells are seen to attach to the clay impurity.

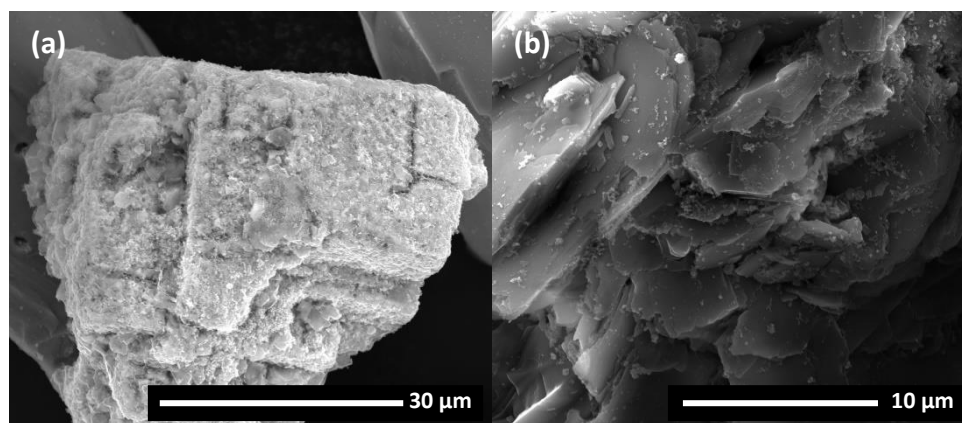


Figure 6.11: SEM image *A. f* adapted to pyrite exposed to pyrite showing attachment to particles of impurity at 72 h exposure, imaged at a magnification of 5000x (a) and 12000x (b) and an accelerating voltage of 20 kV

6.3.2.3 *A. f* Adjusted to Chalcopyrite

The cell attachment of *A. f* to chalcopyrite (+38 – 75μm) was also investigated and imaged at exposure times of 0, 2, 12, 24, 36, 48, 60, 72 and 168 hours. The 0 h exposure time was examined to determine if any cells were settled on the surface at the time of re-culture.

Representative images for 0 h exposure, are shown in Figure 6.12 (a – c), which shows the presence of some debris on the surface. A singular cell was observed on the surface, shown in Figure 6.12 (c), which is expected to have settled on the surface and not be attached. At 2 h the debris on the surface has increased (Figure 6.12 d – f). Similar to the control samples, there is no evidence of leaching although there is the presence of cracks. As this cracking was also observed in the control, this is ascribed to the crushing and grinding process. Multiple single cells are also seen on the surface, although it is likely that these cells are reversibly attached, it does indicate that there is not preferential attachment of the *A. f* cell to either pyrite or chalcopyrite.

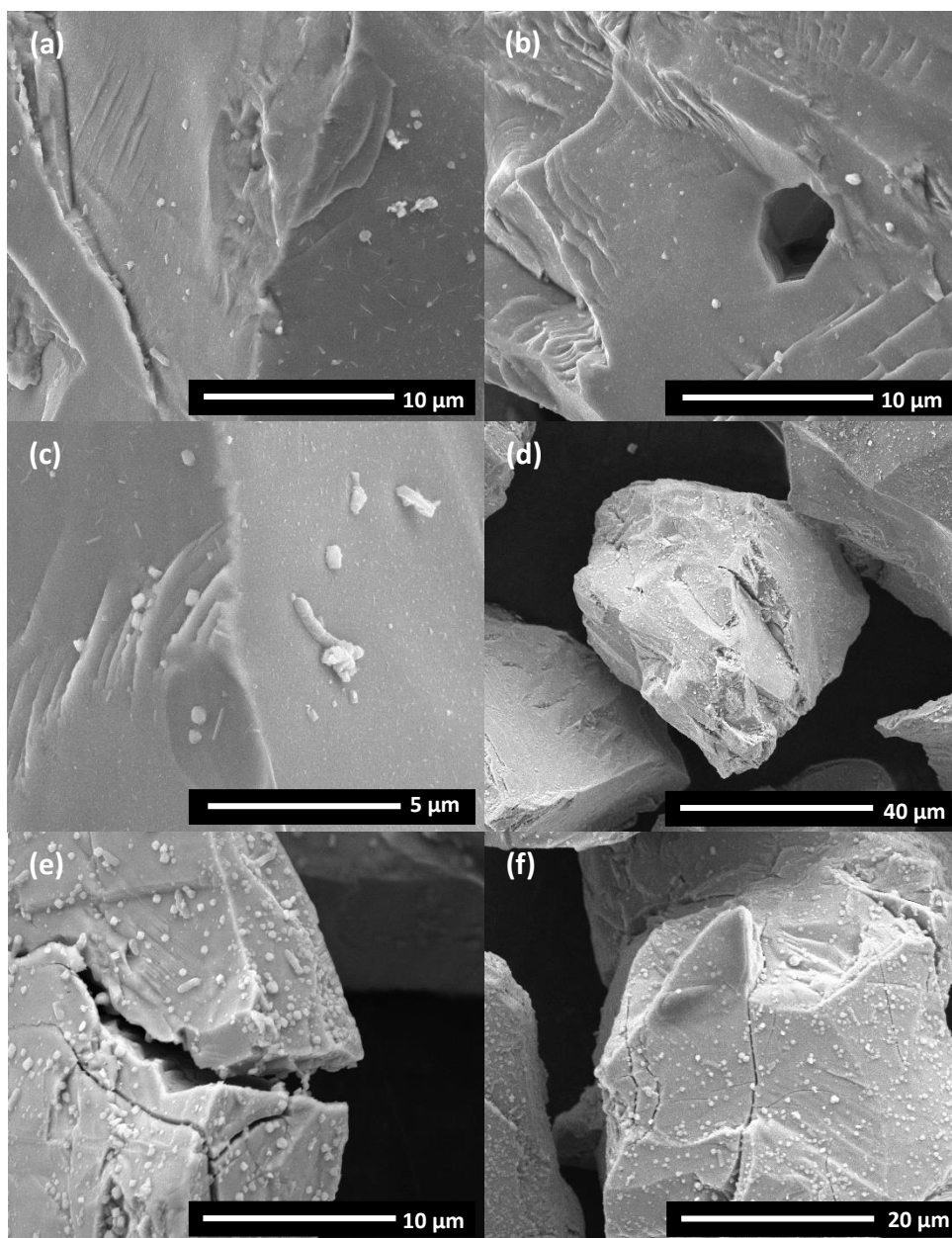


Figure 6.12: SEM image of *A. f* adapted to chalcopyrite exposed to chalcopyrite at an exposure of 0 h (a – c) and 2 h (d – f) imaged at a magnification of 12000x (a, b and e), 24000x (e), 3000x (d), and 6000x (f); with an accelerating voltage of 10 kV

Single cells are also observed on the surface at 12 h exposure. The presence of cells is also accompanied by the presence of EPS/biofilm. EPS/biofilm was also observed at this timeframe for pyrite exposure. However, the EPS/biofilm observed on the chalcopyrite, shown in Figure 6.13 (b), is more localised and shows more structure than what was observed in the pyrite sample. There is also pitting observed on some particles, which was not observed in the control sample. This indicates that the presence of *A. f* increases the leaching of chalcopyrite.

The number of cells observed on the surface increases slightly at 24 h, with surface debris still prominent. Surface defects such as cracks are larger at this time frame.

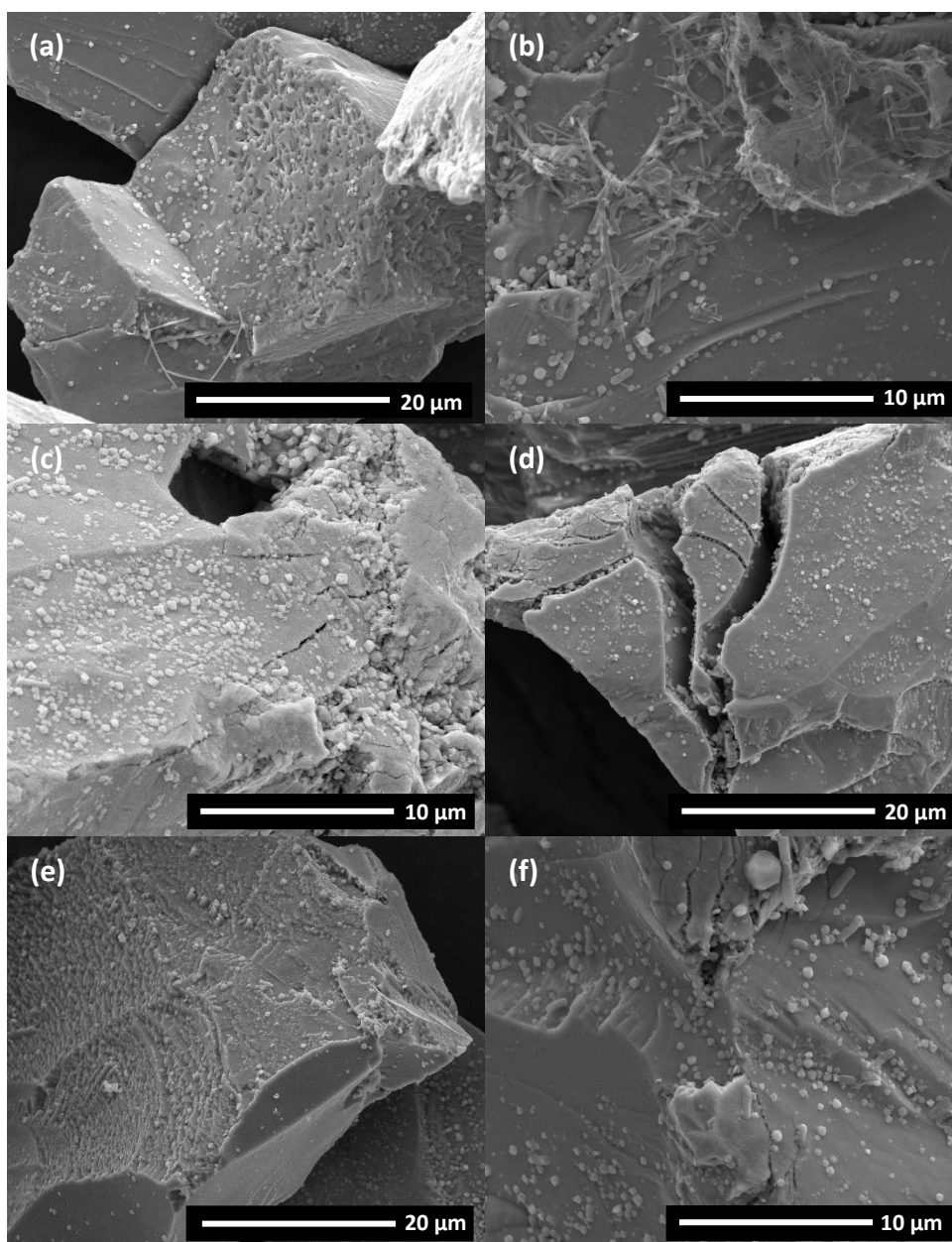


Figure 6.13: SEM image of *A. f* adapted to chalcopyrite exposed to chalcopyrite at an exposure of 12 h (a – c) and 24 h (d – f) imaged at a magnification of 6000x (a, d and f) and 12000x (b, c and f); with an accelerating voltage of 10 kV

As the exposure time increases so does the presence of surface defects. At 36 h exposure, defects such as holes and voids are now present on the surface. As these were not observed in the control sample, this is considered to be influenced by the presence of bacteria. Figure 6.14 (b) shows cells on the chalcopyrite surface with EPS spun across the surface and in some areas it has started to complex into a larger structure. Exposure of 48 h indicates an increase

in leaching through the rounding of edges and multiple voids present on one particle. At this time frame, cells are still seen on the surface and single cells and not in clusters. Clusters of cells were observed at 12 h in the pyrite analysis.

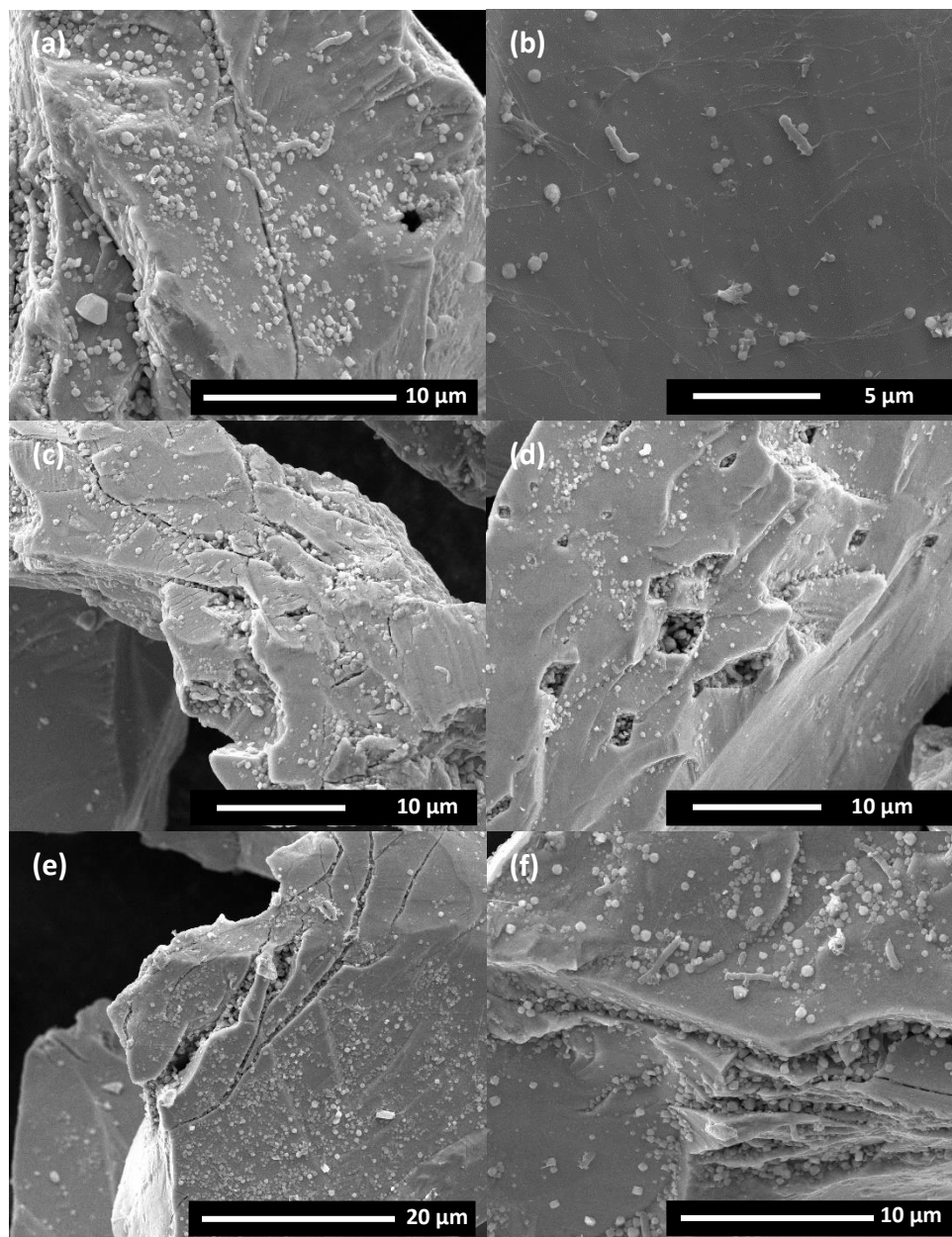


Figure 6.14: SEM image of *A. f* adapted to chalcopyrite exposed to chalcopyrite at an exposure of 36 h (a – c) and 48 h (d – f) imaged at a magnification of 12000x (a and f), 16000x (b), 8000x (c and d), and 6000x (e); with an accelerating voltage of 10 kV

Observations at 60 h are similar to what was seen at 48 h exposure. Finer cracks and leach pits are observed on some particles. While cells are still observed as single cells rather than clusters, the presence of EPS/biofilm has increased. At 72 h, clusters of cells are still not present. However, leach tunnels are now present on some particles (Figure 6.15 e). The lack

of colonisation in the presence of leach tunnels/pits on the surface indicates the *A. f* is surviving through indirect non-contact mechanisms.

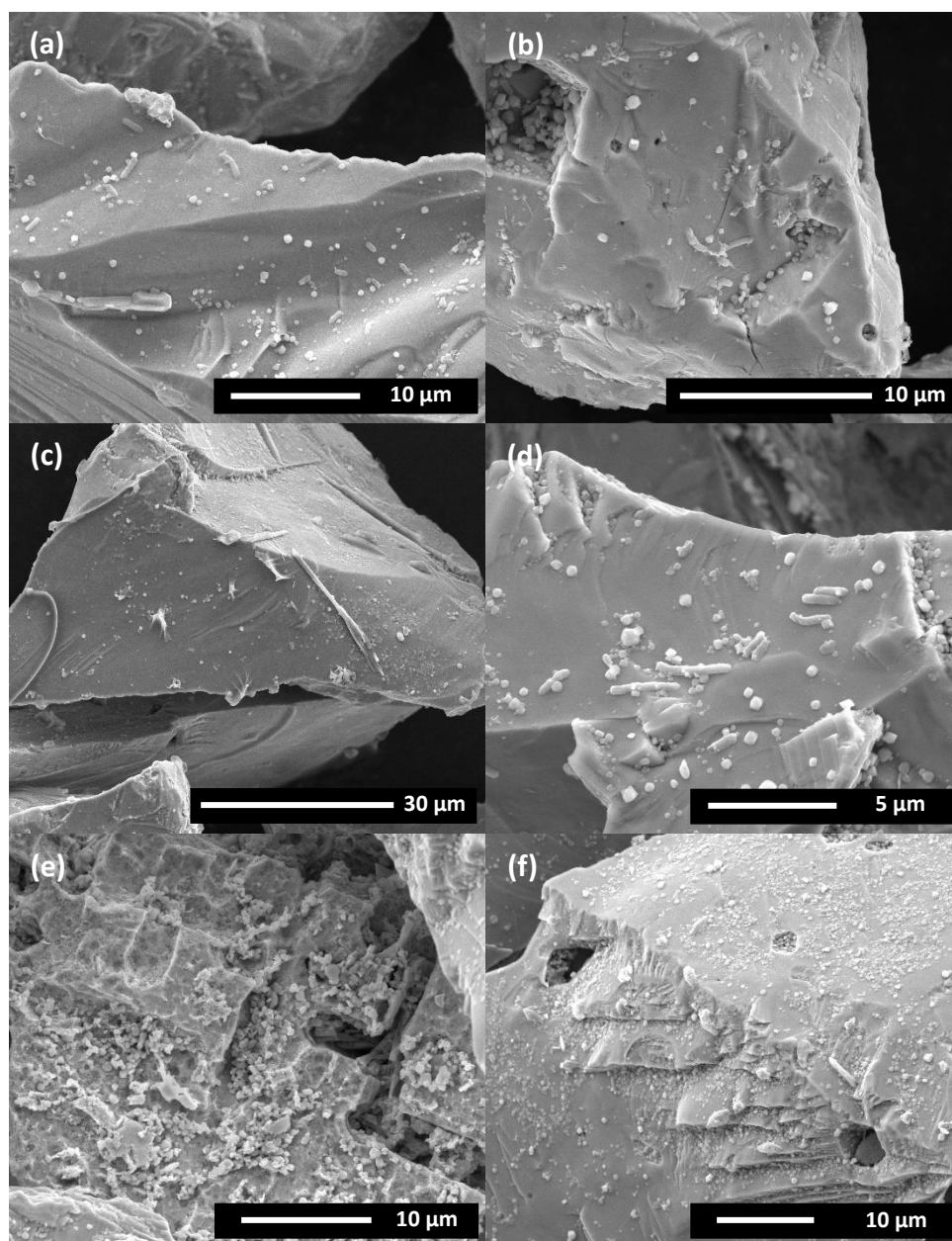


Figure 6.15: SEM image of *A. f* adapted to chalcopyrite exposed to chalcopyrite at an exposure of 60 h (a – c) and 72 h (d – f) imaged at a magnification of 8000x (a and e), 12000x (b), 4000x (c), 16000x (d), and 6000x (f); with an accelerating voltage of 10 kV

At 168 h exposure there is still not indication of colonisation, with cells still observed as single cells only. As colonisation was experienced at this time frame for the *A. f* culture adjusted to pyrite, it suggests that growth on chalcopyrite is plausible, however creates a less desirable environment than pyrite. This is also reflected by the growth curves shown in Figure 6.2 and Figure 6.3 above. At this time frame, the leaching effect is also observed to be increasing with

debris still observed on the surface of all particles. The debris is observed to be greater on some particles than others.

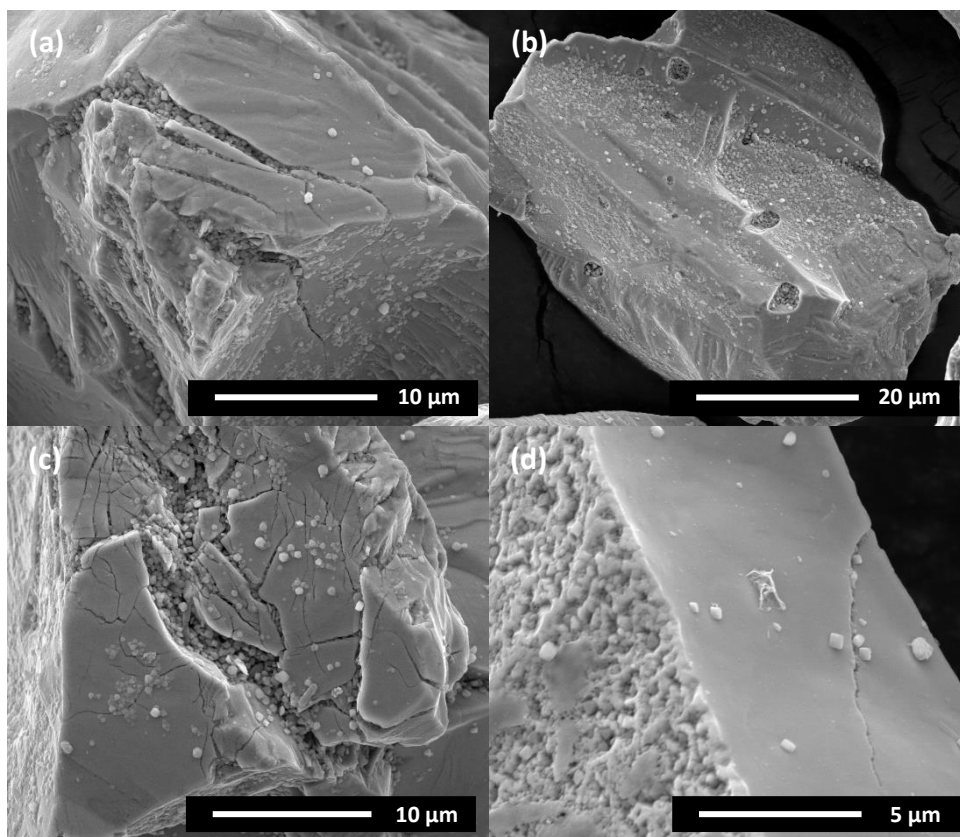


Figure 6.16: SEM image of *A. f* adapted to chalcopyrite exposed to chalcopyrite at an exposure of 168 h imaged at a magnification of 10000x (a and c), 5000x (b) and 20000 (d); with an accelerating voltage of 10 kV

Overall, the *A. f* is observed to be functioning via an indirect non-contact mechanism throughout the exposure time. This is supported by the formation of structures such as leach pits on the surface of the mineral where minimal attachment is observed. The leaching effect is observed by 12 h exposure, which is earlier than that of the chalcopyrite control, indicating the presence of *A. f* increases leaching. The EPS/biofilm formation is observed from 12 h exposure, which is where EPS/biofilm was observed in the pyrite culture.

Below Figure 6.17 exhibits cell and EPS/biofilm attachment to particles of impurity. This is seen to occur from 2 h exposure. This indicates preferential attachment of cells and EPS/biofilm to particles of impurity as earlier time frames. This supports the observation that chalcopyrite is not a favourable environment for *A. f*.

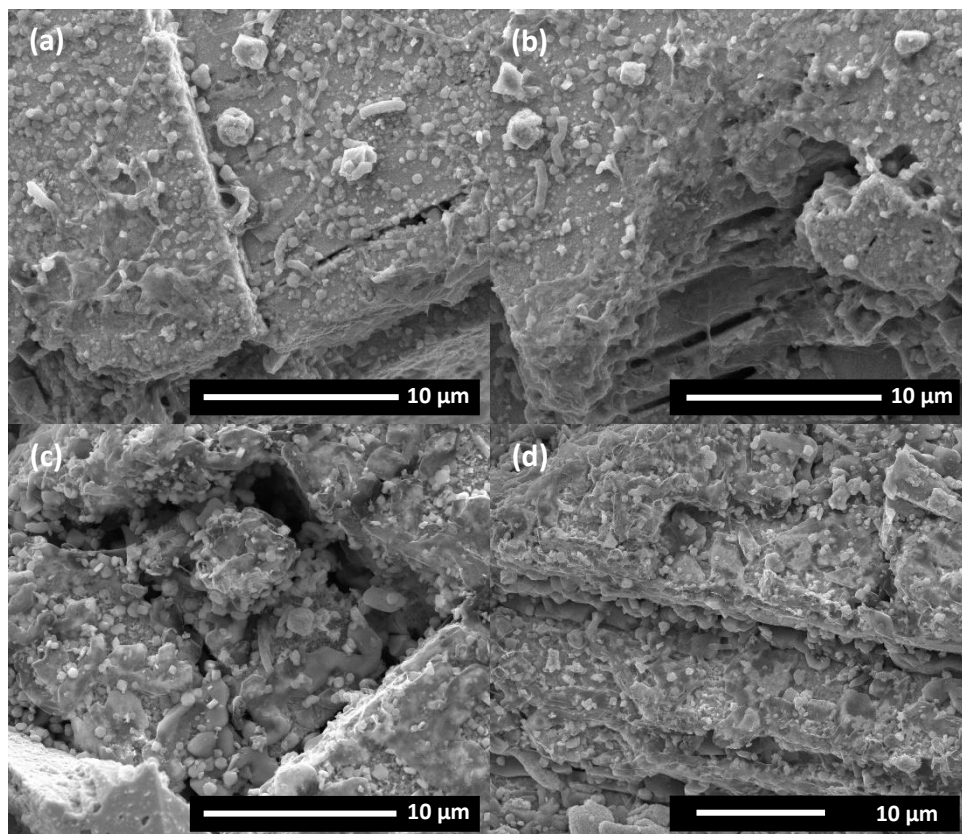


Figure 6.17: SEM image of *A. f* adapted to chalcopyrite exposed to chalcopyrite showing the attachment to particles of impurity at 2 h (a and b), 24 h (e) and 36 h (d), imaged at a magnification of 12000x (a – c) and 8000x (d) with an accelerating voltage of 10 kV

6.3.2.4 FTIR-ATR Analysis

FTIR-ATR was used to analyse the surface chemistry changes of pyrite and chalcopyrite over these exposure times. Some surface chemistry changes catalysed by bacteria can be detected through FTIR-ATR [29]. Figure 6.18 illustrates the changes which occurred on the pyrite surface and chalcopyrite surface when exposed to *A. f* bacteria. The spectra indicate greater change of the pyrite than the chalcopyrite. These changes are observed in the 700 cm^{-1} to 1600 cm^{-1} wavenumber range. While these changes are minor, they do indicate an increase in amides, polysaccharides (C–O, C–O–C), S containing functional groups, and carbohydrates (CH_3 wagging and CH_2 scissor) [30-35]; suggesting the presence of either/both carbohydrates and proteins on the surface. These changes are not noticeable in the chalcopyrite, with the exception of a slight peak at approximately 1090 cm^{-1} , which aligns with aromatic vibrations [31,32], suggesting an increase in the complexity of the carbon component on the surface. The minimal changes in the chalcopyrite are similar to what was observed by Sharma, et al. [36].

These samples were analysed as a slurry, therefore some changes may not have been detected due to the interference of water/media. However, as these samples contain bacteria and EPS/biofilm, dehydrating the sample prior to the analysis will not present a true representation of surface chemistry and changes.

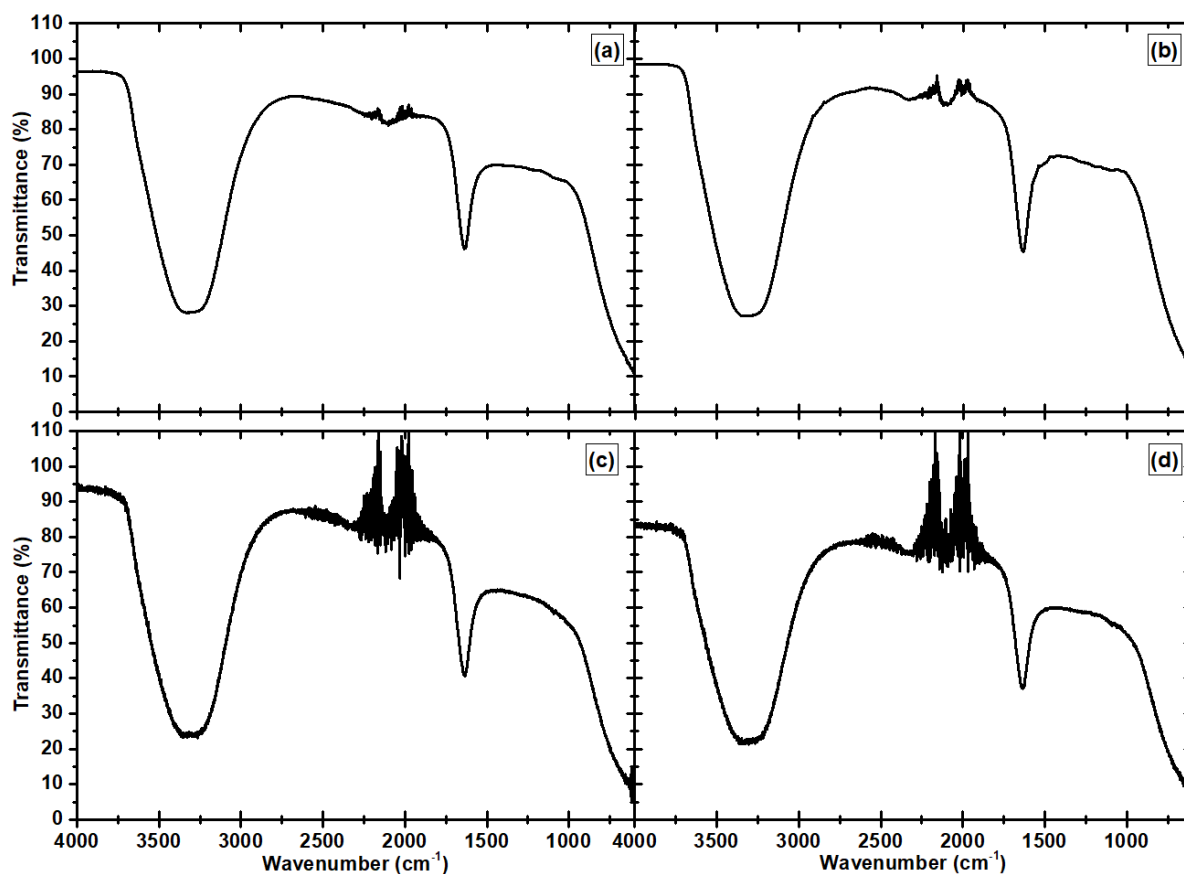


Figure 6.18: FTIR-ATR of pyrite showing pyrite in HH media at 0 h exposure (a), pyrite exposed to *A. f* at 186 h (b), chalcopyrite in HH media at 0 h exposure, and chalcopyrite exposed to *A. f* at 168 h (d)

6.3.3 Micro-Flotation Studies

Micro-flotation tests were carried out as single mineral and mixed mineral tests. The baseline single mineral flotation tests have been previously discussed in this thesis. The single mineral flotation tests for different food source (soluble iron, pyrite, chalcopyrite and arsenopyrite) and EPS conditions resemble the same trends as seen in the mixed mineral flotations. Conditions which included the presence of cells reduced the flotation recovery of both minerals, with the addition of PIPX collector increasing the recovery of both pyrite and chalcopyrite.

6.3.3.1 **Baseline Conditions**

The baseline recoveries from differential flotation tests of HH Media and Milli-Q pH 9, both in the presence of PIPX collector and as collector-free flotation tests, are discussed above in Section 4.3.3.1. The recoveries are shown in Figure 4.26, Figure 4.27 and Figure 4.28. The baseline differential flotation tests suggest that HH Media at a pH of approximately 1.8 supports the separation of chalcopyrite from pyrite, with the greatest separation observed at 48 h exposure.

6.3.3.2 **Growth Condition**

6.3.3.2.1 *A. ferrooxidans* Grown on Iron Sulfate

The flotation recovery for mixed mineral flotation tests of *A. f* grown on iron sulfate is shown in Figure 6.19. Collector-free flotation tests under these conditions result in minimal recovery of chalcopyrite, with 7.0% recovery achieved at 12 h. Similarly, the pyrite recovery was minimised with the greatest recovery observed at 1.1% at 2 h exposure. The greatest separation is observed at 12 h exposure, however because the recovery of chalcopyrite is so low, the separation is not economical.

The recovery in the presence of PIPX is shown in Figure 6.19 (b). Addition of collector increases the recovery of both minerals. The recovery of chalcopyrite fluctuates over exposure time, with the greatest recovery of 81.1% obtained from 2 h exposure and the lowest recovery of 48.1% obtained from 72 h exposure. The pyrite recovery was more consistent, with the maximum recovery achieved at 48 h with a recovery of 23.4% and the minimum recovery of 18.9 % was achieved at 36 h. The best separation was achieved at 2 h exposure.

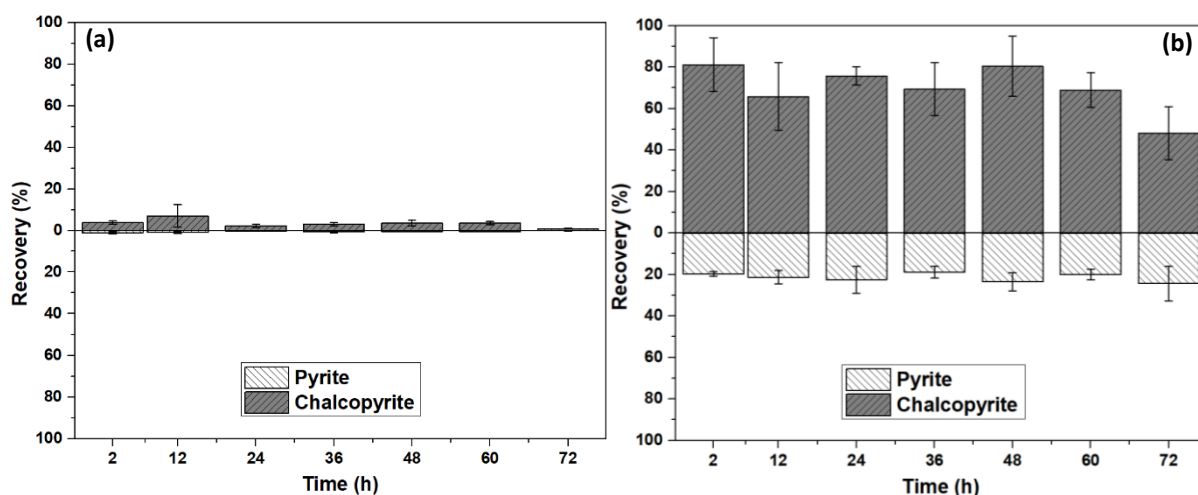


Figure 6.19: Differential flotation test recovery for *A. f* grown on iron sulfate as collector-free flotation tests (a); in the presence of PIPX collector (b)

6.3.3.2.2 *A. ferrooxidans* Grown on Pyrite

The results obtained from *A. f* adjusted to pyrite are similar to what was observed in the *A. f* grown on iron sulfate. The collector-free flotation tests, shown in Figure 6.20 (a), indicates the presence of cells results in suppression of both chalcopyrite and pyrite. Suppression of pyrite is greater than the suppression of chalcopyrite. The greatest recovery of both chalcopyrite and pyrite is observed at 60 h with a recovery of 14.7% and 1.9%, respectively. However, the error calculated for the chalcopyrite recovery indicates a potential fluctuation in recovery for this exposure time. While the recovery of pyrite is minimised, these conditions do not provide suitable conditions for separation of chalcopyrite, as the recovery of chalcopyrite is not adequate.

The addition of PIPX collector results in an increase in recovery of both minerals. However, suppression of both chalcopyrite and pyrite is observed at 60 h exposure, with a recovery of 2.6% and 0.2%, respectively. The greatest chalcopyrite recovery of 57.4% was achieved at 48 h exposure, which is where the highest recovery of pyrite is achieved at 6.4%. However, this exposure time exhibits large errors (28.5% chalcopyrite and 6.0% pyrite) suggesting reproducibility errors which can affect the recovery and efficiency of separation. Due to this, the best separation is achieved at 24 h exposure.

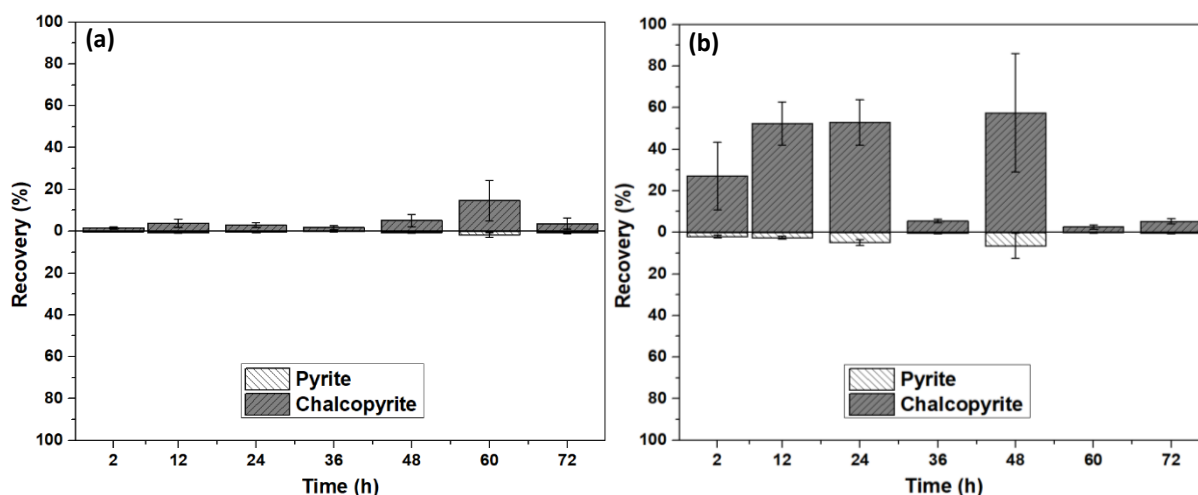


Figure 6.20: Differential flotation test recovery for *A. f* adjusted to pyrite as collector-free flotation tests (a); in the presence of PIPX collector (b)

6.3.3.2.3 *A. ferrooxidans* Grown on Chalcopyrite

The recovery from differential flotation tests for *A. f* grown on chalcopyrite is shown in Figure 6.21 below. These results show some similarities to the results obtained from *A. f* grown on iron sulfate and *A. f* grown on pyrite, with minimal recovery of both minerals obtained at exposure times of 12 h, 24 h, 48 h and 72 h. Of these exposure times, complete suppression of pyrite is observed at 24 h, 48 h and 72 h. For the remaining exposure times (2 h, 36 h and 60 h), recovery increases with the increasing exposure time for both mineral phases. Although the 60 h exposure time results in the greatest recovery of pyrite at 17.2%, this exposure time provides the best separation efficiency with a chalcopyrite recovery of 86.9%. The separation efficiency at 36 h is adequate with chalcopyrite recovery at 53.3% and pyrite recovery of 7.1%. However, the error associated with the chalcopyrite recovery (42.4%) suggests the separation efficiency is susceptible to large variations.

Addition of PIPX collector increases the recovery of both chalcopyrite and pyrite across exposure times, this is similar to what was observed in the *A. f* grown on iron sulfate flotation tests. The recovery trend of chalcopyrite similar to the collector-free flotation tests, with the greatest recoveries achieved at 2 h, 36 h and 60 h exposures. Interestingly, the addition of collector to these exposure times reduces the errors observed for chalcopyrite recovery, with errors ranging between 1.8% at 2 h to 18.2% at 72 h. The addition of PIPX increases the recovery of pyrite, with the minimum recovery of 11.4% at 24 h and maximum recovery of 46.7% at 12 h exposure. This increase in pyrite is expected to be contributed by copper

activation of the pyrite [37,38]. Even with this increase in pyrite recovery, the best separation efficiency is observed at 60 h exposure with 96.7% recovery of chalcopyrite. This is the greatest recovery observed for the 'Food Source' exposure conditions.

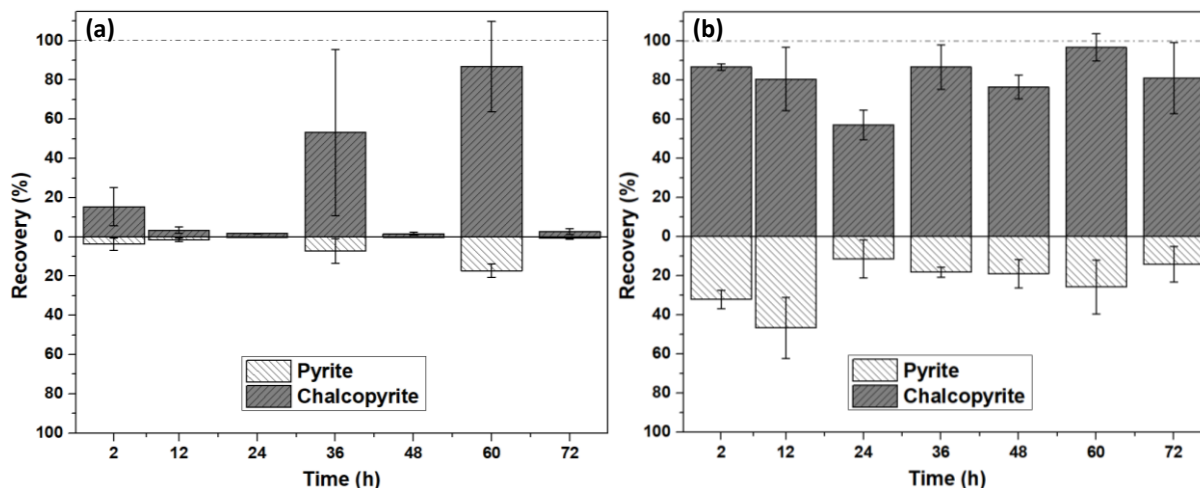


Figure 6.21: Differential flotation test recovery for *A. f* adjusted to chalcopyrite as collector-free flotation tests (a); in the presence of PIPX collector (b)

6.3.3.2.4 *A. ferrooxidans* Grown on Arsenopyrite

The results of the *A. f* grown on arsenopyrite differential flotation tests are illustrated in Figure 6.22. In comparison to the differential flotation tests of the baseline conditions suppression of chalcopyrite is observed, yet the suppression is not as great as what is observed for the other growth conditions. The recovery of chalcopyrite increases as a function of time, up until an exposure time of 48 h where the recovery rapidly decreases before increasing again at 60 h and 72 h. The largest recovery of chalcopyrite is attained at 36 h, with a maximum recovery of 51.0%, which is where the best separation efficiency is achieved. The pyrite recovery is completely suppressed at 2 h and 48 h. The recovery at 12 h, 24 h and 36 h is minimised to 4.2%, 6.9% and 7.9%, respectively. Recovery is increased significantly to 60.8% at 60 h, which is the highest recovery of pyrite, with recovery reduced to 17.4% at 72 h.

Similar to the other flotation conditions, the additions of PIPX collector increased the recovery of both chalcopyrite and pyrite. Surprisingly, the recovery of pyrite is almost equivalent to the recovery of chalcopyrite for all exposure times. Therefore, resulting in very little to no separation efficiency for *A. f* adjusted to arsenopyrite with PIPX.

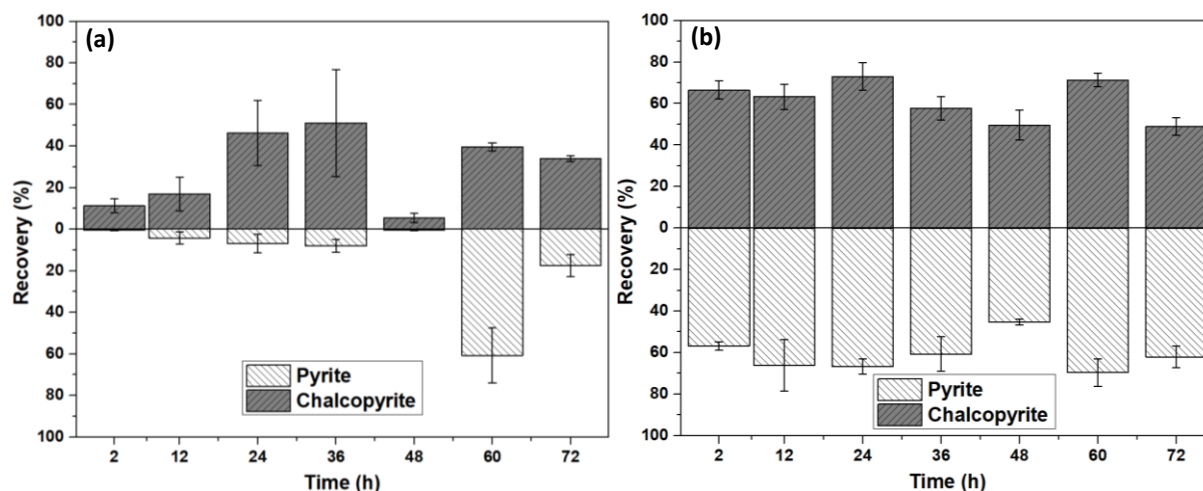


Figure 6.22: Differential flotation test recovery for *A. f* adjusted to arsenopyrite as collector-free flotation tests (a); in the presence of PIPX collector (b)

The differential flotation results from the different growth conditions suggests that there is some selective depression/flotation occurring, which changes with growth conditions. Overall, the presence of cells is seen to decrease the recovery of both chalcopyrite and pyrite, with the greatest suppression observed for the *A. f* grown on pyrite. The differences observed between the growth conditions could be influenced by the EPS produced in the different cultures. To investigate this, differential flotation tests were conducted in the EPS supernatant of these conditions.

6.3.3.3 Extracellular Polymeric Substance Supernatant

6.3.3.3.1 EPS Supernatant of *A. ferrooxidans* Adapted to Pyrite

The differential flotation tests conducted using the EPS supernatant of *A. f* grown on pyrite are shown in Figure 6.23 below. The collector-free flotation results show almost complete suppression of pyrite, with the maximum recovery of 1.1% achieved at 12 h. However, the recovery of chalcopyrite is mediocre, with the maximum recovery of 16.0% obtained at 12 h. This is where the greatest separation efficiency is achieved, although it does not produce an economically efficient recovery.

Addition of the PIPX collector results in a significant increase of chalcopyrite recovery, with an increase of at least 29% for all exposure times. The best recovery of chalcopyrite is observed at 24 h exposure with a recovery of 86.2%. Interestingly, the recovery at the other exposure times remains rather consistent, besides at 36 h where a decrease in recovery is observed. The recovery at 2 h and 12 h is observed at 49.0% and 50.8%, respectively. The

recovery at 48 h, 60 h and 72 h are increased but also consistent with recoveries of 63.7%, 68.7% and 67.8%, respectively. The consistency amongst the results of the different exposure times suggests there is minimal surface chemistry changes between these exposure times. The addition of PIPX has minimal effect on the recovery of pyrite, with the increase of recovery observed to be between 0.4% at 36 h to 8.1% at 24h. The minimal recovery of pyrite results in adequate separation at all time frames, with the greatest separation achieved at 24 h.

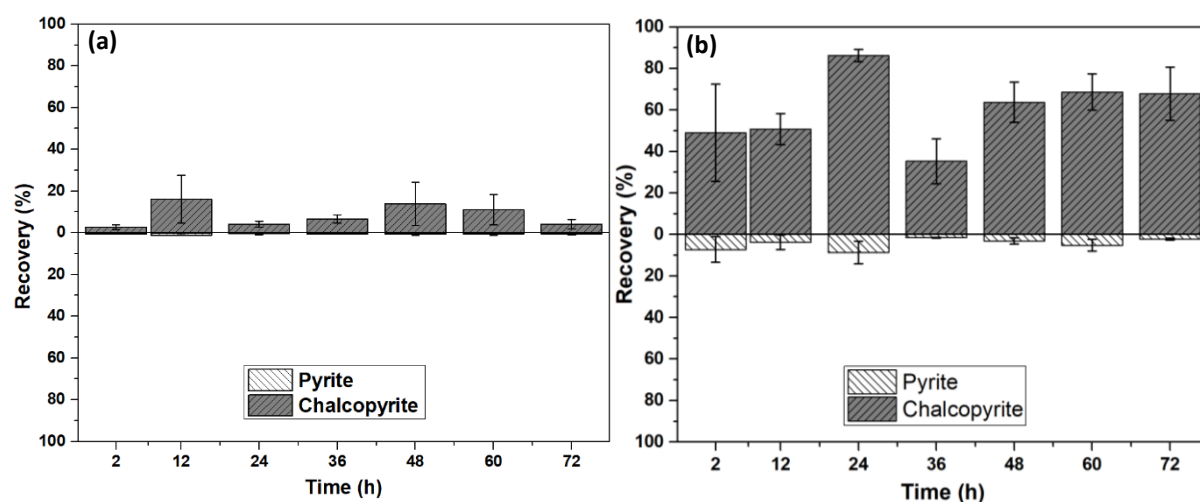


Figure 6.23: Differential flotation test recovery for EPS supernatant of *A. f* adjusted to pyrite as collector-free flotation tests (a); in the presence of PIPX collector (b)

In comparison to the baseline flotation tests, the recovery of both minerals is decreased. However, in comparison to *A. f* grown on pyrite the recovery of chalcopyrite is increased. This suggests that the presence of cells in the system, when they are adapted to grow on pyrite, show little selectivity to pyrite creating a suppression of both minerals. While the EPS supernatant shows some selectivity through the increase in recovery of chalcopyrite.

6.3.3.3.2 EPS Supernatant of *A. ferrooxidans* Adapted to Chalcopyrite

The recoveries obtained from the differential flotation tests for the EPS supernatant of *A. f* grown chalcopyrite is shown in Figure 6.24. The collector-free flotation tests show minimal recovery of pyrite, with the lowest recovery of 2.1% at 2 h and the greatest recovery of 3.2% at 72 h. The recovery of chalcopyrite fluctuates over the exposure times with the lowest recovery of 7.8% at 2 h and the greatest recovery of 30.8% at 72 h. Although the greatest recovery was observed at 72 h, the best separation efficiency is achieved at 12 h.

The addition of PIPX collector increases the recovery of both minerals. It is seen that the recovery of chalcopyrite exceeds 80%, with 2 h exposure resulting in the minimum recovery of 84.5%. The maximum recovery occurs at 36 h with a recovery of 95.8%. Likewise, the recovery of pyrite was increased with the addition of PIPX collector. The recovery of pyrite varies between 14.1% at 24 h and 37.1% at 12 h. The increased recovery of pyrite in the presence of PIPX is attributed to copper activation [37,38]. It is possible that the copper activation is occurring through copper ions which are absorbed/extracted by the EPS during the growth of the culture. The greatest separation is obtained at an exposure of 24 h, narrowly followed by 72 h exposure.

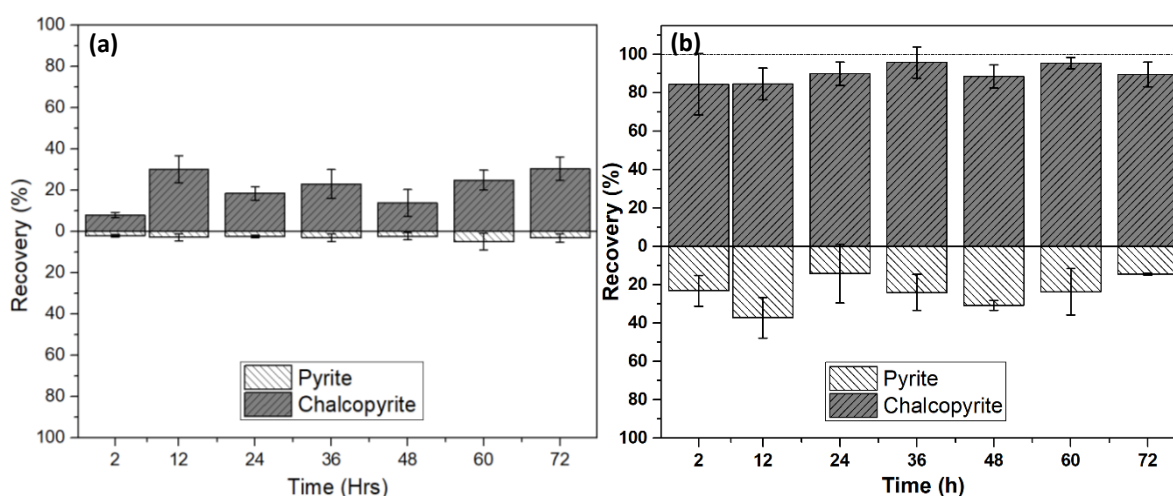


Figure 6.24: Differential flotation test recovery for EPS supernatant of *A. f* adjusted to chalcopyrite as collector-free flotation tests (a); in the presence of PIPX collector (b)

Similar to the EPS supernatant from *A. f* grown on pyrite; the recovery of both minerals in collector-free conditions is decreased in comparison to baseline flotation tests. The EPS supernatant is seen to result in more consistent recovery in collector-free flotation tests and greater recovery and separation in the presence of collector. This change is attributed to the absence of cells, as previous literature has indicated that cell adhesion increases the hydrophilic properties of the surface [39,40]. This also indicates that the EPS supernatant increases the recovery of chalcopyrite in the presence of PIPX collector, in comparison to the baseline conditions.

6.3.3.3.3 EPS Supernatant of *A. ferrooxidans* Adapted to Arsenopyrite

The EPS supernatant was investigated for the separation of chalcopyrite and pyrite with the differential flotation test results shown in Figure 6.25. The results from the collector-free

flotation tests shows an increase in recovery as a function of time for both chalcopyrite and pyrite, with the greatest recovery of both minerals observed at 72 h. Although the recovery of pyrite at 72 h is 13.4%, this is where the greatest separation was achieved.

The PIPX collector increased the recovery of both minerals all exposure times, besides 24 h and 48 h where pyrite recovery is suppressed. For these timeframes the chalcopyrite recovery was also observed to be decreased at 31.9% and 35.8%, respectively. The recovery for the other exposure times ranges from 84.8% at 12 h and 98.6% at 72 h. The pyrite recovery ranges from 1.2% at 24 h to 51.4% at 72 h. The greatest separation is achieved at 60 h, due to the minimal recovery of chalcopyrite at 48 h.

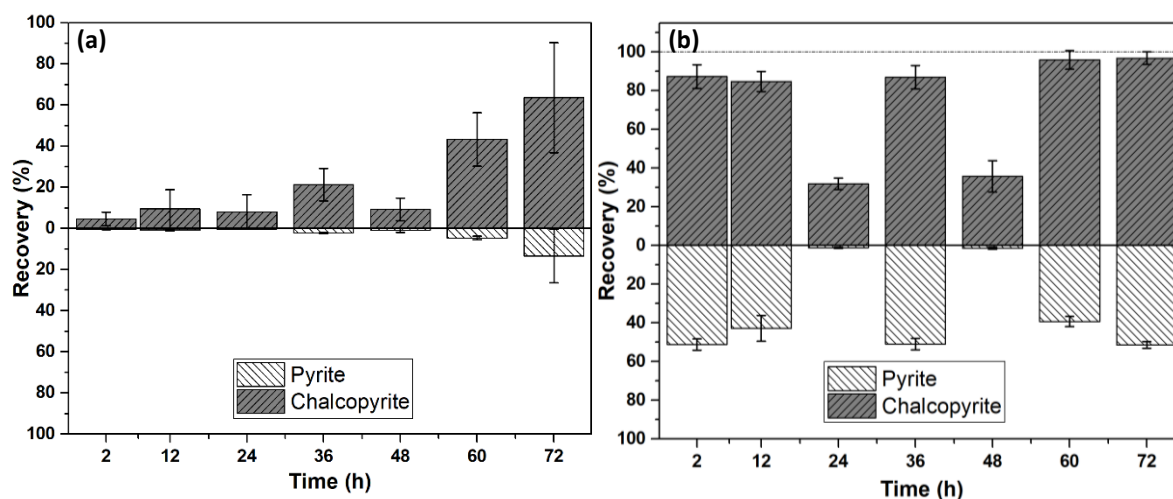


Figure 6.25: Differential flotation test recovery for EPS supernatant of *A. f* adjusted to arsenopyrite as collector-free flotation tests (a); in the presence of PIPX collector (b)

In comparison to the collector-free flotations of the baseline conditions and the *A. f* adjusted to arsenopyrite recovery is seen to be reduced. This is different to what was observed for the EPS supernatant of *A. f* grown on pyrite and *A. f* grown on chalcopyrite. This suggests a difference in either the chemical composition of the EPS or attachment/interaction of EPS to the mineral surface.

6.3.4 XPS Analysis

Pyrite samples exposed to HH media and *A. f* were analysed via XPS to investigate the changing surface conditions. Analysis was conducted on a Kratos AxisUltra at -165°C , using a cold stage, and at ambient temperature to detect volatile elemental sulfur at the surface.

Both survey scans and high-resolution spectra of sulfur, iron, carbon and oxygen were obtained for each sample and analysed using CasaXPS [41].

6.3.4.1 Survey Scan

Survey scans were energy corrected using the carbon peak (284.8 eV [42-44]) and shown in Figure 6.27. The survey scans indicate the presence of iron, sulfur, oxygen, carbon and copper in all samples and nitrogen in all samples besides the unreacted pyrite sample. Therefore, the presence of nitrogen likely originates from the ammonium sulfate ((NH₄)₂SO₄) component of the HH media. The presence of nitrogen in the HH media does create a limitation on what information can be obtained from the nitrogen component. The copper content in the samples is evidence of an impurity. However, the XRD of the sample does not indicate the presence of a copper bearing mineral phase. Therefore, it is determined that the copper is more than likely present in the lattice structure via elemental substitution [26,38]. The atomic percent of elements, shown in Table 6.2 and Table 6.3, indicate the copper content is consistent throughout all samples exposed to HH media, with a slight decrease observed in the *A. f* exposed samples. The SEM images shown in Figure 6.26 below shows the presence of dendritic growth, which EDAX confirms as copper. This confirms the copper content detected is an impurity in the mineral.

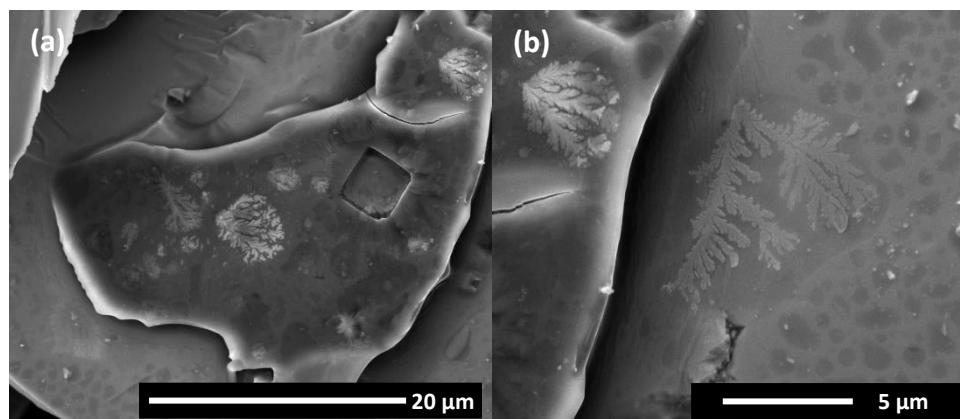


Figure 6.26: SEM image of pyrite illustrating copper impurities on the pyrite surface

The unreacted pyrite sample shows a greater concentration of carbon and oxygen on the surface, indicating potential oxidation from the crushing and grinding process and a baseline for adventitious carbon. The HH media appears to have a ‘cleaning’ effect on the surface at

24 h exposure, with a decrease in carbon and oxygen on the surface and an increase of the iron and sulfur.

In the media controls, the iron content is observed to fluctuate, with the content increasing up until 48 h exposure and then decreasing. This is similar to what is observed for the sulfur content; however, the sulfur is observed to start decreasing after 24 h. This decrease of iron and sulfur correlates with the leaching observed in the SEM analysis. Samples exposed to *A. f* also exhibit this decrease in the sulfur and iron content, although at a greater extent. This is due to the increased leaching effect of the bacteria [1,3,45], which is supported by the increased iron observed in the ferrous iron titrations. The total change in the iron is 8.7%, while the total change in sulfur is 11.6%. Therefore, indicating the preferential attack of sulfur over iron.

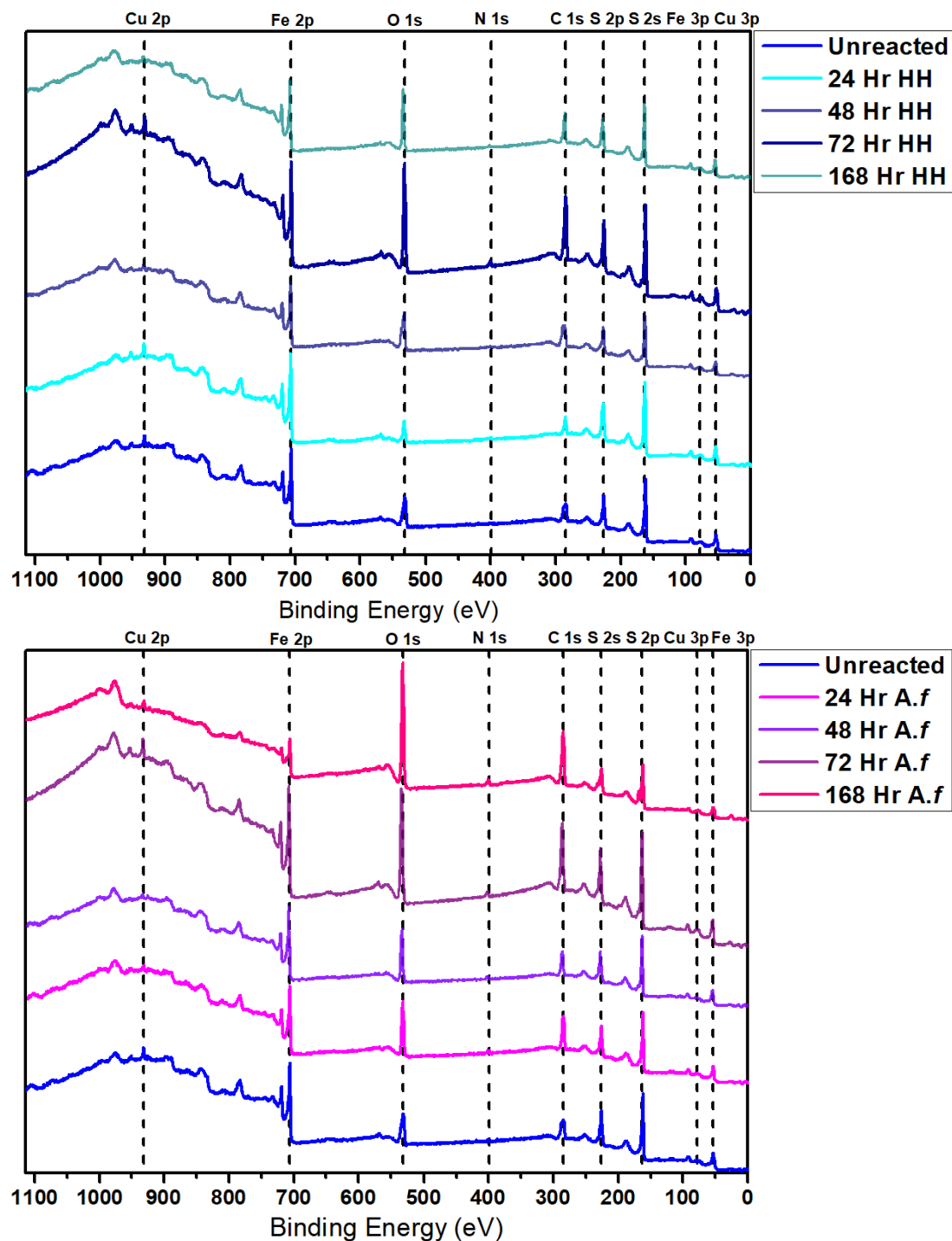


Figure 6.27: Survey scan of unreacted pyrite, HH media controls and *A. f* exposed pyrite samples, collected at -165°C with a monochromatic aluminium $\text{K}\alpha$ source

The carbon and oxygen components are observed to increase as a function of time in both the media control and *A. f* samples. The increase of carbon in the media control is minimal over the exposure time, while the oxygen increases by approximately 7.8%. Indicating the change on the surface is primarily the formation of oxygen species. *A. f* samples on the other hand show a larger change in the carbon and oxygen of approximately 5% and 16%,

respectively. This increase in the carbon and oxygen is a good indication of both organic species and oxide species being present, which can be confirmed through the analysis of high-resolution scans of carbon and oxygen.

Table 6.2: Elemental composition (At %) of survey scans for unreacted pyrite and pyrite exposed to HH media

	Element					
	S 2p 162.7 ± 0.1 eV	Fe 3p 53.6 ± 0.2 eV	C 1s 285.0 ± 0.2 eV	Cu 3p 77.1 ± 1 eV	O 1s 532.2 ± 0.7 eV	N 1s 400.8 ± 0.9 eV
Unreacted	24.0	13.8	37.5	1.9	22.8	-
24 h	35.5	16.9	28.2	1.9	15.7	1.9
48 h	18.1	9.3	44.3	1.4	26.5	0.4
72 h	18.3	9.0	39.9	1.2	30.6	1.0
168 h	22.9	10.4	34.4	1.7	29.6	1.0

Table 6.3: Elemental composition (At%) of survey scans for pyrite exposed to A. f

	Element					
	S 2p 162.7 ± 0.1 eV	Fe 3p 53.6 ± 0.2 eV	C 1s 285.0 ± 0.2 eV	Cu 3p 77.1 ± 1 eV	O 1s 532.2 ± 0.7 eV	N 1s 400.8 ± 0.9 eV
24 h	22.0	10.9	37.4	1.5	26.1	2.1
48 h	24.1	11.1	31.3	1.4	29.2	2.8
72 h	16.8	7.9	43.1	1.3	28.4	2.4
168 h	12.4	5.1	41.0	1.0	38.8	1.7

6.3.4.2 High Resolution Fe 2p, S 2p, C 1s and O 1s

The survey scan is useful for determining what elements are present within a sample, helping identify the composition; however, high-resolution scans provide more in-depth analysis of the specific element, including the oxidation states present. This information is quite often characteristic to individual elements, their oxidation state, and their bonding environment.

The bulk disulfide component at 162.5 eV [46] was used to energy correct the high-resolution spectra. As the hydrocarbon reference component has a shift in the binding energy of 0.4 – 0.6 eV [43], the disulfide component provides a more accurate way to energy correct the samples.

6.3.4.2.1 Iron 2p XPS Spectra

Analysis of the high-resolution iron spectra can help determine the surface states present, as there is sensitivity to oxidation states and bonding environments. The typical Fe 2p XPS

spectrum has the bulk Fe^{II} contribution present near 707.2 or 707.3 eV, with surface Fe^{III} contributions present near 708.7 eV [47]. There is a surface Fe²⁺ contribution which exists as a triplicate of peaks approximately 1 eV apart, starting at 708.1 eV. This triplicate contributes to the asymmetrical tail observed on the spectra that correspond to a S 3*p* to Fe 3*d* ligand to metal transfer and surface oxidation species [47]. All samples resemble a typical pyrite Fe 2*p* spectrum with a distinctly sharp peak at 707 ± 0.1 eV. The asymmetry of the peak is attributed to the presence of Fe^{II} surface state contribution with the broader peak at 708.6 ± 0.1 eV is assigned as the Fe^{II} contribution. Due to the convolution of states which contribute to this peak, the variations observed cannot be attributed to a change in oxidation states of the sample without reference to the high-resolution O 1*s* spectra.

A slight inflection is observed at 711 eV in the unreacted pyrite, 72 h control and 48 h *A. f* samples. Although this feature is likely to be a contribution that result from the presence of oxidation products such as FeOOH [47,48].

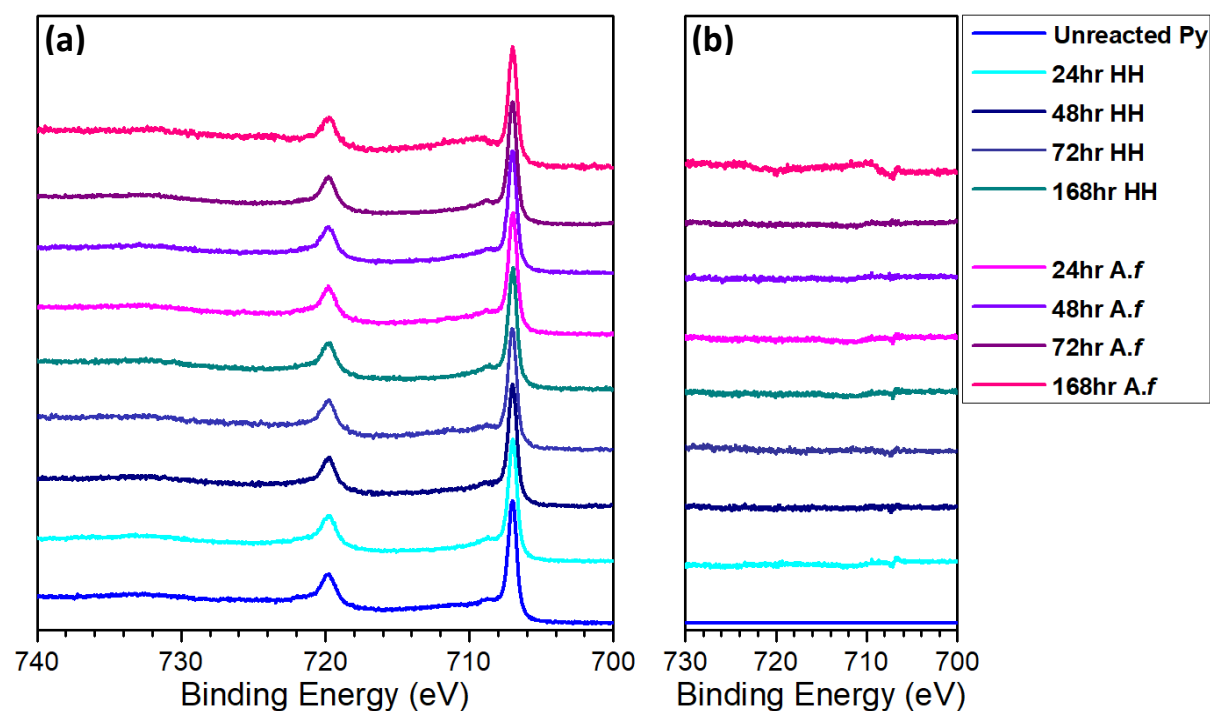


Figure 6.28: High-resolution Fe 2*p* spectra 700 – 740 eV (a) and the difference from the unreacted spectrum through subtraction (b), collected at -165°C with a monochromatic Al K α source

Figure 6.28 above illustrates the high-resolution Fe 2*p* spectra obtained from each sample and the difference of each sample from the unreacted pyrite. This illustrates little to no variation between samples, with greater change observed for the *A. f* exposed samples.

6.3.4.2.2 Sulfur 2p XPS Spectra

Elemental sulfur is a possible product of pyrite oxidation, however elemental sulfur is volatile in vacuum above -133°C . As a result, the high-resolution data was collected at -165°C and then warmed to ambient temperature ($18.4 - 21.7^{\circ}\text{C}$) under vacuum to remove the volatile elemental sulfur. A comparison between the two scans can determine the presence of elemental sulfur.

The high-resolution sulfur spectra change over time and with conditions, as shown in Figure 6.29. The spectra indicate a change in the sulfate region ($168 - 171\text{ eV}$) through changing intensities [42]. This implies an increase in oxidation as a function of exposure time. Component fitting of these spectra can give more information of how the surface is changing.

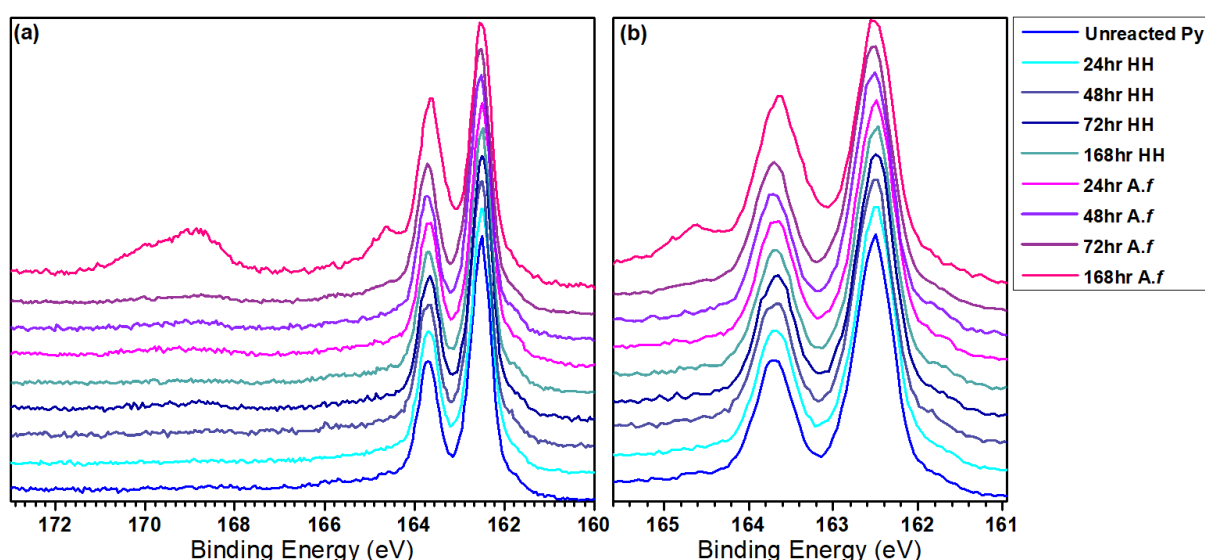


Figure 6.29: High-resolution Sulfur 2p spectra 160 – 173 eV (a) and enlarged S 2p 3/2 (b) of unreacted pyrite, HH media controls and *A. f* exposed samples, collected at -165°C with a monochromatic aluminium $\text{K}\alpha$ source

The high-resolution spectra were energy corrected by the bulk disulfide peak at 162.5 eV [46]. Components of monosulfide, polysulfide, sulfite, thiosulfate, sulfate and an energy loss feature were assigned by their energies and distance from the bulk disulfide according to energies previously reported [42,46,48]. All components, besides the energy loss feature, were fit as a doublet. A combination of these components were used to obtain an accurate fit for both the cold stage and ambient data, as shown in Figure 6.30 and Figure 6.31 for media controls, and Figure 6.32 and Figure 6.33 for *A. f* exposed samples. The component fit information is presented in Appendix III. Interestingly, the components required to obtain a reasonable fit differed between exposure conditions and times. The thiosulfate component

was only fit to the 24 h HH media control cold stage scan, with the sulfite component not fit to the 72 h HH media control and the *A. f* exposed samples at 24 and 48 h.

Overall, the contribution/concentration from the disulfide component is observed to decrease as a function of exposure time, in both the media control and the *A. f* exposed samples for cold and ambient scans. The monosulfide contribution remains constant in the HH media samples, with a slight decrease over exposure time exhibited in the *A. f* exposed samples. The change in the polysulfide contribution for each sample displays a different trend. The contribution in the HH media sample fluctuates, while steadily increasing in the *A. f* samples. The trend observed in the sulfite contribution is also different in the HH media samples than the *A. f* exposed samples. In the HH media samples, the contribution is observed to fluctuate with an overall decrease in concentration over exposure time. This is the opposite of what is observed in the *A. f* samples. The sulfate contribution is observed to increase for all conditions over time, with a greater increase seen after 72 h exposure. While the contribution from the energy loss feature remains relatively consistent throughout the HH media samples. However, this feature decreases as a function of time in the *A. f* exposed samples.

The fits were evaluated by examining the fit residual. A residual feature is observed at 164.5 eV in the cold stage scans for unreacted pyrite, HH media control 24 h and *A. f* exposed samples at 24 h, 72 h and 168 h. This residual feature is expected to be elemental sulfur, as elemental sulfur is expected at 164 eV [47] and this feature is not present in the corresponding ambient scans. As the energy and width of the polysulfide contribution is kept consistent between the cool and ambient scans, the difference between the residuals is a suitable determination for the presence of elemental sulfur.

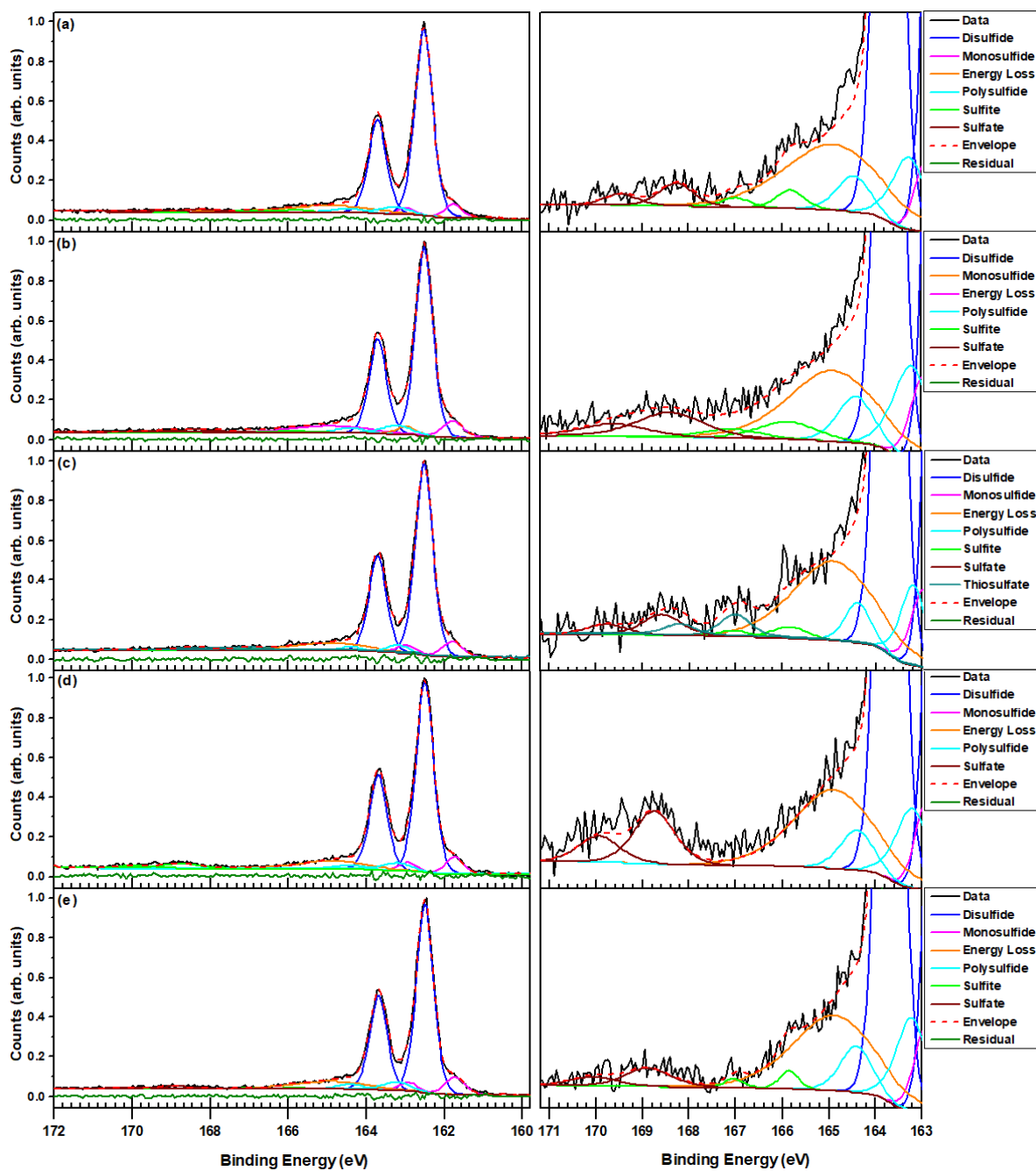


Figure 6.30: Component fits of high-resolution S ($2p_{3/2}$) spectra of unreacted pyrite (a) 24 h HH exposure (b) 48 h HH exposure (c) 72 h HH exposure (d) 168 h HH exposure (e), conducted at $-165\text{ }^{\circ}\text{C}$ with the enlarged 171 – 163 eV area of the respective scan displayed on the right

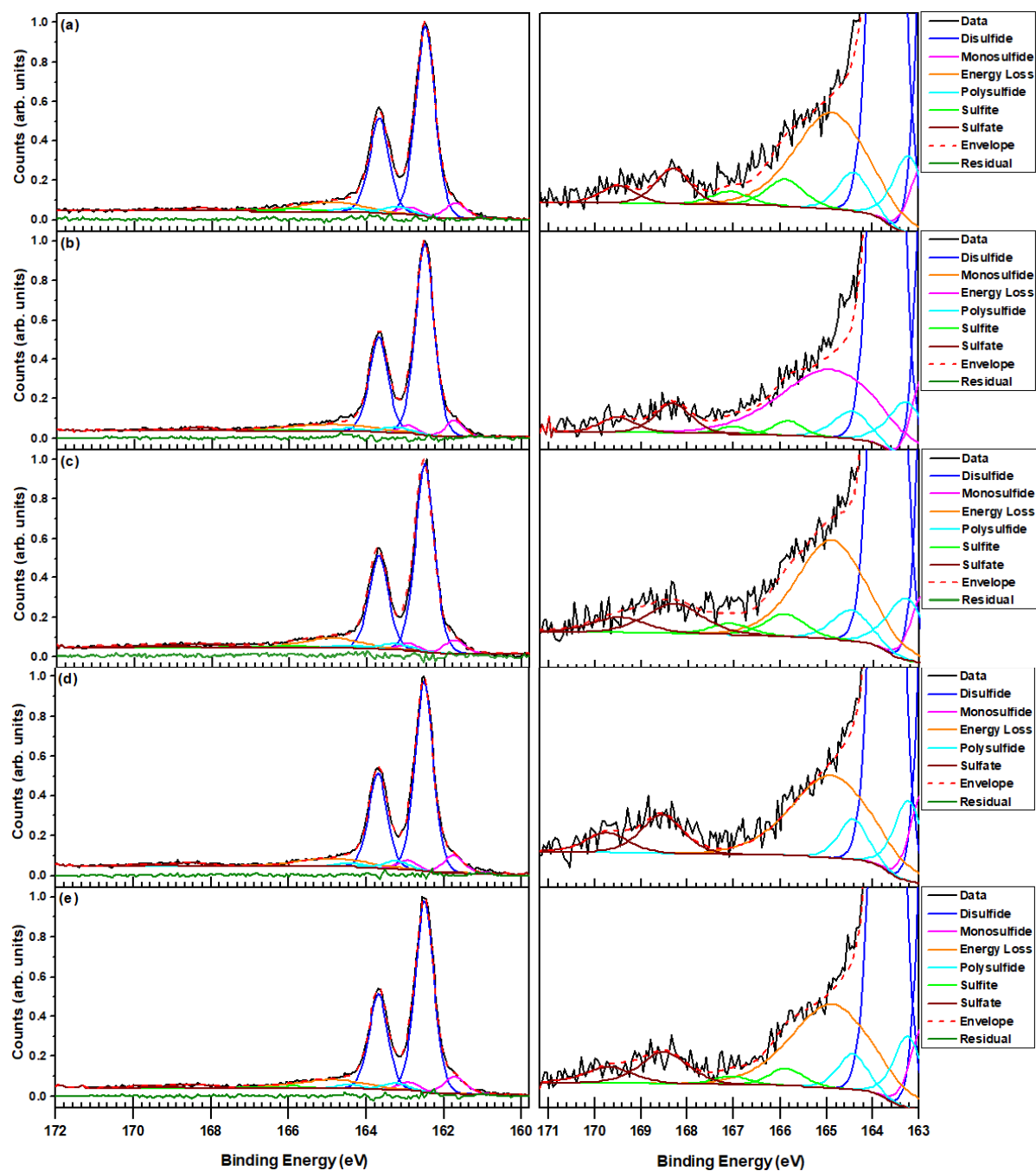


Figure 6.31: Component fits of high-resolution S ($2p_{3/2}$) spectra of unreacted pyrite (a) 24 h HH exposure (b) 48 h HH exposure (c) 72 h HH exposure (d) 168 h HH exposure (e), conducted at ambient temperature (18.4 – 21.7 °C) with the enlarged 171 – 163 eV area of the respective scan displayed on the right

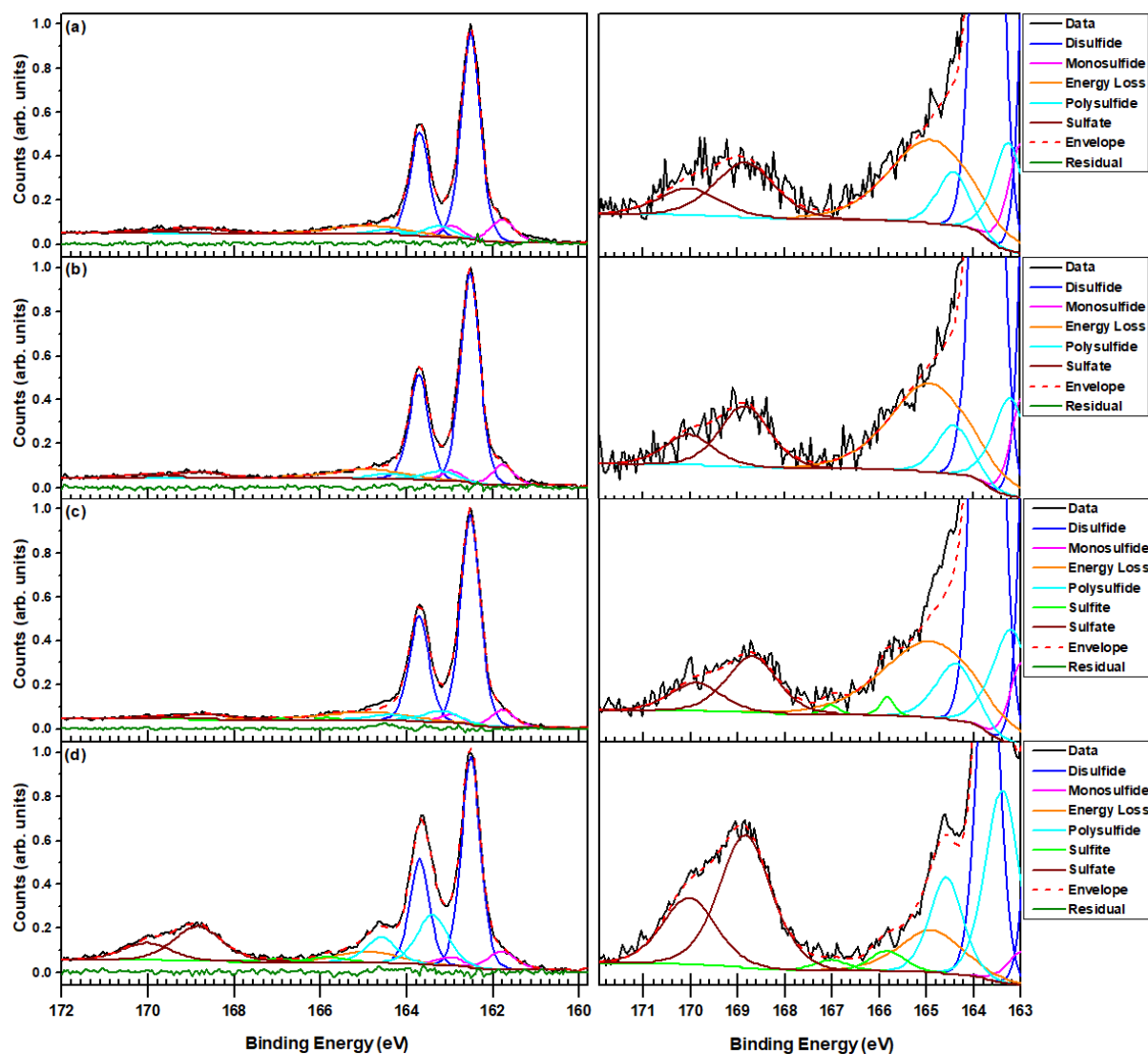


Figure 6.32: Component fits of high-resolution S 2p spectra of *A. f* exposed Py at 24 h (a) 48 h (b) 72 h (c) and 168 h (d), conducted at -165 °C with the enlarged 171 – 163 eV area of the respective scan displayed on the right

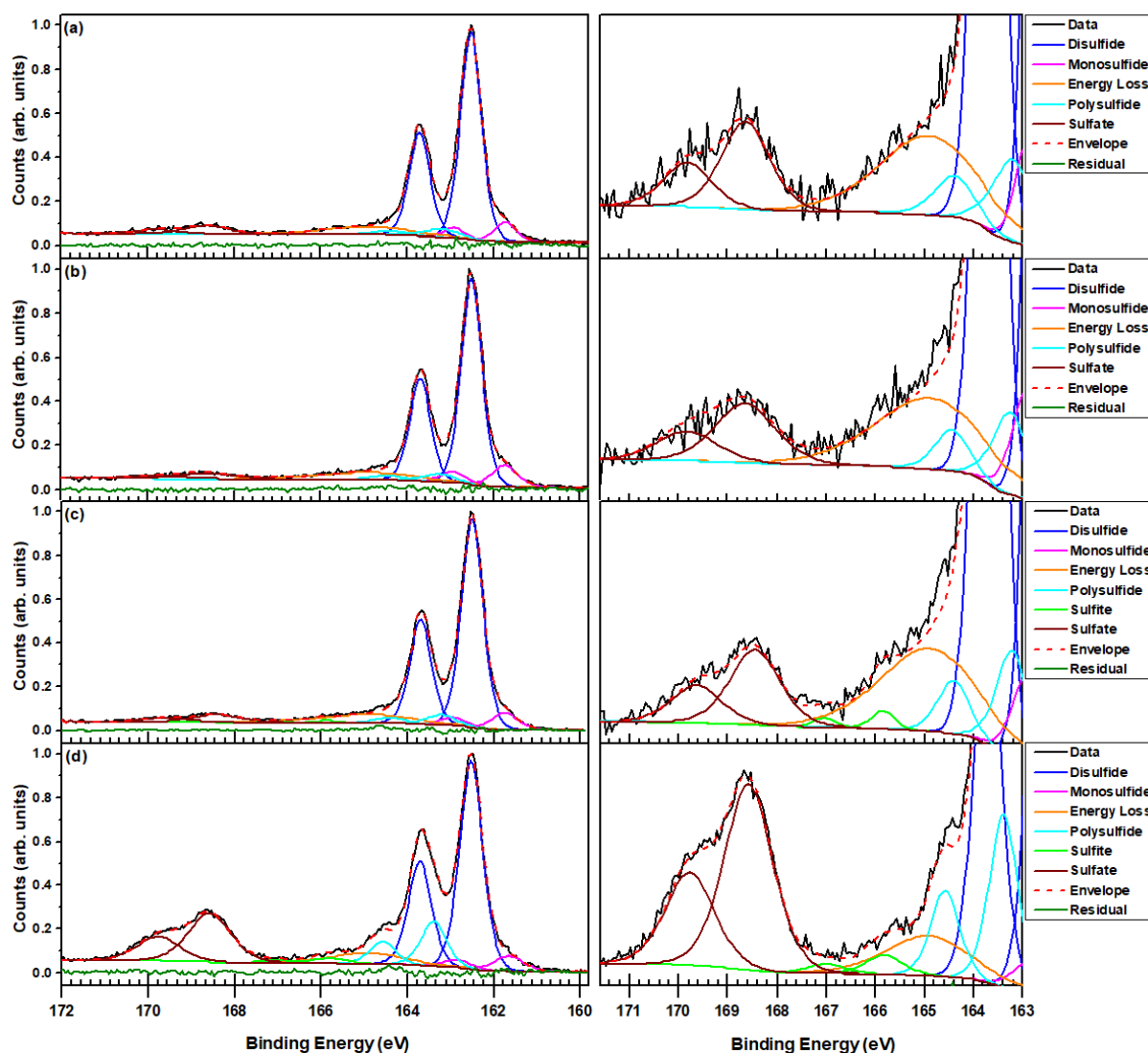


Figure 6.33: Component fits of high-resolution S 2p spectra of *A. f* exposed Py at 24 h (a) 48 h (b) 72 h (c) and 168 h (d), conducted at ambient temperature (18.4 – 21.7 °C) with the enlarged 171 – 163 eV area of the respective scan displayed on the right

The comparison of cold stage and ambient scans shows a difference in the width and intensities of the components, with broadening observed in the ambient spectra. It is expected that the broadening is a result of thermal movement and Doppler broadening [49,50], which is primarily observed in the bulk disulfide. At higher temperatures energy loss through inelastic processes, such as phonon excitation, is more probable and more pronounced [50]. These excitation events are inseparable from the signal of the elastic peak and therefore increases the width [50]. The changes in the intensity between the cold stage and ambient scans is observed between 167.5 and 171 eV, corresponding with the sulfate contribution. This suggests a change in oxidation of the sample over the time it takes to warm to ambient temperature, which is supported by the loss of the thiosulfate component in the

48 h HH media sample. As the concentration difference between the cold stage and ambient scans is slight, the oxidation which occurs in this time frame is negligible and an indication of how the sample changes over time in a vacuum.

6.3.4.2.3 Carbon 1s XPS Spectra

The carbon content of the samples was measured at both cold and ambient temperatures (approximately -165°C and 20° C, respectively). Energy correction was conducted using high-resolution sulfur spectra and components were fit using a Gaussian – Lorentzian line shape with a ratio of 60:40 [35]. A combination of seven components was used to fit the spectra, with the full width half maximum determined by the resolution of the spectra. These components for the cold scans are shown in Table 6.4, with component fits shown in Figure 6.34 and Figure 6.35. Components were assigned using values which have previously been reported in literature [35,42-44,51-55].

The contribution from the C–H/C–C assignment is seen to decrease as a function of time, for both the HH media control and the *A. f* exposed samples. The survey scans, presented in Figure 6.27 above, indicate an overall decrease in the carbon content of the HH media control and an overall increase in the carbon content of the *A. f* exposed samples. Therefore, the decrease of the C–H/C–C component is caused by either a decrease in carbon (as seen in the HH media control) or a decrease in simple carbon structures, as expected in the *A. f* exposed samples. The observed decrease in the C–OH component in the *A. f* samples along with an increase in the components which represent complex carbon structures (C–O–C, C–C=O, O–C=O and CO₃) supports this. The increase in complex carbon structures indicates the presence of organic matter, such as EPS and biofilm, on the surface of the pyrite after exposure to *A. f*. Interestingly, of the functional groups which represent more complex carbon structure only the C–O–C component is seen to increase in the HH media control.

Table 6.4: High resolution C 1s component fit information for cold stage scans

	C–H/C–C 284.5 ± 0.1	C–N 285.3 ± 0.1	C–OH 286.0 ± 0.1	C–O–C 287.0 ± 0.1	C–C–O 288.1 ± 0.1	O–C=O 289.1 ± 0.1	Carbonate 291.3 ± 0.1
Unreacted	38.01	-	14.73	-	14.48	15.35	-
HH 24 h	58.64	7.12	13.42	8.39	5.52	6.91	-
HH 48 h	25.52	5.40	12.40	12.80	10.56	25.78	7.54
HH 72 h	48.26	15.78	13.23	10.68	4.52	5.14	2.40
HH 168 h	46.31	16.57	17.76	10.86	3.62	4.88	-
A. f 24 h	41.75	13.31	22.20	12.06	5.91	4.77	-

A. f 48 h	40.21	14.38	19.26	13.75	4.89	7.52	-
A. f 72 h	40.30	6.80	15.89	20.17	8.0	6.22	2.62
A. f 168 h	24.57	14.74	17.63	24.08	8.35	6.02	4.62

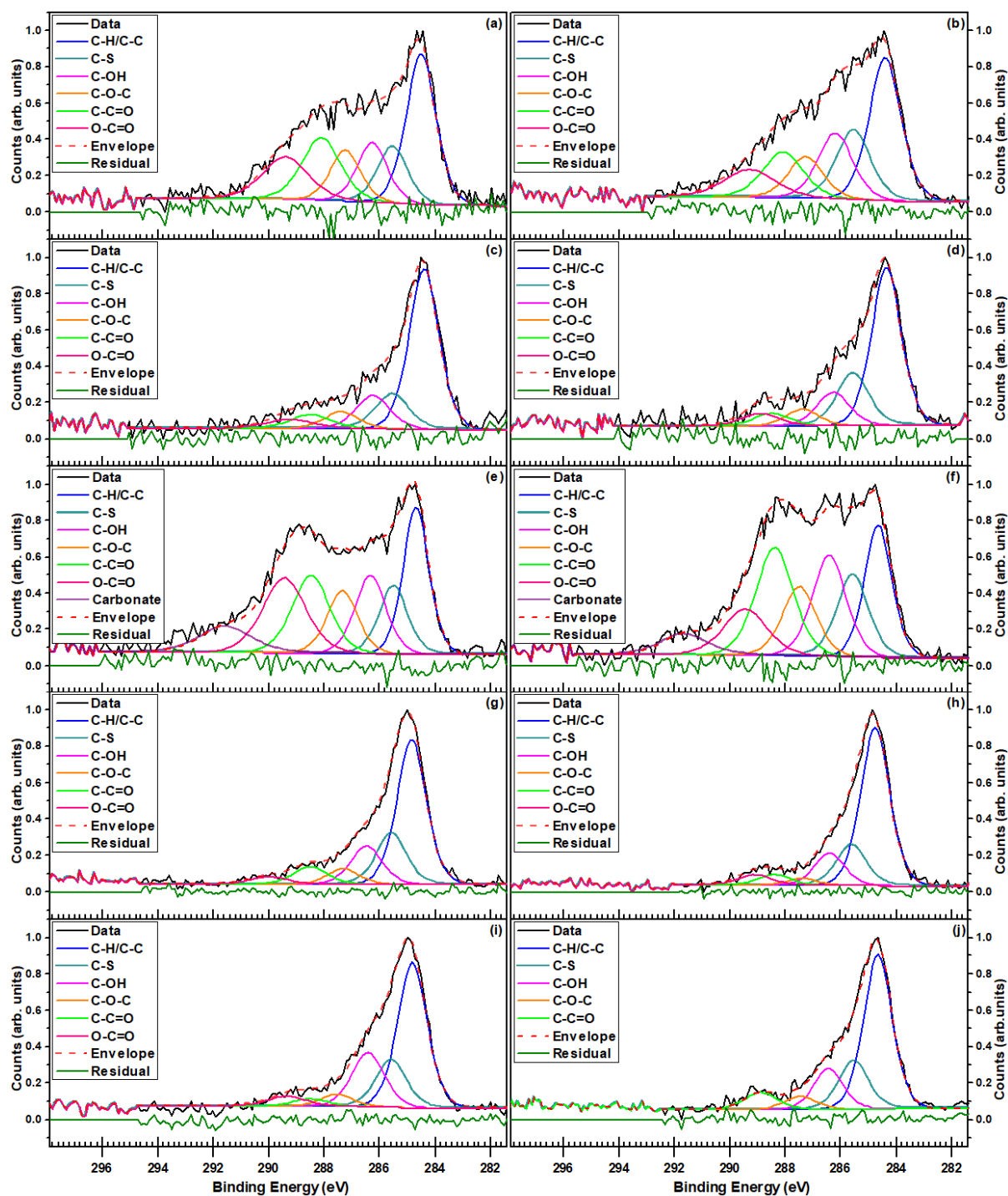


Figure 6.34: Component fits of C 1s spectra of unreacted Py cold stage (a) ambient (b) and the HH media exposures for 24 h cold stage (c) 24 h ambient (d) 48 h cold stage (e) 48 h ambient (f) 72 h cold stage (g) 72 h ambient (h) 168 h cold stage (i) 168 h ambient (j), cold stage scans were conducted at -165 °C and ambient scans between 18.4 and 21.7 °C

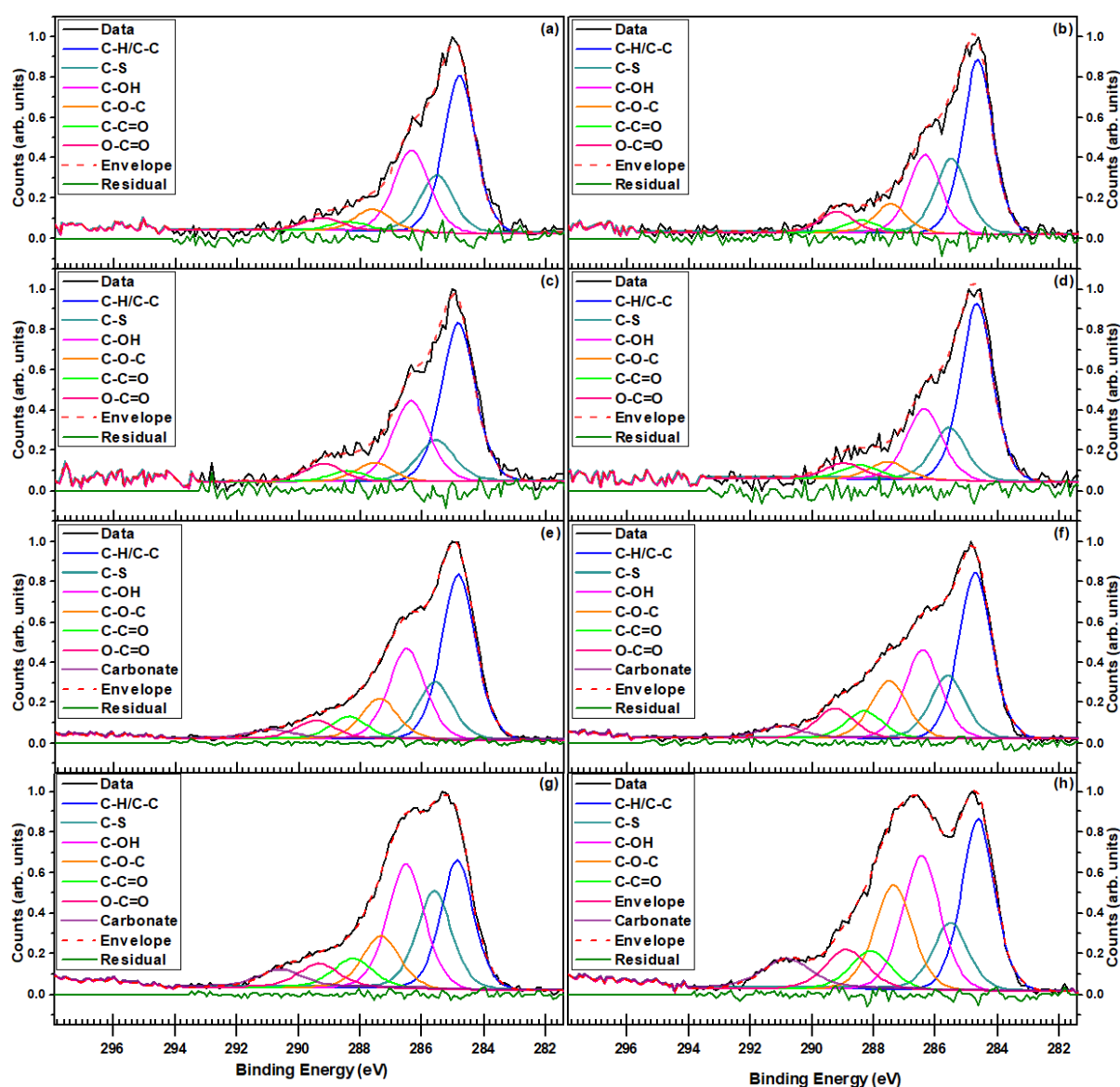


Figure 6.35: Component fits of C 1s spectra of *A. f* exposures to pyrite for 24 h cold stage (a) 24 h ambient (b) 48 h cold stage (c) 48 h ambient (d) 72 h cold stage (e) 72h ambient (f) 168 h cold stage (g) 168 h ambient (h), cold stage scans were conducted at $-165\text{ }^{\circ}\text{C}$ and ambient scans between 18.4 and $21.7\text{ }^{\circ}\text{C}$

6.3.4.2.4 Oxygen 1s

Analysis of the O 1s high-resolution spectra can confirm the presence or absence of oxidation products including hydration. The oxygen component of the samples were fit and assigned according to energies observed in previous studies [35,44,48,51,53-59]. The O 1s spectra was fit using a combination of eight components (metal oxides, sulfate/hydroxide, C–O–C, nitrate, chemi and physisorbed H₂O, O 1s, and NO₂), with assignments shown in Table 6.5.

These results indicate the presence of metal oxides at all exposure times for both the HH media control and *A. f* adjusted to pyrite samples. The contribution of this component is also

seen to decrease as a function of time. The sulfate/hydroxide component is also observed for all samples, with an overall decrease of the contribution observed for the HH media control samples and an increase observed for the *A. f* adjusted to pyrite samples. The difference in the sulfate/hydroxide component indicates greater oxidation for the samples exposed to *A. f* adjusted to pyrite. Interestingly, the opposite trend is observed for the C–O–C component, where the contribution increases with exposure time in the HH media control and decreases in the samples exposed to *A. f*. This decrease in the C–O–C is expected to be an indication of an increase in complex carbon structures, which is supported by the carbon analysis above.

The nitrate component was only assigned to the *A. f* exposed samples, which is expected to arise from either the cells present on the surface or the EPS supernatant. The chemisorbed and physisorbed components were fit to all samples. The chemisorbed component was seen to increase with a function of time for both HH media control and *A. f* exposed samples. While the physisorbed component decreases as a function of exposure time for the HH media control and increases for the *A. f* exposed samples. This suggests extra hydration of the *A. f* exposed samples, which can be contributed to by the presence of cells and/or biofilm. The O 1s unassigned component is present at the same binding energy for the unreacted sample, HH media controls at 24 h and 48 h, and *A. f* exposed samples at 72 h and 168 h. While adsorbed water has been previously observed at this energy [54,57,58], it is likely that this component is molecular O₂ species, such as O₂²⁻ and/or O₂⁻, or carbonate (CO₃) attached to the surface [53,55,56]. The NO₂ component was only detected in the HH media 48 h control sample and is suspected to be an artifact from residual media on the sample.

Table 6.5: High resolution O 1s component fit information for cold stage scans. FWHM held constant at 1.55

	Metal Oxide 530.5 ± 0.2	Sulfate/ hydroxide 531.7 ± 0.2	C–O–C 532.6 ± 0.2	Nitrate 533.2 ± 0.1	Chemisorbed H ₂ O 533.7 ± 0.1	Physisorbed H ₂ O 535.1 ± 0.1	O 1s 536.6 ± 0.1	NO ₂ 537.6
Unreacted	9.77	36.50	8.33	-	17.62	14.22	13.55	-
HH 24 h	7.67	35.16	30.41	-	14.63	7.96	4.18	-
HH 48 h	3.83	19.92	27.16	-	13.87	13.51	14.33	7.37
HH 72 h	2.86	23.61	28.22	-	39.70	5.59	-	-
HH 168 h	2.14	8.40	30.34	-	49.18	9.94	-	-
<i>A. f</i> 24 h	3.36	20.30	38.46	12.57	17.82	7.49	-	-
<i>A. f</i> 48 h	3.05	27.10	38.71	9.00	16.94	5.20	-	-
<i>A. f</i> 72 h	1.55	17.56	29.84	12.03	23.43	12.63	2.96	-
<i>A. f</i> 168 h	1.69	23.08	23.32	14.79	21.39	11.76	3.95	-

6.4 Conclusions

The growth of *Acidithiobacillus ferrooxidans* exhibit different growth curves depending on the growth condition. The *A. f* grown on iron sulfate solution has a rapid growth curve achieving a maximum cell concentration of 5.6×10^7 cell/mL. Both pyrite and chalcopyrite produce suitable growth conditions for *A. f*, with the maximum cell concentration reaching 2.2×10^8 cell/mL and 1.5×10^8 cell/mL respectively, with the pyrite culture growth cycle being shorter than that of chalcopyrite. The culture adjusted to grow on arsenopyrite has the longest growth cycle, with the maximum cell concentration reaching $\times 10^7$. The attachment studies indicate there is no preferential attachment occurring, with single cells observed on both pyrite and chalcopyrite at 2 h exposure. Cell clusters are observed on pyrite by 12 h, suggesting *A. f* swaps from a non-contact mechanism to a contact mechanism. Single cells are only observed on the chalcopyrite, suggesting that *A. f* adjusted to chalcopyrite uses a non-contact mechanism.

The differential flotation tests indicate that the growth conditions of the *A. f* influences the recovery and separation of chalcopyrite from pyrite, with the presence of cells typically reducing the recovery. The best depression of pyrite, as exhibited in the differential flotation tests, occurs in the presence of *A. f* adjusted to pyrite and the resulting EPS supernatant of *A. f* adjusted to pyrite. The best recovery of chalcopyrite is achieved using *A. f* adjusted to chalcopyrite and the EPS supernatant from *A. f* adjusted to chalcopyrite. The *A. f* adjusted to arsenopyrite, and the resulting EPS supernatant does not exhibit much selectivity for separation, as the conditions are favourable to pyrite recovery.

XPS analysis indicates an increase in complex carbon structures (C–O–C, C–C=O, O–C=C, and CO₃) with increasing exposure to *A. ferrooxidans*, with analysis of sulfur, oxygen and iron analysis showing greater oxidation. The oxygen analysis indicates greater hydration of the *A. f* samples, this in combination with the increase in complex carbon structure indicates the presence of cells and biofilm on the pyrite surface. The sulfur analysis indicates the presence of elemental sulfur, which is only detected in the samples exposed to *A. f*. This presence of elemental sulfur indicates that *A. f* influences polysulfide mechanism of oxidation, with the polysulfide concentration increasing with exposure time. The increase in complex carbon structures and oxidation products of the *A. f* exposed samples correlates with the suppression

of pyrite in the micro-flotation tests. Therefore, indicating that *A. f* bacterial cells and their EPS components act as a natural suppressor of pyrite.

6.5 References

1. Diao, M.; Taran, E.; Mahler, S.; Nguyen, T.A.; Nguyen, A.V. Quantifying adhesion of acidophilic bioleaching bacteria to silica and pyrite by atomic force microscopy with a bacterial probe. *Colloids Surf B Biointerfaces* **2014**, *115*, 229-236, doi:10.1016/j.colsurfb.2013.11.047.
2. Cameron, R.A.; Lastra, R.; Mortazavi, S.; Bedard, P.L.; Morin, L.; Gould, W.D.; Kennedy, K.J. Bioleaching of a low-grade ultramafic nickel sulphide ore in stirred-tank reactors at elevated pH. *Hydrometallurgy* **2009**, *97*, 213-220, doi:10.1016/j.hydromet.2009.03.002.
3. Jerez, C.A. Bioleaching and Biomining for the Industrial Recovery of Metals. In *Reference Module in Life Sciences*, Elsevier: 2017; 10.1016/B978-0-12-809633-8.09185-8.
4. Patra, P.; Natarajan, K. Microbially enhanced removal of pyrite and chalcopyrite from oxide gangue minerals with reference to desulfurization of tailings. *Minerals and Metallurgical Processing* **2004**, *21*, 169-178.
5. Chandraprabha, M.N.; Natarajan, K.A.; Modak, J.M. Selective separation of pyrite and chalcopyrite by biomodulation. *Colloids Surf B Biointerfaces* **2004**, *37*, 93-100, doi:10.1016/j.colsurfb.2004.06.011.
6. Chandraprabha, M.N.; Natarajan, K.A.; Somasundaran, P. Selective separation of arsenopyrite from pyrite by biomodulation in the presence of *Acidithiobacillus ferrooxidans*. *J Colloid Interf Sci* **2004**, *276*, 323-332, doi:10.1016/j.jcis.2004.03.047.
7. Hosseini, T.R.; Kolahdoozan, M.; Tabatabaei, Y.S.M.; Oliazadeh, M.; Noaparast, M.; Eslami, A.; Manafi, Z.; Alfantazi, A. Bioflotation of Sarcheshmeh copper ore using *Thiobacillus ferrooxidans* bacteria. *Minerals Engineering* **2005**, *18*, 371-374, doi:10.1016/j.mineng.2004.06.005.
8. Ohmura, N.; Kitamura, K.; Saiki, H. Mechanism of Microbial Flotation Using *Thiobacillus-Ferrooxidans* for Pyrite Suppression. *Biotechnol Bioeng* **1993**, *41*, 671-676, doi:10.1002/bit.260410611.
9. He, H.; Xia, J.L.; Hong, F.F.; Tao, X.X.; Leng, Y.W.; Zhao, Y.D. Analysis of sulfur speciation on chalcopyrite surface bioleached with *Acidithiobacillus ferrooxidans*. *Minerals Engineering* **2012**, *27*, 60-64, doi:10.1016/j.mineng.2011.12.012.
10. Harneit, K.; Göksel, A.; Kock, D.; Klock, J.-H.; Gehrke, T.; Sand, W. Adhesion to metal sulfide surfaces by cells of *Acidithiobacillus ferrooxidans*, *Acidithiobacillus thiooxidans* and *Leptospirillum ferrooxidans*. *Hydrometallurgy* **2006**, *83*, 245-254.
11. Gehrke, T.; Telegdi, J.; Thierry, D.; Sand, W. Importance of Extracellular Polymeric Substances from *Thiobacillus ferrooxidans* for Bioleaching. *Appl Environ Microbiol* **1998**, *64*, 2743-2747.
12. Govender, Y.; Gericke, M. Extracellular polymeric substances (EPS) from bioleaching systems and its application in bioflotation. *Minerals Engineering* **2011**, *24*, 1122-1127, doi:10.1016/j.mineng.2011.02.016.
13. Image Processing and Analysis in Java. Analyze Menu. Available online: <https://imagej.nih.gov/ij/docs/menus/analyze.html> (accessed on 19 March).
14. Monod, J. The Growth of Bacterial Cultures. *Annu Rev Microbiol* **1949**, *3*, 371-394, doi:10.1146/annurev.mi.03.100149.002103.

15. Orell, A.; Navarro, C.A.; Arancibia, R.; Mobarec, J.C.; Jerez, C.A. Life in blue: copper resistance mechanisms of bacteria and archaea used in industrial biomining of minerals. *Biotechnol Adv* **2010**, *28*, 839-848, doi:10.1016/j.biotechadv.2010.07.003.
16. Pearce, C.I.; Patrick, R.A.D.; Vaughan, D.J.; Henderson, C.M.B.; van der Laan, G. Copper oxidation state in chalcopyrite: Mixed Cu d9 and d10 characteristics. *Geochimica et Cosmochimica Acta* **2006**, *70*, 4635-4642, doi:10.1016/j.gca.2006.05.017.
17. Navarro, C.A.; von Bernath, D.; Jerez, C.A. Heavy Metal Resistance Strategies of Acidophilic Bacteria and Their Acquisition: Importance for Biomining and Bioremediation. *Biological Research* **2013**, *46*, 363-371.
18. Hinshelwood, C.N. *The chemical kinetics of the bacterial cell*; 1946.
19. Blowes, D.; Ptacek, C.; Jambor, J.; Weisener, C. The geochemistry of acid mine drainage. *Treatise on geochemistry* **2003**, *9*, 149-204.
20. Corkhill, C.L.; Vaughan, D.J. Arsenopyrite oxidation—A review. *Applied Geochemistry* **2009**, *24*, 2342-2361.
21. Corkhill, C.L.; Wincott, P.L.; Lloyd, J.R.; Vaughan, D.J. The oxidative dissolution of arsenopyrite (FeAsS) and enargite (Cu₃As₄S₄) by *Leptospirillum ferrooxidans*. *Geochimica Et Cosmochimica Acta* **2008**, *72*, 5616-5633, doi:10.1016/j.gca.2008.09.008.
22. Buckley, A.N.; Walker, G.W. The surface composition of arsenopyrite exposed to oxidizing environments. *Applied Surface Science* **1988**, *35*, 227-240, doi:[https://doi.org/10.1016/0169-4332\(88\)90052-9](https://doi.org/10.1016/0169-4332(88)90052-9).
23. Descostes, M.; Vitorge, P.; Beaucaire, C. Pyrite dissolution in acidic media. *Geochimica et Cosmochimica Acta* **2004**, *68*, 4559-4569, doi:10.1016/j.gca.2004.04.012.
24. Chan, C.S.; Fakra, S.C.; Edwards, D.C.; Emerson, D.; Banfield, J.F. Iron oxyhydroxide mineralization on microbial extracellular polysaccharides. *Geochimica Et Cosmochimica Acta* **2009**, *73*, 3807-3818, doi:10.1016/j.gca.2009.02.036.
25. Potter-McIntyre, S.; McCollom, T. Jarosite in Ancient Terrestrial Rocks: Implications for Understanding Mars Diagenesis and Habitability. In Proceedings of Lunar and Planetary Science Conference; p. 1237.
26. Abraitis, P.K.; Patrick, R.A.D.; Vaughan, D.J. Variations in the compositional, textural and electrical properties of natural pyrite: a review. *International Journal of Mineral Processing* **2004**, *74*, 41-59, doi:10.1016/j.minpro.2003.09.002.
27. Mitsunobu, S.; Zhu, M.; Takeichi, Y.; Ohigashi, T.; Suga, H.; Jinno, M.; Makita, H.; Sakata, M.; Ono, K.; Mase, K., et al. Direct Detection of Fe(II) in Extracellular Polymeric Substances (EPS) at the Mineral-Microbe Interface in Bacterial Pyrite Leaching. *Microbes Environ* **2016**, *31*, 63-69, doi:10.1264/jsme2.ME15137.
28. Hsu, L.C.; Fang, J.; Borca-Tasciuc, D.A.; Worobo, R.W.; Moraru, C.I. Effect of micro- and nanoscale topography on the adhesion of bacterial cells to solid surfaces. *Appl Environ Microbiol* **2013**, *79*, 2703-2712, doi:10.1128/AEM.03436-12.
29. Parikh, S.J.; Chorover, J. ATR-FTIR Spectroscopy Reveals Bond Formation During Bacterial Adhesion to Iron Oxide. *Langmuir* **2006**, *22*, 8492-8500, doi:10.1021/la061359p.
30. Wuertz, S.; Spaeth, R.; Hinderberger, A.; Griebel, T.; Flemming, H.C.; Wilderer, P.A. A new method for extraction of extracellular polymeric substances from biofilms and activated sludge suitable for direct quantification of sorbed metals. *Water Sci Technol* **2001**, *43*, 25-31.

31. Schmitt, J.; Flemming, H.C. FTIR-spectroscopy in microbial and material analysis. *International Biodeterioration & Biodegradation* **1998**, *41*, 1-11, doi:10.1016/S0964-8305(98)80002-4.
32. Schmitt, J.; Nivens, D.; White, D.C.; Flemming, H.C. Changes of biofilm properties in response to sorbed substances - An FTIR-ATR study. *Water Science and Technology* **1995**, *32*, 149-155, doi:10.1016/0273-1223(96)00019-4.
33. Parikh, A.; Madamwar, D. Partial characterization of extracellular polysaccharides from cyanobacteria. *Bioresource Technol* **2006**, *97*, 1822-1827, doi:10.1016/j.biortech.2005.09.008.
34. Li, Q.; Wang, Q.F.; Zhu, J.Y.; Zhou, S.; Gan, M.; Jiang, H.; Sand, W. Effect of Extracellular Polymeric Substances on Surface Properties and Attachment Behavior of *Acidithiobacillus ferrooxidans*. *Minerals* **2016**, *6*, 100, doi:ARTN 100 10.3390/min6040100.
35. Akhter, S.; Allan, K.; Buchanan, D.; Cook, J.A.; Champion, A.; White, J.M. XPS and IR study of X-ray induced degradation of PVA polymer film. *Applied Surface Science* **1988**, *35*, 241-258, doi:[https://doi.org/10.1016/0169-4332\(88\)90053-0](https://doi.org/10.1016/0169-4332(88)90053-0).
36. Sharma, P.K.; Das, A.; Rao, K.H.; Forssberg, K.S.E. Surface characterization of *Acidithiobacillus ferrooxidans* cells grown under different conditions. *Hydrometallurgy* **2003**, *71*, 285-292, doi:10.1016/S0304-386x(03)00167-1.
37. Khmeleva, T.N.; Beattie, D.A.; Georgiev, T.V.; Skinner, W.M. Surface study of the effect of sulphite ions on copper-activated pyrite pre-treated with xanthate. *Minerals Engineering* **2003**, *16*, 601-608, doi:10.1016/S0892-6875(03)00133-X.
38. Wills, B.A. *Mineral processing technology: an introduction to the practical aspects of ore treatment and mineral recovery*, 4th ed.; Pergamon Press: New South Wales, Australia, 1988.
39. Vilinska, A.; Rao, K.H. Leptosrillum *ferrooxidans*-sulfide mineral interactions with reference to bioflotation nad bioflocculation. *Transactions of Nonferrous Metals Society of China* **2008**, *18*, 1403-1409.
40. Chandraprabha, M.N.; Natarajan, K.A. Surface chemical and flotation behaviour of chalcopyrite and pyrite in the presence of *Acidithiobacillus thiooxidans*. *Hydrometallurgy* **2006**, *83*, 146-152, doi:10.1016/j.hydromet.2006.03.021.
41. Casa Software Ltd. *CasaXPS*, 2.3.19PR1.0; 2000. Available from
42. Moulder, J.F.; Stickle, W.F.; Sobol, P.E.; Bomben, K.D. *Handbook of X-ray photoelectron spectroscopy*; Physical Electronics Inc.: Minnesota, USA, 1992.
43. Crist, B.V. A review of XPS data-banks. *XPS Reports* **2007**, *1*.
44. Ahimou, F.; Boonaert, C.J.; Adriaensen, Y.; Jacques, P.; Thonart, P.; Paquot, M.; Rouxhet, P.G. XPS analysis of chemical functions at the surface of *Bacillus subtilis*. *J Colloid Interface Sci* **2007**, *309*, 49-55, doi:10.1016/j.jcis.2007.01.055.
45. He, Z.G.; Yang, Y.P.; Zhou, S.; Hu, Y.H.; Zhong, H. Effect of pyrite, elemental sulfur and ferrous ions on EPS production by metal sulfide bioleaching microbes. *Transactions of Nonferrous Metals Society of China* **2014**, *24*, 1171-1178, doi:10.1016/S1003-6326(14)63176-9.
46. Nesbitt, H.W.; Muir, I.J. X-Ray Photoelectron Spectroscopic Study of a Pristine Pyrite Surface Reacted with Water-Vapor and Air. *Geochimica Et Cosmochimica Acta* **1994**, *58*, 4667-4679, doi:10.1016/0016-7037(94)90199-6.
47. Nesbitt, H.W.; Bancroft, G.M.; Pratt, A.R.; Scaini, M.J. Sulfur and iron surface states on fractured pyrite surfaces. *Am Mineral* **1998**, *83*, 1067-1076.

48. Acres, R.G.; Harmer, S.L.; Beattie, D.A. Synchrotron XPS, NEXAFS, and ToF-SIMS studies of solution exposed chalcopyrite and heterogeneous chalcopyrite with pyrite. *Minerals Engineering* **2010**, *23*, 928-936, doi:10.1016/j.mineng.2010.03.007.
49. Baltzer, P.; Karlsson, L.; Lundqvist, M.; Wannberg, B. Resolution and signal-to-background enhancement in gas-phase electron spectroscopy. *Review of Scientific Instruments* **1993**, *64*, 2179-2189, doi:10.1063/1.1143957.
50. Varga, D.; Tórkési, K.; Berényi, Z.; Tóth, J.; Kövér, L.; Gergely, G.; Sulyok, A. Energy shift and broadening of the spectra of electrons backscattered elastically from solid surfaces. *Surface and Interface Analysis* **2001**, *31*, 1019-1026, doi:10.1002/sia.1121.
51. Singh, B.; Fang, Y.Y.; Cowie, B.C.C.; Thomsen, L. NEXAFS and XPS characterisation of carbon functional groups of fresh and aged biochars. *Org Geochem* **2014**, *77*, 1-10, doi:10.1016/j.orggeochem.2014.09.006.
52. Le Normand, F.; Hommet, J.; Szörényi, T.; Fuchs, C.; Fogarassy, E. XPS study of pulsed laser deposited CN x films. *Phys Rev B* **2001**, *64*, 235416.
53. López, G.P.; Castner, D.G.; Ratner, B.D. XPS O 1s binding energies for polymers containing hydroxyl, ether, ketone and ester groups. *Surface and interface analysis* **1991**, *17*, 267-272.
54. Jones, C.F.; LeCount, S.; Smart, R.S.C.; White, T.J. Compositional and structural alteration of pyrrhotite surfaces in solution: XPS and XRD studies. *Applied surface science* **1992**, *55*, 65-85.
55. Descostes, M.; Mercier, F.; Thromat, N.; Beaucaire, C.; Gautier-Soyer, M. Use of XPS in the determination of chemical environment and oxidation state of iron and sulfur samples: constitution of a data basis in binding energies for Fe and S reference compounds and applications to the evidence of surface species of an oxidized pyrite in a carbonate medium. *Applied Surface Science* **2000**, *165*, 288-302, doi:10.1016/S0169-4332(00)00443-8.
56. Campbell, C.T. An XPS study of molecularly chemisorbed oxygen on Ag (111). *Surface Science Letters* **1986**, *173*, L641-L646.
57. Comans, R.N.; Eighmy, T.T.; Shaw, E.L. Reference Spectra for Environmentally Important Secondary Minerals: Ettringite (Ca₆Al₂(SO₄)₃(OH)₁₂·26H₂O) by XPS. *Surface Science Spectra* **1996**, *4*, 150-156.
58. Kalegowda, Y.; Chan, Y.L.; Wei, D.H.; Harmer, S.L. X-PEEM, XPS and ToF-SIMS characterisation of xanthate induced chalcopyrite flotation: Effect of pulp potential. *Surf Sci* **2015**, *635*, 70-77, doi:10.1016/j.susc.2014.12.012.
59. Suzuki, S.; Yanagihara, K.; Hirokawa, K. XPS study of oxides formed on the surface of high-purity iron exposed to air. *Surface and Interface Analysis: An International Journal devoted to the development and application of techniques for the analysis of surfaces, interfaces and thin films* **2000**, *30*, 372-376.

7 CONCLUSIONS AND FUTURE DIRECTIONS

7.1 Conclusions

This thesis has used a combination of microscopic and spectroscopic techniques to investigate the interactions between the microbes, *Leptospirillum ferrooxidans* and *Acidithiobacillus ferrooxidans*, and minerals to better understand their implications on minerals processing. This has required a multilayer approach to understand the attachment mechanism of cells and/or organic matter, surface chemistry changes and the subsequent flotation behaviour.

Adaption of *Leptospirillum ferrooxidans* and *Acidithiobacillus ferrooxidans* to different growth conditions, which stressed the cells in different ways, was conducted to investigate the impact growth conditions have on the cell function. The growth conditions covered a soluble iron source (iron sulfate heptahydrate), a solid source with accessible iron (pyrite), and a solid source where metabolic processes are required to obtain a usable iron source (chalcopyrite and arsenopyrite). *A. ferrooxidans* adapted more readily to all growth conditions than *L. ferrooxidans*. However, cell attachment mechanisms of both *L. ferrooxidans* and *A. ferrooxidans* was found to be specific to the growth condition and not the strain. Attachment to pyrite was identified as an indirect contact mechanism, while attachment to chalcopyrite was identified as an indirect non-contact mechanism. The presence of bacteria increased the leaching of both pyrite and chalcopyrite.

Both *L. ferrooxidans* and *A. ferrooxidans* were found to produce EPS and early formations of biofilm were identified at different time in the growth of the culture. *L. ferrooxidans* adapted to pyrite was first observed with the early stages of a biofilm matrix at 24 h, and 36 h for chalcopyrite cultures. While *A. ferrooxidans* adapted to pyrite were observed to have biofilm formation at 36 h for pyrite and only 12 h for chalcopyrite. This is where the difference in strain and growth conditions became discernible.

The micro-flotation tests conducted clearly determine a link between strain, growth condition and flotation recovery; showing that the optimal bio-flotation conditions heavily rely on the bacterial strain and growth condition. The presence of the cell, either *L. ferrooxidans* or *A. ferrooxidans*, directly impacts the recovery of the micro-flotation tests, by increasing the suppression of minerals even when accompanied by a collector. Interestingly, removing the

cells and only using their metabolic products provides selective suppression of pyrite. However, the degree of suppression is determined by the growth condition and strain of the bacteria. This supports the claim that EPS composition changes amongst strain and growth conditions. The EPS of *L. ferrooxidans* shows selectivity of separation with *L. ferrooxidans* adapted to chalcopyrite and *L. ferrooxidans* adapted to arsenopyrite exhibiting suppression of pyrite and adequate recovery of chalcopyrite. However, the EPS from *A. ferrooxidans* is observed to not have selectiveness, either suppressing both minerals (*A. ferrooxidans* adapted to pyrite) or increasing recovery of both minerals (*A. ferrooxidans*). The EPS from the cultures grown on different minerals correlate with a change in flotation behaviour, with preliminary results indicating this is due to the compositional changes in the produced EPS.

Photoemission electron microscopy (PEEM) and X-ray photoelectron spectroscopy (XPS) analysis allowed for surface sensitive analysis to be conducted. By investigating the surface chemistry changes of pyrite and chalcopyrite, the flotation behaviour observed can be further understood. XPS and PEEM confirmed the presence of complex organic molecule on the surface of pyrite and chalcopyrite, which correlates with the different flotation behaviours observed. PEEM identified the presence of Cu (II) in fresh EPS samples, and greater concentrations of both FeOOH and Fe₂O₃ states in the samples which correlate with better flotation recovery and preferential attachment to pyrite and haematite. XPS analysis of pyrite exposed to *A. ferrooxidans* indicates greater oxidation in comparison to the control samples. This greater oxidation is expected to occur through the polysulfide mechanism as elemental sulfur was also detected. XPS analysis also indicated an increase in complex organic carbon structures when exposed to bacteria. The increase in complex organic carbon structures correlates with the increased suppression of pyrite, therefore indicating the bacterial cells and their EPS are crucial elements when considering bio-reagents for mineral separation. These results from *L. ferrooxidans* and *A. ferrooxidans* indicate that the influence on mineral separation through bio-flotation differs depending on the strain and the growth conditions. Subsequently, this also indicates that the composition of the EPS is also a key factor in the successful separation of chalcopyrite from pyrite through bio-flotations.

7.2 Future Directions

The exact connection between EPS composition and separation efficiency is currently unknown. Understanding this requires further investigation to determine the exact composition of components within the EPS and the concentrations in which they exist. The work presented in this thesis indicates the use of microbes in industrial minerals processing is plausible. The works above present evidence of the importance EPS plays in the surface modification of pyrite and chalcopyrite in bio-flotation. The composition of EPS has previously been determined to change depending on the growth conditions and microbial strain, but the fundamental components identified are neutral sugars, free fatty-acids, eDNA, proteins and uronic acid [1-5]. The studies presented above indicate that the compositional changes arising from different growth conditions influences the flotation behaviour of pyrite and chalcopyrite. To optimise the use of EPS as a bio-reagent, a thorough understanding of the composition and the interactions occurring. While Chapter 5 and Chapter 6 use spectroscopic methods to investigate surface chemistry changes, visualising the distribution of the different EPS components will add depth to the understanding of this complex equation. This should be tackled from two different directions: extraction and identification of components; and visual distribution of attachment.

The identification and quantification of EPS components was attempted in these studies. Presumptive tests were conducted on the EPS in-situ to determine the presence of carbohydrate, protein and DNA components. This analysis consisted of Bradford assay, phenol-sulfuric acid assay and nucleic acid analysis. Changes in concentration of carbohydrates, protein and DNA were observed between strains and growth conditions. However, it was noted that the HH media did produce interference with analysis and therefore these results were considered as only presumptive and not qualitative. Accurate identification and quantification of EPS components may be obtained when extracted from the matrix/supernatant. Some studies have previously extracted EPS components successfully from various microbes and growth conditions, with methods outlined in Section 3.3.6 [6-8]. These methods of extraction were investigated in these studies and were unsuccessful at varying degrees for the cultures investigated.

The extraction method for exopolysaccharides, described in Appendix II: Procedures, was successful for the chalcopyrite and arsenopyrite cultures of *L. ferrooxidans* and *A. ferrooxidans*. The resulting precipitates, expected to be exopolysaccharides, were analysed via FTIR-ATR and NMR. The FTIR-ATR spectrums for *L. ferrooxidans* and *A. ferrooxidans* adjusted to chalcopyrite and arsenopyrite are shown in Figure 7.1. These spectra show changes in the OH region ($\sim 3250\text{ cm}^{-1} - 3750\text{ cm}^{-1}$), fatty acid region ($\sim 1700\text{ cm}^{-1} - 1900\text{ cm}^{-1}$), amide region ($\sim 1500\text{ cm}^{-1} - 1700\text{ cm}^{-1}$), protein hydrocarbon region ($\sim 1300\text{ cm}^{-1} - 1500\text{ cm}^{-1}$), and carbohydrate region ($\sim 600\text{ cm}^{-1} - 1300\text{ cm}^{-1}$), indicating growth condition and strain do impact the composition of EPS. Using this information in correlation with the flotation test data presented above, a clear link between composition and separation efficiency can be made and further investigation in the carbohydrate composition is required.

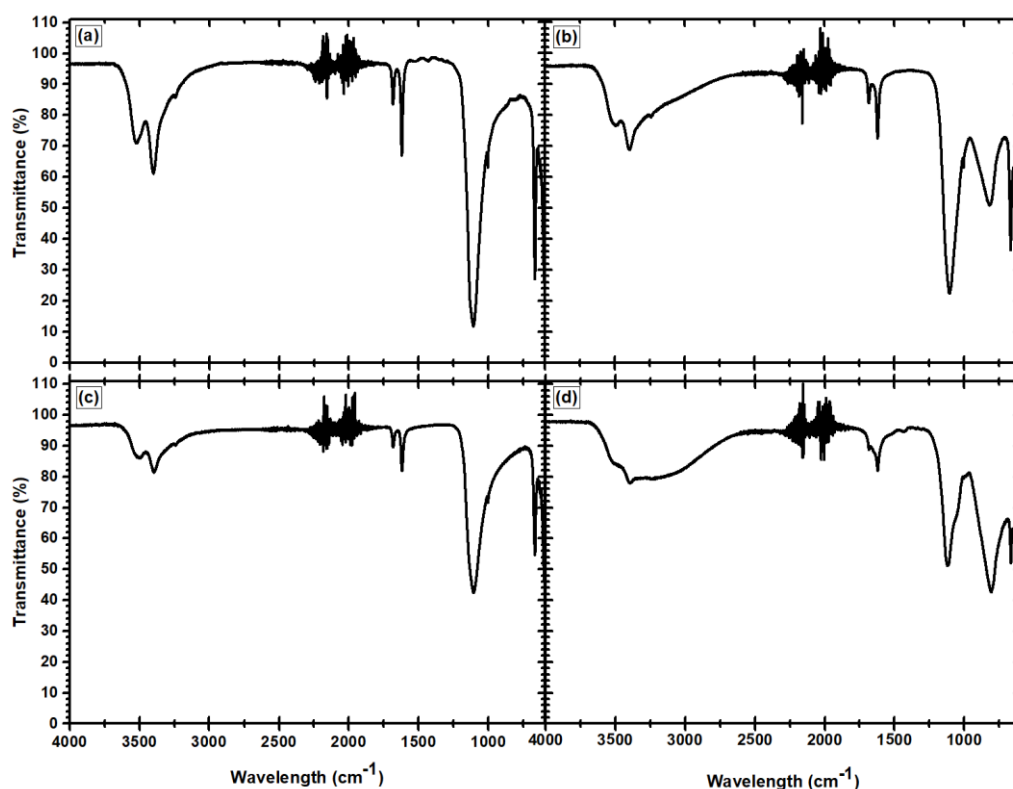


Figure 7.1: FTIR-ATR analysis of EPS precipitate from extraction showing *L. ferrooxidans* adapted to chalcopyrite (a), adapted to arsenopyrite (b), and *A. ferrooxidans* adapted to chalcopyrite (c) adapted to arsenopyrite (d)

Nuclear Magnetic Resonance (NMR) spectroscopy was also investigated to acquire more in-depth information on the carbohydrate components; however, the precipitates were insoluble in deuterated water, chloroform, acetone and DMSO, creating difficulty for solution analysis and solid-state NMR resulted in low signal. To counteract this, acid hydrolysis of the

exopolysaccharide was attempted with the procedure outlined in Appendix II: Procedures. The results confirmed the precipitate contained hydrocarbon chains, O-H groups and aromatics, which was supported by the gas chromatography mass spectra. However, the results also indicated that the hydrolysis process was quite vigorous, resulting in the presence of small fractions and a need to refine the process further.

Interestingly, even though the presence of fatty acids, amides and proteins were indicated in the extracted precipitate, isolation of these components from the EPS supernatant was not successful. The poor extraction of proteins and lipids may be attributed to the concentration in which these components exist. As extraction of components other than exopolysaccharides was not successful, other methods of analysis were trialled to investigate the carbohydrate components further. This includes flow cytometry for eDNA analysis within the EPS structure. The eDNA was investigated as DNA is a structural scaffold in biofilm formation which is hypothesised to facilitate carbohydrate attachment to mineral surfaces [5].

Flow cytometry can characterise scatter characteristics of cells and complex biological compounds in solution which provide the size and complexity of the cell or compound [9]. For this to be achieved, the cells or compounds need to be tagged with fluorophores, before being passed through a laser and producing a 'scatter' pattern which is measured by multiple detectors. This scatter pattern is produced when the laser excites the fluorophores, and a characteristic wavelength is emitted. The eDNA within the EPS supernatant was stained with 4',6-Diamidino-2-Phenylindole, Dihydrochloride (DAPI), which binds to the double helix structure, therefore only indicating the presence of double stranded DNA. While refinement of the flow cytometry methodology is required, the results indicate a change in particle size and complexity between the EPS originating from the pyrite cultures and the chalcopyrite cultures. This trend was also observed to occur with increasing exposure time for both growth conditions.

The physical distribution and attachment of eDNA was investigated through epifluorescence microscopy on mineral coupons. This was conducted on pyrite coupons, as the studies above suggest greater attachment of the EPS on pyrite over chalcopyrite. Figure 7.2 illustrates the fluorescence observed at 24 h and 48 h. These results indicate that there is some eDNA attachment on the pyrite surface, increasing as a function of time. However, the

concentration could not be quantified. The negative control also indicates that this process is not yet optimised as autofluorescence was observed. This may be a result of the mineral coupon preparation, as it they were polished to a mirror finish.

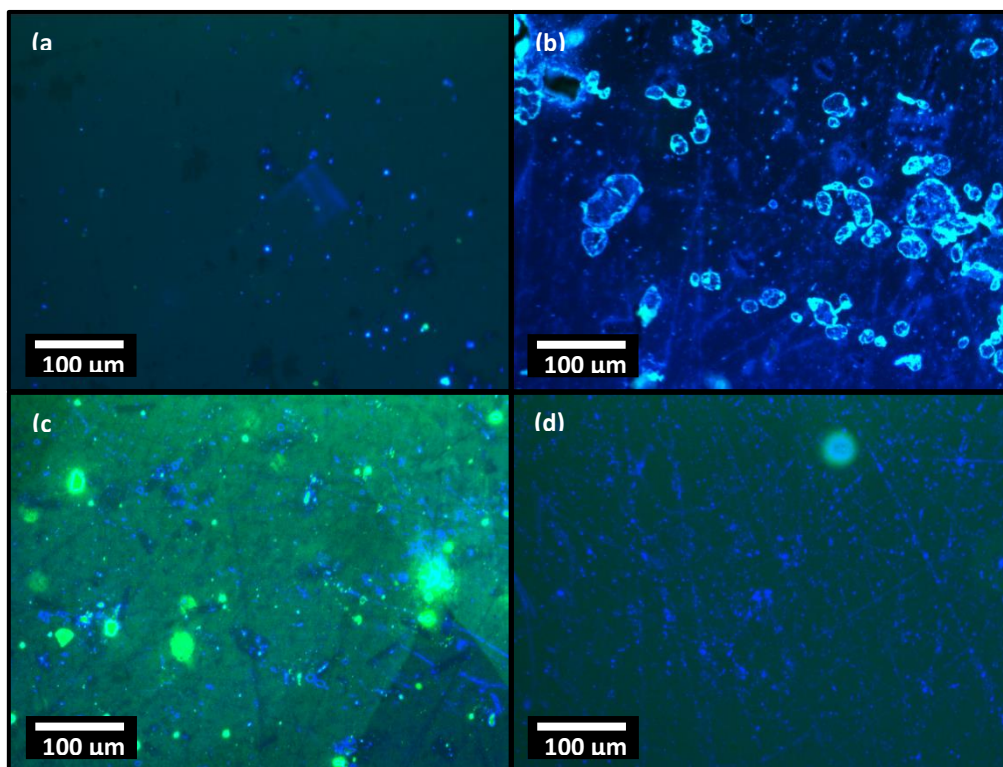


Figure 7.2: Epifluorescence of eDNA in the DAPI and GFP region showing auto-fluorescence on the pyrite negative control (a), positive control of 0.1μg/mL DNA in HH Media for 24 h on pyrite (b), pyrite exposed to EPS from *L. ferrooxidans* adapted to chalcopyrite for 24 h (c), and 48 h (d)

Refining these methods and expanding these investigations to explore all components of EPS will further the understanding of how EPS and biofilms interact and alter the surface chemistry of minerals. These interactions need to be thoroughly understood to optimise the bio-flotation process.

7.3 References

1. Harneit, K.; Göksel, A.; Kock, D.; Klock, J.-H.; Gehrke, T.; Sand, W. Adhesion to metal sulfide surfaces by cells of *Acidithiobacillus ferrooxidans*, *Acidithiobacillus thiooxidans* and *Leptospirillum ferrooxidans*. *Hydrometallurgy* **2006**, *83*, 245-254.
2. Bleeze, B.; Zhao, J.; Harmer, S.L. Selective Attachment of *Leptospirillum ferrooxidans* for Separation of Chalcopyrite and Pyrite through Bio-Flotation. *Minerals* **2018**, *8*, 86.
3. Comte, S.; Guibaud, G.; Baudu, M. Effect of extraction method on EPS from activated sludge: an HPSEC investigation. *J Hazard Mater* **2007**, *140*, 129-137, doi:10.1016/j.jhazmat.2006.06.058.
4. Desmond, P.; Best, J.P.; Morgenroth, E.; Derlon, N. Linking composition of extracellular polymeric substances (EPS) to the physical structure and hydraulic resistance of membrane biofilms. *Water Res* **2018**, *132*, 211-221, doi:10.1016/j.watres.2017.12.058.
5. Flemming, H.-C.; Neu, T.R.; Wozniak, D.J. The EPS matrix: the “house of biofilm cells”. *Journal of bacteriology* **2007**, *189*, 7945-7947.
6. Weaver, D.T.; Hicks, R.E. Biodegradation of *Azotobacter vinelii* exopolymer by Lake Superior microbes. *Limnol. Oceanogr* **1995**, *40*, 1035-1041.
7. Lima, L.F.; Habu, S.; Gern, J.C.; Nascimento, B.M.; Parada, J.L.; Nosedá, M.D.; Goncalves, A.G.; Nisha, V.R.; Pandey, A.; Soccol, V.T., et al. Production and characterization of the exopolysaccharides produced by *Agaricus brasiliensis* in submerged fermentation. *Appl Biochem Biotechnol* **2008**, *151*, 283-294, doi:10.1007/s12010-008-8187-2.
8. Jiao, Y.; Cody, G.D.; Harding, A.K.; Wilmes, P.; Schrenk, M.; Wheeler, K.E.; Banfield, J.F.; Thelen, M.P. Characterization of extracellular polymeric substances from acidophilic microbial biofilms. *Appl Environ Microb* **2010**, *76*, 2916-2922, doi:10.1128/AEM.02289-09.
9. Harnisch, F.; Koch, C.; Patil, S.A.; Hubschmann, T.; Müller, S.; Schroder, U. Revealing the electrochemically driven selection in natural community derived microbial biofilms using flow-cytometry. *Energ Environ Sci* **2011**, *4*, 1265-1267, doi:10.1039/c0ee00605j.

APPENDIX I: BIO-FLOTATION LITERATURE COMPARISON

Pecina, et al. [1], Patra and Natarajan [2] and Subramanian, et al. [3] used nitrogen to float the minerals while other studies did not disclose what gas was used in the system. Subramanian, et al. [3] also used CuSO_4 to activate the sphalerite to assist with the efficiency of the separation, while Govender and Gericke (2011) conducted flotation tests with different EPS concentrations (1.7×10^{-3} , 8.6×10^{-3} , 1.7×10^{-2} , 3.5×10^{-2} , 6.9×10^{-2} , 1.7×10^{-1} and 3.1×10^{-1} mg/g).

Table 0.1:

Author	Minerals	Sample Size (g)	Particle Size (μm)	Bacteria	Cell Conc. (cell/mL)	Collector Conc.	Exposure Time (min)	Flow Rate (mL min^{-1})	Flotation Time (min.)	pH
Pecina, et al. [1]	Chalcopyrite Sphalerite Pyrrhotite	2	-150 + 75-	<i>L. ferrooxidans</i>	1.45×10^7	10^{-5} M XEK	-	23	1, 2, 4, 6 and 8	9
Vilinska and Rao [4]	Chalcopyrite Pyrite	1	-106 + 38	<i>L. ferrooxidans</i>	Varying-	10^{-5} M PIPX	Bacterial: 30 Collector: 5	200	1	Varying
Chandraprabha, et al. [5]	Chalcopyrite Pyrite	1	-106 + 75	<i>A. ferrooxidans</i>	4×10^8	10^{-4} M PIPX	Bacterial: 10 Collector: 5	40	3	Varying
Govender and Gericke [6]	Chalcopyrite Pyrite	1	75	<i>A. ferrooxidans</i>	1×10^6 ; 1×10^8	10^{-6} - 10^{-4} SIBX	-	200	2	4
Chandraprabha, et al. [7]	Pyrite Arsenopyrite	1	-106 + 75	<i>A. ferrooxidans</i>	4×10^8	10^{-4} M PIPX	5	40	3	Varying
Chandraprabha and Natarajan [8]	Chalcopyrite Pyrite	1	-106 + 75	<i>A. thiooxidans</i>	4×10^8	10^{-4} M PIPX	Collector: 10	40	3	Varying
Hosseini, et al. [9]	Chalcopyrite Pyrite	820	-	<i>T. ferrooxidans</i>	-	Xanthate (200g/t; 100g/t)	Bacterial: 15 Collector: 5	-	6	Neutral
Patra and Natarajan [10]	Chalcopyrite Pyrite Quartz Calcite	1	-105 + 74; -37	<i>B. polymyxa</i>	5×10^8	Hexamine	30	40	3	8
Subramanian, et al. [3]	Galena Sphalerite	1 (1:1)	-105 + 63	<i>B. polymyxa</i>	-	10^{-4} M PIPX	Metabolite: 15 Collector: 15	40	3	3.2-3.4; 9-9.5

Appendix I: Bio-flotation Literature Comparison

Deo and Natarajan [11]	Quartz Calcite Haematite Corundum	1	-106 + 75	<i>B. polymyxa</i>	1x10 ⁹	-	Bacterial: Alternating	40	5	7-9
Patra and Natarajan [2]	Chalcopyrite Pyrite Calcite	1	-105 + 63	<i>B. polymyxa</i>	5x10 ⁸	Hexamine	30	40	3	Neutral
Dubel, et al. [12]	Haematite	1	-20; - 53; + 20	<i>M. phlei</i>	-	-	10	-	3, 10	Varying
Ohmura, et al. [13]	Pyrite	4	-75 + 36	<i>T. ferrooxidans</i>	-	Methyl isobutyl carbinol	Varying	1000	2	2

*Bacterial abbreviations: L = Leptospirillum, B = Bacillus, T = Thiobacillus, A = Acidithiobacillus, M = Mycobacterium

** XEK – Potassium Ethyl Xanthate; PIPX – Potassium Isopropyl Xanthate; SIBX – Sodium Isobutyl Xanthate

References

1. Pecina, E.T.; Rodriguez, M.; Castillo, P.; Diaz, V.; Orrantia, E. Effect of Leptospirillum ferrooxidans on the flotation kinetics of sulphide ores. *Minerals Engineering* **2009**, *22*, 462-468, doi:10.1016/j.mineng.2008.12.008.
2. Patra, P.; Natarajan, K.A. Microbially induced flocculation and flotation for separation of chalcopyrite from quartz and calcite. *International Journal of Mineral Processing* **2004**, *74*, 143-155, doi:10.1016/j.minpro.2003.10.006.
3. Subramanian, S.; Santhiya, D.; Natarajan, K.A. Surface modification studies on sulphide minerals using bioreagents. *International Journal of Mineral Processing* **2003**, *72*, 175-188, doi:10.1016/S0301-7516(03)00097-8.
4. Vilinska, A.; Rao, K.H. Leptosirillum ferrooxidans-sulfide mineral interactions with reference to bioflotation nad bioflocculation. *Transactions of Nonferrous Metals Society of China* **2008**, *18*, 1403-1409.
5. Chandraprabha, M.N.; Natarajan, K.A.; Modak, J.M. Selective separation of pyrite and chalcopyrite by biomodulation. *Colloids Surf B Biointerfaces* **2004**, *37*, 93-100, doi:10.1016/j.colsurfb.2004.06.011.

6. Govender, Y.; Gericke, M. Extracellular polymeric substances (EPS) from bioleaching systems and its application in bioflotation. *Minerals Engineering* **2011**, *24*, 1122-1127, doi:10.1016/j.mineng.2011.02.016.
7. Chandraprabha, M.N.; Natarajan, K.A.; Somasundaran, P. Selective separation of arsenopyrite from pyrite by biomodulation in the presence of *Acidithiobacillus ferrooxidans*. *J Colloid Interf Sci* **2004**, *276*, 323-332, doi:10.1016/j.jcis.2004.03.047.
8. Chandraprabha, M.N.; Natarajan, K.A. Surface chemical and flotation behaviour of chalcopyrite and pyrite in the presence of *Acidithiobacillus thiooxidans*. *Hydrometallurgy* **2006**, *83*, 146-152, doi:10.1016/j.hydromet.2006.03.021.
9. Hosseini, T.R.; Kolahdoozan, M.; Tabatabaei, Y.S.M.; Oliazadeh, M.; Noaparast, M.; Eslami, A.; Manafi, Z.; Alfantazi, A. Bioflotation of Sarcheshmeh copper ore using *Thiobacillus ferrooxidans* bacteria. *Minerals Engineering* **2005**, *18*, 371-374, doi:10.1016/j.mineng.2004.06.005.
10. Patra, P.; Natarajan, K. Microbially enhanced removal of pyrite and chalcopyrite from oxide gangue minerals with reference to desulfurization of tailings. *Minerals and Metallurgical Processing* **2004**, *21*, 169-178.
11. Deo, N.; Natarajan, K.A. Interaction of *Bacillus polymyxa* with some oxide minerals with reference to mineral beneficiation and environmental control. *Minerals Engineering* **1997**, *10*, 1339-1354, doi:10.1016/S0892-6875(97)00125-8.
12. Dubel, J.; Smith, R.W.; Misra, M.; Chen, S. Microorganisms as chemical reagents: The hematite system. *Minerals Engineering* **1992**, *5*, 547-556, doi:[https://doi.org/10.1016/0892-6875\(92\)90233-Y](https://doi.org/10.1016/0892-6875(92)90233-Y).
13. Ohmura, N.; Kitamura, K.; Saiki, H. Mechanism of Microbial Flotation Using *Thiobacillus-Ferrooxidans* for Pyrite Suppression. *Biotechnol Bioeng* **1993**, *41*, 671-676, doi:10.1002/bit.260410611.

APPENDIX II: PROCEDURES

Bradford Assay Procedure

This procedure has been adapted from Thermo Scientific [1].

Before beginning, invert the Coomassie reagent gently to mix (do not shake). Remove the amount of reagent required and leave to equilibrate to room temperature before use. Protein – dye complex's absorbance occurs at 595 nm for the 1mm path length and normalised at 750nm.

Prepare the BSA standard solutions for the calibration curve as per the dilutions below.

Working range: 125 – 1500 µg/mL			
<u>Vial</u>	<u>Volume of Diluent (µL)</u>	<u>Volume and source of BSA (µL)</u>	<u>Final BSA concentration (µg/mL)</u>
A	0	300 of stock	2000
B	125	375 of stock	1500
C	325	325 of stock	1000
D	175	175 of vial B dilution	750
E	325	325 of vial C dilution	500
F	325	325 of vial E dilution	250
G	325	325 of vial F dilution	125
H	400	100 of vial G dilution	25
I	400	0	0 = blank

Working range: 1 – 25 µg/mL			
<u>Vial</u>	<u>Volume of Diluent (µL)</u>	<u>Volume and source of BSA (µL)</u>	<u>Final BSA concentration (µg/mL)</u>
A	2370	30 of stock	25
B	4950	50 of stock	20
C	3970	30 of stock	15
D	2500	2500 of vial B dilution	10
E	2000	2000 of vial D dilution	5
F	1500	1500 of vial E dilution	2.5
G	5000	0	0 = blank

Sample preparation for working range of 125 – 1500 µg/mL

1. Pipette 0.03 mL (30 µL) of each sample (standard or unknown) into appropriately labelled test tubes.
2. Add 1.5 mL of Coomassie Reagent to each tube and mix well (ensure reagent is at room temperature). For optimal results that are more consistent, incubate samples at room temperature for 10 minutes.

Sample preparation for working range of 1 – 25 µg/mL

1. Pipette 1.0 mL of each sample (standard or unknown) into appropriately labelled test tubes.
2. Add 1.0 mL of the Coomassie Reagent to each test tube and mix well (ensure reagent is at room temperature). For optimal results that are more consistent, incubate samples at room temperature for 10 minutes.

Making Bradford Protein Measurements on Nano Drop

With the sampling arm in the down position, start the operating software by selecting the following path: Start → Programs → NanoDrop → ND-1000. Select the Protein Bradford module.

1. Measure the reference sample (Bradford reagent with no protein – the blank)
2. Measure the standards for the calibration curve. NOTE: the software allows up to 5 replicates of each standard, up to 7 standards. It is good practice to make measurements in triplicate.
3. Measure samples. NOTE: Sample concentration is calculated using linear interpolation and polynomial fitting. To obtain a concentration value (mg/mL) the sample (unknown) must fall within the limits of the standard curve. Ensure all samples are processed before exiting the Bradford module.

Phenol – Sulfuric acid Assay

Preparation of 5% phenol solution: Weigh out 5g of phenol crystals. Add 95mL of Milli-Q water and shake until dissolved.

Preparing D-Glucose stock solution (2000 μ g/mL): Weigh out 0.002g D-Glucose. Add 10mL of 0.2 μ m Milli-Q water and shake until dissolved.

Prepare the D-Glucose standard solutions for the calibration curve as per the dilutions below.

Working range: 125 – 1500 μg/mL			
<u>Vial</u>	<u>Volume of Diluent (μL)</u>	<u>Volume and source of D-Glucose (μL)</u>	<u>Final D-Glucose concentration (μg/mL)</u>
A	0	300 of stock	2000
B	125	375 of stock	1500
C	325	325 of stock	1000
D	175	175 of vial B dilution	750
E	325	325 of vial C dilution	500
F	325	325 of vial E dilution	250
G	325	325 of vial F dilution	125
H	400	100 of vial G dilution	25
I	400	0	0 = blank
Working range: 1 – 25 μg/mL			
<u>Vial</u>	<u>Volume of Diluent (μL)</u>	<u>Volume and source of D-Glucose (μL)</u>	<u>Final D-Glucose concentration (μg/mL)</u>
A	2370	30 of stock	25
B	4950	50 of stock	20
C	3970	30 of stock	15
D	2500	2500 of vial B dilution	10
E	2000	2000 of vial D dilution	5
F	1500	1500 of vial E dilution	2.5
G	5000	0	0 = blank

Sample preparation for working range of 125 – 1500 µg/mL and 1 – 25 µg/mL

3. Pipette 0.05 mL (50 µL) of each sample (standard or unknown) into appropriately labelled 1.5mL centrifuge tube.
4. Rapidly add 150µL of concentrated sulphuric acid (98%) and shake.
5. Immediately add 30µL of phenol (5%) and incubate the sample at 90°C for 5 minutes.
6. Cool samples to room temperature in another water bath for 5 minutes.
7. Wipe samples dry and analyse at 490nm.

An internal standard of 100 nM can be used to calculate a relative absorbance. A linear relationship between absorbance and sugar concentration exists between the concentrations of 1-150nM.

Making Phenol Sulfuric Acid Assay measurements on Nano Drop

With the sampling arm in the down position, start the operating software by selecting the following path: Start → Programs → NanoDrop → ND-1000. Select UV-Vis module.

Absorbance for the Nano drop in UV-Vis mode is from 220 nm – 750 nm

1. Set the wavelength (λ) to 490nm by selecting the λ 1 box and entering the wavelength.
2. Measure the reference sample (Assay with no carbohydrates – the blank).
3. Measure the standards for the calibration curve. NOTE: the baseline can be set by the horizontal cursor (user selectable-baseline). This absorbance value is subtracted from the absorbance of the spectrum.
4. Measure samples. NOTE: Remember to blank in between samples.

Nuclear Magnetic Resonance Spectroscopy (NMR)

Background

Nuclear Magnetic Resonance (NMR) spectroscopy is a non-destructive spectroscopy technique discovered in 1946, with high resolution NMR becoming one of the most common analytical techniques for the determination of molecular structure [2]. NMR uses the interaction of matter with microwaves to determine complete structural and conformational analysis of complex structures [2,3]. The non-destructive nature allows for chemical analysis in vivo and in vitro [2]. Although NMR has its benefits the detection sensitivity level is considerably low in comparison to other spectroscopy techniques such as mass spectroscopy, immunoassays and gas chromatography [2].

The most common magnetic nuclei/isotopes used for NMR analysis is H^1 (proton NMR) and C^{13} , with other nuclei such as fluorine (F^{19}), sodium (Na^{23}), phosphorus (P^{31}), lithium (Li^7), silicon (Si^{29}) and aluminium (Al^{27}) used less commonly [2,4]. Of these, proton (H^1) NMR spectroscopy is the most sensitive [2]. Nuclei which have neither a magnetic moment or spin are not detectable via NMR [4]. NMR spectroscopy can be used as a fingerprinting tool for compounds as each atomic nuclei has only one resonance frequency when placed in a constant magnetic field under vacuum [2]. For resonance of the nuclei to occur the radio frequency is equivalent to the precessional frequency (proportional to the strength of the magnetic field generated by the electron density) of the given nuclei [2].

As NMR is a spectroscopic technique, it looks at the absorption and emission of radio frequency (rf) energy of a nucleus placed in a magnetic field [2]. This is based on the concept that when a nucleus is placed in a magnetic field, transitions between the Zeeman levels are induced [4]. Transitions can occur from both lower energy to higher energy and higher energy to lower energy, with the lower energy level being more densely populated as stated by Boltzmann distribution [2,4]. The magnetic field can influence the population between the different states as the energy difference is proportional to the magnetic field strength [2]. The signal intensifies when the difference between the low energy state and the high energy state increases, leading to an overall absorption of radio frequency producing a spectrum [2].

There are three important components to a NMR spectrometer being the magnet, the probe and the computer [2]. The solenoid magnet used is a superconductor, typically produced from

an alloy of titanium and niobium coil, to ensure the magnetic field is stable and strong (field strengths up to 750 Hz for H^1) [2]. To ensure that the magnet can carry a high current without detrimental effects such as heat generation or electron loss, it is kept at an extremely low temperature (approximately $-269\text{ }^\circ\text{C}$) [2]. The probe has a sample cavity, which allows for spinning of the sample, along with a transmitter coil and a receiver coil [2]. These coils are important as they produce smaller magnetic fields of different shapes. The production of these smaller fields guarantees a homogeneous field around the sample [2]. The homogeneity of the magnetic field and the spinning of the sample is used to produce higher spectral resolution [2]. The computer and electronic devices used to collect the data are also important, as they are used to detect, amplify and display the signal collected [2]. Solid, liquid and gaseous samples can be analysed, with liquid samples giving higher amplitude signals [4]

NMR can be used as a quantitative technique to help determine articular compounds, such as carbohydrates and their concentration along with measuring the moisture concentration of a sample [4,5]. Moisture within a sample can be detected as the hydrogen nuclei present in a water molecule interacts differently than hydrogen nuclei present in a solid. The different interactions leads to a difference in signals, with water producing an intense sharp peak, while the solid produces a slightly broader peak [4]. The peak areas of the spectrum can be used to determine concentration [2].

Characterisation of compounds and complex molecules uses the chemical shift of the nuclei being studied. Chemical shift (δ) occurs when the atom forms different types of bonds within the molecule [2,4]. A reference compound, for the selected nuclei, is used to determine the extent of the chemical shift is used. The shift is typically reported as parts per million (ppm) and in the order of 10^{-6} [2,4]. Significant shifts can occur due to the field inside the electron shell or alterations of the applied field inside the sample [4]. Splitting of the resonance occurs due to electronic orbital motions and is field independent [4]. This splitting arises from interactions with neighbouring nuclei which are chemically different [4]. The structure of the compound, such as the number and type of bonds, influences the coupling and spacing of the resonance [4]. The resonance is influenced by the shielding effects of the electron cloud, an increase in the density of the electron cloud increases the shielding [2] with less shielded nuclei appearing at the lowest applied field [4]. These shifts and couplings are characteristic and can be used for both identification and quantification of compounds [2].

Sample Preparation

NMR was conducted on both crude EPS and the isolated exopolysaccharide component; extraction methods are covered in Section 3.3.6. Complex carbohydrate structures can sometimes create issues (solubility and decreased amplitude of signal), therefore further reduction of the isolated exopolysaccharide was conducted. Figure 3.7 below illustrates the hydrolysis, reduction and acetylation reaction undertaken to reduce the polysaccharide to acetylated monosaccharides. The acetylated monosaccharides are then able to be analysed through gas chromatography.

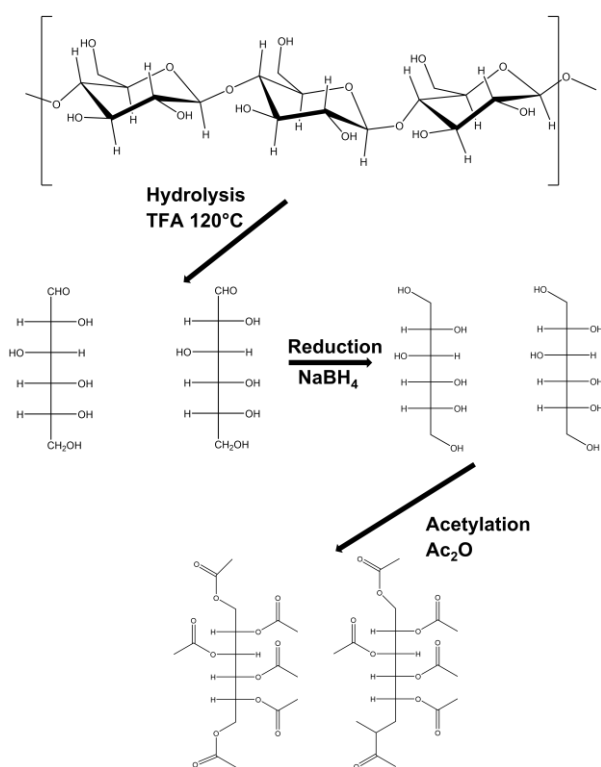


Figure 0.1: Hydrolysis, reduction and acetylation reaction for polysaccharides

Isolation of Exopolysaccharide

Method adapted from Lima, et al. [6], Patra and Natarajan [7], and Weaver and Hicks [8]

1. Cells and mineral particles are removed through filtration using a 0.4 μ m filter under slight vacuum.
2. TCA (80%) is added to the EPS supernatant at a 1:6 ratio and homogenised using a vortex mixer. Once homogenised, the solution is centrifuged at 10,000 x g for 10 minutes. Supernatant is decanted, collected and stored at -80°C before precipitation.

NOTE: Addition of the TCA should induce protein precipitation

3. Ice cold ethanol (96°GL) is added to the EPS supernatant in a ratio of 4:1 and the sample homogenised before being left to rest at 4°C for a minimum of 18 h.
4. Precipitate is collected through centrifugation (10,000 x g for 10 minutes) and washed with cold ethanol at least twice. Precipitate is dried under reduced pressure.

Total acid Hydrolysis of Carbohydrates

Method adapted from Lima, et al. [6], and Aires, et al. [9]

5. Approximately 2mg of sample is treated with 0.5mL trifluoroacetic acid (2M) for 1 hour at 120°C. The acid was removed by evaporation under reduced pressure.
6. Sample was redissolved in 0.7 M NH₄OH (500µL) and held at room temperature for 10 minutes.
7. 1mg NaBH₄ was added and the solution was maintained at 100°C for 10 minutes.
8. The product was dried and excess NaBH₄ removed by the addition of HOAc (100µL). Boric acid was removed by the addition of methanol (2 x 2mL) followed by evaporation.
9. Acetylation was performed in 400µL Pyridine:Ac₂O (1:1 v/v) at 100°C for 30 minutes.
10. Iced water was added and the alditol acetates were extracted with ~1mL CHCl₃.

Analysis through Gas Chromatography

Initial temperature 50°C, held for 2 minutes.

Ramp 1: 20°C/minute to 220°C, held for 5 minutes

Ramp 2: 40°C/minute to 280°C held for 2 minutes

References

1. Thermo Scientific. Coomassie (Bradford) Protein Assay Kit. ThermoFisher Scientific: 2013; Vol. 23200, p 7.
2. Smith, I.C.; Blandford, D.E. Nuclear magnetic resonance spectroscopy. *Anal Chem* **1995**, *67*, 509R-518R.
3. Donati, E.R.; Sand, W. *Microbial processing of metal sulfides*; Springer: Dordrecht, Netherlands, 2007.
4. Shoolery, J.N. Nuclear Magnetic Resonance Spectroscopy. *Analytical Chemistry* **1954**, *26*, 1400-1403, doi:10.1021/ac60093a002.
5. Albalasmeh, A.A.; Berhe, A.A.; Ghezzehei, T.A. A new method for rapid determination of carbohydrate and total carbon concentrations using UV spectrophotometry. *Carbohydr Polym* **2013**, *97*, 253-261, doi:10.1016/j.carbpol.2013.04.072.
6. Lima, L.F.; Habu, S.; Gern, J.C.; Nascimento, B.M.; Parada, J.L.; Nosedá, M.D.; Goncalves, A.G.; Nisha, V.R.; Pandey, A.; Soccol, V.T., et al. Production and characterization of the exopolysaccharides produced by *Agaricus brasiliensis* in submerged fermentation. *Appl Biochem Biotechnol* **2008**, *151*, 283-294, doi:10.1007/s12010-008-8187-2.
7. Patra, P.; Natarajan, K.A. Microbially induced flocculation and flotation for separation of chalcopyrite from quartz and calcite. *International Journal of Mineral Processing* **2004**, *74*, 143-155, doi:10.1016/j.minpro.2003.10.006.
8. Weaver, D.T.; Hicks, R.E. Biodegradation of Azotobacter vinehni exopolymer by Lake Superior microbes. *Limnol. Oceanogr* **1995**, *40*, 1035-1041.
9. Aires, C.P.; Koo, H.; Sasaki, G.L.; Iacomini, M.; Cury, J.A. A procedure for characterizing glucans synthesized by purified enzymes of cariogenic *Streptococcus mutans*. *International Journal of Biological Macromolecules* **2010**, *46*, 551-554, doi:<https://doi.org/10.1016/j.ijbiomac.2010.01.018>.

APPENDIX III: SULFUR XPS

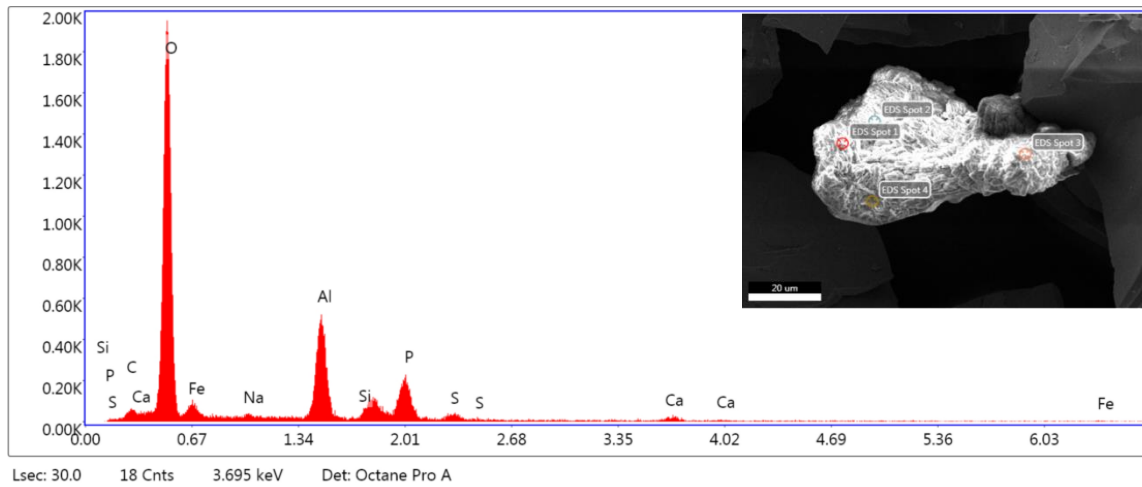
Table 0.1: High-resolution S 2p fit component information for cold stage scans

Sample	Component													
	Disulfide 162.50 ± 0.01 eV		Monosulfide 161.75 ± 0.04 eV		Polysulfide 163.23 ± 0.16 eV		Sulfite 165.84 ± 0.03 eV		Thiosulfate 166.99 eV		Sulfate 168.57 ± 0.32 eV		Energy Loss Feature 164.90 ± 0.01 eV	
	FWHM	Conc.	FWHM	Conc.	FWHM	Conc.	FWHM	Conc.	FWHM	Conc.	FWHM	Conc.	FWHM	Conc.
Unreacted	0.52	79.02	0.48	5.19	0.83	4.80	0.75	1.03	-	-	0.84	1.53	2.26	8.43
HH 24 h	0.51	73.32	0.61	7.58	0.91	6.30	1.47	1.92	-	-	1.68	1.05	2.23	7.82
HH 48 h	0.51	76.87	0.61	7.40	0.63	3.94	0.86	0.75	0.76	1.24	1.01	1.59	2.02	8.20
HH 72 h	0.51	75.84	0.53	6.90	0.83	5.07	-	-	-	-	1.02	4.11	2.02	8.09
HH 168 h	0.51	76.02	0.56	7.85	0.78	5.73	0.46	0.64	-	-	1.15	1.65	2.06	8.11
Af 24 h	0.51	71.43	0.66	9.89	0.78	5.65	-	-	-	-	1.49	5.41	2.06	7.62
Af 48 h	0.51	73.86	0.57	7.73	0.85	5.58	-	-	-	-	1.21	4.95	1.98	7.88
Af 72 h	0.52	73.2	0.61	6.78	0.97	7.12	0.34	0.41	-	-	1.24	4.59	2.35	7.81
Af 168 h	0.51	48.3	0.73	5.73	0.82	18.57	0.85	1.99	-	-	1.31	20.25	1.57	5.15

Table 0.2: High-resolution S 2p fit component information for ambient scans

Sample	Component													
	Disulfide 162.50 ± 0.01 eV		Monosulfide 161.75 ± 0.04 eV		Polysulfide 163.23 ± 0.16 eV		Sulfite 165.84 ± 0.03 eV		Thiosulfate 166.99 eV		Sulfate 168.57 ± 0.32 eV		Energy Loss Feature 164.90 ± 0.01 eV	
	FWHM	Conc.	FWHM	Conc.	FWHM	Conc.	FWHM	Conc.	FWHM	Conc.	FWHM	Conc.	FWHM	Conc.
Unreacted	0.58	77.02	0.65	6.75	0.78	4.20	0.95	1.75			0.85	2.06	1.85	8.22
HH 24 h	0.56	78.84	0.52	6.30	0.91	3.71	0.74	0.78			0.90	1.97	2.55	8.41
HH 48 h	0.56	77.01	0.61	6.02	0.95	4.19	1.00	1.60			1.39	2.97	1.74	8.21
HH 72 h	0.54	76.50	0.60	8.02	0.73	4.33	-	-			1.05	3.00	2.02	8.16
HH 168 h	0.55	76.95	0.64	7.88	0.73	3.21	0.86	1.08			1.18	2.68	2.04	8.21
Af 24 h	0.56	73.58	0.58	7.38	0.95	4.91	-	-			1.14	6.28	2.36	7.85
Af 48 h	0.55	73.11	0.69	9.45	0.81	4.26	-	-			1.42	5.37	2.58	7.80
Af 72 h	0.57	74.2	0.69	6.99	0.75	4.86	0.52	0.58			1.19	5.46	2.35	7.91
Af 168 h	0.62	52.47	0.80	4.98	0.68	12.45	0.88	1.77			1.15	22.74	1.99	5.60

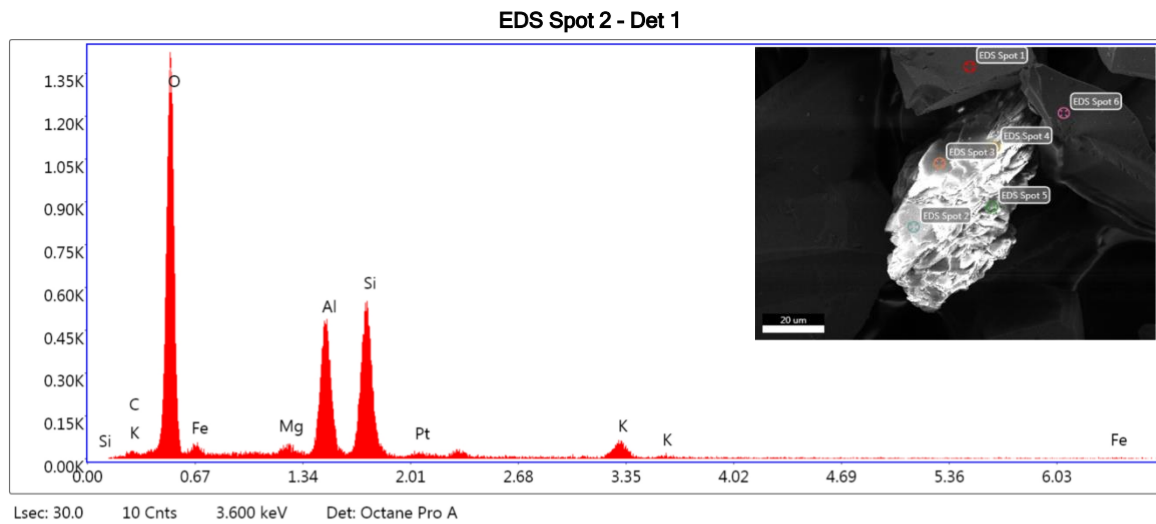
APPENDIX IV: EDAX ANALYSIS



eZAF Smart Quant Results

Element	Weight %	Atomic %	Net Int.	Error %	Kratio	Z	A	F
C K	1.14	1.90	4.35	83.29	0.0033	1.1290	0.2584	1.0000
O K	55.61	69.85	793.39	6.17	0.3809	1.0676	0.6415	1.0000
FeL	4.52	1.63	15.84	21.90	0.0205	0.7954	0.5691	1.0000
NaK	0.21	0.19	2.31	99.99	0.0014	0.9570	0.6733	1.0024
AlK	18.38	13.69	267.05	4.88	0.1508	0.9308	0.8776	1.0040
SiK	3.01	2.15	40.11	8.60	0.0248	0.9482	0.8633	1.0060
P K	12.06	7.82	119.17	6.77	0.0993	0.9079	0.9036	1.0036
S K	1.76	1.10	16.07	22.66	0.0149	0.9230	0.9110	1.0046
CaK	3.31	1.66	13.97	23.39	0.0291	0.8780	0.9857	1.0157

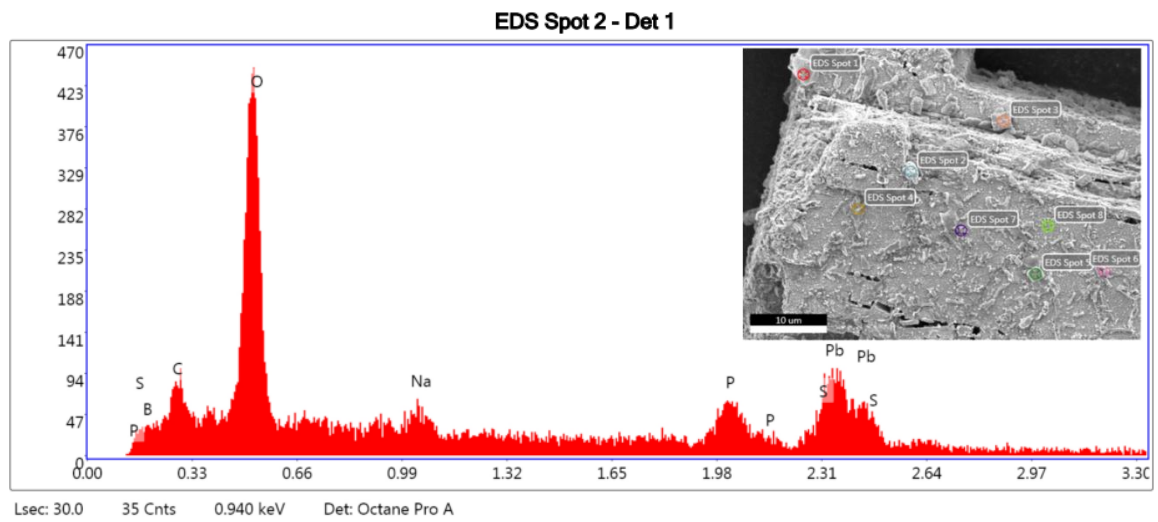
Figure 0.1: EDAX of impurity with multiple faces/cleavages observed in the chalcopyrite sample



eZAF Smart Quant Results

Element	Weight %	Atomic %	Net Int.	Error %	Kratio	Z	A	F
C K	0.26	0.46	0.87	98.31	0.0007	1.1410	0.2409	1.0000
O K	45.72	60.79	547.30	6.99	0.2846	1.0794	0.5767	1.0000
FeL	2.16	0.82	7.53	34.38	0.0106	0.8043	0.6090	1.0000
MgK	1.55	1.35	22.05	12.39	0.0126	0.9810	0.8230	1.0041
AlK	18.53	14.61	255.50	4.69	0.1559	0.9415	0.8899	1.0041
SiK	23.52	17.81	294.25	4.93	0.1964	0.9592	0.8692	1.0016
PtM	0.79	0.09	3.00	42.27	0.0051	0.5668	1.0700	1.0641
K K	7.47	4.06	37.48	13.48	0.0638	0.8758	0.9712	1.0046

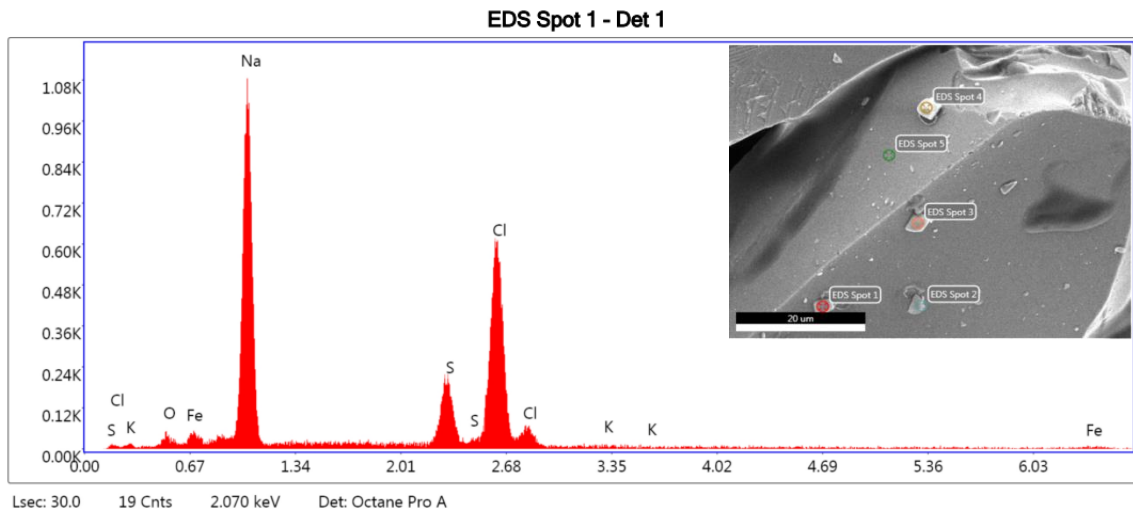
Figure 0.2: EDAX of impurity with multiple thin layers suspected to be a clay like mineral



eZAF Smart Quant Results

Element	Weight %	Atomic %	Net Int.	Error %	Kratio	Z	A	F
B K	3.46	12.32	7.52	23.94	0.0314	1.5739	0.5764	1.0000
C K	3.88	12.44	24.42	15.86	0.0363	1.6354	0.5719	1.0000
O K	19.79	47.57	170.76	9.18	0.2049	1.5388	0.6729	1.0000
NaK	1.19	2.00	6.93	73.81	0.0135	1.3755	0.8199	0.9999
P K	11.25	13.97	32.78	17.75	0.1426	1.3140	0.9638	1.0009
S K	0.49	0.59	1.11	99.99	0.0064	1.3417	0.9662	1.0017
PbM	59.93	11.12	51.55	15.48	0.4227	0.6892	1.0244	0.9990

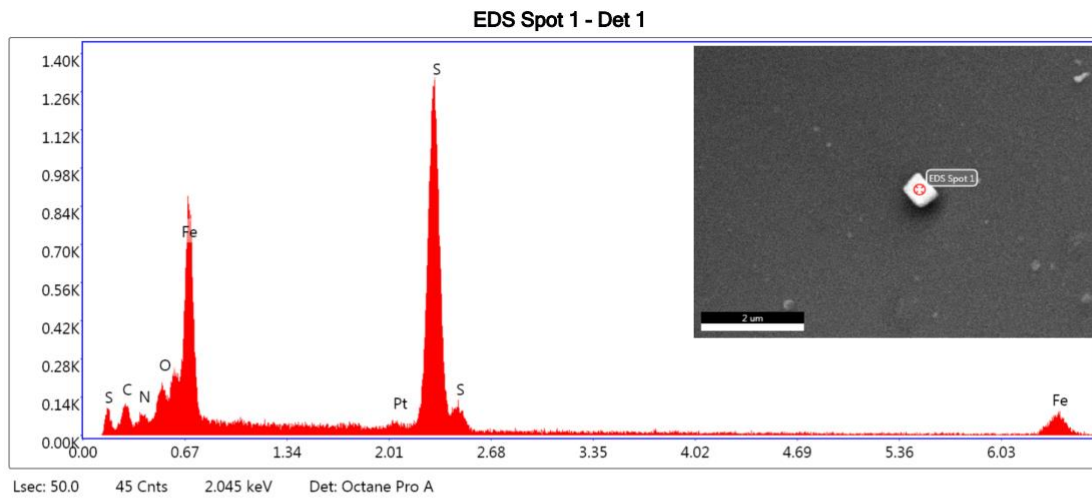
Figure 0.3: EDAX of the cubic impurity found in chalcopyrite, with the lead:sulfur ratio indicating a galena phase



eZAF Smart Quant Results

Element	Weight %	Atomic %	Net Int.	Error %	Kratio	Z	A	F
K L	0.00	0.00	0.00	99.99	0.0000	0.9598	0.2023	1.0000
O K	0.37	0.67	2.90	79.17	0.0015	1.1685	0.3537	1.0000
FeL	0.79	0.42	3.98	52.51	0.0056	0.8712	0.8147	1.0000
NaK	35.96	45.85	479.67	4.73	0.3109	1.0492	0.8228	1.0014
S K	12.27	11.22	120.47	6.32	0.1212	1.0138	0.9550	1.0197
ClK	50.60	41.84	391.32	3.96	0.4613	0.9618	0.9468	1.0009

Figure 0.4: EDAX of precipitated salts on the pyrite surface



eZAF Smart Quant Results

Element	Weight %	Atomic %	Net Int.	Error %	Kratio	Z	A	F
C K	8.56	21.72	15.90	19.32	0.0142	1.2423	0.1337	1.0000
N K	1.49	3.24	5.30	40.00	0.0041	1.2082	0.2296	1.0000
O K	3.77	7.19	31.98	13.56	0.0180	1.1785	0.4044	1.0000
FeL	32.35	17.65	147.41	5.22	0.2231	0.8792	0.7845	1.0000
PtM	1.20	0.19	6.89	40.85	0.0127	0.6231	1.1358	1.5005
S K	52.63	50.02	477.85	3.46	0.5182	1.0269	0.9575	1.0012

Figure 0.5: EDAX of singular cubic debris on the pyrite surface